Magnetic Anisotropy in Epitaxial Ni/Cu (001) Thin Films and Cu/Ni/Cu (001) Sandwiches

by

Gabriel Bochi

Bachelor of Science in Physics
Mc Gill University (1990)

Submitted to the Department of Materials Science and Engineering
in partial fulfillment of the requirements for the degree of

Doctor of Philosophy

at the

Massachusetts Institute of Technology

June 1995

Author.....
Department of Materials Science and Engineering
May 5, 1995

Certified by.....
Robert C. O'Handley
Senior Research Scientist
Thesis Supervisor

Certified by.....
Carl V. Thompson II
Professor of Electronic Materials
Thesis Supervisor

Accepted by.....
Carl V. Thompson II
Professor of Electronic Materials
Chair, Departmental Committee on Graduate Students

To Angéline,
for her infinite love, her sacrifices, and her determination.

To Michel,
for his continuous encouragement and his wise teachings.

To Ronald,
for believing in me.

To Juan and Ariette,
for their love and generosity.

To my teachers of the Lycée Stendhal,
for making me thirsty of knowledge, for strengthening my passion for science, and for teaching me to appreciate the arts.

Magnetic Anisotropy in Epitaxial Ni/Cu (001) Thin Films and Cu/Ni/Cu (001) Sandwiches

by

Gabriel Bochi

Submitted to the Department of Materials Science and Engineering
on May 5, 1995, in partial fulfillment of the requirements for the degree of
Doctor of Philosophy

Abstract

We have studied the magnetic anisotropy in epitaxial Ni/Cu/Si (001) thin films and Cu/Ni/Cu/Si (001) sandwiches. The Ni thickness ranged between 10 Å and 150 Å. The films were deposited using molecular beam epitaxy and were characterized using several techniques. The magnetic properties were determined *in-situ* using the magneto-optic Kerr effect and *ex-situ* using a vibrating sample magnetometer. The average in-plane strain $e_0(h)$ in the Ni films was measured *ex-situ* using an optical interferometry apparatus. We discovered that the preferred direction of magnetization is perpendicular to the films over an exceptionally broad Ni thickness range: from $h \approx 10$ Å to $h \approx 60$ Å in films characterized *in-situ;* it extends up to $h \approx 125$ Å when the films are exposed to air or capped with a Cu layer. In Fe/Cu (001) thin films, the perpendicular region extends only up to $h \approx 11$ Å. We have analyzed our quantitative measurements of the effective magnetic anisotropy energy K^{eff} as a function of film thickness in Cu/Ni/Cu sandwiches using our measurements of the strain and a phenomenological model that includes surface magnetocrystalline (K^s/h) and both bulk ($B^b e_0$) and surface ($B^s e_0/h$) magnetoelastic anisotropy energies. We showed that one cannot explain the behavior of $K^{eff}(h)$ without the inclusion of a surface magnetoelastic coupling coefficient B^s in the free energy. We find that K^s(Ni/Cu) (001) $\approx +0.85$ erg/cm^2 and that B^s(Ni/Cu) (001) ≈ -50 erg/cm^2. In agreement with the Néel model, K^s and B^s have opposite signs. The origin of the strong perpendicular magnetic anisotropy in Ni/Cu (001) lies in the surface energy K^s and the bulk magnetoelastic anisotropy energy. The surface energy $B^s e_0$ favors an in-plane magnetization. The effective magnetoelastic coupling coefficient $B^{eff} = B^b + \frac{B^s}{h}$ depends strongly on h for $h \leq 200$ Å and changes sign near $h = 80$ Å. The two observed in-plane to out-of-plane magnetization easy-axis transition thicknesses are also qualitatively predicted by our phenomenological model. The lower transition thickness ($10 \text{ Å} \leq h \leq 20$ Å) is most likely not due to the onset of misfit dislocations at the Ni/Cu interface.

Thesis Supervisor: Robert C. O'Handley

Title: Senior Research Scientist

Thesis Supervisor: Carl V. Thompson II

Title: Professor of Electronic Materials

Acknowledgments

I am very grateful to Dr. Robert C. O'Handley, my research supervisor, for his excellent guidance, his encouragement, his enlightening suggestions, and for always being available when I needed his support. I thank him for giving me the opportunity to work on a very interesting and challenging project, and to attend several international conferences. I also thank him for simultaneously assigning me demanding responsibilities and granting me much freedom to conduct original research. His human warmth, his sense of humor, and his broad interests in life have made it a great pleasure to work for him.

I wish to thank Dr. Craig A. Ballentine for his outstanding technical support, his challenging discussions, and for teaching me to smile in the most frustrating situations in an ultra-high vacuum laboratory.

I thank the members of my thesis committee: Prof. Carl V. Thompson, for being my co-advisor, for his very encouraging comments, and for expressing a continuous interest in my research; Prof. Harry L. Tuller, for his encouragement and for being my first teacher in our department; Prof. Gerbrand Ceder, for his interest in my work and his very useful advises regarding writing the present thesis.

I thank all the members of the Thin Film Magnetism group. I am very grateful to Heather E. Inglefield, my partner in this project, for giving me very useful experimental information on the microstructure of the Ni/Cu thin films, for teaching me how to use the MBE system, and for depositing some films for me. I thank Dr. Donna S. Chuang for always being there when I needed her help and for very stimulating discussions on surface magnetism. Her good nature and cheerful character made it a pleasure to work with her. I thank Dr. Ohsung Song for many useful suggestions concerning the General Examination in Electronic Materials. I have greatly enjoyed sharing my office with Dr.

Chang-Kyung Kim. I have enjoyed many entertaining conversations with Robin Lippincott on literature and jazz which are unfortunately rare disciplines at MIT.

I thank Prof. George Koster of the Physics Department of MIT for assigning me a Teaching Assistant position in the spring of 1991.

Dr. Paul D. Bristowe helped me with the embedded-atom method calculations.

The help and suggestions of the technicians and machinists of MIT is gratefully acknowledged. In particular, I thank Tim McClure and Rich Perilli.

I thank Dr. Fayez Kebe, Nicolaki Kebe, and Yolanda Kebe de Hatem for their affection, their continuous interest in my career plans, their advises, and their encouragement.

I have enjoyed many friendships within the international and multicultural community of MIT. The number of people that I need to thank for their unique company and their moral support is infinite.

I thank the Natural Sciences and Engineering and Research Council of Canada for awarding me a Postgraduate Scholarship and allowing me to bring it to the US.

This work was supported by grants from the National Science Foundation and the Army Research Office.

Table of Contents

List of Illustrations and Figures

List of Tables

Chapter 1
Introduction

Magnetic thin films have attracted tremendous attention in the past decade largely due to the crucial role they play in information storage technology [Falicov *et al.*, 1990; Hadjipanayis and Prinz, 1991; Freeman and Gschneider, 1991; Gradmann, 1993; Allenspach, 1994]. The ever-growing need for denser storage media and faster read-write magnetic heads has led to very significant advances in the science and technology of magnetic recording such as the discovery of the giant magnetoresistance (GMR) effect [Falicov, 1992; White, 1992] and the demonstration of perpendicular magnetic recording [Zeper *et al.*, 1991], both of which require the deposition of high quality films and multilayers often thinner than 100 Å. In this thickness regime, unique physical and chemical phenomena prevail in thin films, making them behave very differently from bulk materials.

The surface of a solid is generally subject to relaxation strains normal to the surface which can be either tensile or compressive and which can be as large as 10% [Freeman and Fu, 1987; Davis *et al.*, 1992]. These strains are due to the broken symmetry in the atomic coordination at the surface which yields different electronic and spin density distributions there compared to the bulk. As a result, the first few atomic layers near the surface of a cubic solid are generally distorted tetragonally compared to the bulk. The surface of a thin film is subject to the same relaxation effects as the surface of a bulk material. This can have tremendous consequences on the magnetic anisotropy of the film through magnetoelastic interactions, especially when the film is ultrathin. In addition, epitaxial thin films are subject to in-plane biaxial misfit strains arising from the lattice mismatch between the thin film and the thick substrate [Nix, 1989]. These strains, which also deform thin films tetragonally, are less than 10% in magnitude. Other sources of strain which are potentially important but are not always well understood are

interfacial misfit dislocations [Clemens *et al.*, 1991], surface roughness [Spencer *et al.*, 1993], and film-substrate thermal expansion coefficient mismatch [Nix, 1989]. Two important interfacial chemical phenomena are also significant in magnetic thin films: interdiffusion and surface segregation.

The above modifications to the structural, chemical and electronic properties of thin films due to interfacial phenomena can give rise to dramatic changes in the fundamental properties of the films. These changes have been predicted theoretically and observed experimentally, and include: enhanced or reduced magnetic moments at film-substrate interfaces [Tersoff and Falicov, 1982; Zhu *et al.*, 1984; Fu and Freeman, 1987; Wooten *et al.*, 1994]; strong uniaxial magnetic surface anisotropy [Gay and Richter, 1986; Gradmann, 1993] often considered to be the origin of the perpendicular magnetic anisotropy in thin films and multilayers; enhanced or reduced Curie temperatures compared to the bulk [Rau and Robert, 1987; Tjeng *et al.*, 1991; Huang *et al.*, 1994]; giant magnetoelastic coupling coefficients [Song *et al.*, 1994; Weber *et al.*, 1994]; and anomalous elastic constants [Cammarata and Sieradzki, 1989].

These unique properties make magnetic thin films one of the most challenging classes of condensed matter both from scientific and technological points of view. In fact, the explosive growth witnessed in recent years in the field of thin film magnetism has only been possible through an impressive development of several state-of-the-art experimental and computational techniques. Three major advances need to be emphasized:

i) the development of very sophisticated ultra-high vacuum evaporation techniques, such as molecular beam epitaxy (MBE), which are capable of depositing high-quality thin films with sub-monolayer thickness resolution at temperatures ranging from below 100 K to several hundred degrees.

ii) the availability of very high resolution structural, chemical, and magnetic characterization techniques which are ultra-high vacuum compatible. Electron diffraction techniques such as RHEED and LEED are used very frequently to study *in-situ* the surface crystallography of thin films. Other techniques are capable of the nearly atomic resolution of the topography and structure of thin films. They include scanning tunneling microscopy (STM), high-resolution transmission electron microscopy (TEM), and high-resolution X-ray diffraction requiring synchrotron sources. Auger electron spectroscopy (AES) has been developed to investigate the chemical properties of thin films but it is

also useful to indirectly measure the thickness and the growth mode of ultrathin films because of its extremely shallow surface sensitivity. Measurement techniques capable of a monolayer resolution have also been developed and include X-ray and UV photoelectron spectroscopies [Egelhoff, 1994]. The magnetic properties of ultrathin films can be investigated *in-situ* using the magneto-optic Kerr effect (MOKE) which can detect the magnetic anisotropy of films as thin as one monolayer [Bader, 1991]. Other instruments such the spin-polarized SEM (known as SEMPA) and the magnetic force microscope (MFM) are capable of resolving domain walls in ultrathin films [Allenspach, 1994].

iii) the development of very sophisticated *ab initio* computation techniques that can be used to calculate the thickness dependence, crystallographic orientation dependence, and interfacial dependence of the magnetic anisotropy in ultrathin films and superlattices [Gay and Richter, 1986; Daalderop *et al.*, 1992; Victora and MacLaren, 1993]. The application of these complex calculations to realistic thin film systems has been made possible by the increasing availability of fast, operationally inexpensive, and numerically intensive computers.

Several epitaxial magnetic thin film systems have been investigated both experimentally and computationally in the past ten years. In some of these systems, such as fcc Fe/Cu thin films , bcc Fe/Ag thin films and multilayers, and Co/Pd superlattices, it was found that the magnetization prefers to point perpendicular to the film plane over a finite film thickness range. Other epitaxial systems, such as Co/Cu thin films and multilayers, did not exhibit this unusual and intriguing property. The Ni/Cu epitaxial system has received less attention than the above systems possibly because of the relatively weak magnetic moment of Ni. However, Ni thin films are very appealing because of the very strong magnetoelastic interactions in Ni which, coupled to a significant misfit strain (2.6% in the case of Ni/Cu (001)), could give rise to an important contribution to the magnetic anisotropy.

In this thesis, we present our experimental results on the magnetic anisotropy in Ni/Cu (001) thin films and Cu/Ni/Cu (001) sandwiches. The films were deposited on Si (001) wafers using MBE and were characterized *in-situ* using MOKE and *ex-situ* using a vibrating sample magnetometer (VSM). The crystallographic orientation and the interfacial properties of the films as well as the thickness dependence of the strain have been investigated using various *in-situ* and *ex-situ* techniques. We have discovered that the Ni/Cu (001) system exhibits the largest thickness range of perpendicular

magnetization of any epitaxial thin film system reported so far. In order to understand the origin of the strong perpendicular magnetic anisotropy in Ni/Cu (001) thin films, we have analyzed our quantitative measurements of the effective magnetic anisotropy energy density as a function of film thickness using a complete phenomenological model and our own measurements of the thickness dependence of the strain in the Ni films. Although the importance of misfit strain on the magnetic anisotropy of heteroepitaxial thin films has already been pointed out [Gradmann, 1966; Chappert and Bruno, 1988], very few research groups have simultaneously reported measurements of strain and magnetic anisotropy in their thin films [Lee *et al.*, 1990; Engel *et al.*, 1991] and carried their analysis to the level we did. Our analysis yields new and important results on the magnetic surface anisotropy energy of the Ni/Cu (001) interface and the thickness dependence of the magnetoelastic coupling coefficients in Ni/Cu (001) thin films.

This thesis is organized as follows. We will start by explaining the various forms of magnetic anisotropy in bulk materials and in thin films. In chapter 3, we will review the results of the recent pioneering works that led to the discovery of perpendicular magnetic anisotropy in epitaxial thin films and multilayers. Based on these results and the first study of the magnetic anisotropy in ultrathin epitaxial Ni/Cu (001) thin films [Ballentine, 1989] we will ask a series of key questions on the complex behavior of the magnetic anisotropy in Ni/Cu (001). These questions justify the directions that we have undertaken and motivate the experiments that we have performed in this thesis. We will attempt to answer these questions in chapters 6 to 9. In chapter 4, we will review the mechanisms of misfit strain accommodation in epitaxial thin films. We will emphasize misfit strain relief through the onset of interfacial misfit dislocations and will quantitatively describe the huge strain fields that develop around the dislocation cores. We will also present recent measurements of the thickness dependence of average in-plane biaxial tensile misfit strain in Ni/Cu (001) and compare them to the theoretical predictions of the Matthews-Blakeslee thermodynamic model. The experimental procedures we used to deposit and characterize our thin films are presented in chapter 5 which also includes the main experimental results on the growth mode in Ni/Cu/Si (001). In chapter 6, we present our experimental results on the behavior of the magnetic anisotropy in Ni/Cu (001) thin films and Cu/Ni/Cu (001) sandwiches. We will show how the commonly used phenomenological model presented in chapter 2 is inadequate to explain the thickness dependence of the effective magnetic anisotropy energy in Cu/Ni/Cu (001). In chapter 7, we will present and explain a more complete phenomenological model, developed recently by Chuang *et al.* [1994], which is based on

the Néel model but that also includes strain-dependent interactions in the computation of the magnetic surface anisotropy energy. In chapter 8, we will re-analyze the data of chapter 6 in the light of the results of chapter 7 and propose an explanation for the origin of the strong perpendicular magnetic anisotropy in Ni/Cu (001) thin films. We will also analyze published data on the thickness dependence of the magnetic anisotropy and of the misfit strain in fcc Co/Cu (111) superlattices using the model of chapter 7 and will obtain new results on the magnetoelastic coupling in fcc Co ultrathin films and the magnetic surface anisotropy energy corresponding to the fcc Co/Cu (111) interface. In chapter 9, we will draw our main conclusions and in chapter 10 we will suggest a series of experiments that can further extend our understanding of the magnetic anisotropy in Ni/Cu (001) thin films. Finally, we will present our preliminary results on the computation of the stress relaxation at the Ni/Cu (001) interface using the semi-empirical embedded-atom method in the appendix.

Chapter 2
Magnetic Anisotropy

The preference of the magnetization to lie in a particular direction in a ferromagnetic solid is called magnetic anisotropy. It finds its origin in the shape of the sample (magnetostatic anisotropy), in the symmetry of the crystal field of a bulk material (magnetocrystalline anisotropy), in the broken symmetry of the atomic coordination at the solid's interfaces (magnetic surface anisotropy), or in the state of strain of the solid (magnetoelastic anisotropy). The magnetostatic anisotropy has a macroscopic origin based on the dipole-dipole interaction. The three other forms of magnetic anisotropy have a microscopic origin based on atomic arrangements and on the spin-orbit interaction. We will review each form of magnetic anisotropy separately from a phenomenological point of view.

2.1. Magnetostatic Anisotropy

Magnetostatic (MS) or shape anisotropy has its origin in the dipole-dipole interaction between neighboring magnetic moments in a magnetic material. When a ferromagnetic material is magnetized along a certain direction, positive and negative magnetic "charges" accumulate at the north and south pole respectively. These "charges" create an internal field $\mathbf{H_d}$ (pointing from the positive to the negative "charges") which tends to demagnetize the material in its own field! The larger the ratio of lateral extent to the closeness of the boundaries bearing these charges, the stronger $\mathbf{H_d}$. It is therefore much easier to magnetize a rod along its length and a thin film in its plane than perpendicular to it. This phenomenon is illustrated schematically in Fig. 2.1. Figure 2.1.a shows a sample magnetized parallel to a short direction. The orientation of

magnetic moments inside the sample indicates that there are fewer North-South pairs (head-to-tail arrows) relative to North-North (head-to-head arrows) and South-South (tail-to-tail arrows) pairs. The dipole-dipole interaction, which favors the alignment of neighboring magnetic dipoles in a chain, makes this a high energy configuration. The situation depicted in Fig. 2.1.b with the external magnetic field applied along a long dimension of the sample represents a much lower energy configuration. Even though the magnetic "charge" density on the boundaries is the same as the one in Fig. 2.1.a there are more North-South pairs relative to North-North and South-South pairs. That is the extensive magnetostatic energy is what is important in making configuration b favored over a.

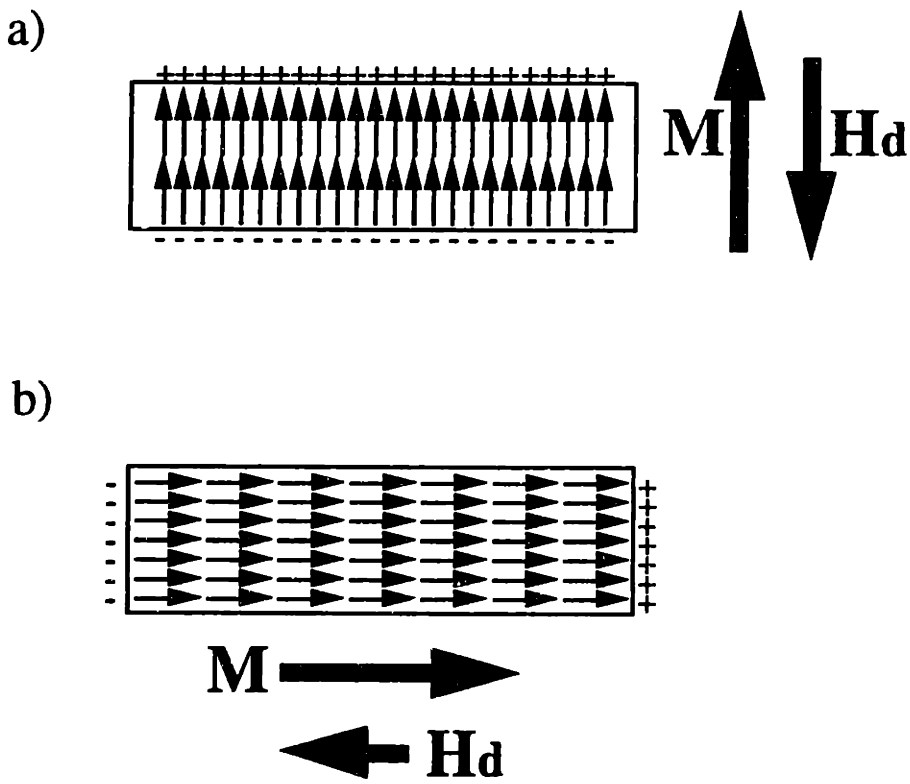

Figure 2.1: Illustration of the concept of shape anisotropy. a) Highest energy configuration state in which the elongated material is magnetized in a direction perpendicular to its length thus creating a relatively large demagnetizing field. b) Lowest energy configuration state in which the elongated material is magnetized along its length thus creating a relatively small demagnetizing field. The small arrows drawn inside the material represent the individual local magnetic moments.

The energy density associated with the shape anisotropy of a thin film can be expressed approximately as follows:

$$K^{MS} = - 2\pi M_s^2 \sin^2\theta , \qquad (2.1)$$

in cgs units. M_s is the saturation magnetization and θ is the angle that the magnetization vector makes with the film normal. In agreement with the above discussion, this energy reaches a minimum when $\theta = 90°$, i. e. when the magnetization lies in-plane. Among the three ferromagnetic materials iron, nickel and cobalt, nickel has the smallest saturation magnetization ($2\pi M_s^2 = 1.5 \times 10^6$ erg/cm^3) and hence has the smallest energy cost associated with magnetization in a short direction.

2.2. Magnetocrystalline Anisotropy

In crystalline bulk ferromagnetic materials, the atomic coordination in the lattice gives rise to the magnetocrystalline anisotropy. This form of anisotropy is responsible for the preference of the magnetization to point along certain directions, called magnetization easy-axes, in the absence of an externally applied magnetic field **H**. How do the local magnetic moments distinguish between the different crystallographic directions? The answer lies in the coupling between the spin part of the magnetic moment to the electronic orbital shape and orientation (spin-orbit coupling ξ **L.S**) and in the chemical bonding of a given atom to its local environment (crystal electric field) [O'Handley, unpublished]. If the local atomic coordination seen by an atom in a crystal has a low symmetry and if the bonding electrons of that atom have an asymmetric charge distribution, then its atomic orbitals and the spin part of the magnetic moment interact with the crystal field anisotropically. That is, certain orientations of the molecular orbitals become energetically preferred.

Figure 2.2 illustrates the magnetocrystalline anisotropy in the three most common ferromagnetic crystals along with the magnetization curves corresponding to three crystallographic directions. As shown in the figure, in bcc iron the magnetization easy axes are along the <100> directions and the magnetization hard axes are along the <111> directions. That is, the field necessary to magnetize single-crystal iron to saturation along the <100> directions is smaller than along any other direction. In fcc Ni, the easy axes are the <111> directions whereas the hard axes are <100>. In hcp cobalt, the c-axis represents the magnetization easy axis whereas the <1000> directions in the base plane

constitute the hard directions. The field required to saturate the magnetization along a hard axis is a quantitative measure of the strength of the anisotropy and is called the anisotropy field H_k. Among these three materials hcp cobalt has the largest anisotropy field, followed by bcc iron and then by fcc nickel, as shown in Fig. 2.2.

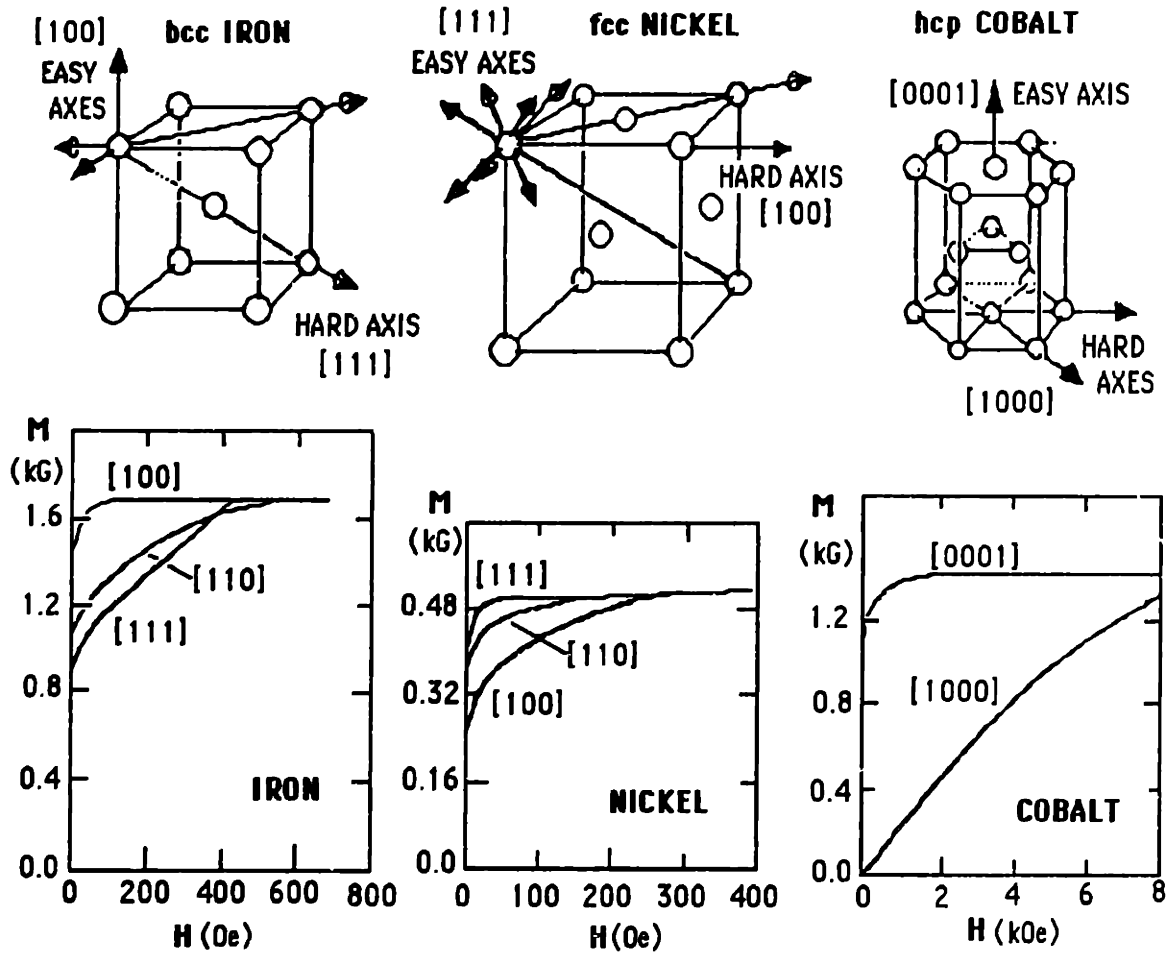

Figure 2.2: Schematic illustration of the magnetocrystalline anisotropy in bcc iron, fcc nickel, and hcp cobalt crystals. Also shown are the magnetization curves for the three solids corresponding to different crystallographic directions [O'Handley, unpublished].

In a cubic crystal, the magnetocrystalline anisotropy energy density can be phenomenologically expanded in terms of the direction cosines α_1, α_2, and α_3 of the magnetization vector **M** with respect to the <100> directions:

$$K^{MC} = K_1 \left(\alpha_1^2 \alpha_2^2 + \alpha_2^2 \alpha_3^2 + \alpha_3^2 \alpha_1^2\right) + K_2 \, \alpha_1^2 \alpha_2^2 \alpha_3^2 \qquad (2.2)$$

where K_1 and K_2 are the first order bulk magnetocrystalline energy densities and represent a phenomenological measure of the strength of the magnetocrystalline anisotropy. By expressing the direction cosines in Eq. (2.2) as a function of the polar spherical coordinates θ and ϕ and minimizing K^{MC} as a function of these angles, one can analytically find the magnetization easy and hard axes given the signs of K_1 and K_2. Magnetocrystalline anisotropy in nickel is relatively small compared to that in other materials and is essentially negligible in Ni thin films compared to the other sources of magnetic anisotropy, as we will show later. For bcc iron, $K_1 = 4.8 \times 10^5$ erg/cm^3 and $K_2 = -1.5 \times 10^5$ erg/cm^3 whereas for fcc nickel $K_1 = -4.5 \times 10^4$ erg/cm^3 and $K_2 = 2.3 \times 10^4$ erg/cm^3.

2.3. Magnetic Surface Anisotropy

The reduced symmetry in the atomic coordination at the surface or at the interface of a heteroepitaxial system gives rise to the magnetic surface anisotropy (MSA) [Néel 1953, 1954; Gradmann, 1986] which can either favor a perpendicular or an in-plane magnetization. In the simplest terms, the microscopic origin of MSA can be understood in the following way. The broken atomic symmetry at a surface can cause the confinement of the electronic orbitals to the plane of the film (which makes the orbitals oblate-like). In this case the angular momentum **L** of the electrons would be normal to the film which would favor the orientation of the spin part of the magnetic moments perpendicular to the film through a positive spin-orbit interaction (ξ **L**.**S** > 0), hence giving rise to perpendicular magnetic anisotropy.

The energy density K^{MSA} associated with this form of magnetic anisotropy may be relatively large in the case of a film but decreases as the film gets thicker due to a reduced surface to volume ratio. As proposed by Néel, this anisotropy energy density can be represented phenomenologically in the following fashion:

$$K^{MSA} = \frac{K_1^s + K_2^s}{h} \sin^2\theta, \qquad (2.3)$$

where h is the thickness of the ferromagnetic film and where K_1^s and K_2^s are the magnetic surface anisotropy energy densities corresponding to the two interfaces of the film. If these interfaces are identical, as in ideal Cu/Ni/Cu sandwiches, then $K_1^s + K_2^s = 2K^s$ and:

$$K^{MSA} = \frac{2K^s}{h} \sin^2\theta. \qquad (2.4)$$

K_1^s and K_2^s have units of energy per unit area and are strongly dependent on the chemical composition and the structure of the interface. For example, the Ni/Cu (100) and the Ni/Cu (111) could have opposite contributions to the magnetic anisotropy: one could favor a magnetization easy-axis perpendicular to the film while the other favors an in-plane magnetization. By convention, depending on whether these energies are positive or negative, they favor perpendicular or in-plane magnetization, respectively. We will discuss the Néel pair-interaction model more in detail in chapter 7.

As we will show in chapters 6 and 8, the magnetic surface anisotropy energy densities are obtained by measuring the effective anisotropy energy density as a function of ferromagnetic film thickness and fitting the results with phenomenological models. The magnetic surface anisotropy energy densities for several heteroepitaxial systems are summarized in publications by Gradmann [1986] and Bruno and Renard [1989]. However, recent state-of-the-art calculations on Co/Ni multilayers [Daalderop *et al.*, 1992], on Co/Pd multilayers [Victora and Mac Laren, 1993], and on Fe monolayers [Wang *et al.* 1993] have shown that it is also possible to compute magnetic surface anisotropy energies from first-principles with a good accuracy.

2.4. Magnetoelastic Anisotropy

Changing the direction of magnetization in a magnetic material by applying an external field causes the material to strain anisotropically. This property is called magnetostriction. Conversely, straining a magnetic material can produce a change in its preferred magnetization direction or easy-axis. This property is called piezomagnetism. In other words, strain gives rise to a magnetoelastic (ME) anisotropy whose energy density K^{ME} can be phenomenologically expressed as a Taylor expansion in the strain and the direction cosines of the magnetization vector. For cubic materials, the lowest order term in K^{ME} can be written as follows [Chikazumi, 1964]:

$$K^{ME} = B_1 \left(e_{xx}\,\alpha_1^2 + e_{yy}\,\alpha_2^2 + e_{zz}\,\alpha_3^2\right) + B_2 \left(e_{xy}\,\alpha_1\,\alpha_2 + e_{yz}\,\alpha_2\,\alpha_3 + e_{zx}\,\alpha_3\,\alpha_1\right) \qquad (2.5)$$

where e_{ij} (i, j = 1,2,3) refer to shear strain, e_{ii} (i=1,2,3) refer to strain along the crystallographic <100> directions and B_1 and B_2 are first and second order bulk ME

coupling coefficients, respectively. α_1, α_2 and α_3 are the direction cosines of the magnetization vector in the <100> crystallographic coordinate system.

The strain experienced by an epitaxial cubic thin film growing in a [001] direction on a (001) oriented cubic substrate is generally biaxial (e.g. misfit strain) and can be represented approximately by the following tensor in the <100> crystallographic frame:

$$e = e_0 \begin{pmatrix} 1 & 0 & 0 \\ 0 & 1 & 0 \\ 0 & 0 & \frac{-2\nu}{1-\nu} \end{pmatrix} \approx e_0 \begin{pmatrix} 1 & 0 & 0 \\ 0 & 1 & 0 \\ 0 & 0 & -1 \end{pmatrix} \qquad (2.6)$$

where $e_0 > 0$ and $e_0 < 0$ mean that the film is under biaxial in-plane tensile and compressive stress, respectively. Here we have assumed that the film is elastically isotropic and have used the value $\nu = 1/3$ for Poisson's ratio which is reasonable for most transition metals. As expected, Eq. (2.6) shows that when the film is under biaxial in-plane tensile strain it is also compressed along its normal, and vice-versa. It is important to realize that the strain e_0 is an average strain and that the local strain e(x,y,z) can vary significantly on an atomic scale especially in the film/substrate interface where misfit dislocations are sometimes present [Clemens *et al.*, 1991]. We will discuss this idea more in detail in chapter 4. Substituting the strain tensor of Eq. (2.6) in Eq. (2.5) and keeping only angle dependent terms leads to:

$$K^{ME} = 2 B_1 e_0 \sin^2\theta \qquad (2.7)$$

which has the same form as the Néel magnetic surface anisotropy energy density (equations (2.3) and (2.4)). When $B_1 > 0$ and the film is under biaxial in-plane tensile strain, as in the case of Ni/Cu (001) films, $K^{ME} > 0$, i. e. bulk ME anisotropy favors perpendicular magnetization as illustrated in Fig. 2.3.

In nickel, ME interactions are particularly strong and $B_1 = 6.2 \times 10^7$ erg/cm^3. A strain $e_0 = 2\%$, which is characteristic of Ni ultrathin films deposited on Cu (001) substrates, implies a magnetoelastic energy density $K^{ME} \approx 10^6$ erg/cm^3. This energy is much larger than the magnetocrystalline energy density but comparable to the magnetostatic energy density of Ni. It is important to note that the magnetoelastic coupling coefficients at surfaces and in thin films can be very different from the ones of the bulk so B_1(bulk) may not apply for Ni thin films [Sun and O'Handley, 1991;

O'Handley and Sun, 1992; Song *et al.*, 1994]. This is analogous to the idea that bulk magnetocrystalline anisotropy is not necessarily adequate to explain the magnetic anisotropy in a thin film due to the broken atomic symmetry at the film's interfaces. A magnetic surface anisotropy may be necessary, as discussed in section 2.3. We will review these important ideas in more detail in chapter 7.

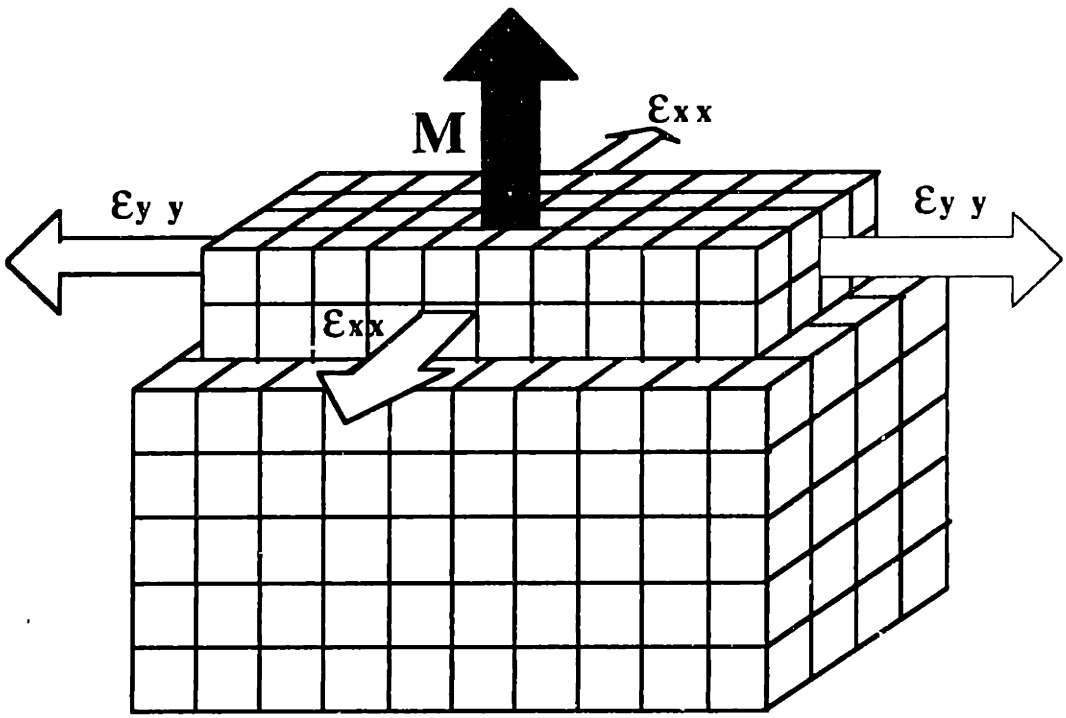

Figure 2.3 : Bulk magnetoelastic coupling in Ni thin films deposited on a Cu substrate. As illustrated here, the film grows under in-plane biaxial tensile misfit strain along the [100] and [010] directions. As a result, the bulk magnetoelastic coupling favors a magnetization easy axis perpendicular to the film.

In summary, the total magnetic anisotropy energy density of an epitaxial (001) ferromagnetic film with negligible magnetocrystalline anisotropy can be written as follows:

$$F = K^{eff} \sin^2\theta \tag{2.8}$$

where $$K^{eff} = 2 B_1 e_0 - 2\pi M_s^2 + \frac{K_1^s + K_2^s}{h} = K^v + \frac{K^s}{h} \tag{2.9}$$

and where K^v and K^s are the volume and surface magnetic anisotropy energies, respectively. A plot of K^{eff}. h versus h is often used to obtained the magnetic surface anisotropy energy density [Gradmann, 1986]. This method will be illustrated with an example in section 3.3. Depending on their signs, the bulk magnetoelastic anisotropy and the magnetic surface anisotropy energy densities either favor an in-plane or an out-of-plane magnetization easy-axis but their magnitudes always decrease with increasing film thickness. On the other hand, the magnetostatic anisotropy energy density always favors an in-plane magnetization and dominates the total magnetic anisotropy energy density in thick films. The magnetostatic, magnetocrystalline, and magnetoelastic anisotropy energy densities of bulk bcc Fe, hcp and fcc Co, and fcc Ni are summarized in Table 2.1.

	$2\pi M_s^2$ (erg/cm^3)	K_1 (erg/cm^3)	$B_1 e_0$ (erg/cm^3)
bcc Fe	1.9×10^7	4.8×10^5	-6×10^5
hcp Co	1.1×10^7	3.5×10^6	
fcc Co	1.1×10^7	-1.2×10^6	-3×10^6
fcc Ni	1.5×10^6	-4.5×10^4	10^6

Table 2.1: Magnetostatic, first order magnetocrystalline, and first order magnetoelastic anisotropy energy densities for bulk bcc Fe, hcp and fcc Co, and fcc Ni. A strain of 2% was used to compute the magnetoelastic energy density. Note that fcc Ni has the largest ratio of $B_1 e_0$ to $2\pi M_s^2$ with a positive magnetoelastic anisotropy energy density.

Experimentally, the effective anisotropy energy density is defined by:

$$K^{eff} = \int_0^{M_s} H_{//}\, dM - \int_0^{M_s} H_{\perp}\, dM \qquad (2.10)$$

where $H_{//}$ and $H_{\perp}$ correspond to the magnetic field applied in the film plane and perpendicular to it, respectively. In practice, K^{eff} is the difference in work done by an external magnetic field in taking the material from a demagnetized state to full saturation with the field applied in-plane and perpendicular to the film. We use the convention that $K^{eff} > 0$ corresponds to perpendicular magnetization. The work done by the external

field or conversely the value of an integral in Eq. (2.10) is illustrated schematically in Fig. 2.4.

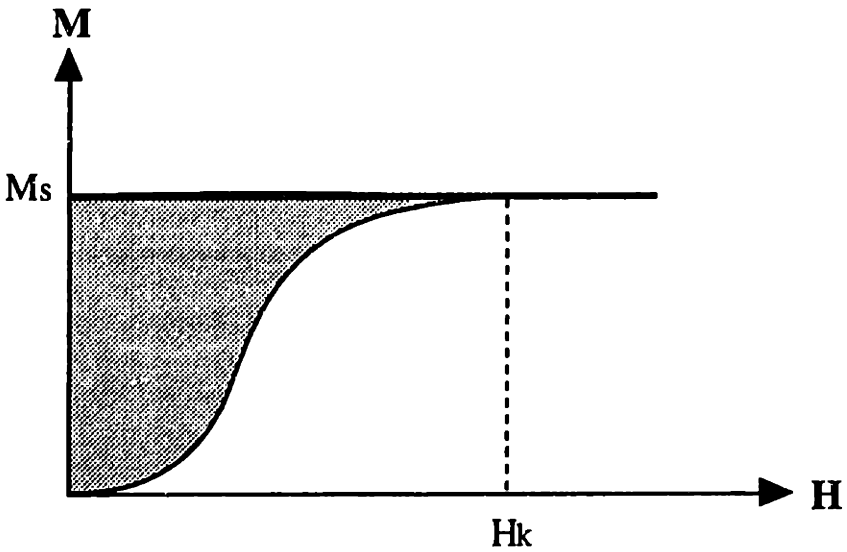

Figure 2.4: Response of an initially demagnetized ferromagnetic material to an external magnetic field. M_s and H_k are the saturation magnetization and the anisotropy field, respectively. The shaded area represents the work done by the external magnetic field in taking the sample from a demagnetized state to full saturation along the direction of the applied field.

Chapter 3

Perpendicular Magnetic Anisotropy in Thin Films and Multilayers

The issue of perpendicular magnetic anisotropy (PMA) in ultrathin films is a very interesting and challenging concept since the magnetostatic anisotropy energy, which is very strong in thin films, always favors an in-plane magnetization easy-axis. In the past ten years, PMA and giant magnetoresistance (GMR) in thin films and multilayers have been at the center of the attention of the international magnetism community. Considerable experimental effort has been focused on PMA since the pioneering work of Gradmann [1966, 1974, 1986] and the more recent theoretical predictions of Gay and Richter [1986]. The number of experimental techniques used to study this phenomenon is impressive and includes various forms of magnetometry, the magneto-optic Kerr effect (MOKE), spin-polarized photoemission (SPP), secondary electron spin-polarized analysis (SESPA), ferromagnetic resonance (FMR), and very sophisticated techniques such as scanning electron microscopy with polarization analysis (SEMPA) which is capable of resolving magnetic domains through its nanometer resolution [Allenspach, 1994].

The most important heteroepitaxial systems that have been investigated and that have exhibited a strong PMA are bcc Fe/Ag (001) [Koon *et al.*, 1987; Stampanoni *et al.*, 1987; Heinrich *et al.*, 1987; Araya-Pochet *et al.*, 1988; Ballentine *et al.*, 1989; Qiu *et al.*, 1993], fcc Fe/Cu (001) [Pescia, Stampanoni, *et al.*, 1987; Liu *et al.*, 1988; Pappas *et al.*, 1990; Pappas *et al.*, 1991; Allenspach and Bischof, 1992; Thomassen *et al.*, 1992; Swartzendruber *et al.*, 1993], Co/Pd superlattices [Engel *et al.*, 1991; den Broeder *et al.*, 1991], Co/Au (111) thin films and superlattices [Lee *et al.*, 1990; Allenspach *et al.*, 1990; Kingetsu and Sakai, 1993], Ni/Cu (001) [Ballentine, 1989; Bochi *et al.*, 1993; Huang *et al.*, 1994], Ni/Cu (111) [Ballentine, 1989; Huang *et al.*, 1994], and Cu/Ni/Cu (001)

sandwiches [Chang, 1990; Naik *et al.*, 1993; Jungblut *et al.*, 1994]. In other epitaxial systems, such as fcc Co/Cu (001) thin films [Pescia, Zampieri, *et al.*, 1987; Krams *et al.*, 1992], fcc Co/Cu (111) superlattices [Lee *et al.*, 1990], and fcc Co/Ag (111) superlattices [Kingetsu and Sakai, 1993], no experimental evidence of perpendicular magnetization has been found. In most of the above structures exhibiting perpendicular magnetization, PMA was found to dominate only in the first few atomic monolayers (ML) of the thin film. However, as we will show in chapter 6, Ni/Cu (001) structures exhibit perpendicular magnetization over an abnormally large range extending up to 100 Å.

Although many of the experiments performed in the past few years have often been carried out diligently and have involved state-of-the-art measurement techniques, the analysis of the behavior of the magnetic anisotropy has often been limited to qualitative arguments: the origin of PMA often has been attributed to the strength of the magnetic surface anisotropy (due to the broken symmetry at the film's interfaces) relative to the shape anisotropy which tends to keep the magnetization in-plane. Very few research groups have achieved a quantitative understanding of the magnetic anisotropy through a thorough characterization of their heteroepitaxial structures that includes measurements of the saturation magnetization and of the film thickness dependence of the strain in the films [Lee *et al.*, 1990; Engel *et al.*, 1991]. In the following section, we will review the most important results on the magnetic anisotropy in the three most commonly studied systems (bcc Fe/Ag, fcc Fe/Cu, and Co/Pd superlattices) and the early results on Ni/Cu (001) thin films. We will conclude by asking some fundamental questions that have served us as a guide throughout our work.

3.1. bcc Fe/Ag (001) Thin Films and Superlattices

The first direct evidence of perpendicular magnetization in Fe/Ag (001) was found by Koon *et al.* [1987]. This epitaxial system is attractive because of the relatively large magnetic moment of Fe and the small lattice mismatch (0.8%) between the α-Fe (001) and the Ag (001) surface nets, which is particularly favorable for good epitaxial growth. The Fe/Ag (001) superlattices were grown at room temperature and characterized at T = 15 K by conversion electron Mössbauer spectroscopy. The magnetization was found to be perpendicular to superlattices with 1.8 Å and 4.3 Å thick Fe films. The magnetization easy-axis was found in-plane when the Fe film thickness

was about 10 Å. Koon *et al.* suggested that the PMA in this system is mainly due to a uniaxial magnetic anisotropy arising from the broken symmetry at the Fe/Ag interface.

A very interesting study of magnetic anisotropy of epitaxial bcc Fe/Ag (001) thin films was conducted by Stampanoni *et al.* [1987] using spin-polarized photoemission. The Fe films were grown at room temperature and the film thickness ranged from 1.5 Å to 18 Å. By applying a magnetic field normal to the films and measuring the spin polarization of the photoemitted electrons, it was possible to make a direct observation of the component of the magnetization perpendicular to the films. The experimental results are shown in Fig. 3.1. After cooling the samples down to 30 K, Stampanoni *et al.* found that the perpendicular remanence vanishes for films thinner than 2 ML (3.6 Å) and thicker than 5 ML (8.9 Å). For an intermediate thickness range - 3 to 4 ML (i.e. 5.3 to 7.1 Å) - a perpendicular remanence amounting to almost full saturation was observed. Moreover, above T = 100 K, perpendicular remanence was found to vanish for all film thicknesses. No satisfactory explanation was given as to the origin and temperature dependence of PMA in these films. Stampanoni *et al.* only speculated that the most likely cause of perpendicular magnetization in their films may be found in the microstructure of the Fe/Ag interface.

Finally, magneto-optic Kerr effect (MOKE) studies on Fe/Ag (001) thin films [Ballentine *et al.*, 1989] grown at room temperature have shown that at T = 100 K the magnetization easy-axis is perpendicular to the film for thicknesses smaller than 3.6 Å but in-plane for thicker films. As the temperature was decreased to 30 K, Ballentine *et al.* found that films up to 5.3 Å thick exhibit a perpendicular easy axis. As far as the origin of PMA in this epitaxial system is concerned, Ballentine *et al.* only mentioned that the substrate can influence the magnetic properties of the film *via* electronic coupling effects such as charge transfer and sp-d hybridization between the electronic states of the film and the substrate.

In summary, bcc Fe/Ag (001) thin films exhibit a perpendicular magnetization easy-axis for Fe film thickness between 4 Å and 7 Å and an in-plane magnetization for films thinner than 4 Å and thicker than 7 Å. The PMA was shown to vanish at room temperature. A quantitative mechanism explaining this complex magnetization easy-axis "switching" behavior is still missing.

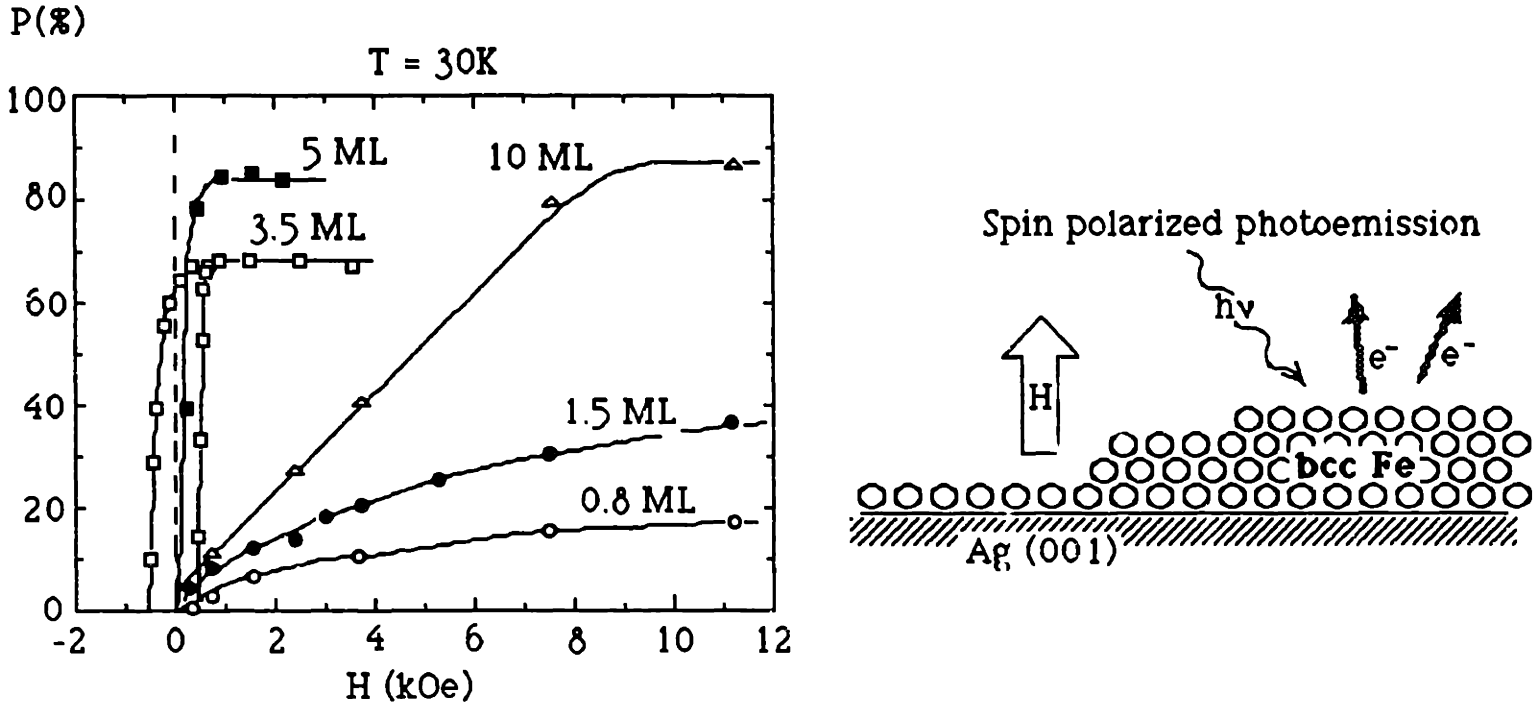

Figure 3.1: Magnetic anisotropy in bcc Fe/Ag (001) thin films studied with spin-polarized photoemission [Stampanoni *et al.*, 1987]. The schematic diagram on the right hand side represents the spin-polarized photoemission experiment while the graph on the left hand side shows the M-H loops obtained from these films with the magnetic applied perpendicular to the film. On each loop, the thickness of the Fe film is shown in monolayers. The polarization measurements were conducted at 30 K.

3.2. fcc Fe/Cu (001) Thin Films

fcc Fe/Cu (001) is also a very attractive epitaxial system to study, not only because of the relatively large magnetic moment of Fe but also because it allows one to examine the magnetic properties of fcc Fe which is metastable at room temperature. In fact, fcc Fe is thermodynamically stable only between 1184 K and 1665 K. Also, the experimental investigations of this epitaxial system have been the source of many controversial discussions on the growth mode of Fe ultrathin films on Cu (001) substrates near room temperature [Steigerwald and Egelhoff, 1988; Pescia *et al.*, 1988] and its effects on the magnetic anisotropy [Swartzendruber *et al.*, 1993].

Fcc Fe films grown on Cu (001) substrates at room temperature were first studied by spin-polarized photoemission by Pescia, Stampanoni *et al.* [1987]. Their measurements at T = 30 K indicate that 9 Å thick Fe films have a perpendicular magnetization easy-axis whereas thinner films are either magnetized in-plane or else exhibit no detectable ferromagnetic order.

A very interesting experimental work on fcc Fe/Cu (001) was also performed by Liu *et al.* [1988] where the Fe films were grown at various temperatures extending from 100 K to 350 K and characterized using the polar Kerr effect. Their results are summarized in Fig. 3.2 where the region of predominant perpendicular magnetization is bound by the solid line. The figure indicates that for all growth temperatures the magnetization starts in-plane for ultrathin films, then prefers a perpendicular easy axis, and finally falls in-plane again for thicker Fe films. This scenario qualitatively follows the one we described in section 3.1 for Fe/Ag (001). However, the region of perpendicular magnetization in Fe/Cu (001) is wider than in Fe/Ag (001). In fact, the solid line in Fig. 3.2 indicates that this region extends up to 11 Å (6 ML) in Fe/Cu (001) compared to approximately 7 Å in Fe/Ag (001). Liu *et al.* pointed out that their results can be explained in the light of a competition between the magnetostatic anisotropy energy and a uniaxial magnetic surface anisotropy energy which favors perpendicular magnetization. However, their arguments remained very qualitative.

Other significant experimental studies of the magnetic anisotropy in Fe/Cu (001) were conducted by Pappas *et al.* [1990, 1991] and Allenspach and Bischof [1992] who deposited their films at temperatures close to 100 K. Their measurements support the observations of Liu *et al.* [1988] on the extent of the region of perpendicular

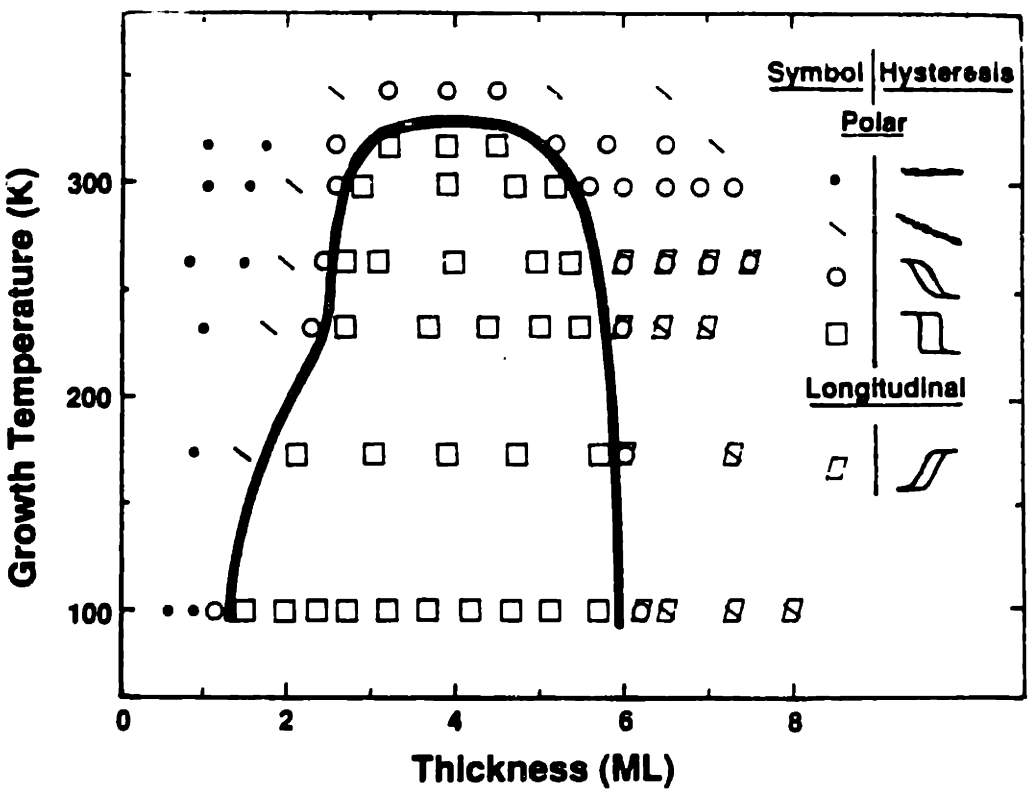

Figure 3.2: Magnetic anisotropy in fcc Fe/Cu (001) thin films deposited at temperatures ranging from 100 K to 350 K [Liu *et al.*, 1988]. The region of perpendicular magnetization is outlined by the solid line. The Kerr effect measurements of the M-H loops were carried at the growth temperature.

magnetization for Fe films deposited and characterized at very low temperatures. Pappas *et al.* [1991] also showed that the vacuum/Fe interface plays a fundamental role in determining the PMA in the vacuum/Fe/Cu (001) epitaxial system. By depositing small amounts of O_2 (approximately half a monolayer) on the surface of the Fe films, whose thickness ranged from 6 Å (3.4 ML) to 11 Å (6 ML), Pappas *et al.* showed that the magnetization easy axis switches from perpendicular to in-plane. This observation supports the conclusions of Heinrich *et al.* [1989] drawn from ferromagnetic resonance data on Fe/Ag (001) that the vacuum/Fe interface gives rise to a strong perpendicular magnetic interface anisotropy.

3.3. Epitaxial Co/Pd Superlattices

The Co/Pd epitaxial system has been investigated extensively because of its potential applications as a magneto-optic recording medium [Zeper *et al.*, 1991]. One of the most revealing and thorough studies of this system has been conducted by Engel *et al.* [1991] who have quantitatively measured the behavior of the magnetic anisotropy and the saturation magnetization in (100), (110), and (111) oriented Co/Pd epitaxial superlattices and have characterized the state of strain of the Co layers using X-ray diffraction measurements. The Pd spacer layer thickness was fixed at 10 Å whereas the Co film thickness was varied between 1 and 25 Å. The results of the magnetic anisotropy measurements are shown in Fig. 3.3 where the effective magnetic anisotropy energy density times the Co film thickness is plotted as a function of Co film thickness for all three growth orientations. The first conclusion that one can make from Fig. 3.3 is that perpendicular magnetization ($K^{eff} > 0$) exists for all three orientations but its strength is strongly orientation dependent. The superlattices with a (111) orientation exhibit the largest extent of perpendicular magnetization (up to 25 Å Co) whereas the (100) oriented superlattices sustain the smallest range of perpendicular magnetization (up to 3 Å only). Engel *et al.* analyzed their results in terms of the phenomenological model presented in chapter 2. The straight lines shown in Fig. 3.3 are the fits of the data points using a equation similar to Eq. (2.9). The first and most important result of the fit is that all the straight lines intersect the vertical axis at the same point. This intercept represents the magnetic surface anisotropy energy density of the Co/Pd interfaces. The fact that all the straight lines intersect at the same positive intercept indicates that the Co/Pd interfaces contribute to perpendicular magnetic anisotropy to the same extent irrespective of

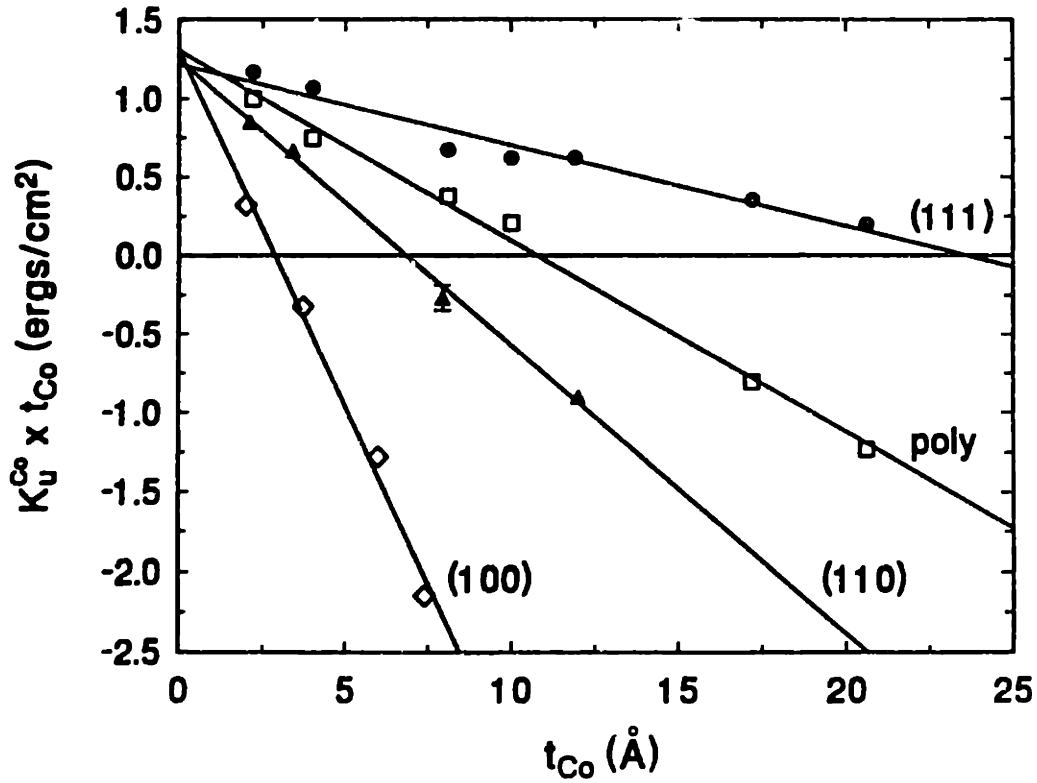

Figure 3.3: Effective anisotropy energy density times the Co film thickness as a function of Co film thickness for (100), (110), (111) oriented and polycrystalline Co/Pd superlattices [Engel *et al.*, Phys. Rev. Lett., 1991]. Note the convergence of the four straight lines to a same intercept on the vertical axis indicating that the Co/Pd interfaces all have the same contribution to magnetic interface anisotropy, irrespective of the superlattice orientation.

superlattice orientation. The slopes of the lines in Fig. 3.3 are equal to the volume component of the magnetic anisotropy which is comprised of the magnetostatic anisotropy energy, the volume magnetoelastic anisotropy energy, and the magnetocrystailine anisotropy energy (which we purposely had omitted in Eq. (2.9)). After subtracting the contribution of the magnetostatic anisotropy energy, Engel *et al.* showed that the main contribution to the volume magnetic anisotropy energy in (111) Co/Pd superlattices arises from the magnetocrystalline anisotropy energy of hcp Co with a relatively small contribution from the magnetoelastic anisotropy energy favoring an in-plane magnetization. For the (100) oriented Co/Pd superlattices, Engel *et al.* showed that the main contribution to the volume magnetic anisotropy energy comes from the magnetoelastic anisotropy energy favoring an in-plane magnetization. This conclusion is supported by the existence of a large strain in the (100) Co films, as indicated by X-ray diffraction measurements [Engel *et al.*, 1991].

3.4. fcc Ni/Cu (001) Thin Films

The behavior of the magnetic anisotropy in Ni/Cu thin films has received less attention than Fe/Ag and Fe/Cu thin films. This may be due to the relatively small magnetic moment of Ni compared to the moment of Fe ($\mu_{Ni} \approx 1/3\ \mu_{Fe}$), to the relatively small Curie temperature of Ni (T_c = 354 °C), and/or to the potential growth problems of Ni thin films on Cu substrates, namely segregation of Cu atoms at the surface of Ni and intermixing of Ni and Cu atoms at the Ni-Cu interface. However, the relatively small magnetostatic energy density of Ni (K^{MS} (Ni) ≈ 1/10 K^{MS} (Fe)), which constitutes the main resistance to perpendicular magnetization, the large magnetoelastic coupling in Ni, and the relatively small lattice misfit (2.6%) between Ni and Cu make the Ni/Cu (001) epitaxial system very appealing for the study of magnetic anisotropy in thin films.

The magnetic anisotropy in Ni/Cu (001) thin films was first investigated by Ballentine [1989] using MOKE as the magnetic probe. The films were grown at room temperature and characterized at T = 100 K. The magnetization was found to lie in-plane for Ni thicknesses up to 3.1 ML (5.5 Å). A mixed behavior in the magnetic anisotropy was observed for 4.7 ML (8.3 Å) thick films, manifested in the large remanence obtained when the magnetic field was applied perpendicular to the films. The M-H loops showing this behavior are displayed in Fig. 3.4. The appearance of a strong perpendicular component of the magnetization at Ni thicknesses of about 15 Å was also confirmed by

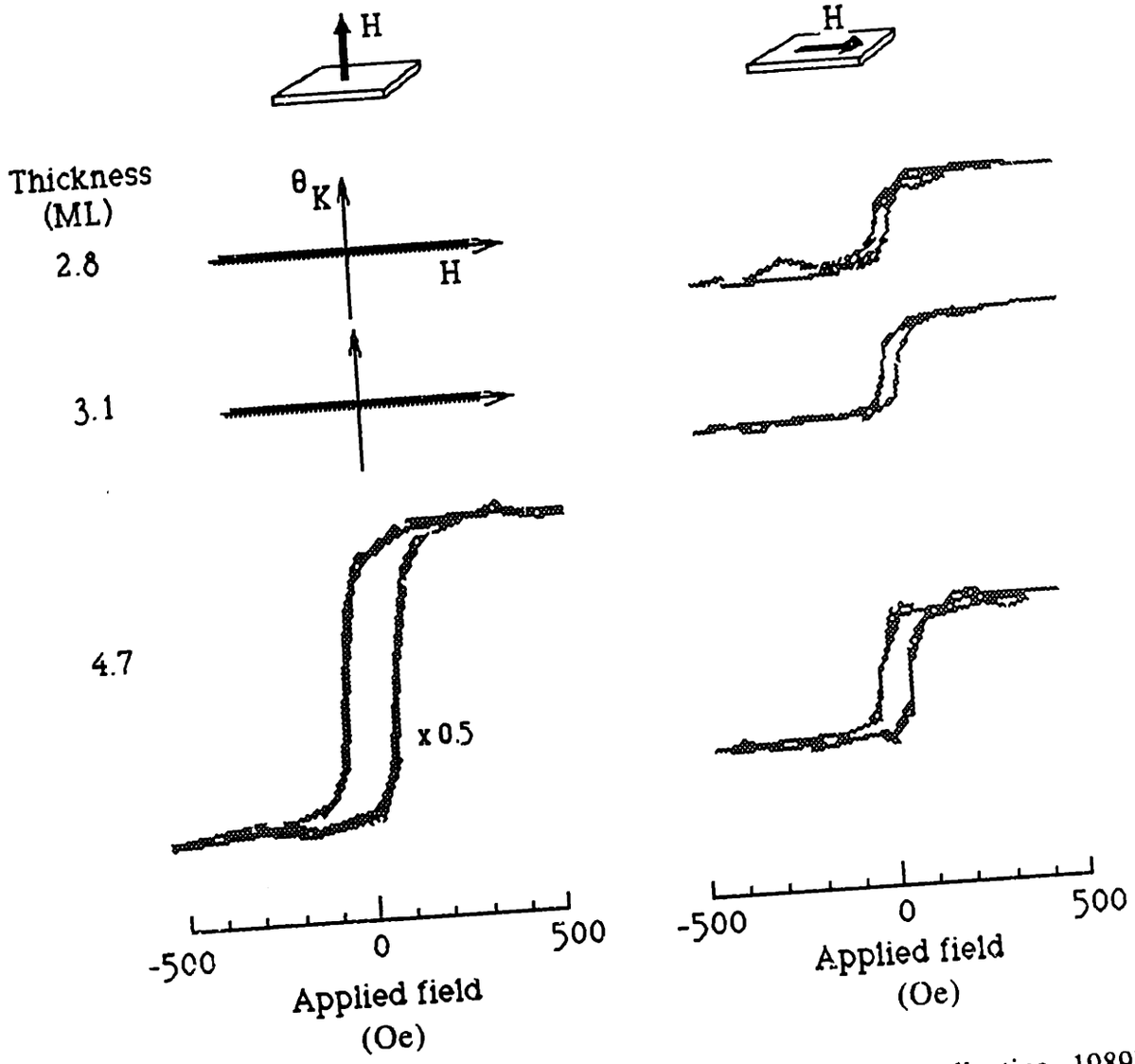

Figure 3.4: Magnetic anisotropy in Ni/Cu (001) ultrathin films [Ballentine, 1989] measured using the magneto-optic Kerr effect (MOKE). The M-H loops are shown for magnetic field applied perpendicular to the film (left hand side) and for the field applied in the film plane (right hand side). The thickness of the Ni film is shown on the left hand side and is expressed in monolayers (ML). The magnetization easy axis is in plane for 2.8 ML (5 Å) and 3.1 ML (5.5 Å) but a mixed behavior can be seen at 4.7 ML (8.3 Å) where a large perpendicular remanence can be seen. The films were deposited at room temperature but the MOKE measurements were performed at 100 K.

Bochi *et al.* [1993] and Huang *et al.* [1994]. Ballentine pointed out that the magnetization easy-axis reversal illustrated in Fig. 3.4 may be due to the onset of misfit dislocations at the Ni/Cu (001) interface. Using positron annihilation spectroscopy, Gidley [1989] experimentally found that a structural change in the Ni/Cu (001) thin films occurs at a Ni thickness h ≤ 9 Å. He attributed this change to the appearance of misfit dislocations at the Ni/Cu interface. Evidence of a strong correlation between a magnetization easy-axis reversal and a plastic microstructural change has been observed in fcc Fe/Cu (001) thin films [Thomassen *et al.*, 1992] where the magnetization easy-axis was found to switch from perpendicular to in-plane at an Fe film thickness coinciding with a phase transformation of the Fe films from fcc to bcc (11 Å). An interesting reversal in magnetic anisotropy has also been observed in Cu/Ni/Cu (001) sandwiches where the Cu layer thickness was 1000 Å and which were characterized in air using a vibrating sample magnetometer [Chang, J. Appl. Phys. **68**, 4873 (1990)]. The magnetization easy-axis was found to lie in-plane for Ni thicknesses of 500 Å and above and perpendicular to the film for 50 Å thick Ni films. The out-of-plane to in-plane transition thickness was around 100 Å.

With the above intriguing observations in mind, we asked ourselves the following questions on the Ni/Cu (001) epitaxial system:

a) Is the appearance of perpendicular magnetization easy-axis systematically reproducible?

b) What is the Ni thickness extent of the perpendicular region?

c) What is the perpendicular region due to?

d) Is the onset of misfit dislocations responsible for the in-plane to out-of-plane magnetic easy-axis reversal?

e) What energies dominate the balance in causing PMA?

f) How can we explain the magnetization going out-of-plane and back in-plane (i. e. the existence of two magnetization easy-axis transition thicknesses) based on the phenomenological model of chapter 2?

g) What is the effect of the Ni thickness-dependent misfit strain on the magnetic anisotropy?

h) What are the signs and the magnitude of the magnetic surface anisotropy energy?

i) Are there any further tests of the importance of interfacial magnetic anisotropy?

We will attempt to answer all of the above questions in chapters 6 to 9. First, we will review the growth mechanisms in the Ni/Cu/Si (001) heteroepitaxial system and the experimental procedures used for the films preparation.

Chapter 4
Misfit Strain Accommodation in Thin Films

When a thin film is evaporated on a thick single-crystal substrate at a slow rate and at a finite temperature, it may grow as a single-crystal if the film-substrate lattice mismatch is small enough (typically less than 10%). This phenomenon is called epitaxy. In the early stages of epitaxy, i.e. when the film is ultrathin, the film tends to deform elastically in order to adopt the lattice parameter of the substrate. A perfect registry is then achieved between the film and the substrate. The film-substrate interface is said to be coherent and the thin film is said to be pseudomorphic to the substrate. This phenomenon is illustrated in Fig. 4.1 where an ultrathin film is grown on a substrate that has a larger equilibrium lattice parameter than the film. The film is under an in-plane biaxial tensile misfit strain and is compressed along its normal due to Poisson contraction. The strain tensor describing this state of strain is given by Eq. (2.6). This situation is experienced by Ni ultrathin films grown epitaxially on Cu (001) substrates since Ni has a smaller bulk equilibrium lattice parameter (a_0(Ni) = 3.52 Å, at room temperature) than Cu (a_0(Cu) = 3.615 Å, at room temperature). In Ni/Cu (001) thin films, tensile strain occurs along the [100] and [010] directions. In a pseudomorphic film, the in-plane biaxial tensile misfit strain appearing in Eq. (2.6) is equal to the film-substrate lattice mismatch η which is defined by:

$$\eta = \left| \frac{a_s - a_f}{a_f} \right|, \tag{4.1}$$

where a_s and a_f are the bulk equilibrium lattice parameters corresponding to the substrate and the film, respectively. For Ni/Cu (001) thin films η = 2.6% at room temperature.

When the film reaches a critical thickness h_c, the elastic energy of the film associated with misfit strain becomes too large and the onset of misfit dislocations at the

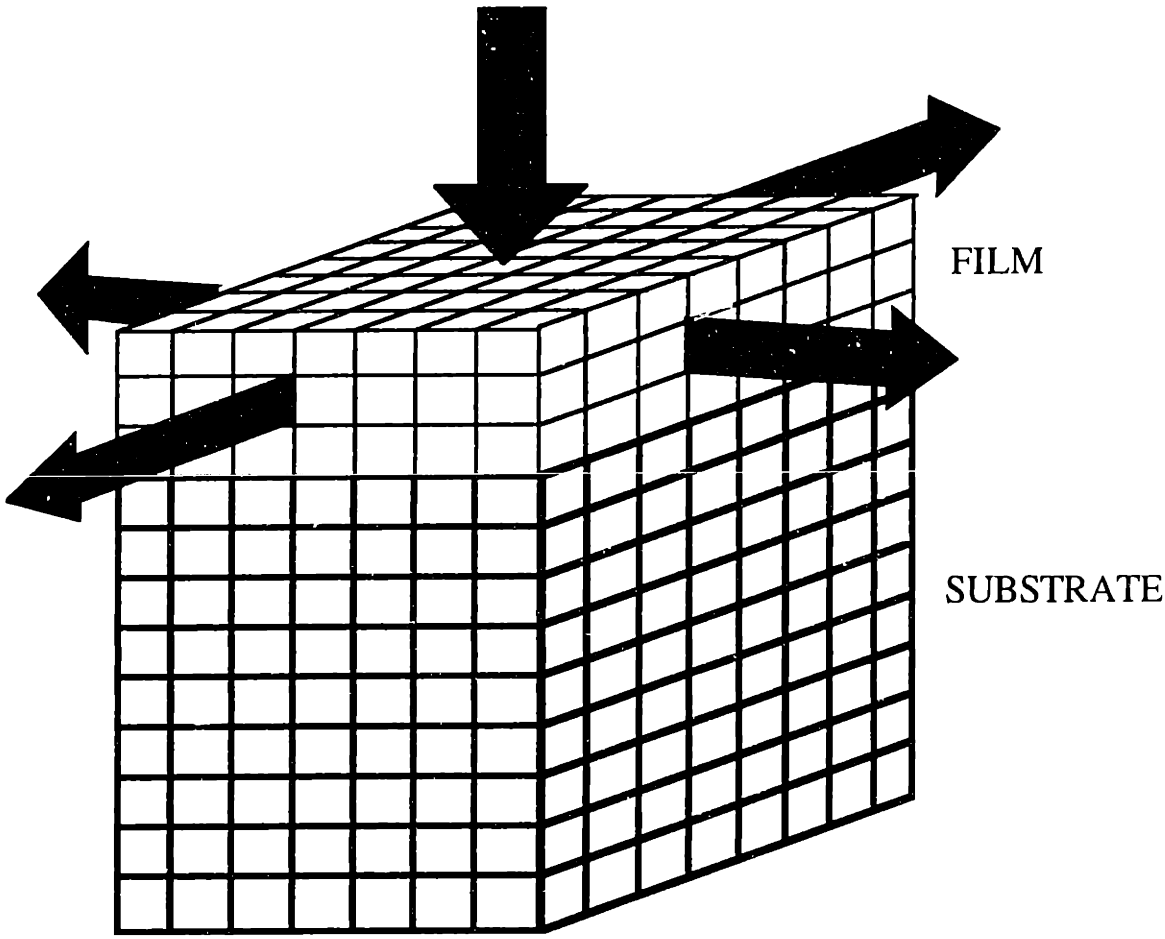

Figure 4.1: Pseudomorphic growth of an ultrathin film on a single-crystal simple-cubic substrate. The film has a smaller equilibrium bulk lattice parameter than the substrate. As a result, the film is under a biaxial in-plane tensile misfit strain and is compressed along its normal, as indicated by the arrows.

heteroepitaxial interface becomes thermodynamically favorable. The perfect registry between the film and the substrate is then broken and the film-substrate interface becomes semi-coherent. The heterointerface is then plastically deformed through the presence of the dislocations. This situation is illustrated schematically in Fig. 4.2 for a simple-cubic film with $h > h_c$ grown epitaxially on a simple-cubic substrate which has a larger lattice parameter. The misfit dislocations shown here are edge dislocations indicated with the symbol $\perp$ and run along the [010] direction in the heteroepitaxial interface corresponding to the y axis in Fig. 4.2. The misfit strain relief caused by the dislocations in the film can be seen through the introduction of atomic planes perpendicular to the heterointerface and ending above the misfit dislocations. As a result, the atomic spacing in the film plane is reduced, approaching the film's bulk equilibrium

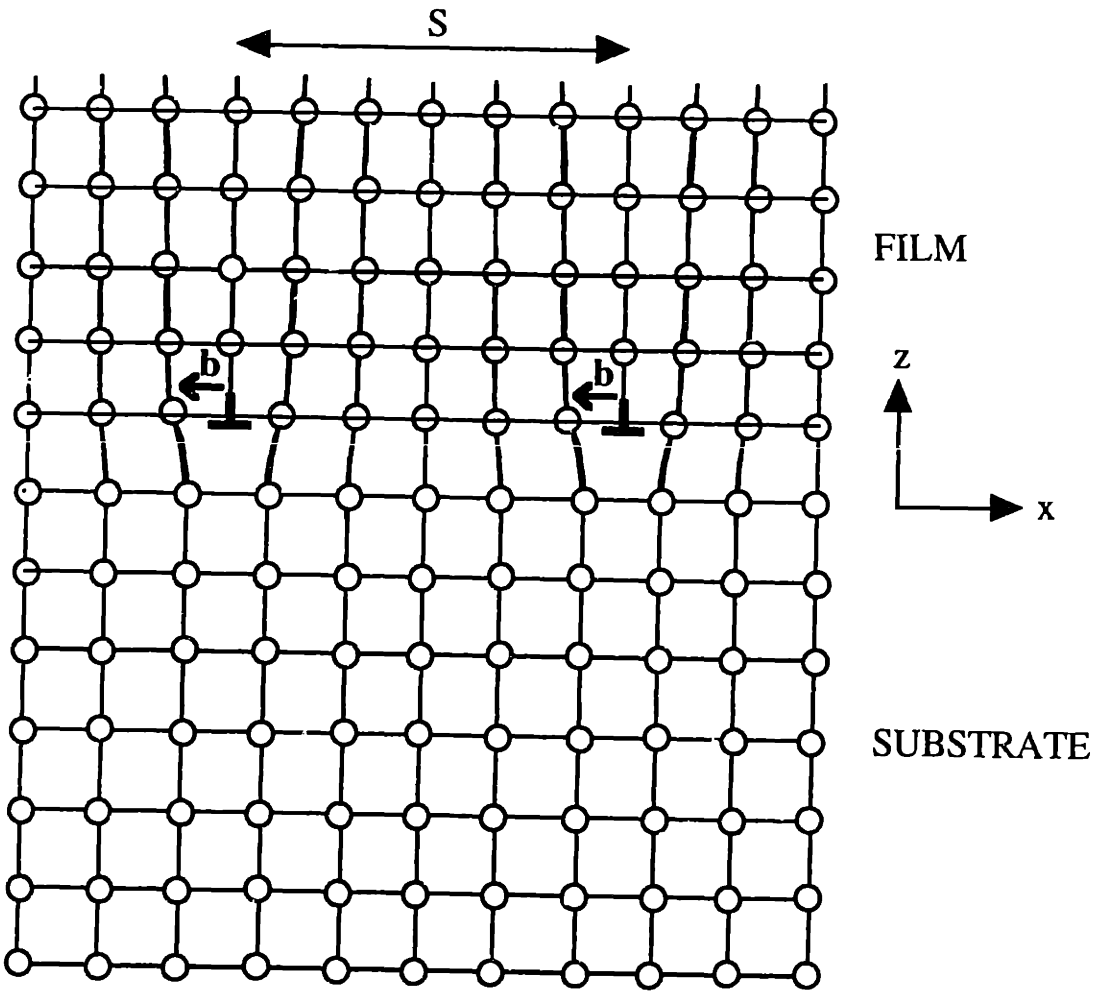

Figure 4.2: Schematic cross-sectional view of 90° misfit dislocations in a simple-cubic heteroepitaxial system. The misfit dislocations lie in the film-substrate interface and run along <100> directions. In this example, the film has a smaller equilibrium bulk lattice parameter than the substrate and is under an in-plane biaxial tensile misfit strain. The edge dislocations are indicated with the symbol ⊥. The distance S separating two neighboring dislocations and the Burgers vector **b** are also shown in the figure.

spacing: there are seven atomic planes in the film for every six atomic planes in the substrate. The direction $\vec{\xi}$ (also called the sense) of the dislocation lines shown in Fig. 4.2 is parallel to the direction of the positive y axis, while the Burgers vector **b** points along the direction of the negative x axis. The Burgers vector is defined geometrically as follows [Hirth and Lothe, 1992]. Consider a plane perpendicular to the dislocation line, for example the plane y = 0. In this plane, we form a closed clockwise circuit that encloses the dislocation line and that follows the atomic positions shown in Fig. 4.2. Then we draw the same circuit in the perfect reference lattice, i. e. the one containing a

perfectly coherent interface. The vector required to close the circuit in the pseudomorphic structure is defined as the Burgers vector. In other words, the Burgers vector is given by the line integral, taken in a right-handed sense relative to $\vec{\xi}$, of the elastic displacement around the dislocation. The condition $\vec{\xi} \cdot \mathbf{b} = 0$ is characteristic of edge dislocations. Another set of edge dislocations, not shown in Fig. 4.2, runs parallel to the [100] direction which corresponds to the x axis in Fig. 4.2.

In fcc crystals such as Ni/Cu (001), the structure of the misfit dislocations is more complex as it combines both an edge-like and a screw-like character [Tsao, 1993]. The Burgers vector **b** makes an angle of 60 degrees with the direction that is both perpendicular to the dislocation line and that lies in the heterointerface. For this reason, these misfit dislocations are called 60° dislocations. It is important to note that only the component of the dislocation that is edge-like and that has a non-zero projection of the Burgers vector in the heterointerface contributes to relieving misfit strain. The 60° dislocations glide on (111) planes and run along [110] and [1$\underline{1}$0] directions in the heterointerface forming a square grid in the Ni/Cu (001) interface. A transmission electron micrograph indicating the misfit dislocations grid in the interface of Ni/Cu (001) thin films is shown in Fig. 4.3 [Inglefield *et al.*, 1993].

As we will show in section 4.2, the value of the critical thickness h_c depends on the physical properties of the heteroepitaxial system, such as the lattice mismatch between the film and the substrate and the elastic constants of the film and the substrate. But most importantly h_c is governed by the interplay between the energy needed to form a unit length of misfit dislocation (energy cost) and the elastic strain energy recovered by the film through the introduction of a misfit dislocation (energy relief).

In the above discussion of strain in thin films we have only focused on misfit strain. Other forms of strain such as thermal strain, arising from the mismatch of thermal expansion coefficients between the film and the substrate [Nix, 1989], and strain due to film surface roughness [Spencer *et al.*, 1993] are sometimes present in thin films. However, we believe that in Ni/Cu (001) these other sources of strain are negligible compared to misfit strain and we will therefore omit them in our discussions. We will discuss roughness in Ni/Cu (001) briefly in chapter 5. Before reviewing the energetics of misfit dislocations, we will describe the localized strain fields arising from dislocations in the following section.

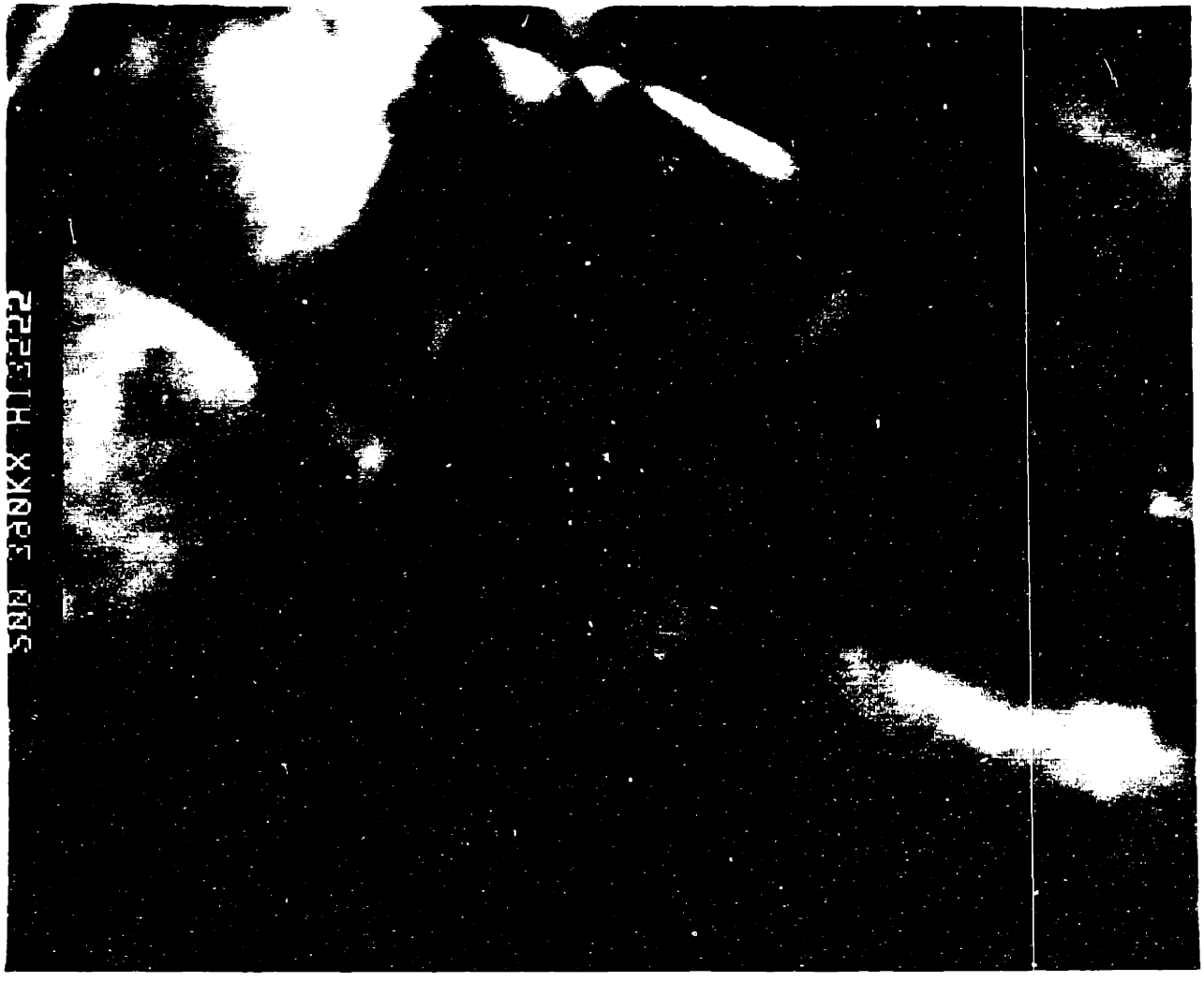

Figure 4.3: Plan-view transmission electron micrograph of a 50 Å Ni/2000 Å Cu/NaCl (001) thin film [Inglefield *et al.*, 1993]. The micrograph shows the 60° dislocations running along the <110> directions in the plane of the Ni/Cu (001) interface.

4.1. Localized Strain Fields around Misfit Dislocations

The first quantitative model describing the localized strain created around edge dislocations and taking into account the discrete nature of the lattice was proposed by Peierls and Nabarro [Hirth and Lothe, 1992]. This one-dimensional model considers two semi-infinite simple-cubic crystals with their [100] and [010] axes parallel but with an initial lattice mismatch in the x direction across the z = 0 plane, where the (x,y,z) cartesian coordinate system is the same as the one in Fig. 4.2. Antisymmetric displacements about the z = 0 plane are then imposed on the two half-crystals which are then joined to form the edge dislocation shown in Fig. 4.2. The boundary conditions are such that the lattice mismatch between the two half-crystals is nil at $x = \pm \infty$. By convention, the sense and Burgers vector of this simple edge dislocation are given by $\vec{\xi} = \mathbf{j}$ and $\mathbf{b} = -b\,\mathbf{i}$, respectively, where **i** and **j** are the unit vectors along the x and y directions, respectively. Assuming that the two media are elastically isotropic, the localized stress field generated around the dislocation line is given by the following equations in the (x,y,z) coordinate system of Fig. 4.2:

$$\sigma_{xx} = -\frac{\mu b}{2\pi(1-\nu)}\left[\frac{3z+2\zeta}{x^2+(z+\zeta)^2} - \frac{2z(z+\zeta)^2}{(x^2+(z+\zeta)^2)^2}\right] \tag{4.2}$$

$$\sigma_{yy} = -\frac{\mu b \nu}{\pi(1-\nu)}\frac{z+\zeta}{x^2+(z+\zeta)^2} \tag{4.3}$$

$$\sigma_{zz} = -\frac{\mu b}{2\pi(1-\nu)}\left[\frac{z}{x^2+(z+\zeta)^2} - \frac{2x^2 z}{(x^2+(z+\zeta)^2)^2}\right] \tag{4.4}$$

$$\sigma_{xz} = \frac{\mu b}{2\pi(1-\nu)}\left[\frac{x}{x^2+(z+\zeta)^2} - \frac{2xz(z+\zeta)}{(x^2+(z+\zeta)^2)^2}\right] \tag{4.5}$$

where $z > 0$ and where $\zeta = \frac{d}{2(1-\nu)}$ with d being the interplanar spacing. The stresses σ_{xy} and σ_{yz} are nil for all (x,y,z). Here we use $d = b = a_0(\text{Ni})$. μ is the shear modulus and ν is Poisson's ratio. The value 2ζ is called the width of the dislocation and it gives a rough measure of the extent of the core region which cannot be described by linear elasticity. The strain field can be obtained from the stress field by using the following equations which apply for linearly isotropic media [Hirth and Lothe, 1992]:

$$\varepsilon_{xx} = \frac{1}{E}[\sigma_{xx} - \nu(\sigma_{yy} + \sigma_{zz})] \quad (4.6)$$

$$\varepsilon_{yy} = \frac{1}{E}[\sigma_{yy} - \nu(\sigma_{xx} + \sigma_{zz})] \quad (4.7)$$

$$\varepsilon_{zz} = \frac{1}{E}[\sigma_{zz} - \nu(\sigma_{xx} + \sigma_{yy})] \quad (4.8)$$

$$\varepsilon_{xz} = \frac{1}{2\mu}\sigma_{xz} \quad (4.9)$$

where $E = 2\mu(1 + \nu)$ is Young's modulus. For Ni, $\mu = 9.47 \times 10^{10}$ Pa and $\nu = 0.276$ [Hirth and Lothe, 1992] yielding $E = 2.42 \times 10^{11}$ Pa .

The plots of the strains e_{xx}, e_{zz}, and e_{xz} as a function of the variable x (i.e. as a function of distance away from the dislocation core) and with $z = 0$ (i. e. in the plane of the interface) are shown in Figs. 4.4, 4.5, and 4.6, respectively. The strain e_{yy} is nil for all x, i. e. no strain is experienced along the length of the dislocation core due to the presence of the edge dislocation. The first important result of Figs. 4.4 to 4.6 is that misfit dislocations give rise to very large strains, especially when compared to the maximum misfit strain of 2.6% for the Ni/Cu (001) system. In particular, the strain $|e_{xx}|$ ($z = 0$) achieves a maximum larger than 20% at the dislocation core ($x = 0$, $z = 0$). This huge compressive strain due to the misfit dislocation is the strain that one would experience in the x direction by crossing the dislocation line in the heterointerface ($z = 0$) along a direction perpendicular to the dislocation line. On the other hand, the strain e_{zz} ($z = 0$), which is the strain that one would experience normal to the interface by crossing the dislocation line in the heterointerface along a direction perpendicular to the dislocation line, is tensile, large, and reaches a maximum of approximately 10% at the dislocation core ($x = 0$, $z = 0$). The second very important result of Figs. 4.4 to 4.6 is that the strain field generated by a misfit dislocation is very localized. In fact, the large strains $e_{xx}(z = 0)$ and $e_{zz}(z = 0)$ drop to zero when one moves away from the dislocation core by only 20 Å in the heterointerface. A natural question arises following these observations: how fast does the large strain e_{xx} at the dislocation core drop as one moves away from the core in a direction perpendicular to the film? The answer is given by Fig. 4.7 which is a plot of $e_{xx}(x = 0)$ as a function of z for $z > 0$. The figure shows that the strain $e_{xx}(x = 0)$ due to the dislocation drops to nearly zero when one moves away from the core approximately by a distance $z = 20$ Å in the direction normal to the interface. This decay is very similar to the one of $e_{xx}(z = 0)$ when one moves away from the core in the heterointerface along the x direction, as can be seen by comparing Fig. 4.4. and 4.7.

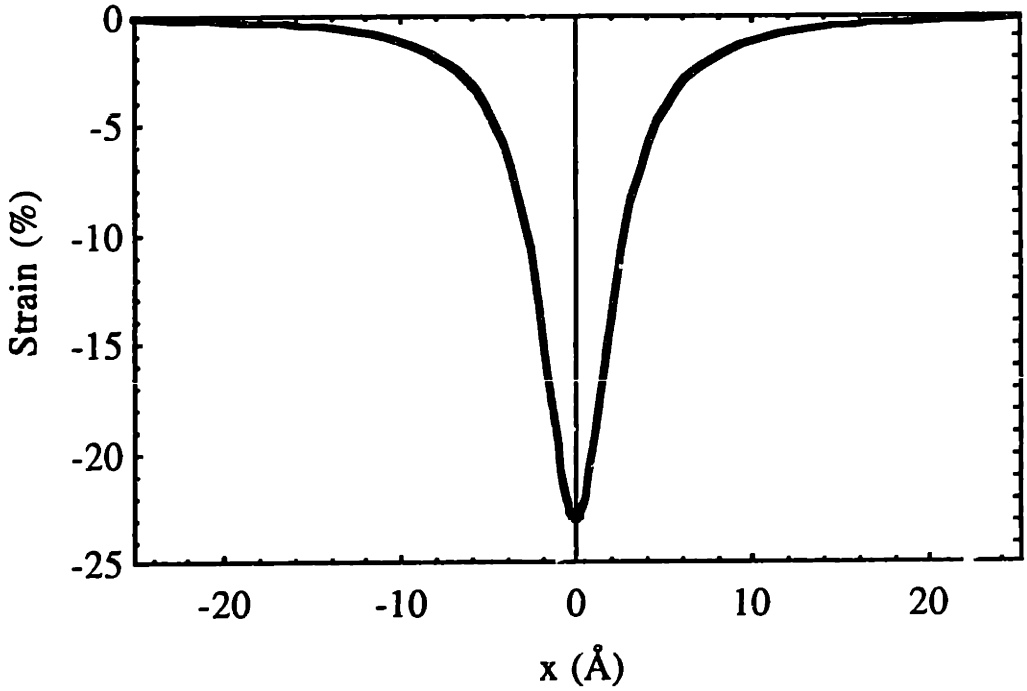

Figure 4.4: Strain experienced along the x direction by crossing the dislocation line in the heterointerface (z = 0) along a direction perpendicular to the dislocation line.

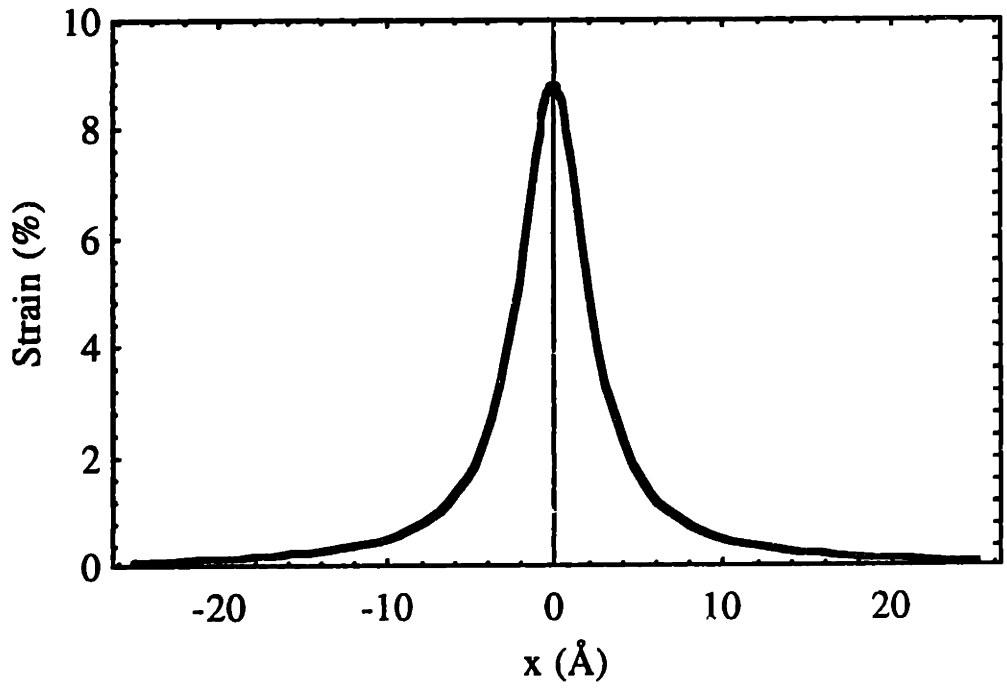

Figure 4.5: Strain experienced along the z direction by crossing the dislocation line in the heterointerface (z = 0) along a direction perpendicular to the dislocation line.

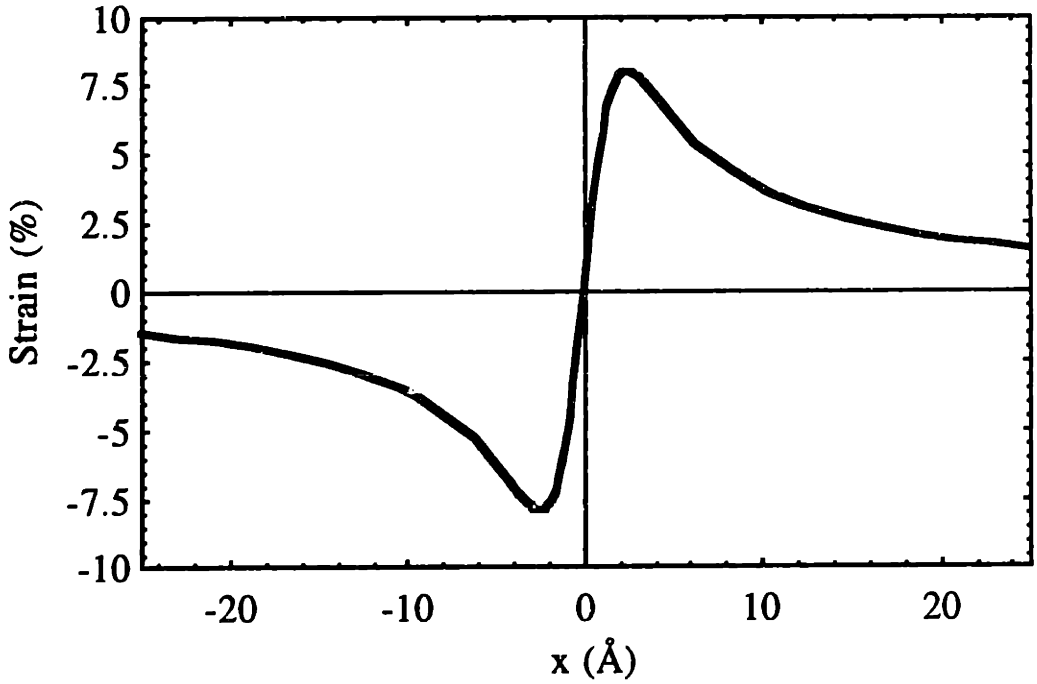

Figure 4.6: Shear strain e_{xz} experienced by crossing the dislocation line in the heterointerface (z = 0) along a direction perpendicular to the dislocation line.

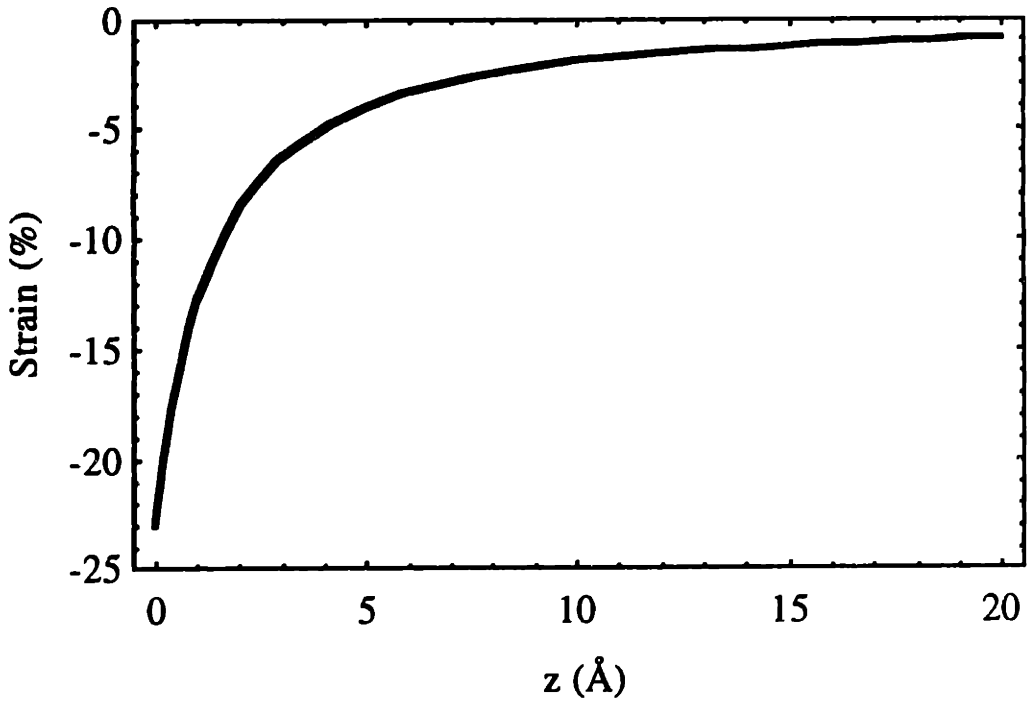

Figure 4.7: Strain experienced along the x direction by moving away from the dislocation core in a direction normal to the heterointerface (x = 0).

Although the Peierls-Nabarro model takes into account the discreteness and the periodicity of the crystal lattice and therefore removes the artificial divergence at the core of the dislocation, which arose in previous idealized continuum theories, it suffers from several shortcomings. First of all, the Peierls-Nabarro model assumes that the two materials making up the heterostructure are semi-infinite in the direction perpendicular to the interface. Second, the model considers a one-dimensional periodic simple-cubic lattice which does not distinguish between bcc and fcc crystal structures. Third, it makes use of linear elasticity theory. However, strains at the dislocation core are so large that it is questionable whether Hooke's law applies. Fourth, the above model does not take into account dislocation interactions. A more accurate description of the localized strain around dislocation cores in thin films can be obtained by performing semi-empirical atomic calculations using the embedded-atom potential method. We have done a feasibility study of the stress relaxation in Ni/Cu (001) bicrystals using this method and have obtained some interesting preliminary results which are presented and explained in the Appendix.

The strain that we described in this section is the localized strain due only to the dislocations. When this strain is superimposed on top of the 2.6% in-plane biaxial tensile misfit strain due to the Ni-Cu lattice mismatch, one then obtains the total misfit strain in the film. The average of the latter strain gives the in-plane biaxial misfit strain e_0 of Eq. (2.6). The dependence of e_0 on the Ni film thickness h above the critical thickness h_c forms the subject of the following two sections.

4.2. The Matthews-Blakeslee Thermodynamic Model

The equilibrium theory of strain relaxation in thin films was originally described by Franck and van der Merwe [1949] and van der Merwe [1963], and was extended by Matthews and Blakeslee [1974, 1975]. The Matthews-Blakeslee model yields useful results and is the main subject of this section. Its primary limitations are that it induces a singularity in the stress field at the dislocation core (a feature which is nonphysical) and that it considers misfit dislocations as the only mechanism for misfit strain relief. Modified theories of misfit dislocation energetics have been proposed more recently [Dunstan *et al.*, 1991; Payne *et al.*, 1993] which overcome some limitations of the Matthews-Blakeslee model.

In the early stages of epitaxy, the pseudomorphic film experiences an anisotropic strain described by Eq. (2.6) with $e_0 = \eta$. The coherency energy per unit area associated with the strain in the epitaxial layer is given by [Tsao, 1993]:

$$u_{coh} = 2\,\mu \left(\frac{1+\nu}{1-\nu}\right) h\, e_0^2 = 2\,\mu \left(\frac{1+\nu}{1-\nu}\right) h\, \eta^2, \tag{4.10}$$

where h is the thickness of the film. Above the critical thickness h_c, the introduction of misfit dislocations becomes energetically favorable and partially relieves the misfit strain in the film. The dislocations form a square grid in the plane of the film-substrate interface and are separated by a distance S. The linear density of dislocations running along a specific direction (i. e. [110] or [1$\bar{1}$0] in fcc crystals) is $\rho_{md} = 1/S$. As mentioned above, misfit dislocations in fcc crystals have Burgers vectors that make an angle of $\lambda = 60^\circ$ with the direction that is both perpendicular to the dislocations and that lies in the plane of the interface. Only the component b cosλ acts to relieve lattice misfit strain. The average in-plane biaxial misfit strain remaining for $h > h_c$ is given by:

$$e_0 = \eta - \langle e_{md} \rangle, \tag{4.11}$$

where $\langle e_{md} \rangle$ is the contribution of the misfit dislocation to the strain in the film, averaged over the volume of the film. The incoherency strain in Eq. (4.11) can be approximated by [Tsao, 1993]:

$$e_0 = \eta - \frac{b\cos\lambda}{S} = \eta - \rho_{md}\, b \cos\lambda. \tag{4.12}$$

In a fully coherent interface $S = \infty$, and one recovers the result $e_0 = \eta$. For $h > h_c$, the dependence of the incoherency strain energy density on misfit dislocations density is then given by:

$$u_{incoh} = 2\,\mu \left(\frac{1+\nu}{1-\nu}\right) h\, e_0^2 = 2\,\mu \left(\frac{1+\nu}{1-\nu}\right) h \left(\eta - \rho_{md}\, b \cos\lambda\right)^2. \tag{4.13}$$

While acting to relieve misfit strain, misfit dislocations also cost energy due to the disruption in bonding associated with the atoms located in the interface around the cores, and to the huge strain fields generated away from the cores. The areal energy density associated with each of the two dislocation arrays is given by the linear dislocation density times the energy of an isolated dislocation [Tsao, 1993]:

$$u_{md} = \rho_{md}\, \frac{\mu\, b^2}{4\,\pi} \left(\frac{1 - \nu\cos^2\beta}{1-\nu}\right) \ln\left(\frac{4\,h}{b}\right), \tag{4.14}$$

where β is the angle given by $\cos\beta = \vec{\xi} \cdot \frac{\mathbf{b}}{b} = \cos 60^\circ = 1/2$, for fcc crystals. For $h > h_c$, the total areal elastic energy density is the sum of areal energy densities associated with the incoherency strain and both of the dislocation arrays, i. e.:

$$u_{tot} = u_{incoh} + 2u_{md} \tag{4.15}$$

$$\Rightarrow u_{tot} = 2\mu\left(\frac{1+\nu}{1-\nu}\right)h\left(\eta - \rho_{md}\, b \cos\lambda\right)^2 + \rho_{md}\,\frac{\mu\, b^2}{2\pi}\left(\frac{1-\nu\cos^2\beta}{1-\nu}\right)\ln\left(\frac{4h}{b}\right) \tag{4.16}$$

The dependence of u_{tot} on ρ_{md} displays two distinct kinds of behavior. For thin films or low misfit systems, the total energy density is minimum at $\rho_{md} = 0$. Misfit dislocations cost more energy than is regained by the release of misfit strain. The fully strained coherent epilayer is thermodynamically more stable. This situation corresponds to:

$$\left[\frac{\partial u_{tot}}{\partial \rho_{md}}\right]_{\rho_{md}=0} > 0. \tag{4.17}$$

On the other hand, for thick films or high misfit systems, the total energy density is minimum for $\rho_{md} > 0$. The introduction of some misfit dislocations costs less energy than is gained by the release of misfit strain. The semi-coherent interface is thermodynamically more stable. This situation corresponds to:

$$\left[\frac{\partial u_{tot}}{\partial \rho_{md}}\right]_{\rho_{md}=0} < 0. \tag{4.18}$$

The critical thickness for the onset of misfit dislocations is given by the condition $\left[\frac{\partial u_{tot}}{\partial \rho_{md}}\right]_{\rho_{md}=0} = 0$, or:

$$h_c = \frac{b}{8\pi\eta\cos\lambda}\left(\frac{1-\nu\cos^2\beta}{1+\nu}\right)\ln\left(\frac{4h_c}{b}\right). \tag{4.19}$$

The most common type of Burgers vectors in fcc crystals are of the $\frac{1}{2}$<110> type, yielding $b = \frac{1}{\sqrt{2}}a_0$ (film). Using $\beta = \lambda = 60^\circ$, one finds that $h_c \approx 18$ Å in Ni/Cu (001). This value of h_c has been observed experimentally by Matthews and Crawford [1970], Inglefield *et al.* [1993], and Jungblut *et al.* [1994]. The equilibrium linear dislocation density can be found by minimizing u_{tot} with respect to ρ_{md}:

$$\frac{1}{S} = \rho_{md} = \frac{\eta}{b\cos\lambda}\left[1 - \frac{h_c}{h}\frac{\ln\left(\frac{4h}{b}\right)}{\ln\left(\frac{4h_c}{b}\right)}\right]. \qquad (4.20)$$

We plot the dislocation spacing as a function of film thickness for the Ni/Cu (001) system, as predicted by Eq. (4.20), in Fig. 4.8. The dislocations spacing decreases as the film grows thicker and converges to the limit $S \approx 50$ Å. Substituting Eq. (4.20) into Eq. (4.12) yields the average in-plane biaxial misfit strain in a semi-coherent film:

$$e_0(h) = \eta\frac{h_c}{h}\frac{\ln\left(\frac{4h}{b}\right)}{\ln\left(\frac{4h_c}{b}\right)}. \qquad (4.21)$$

This strain can be approximated by:

$$e_0(h) = \eta\frac{h_c}{h} \qquad (4.22)$$

which has been proposed by Chappert and Bruno [1988] and has been frequently referred to in the thin film magnetism community. The strains of Eqs. (4.21) and (4.22) are plotted in Fig. 4.9 for Ni/Cu (001) thin films. Notice the kink in the plots at the critical thickness $h_c = 18$ Å.

A very interesting result falls out of Eqs. (4.19) and (4.21). Consider a thin film growing epitaxially on two different substrates such as Cu (001) and $Cu_{60}Ni_{40}$ (001) where the lattice mismatch is 2.6% and 1.6%, respectively, and where the critical thickness is 18 Å and 35 Å, respectively. Then, according to Eq. (4.21), the average in-plane biaxial tensile misfit strain in the Ni film is the same in Ni/Cu (001) and in $Ni/Cu_{60}Ni_{40}$ (001) for all thicknesses $h > 35$ Å. This result is illustrated graphically in Fig. 4.10. A phase diagram showing the critical thickness h_c and the lattice mismatch η corresponding to Ni thin films grown epitaxially on $Cu_{1-x}Ni_x$ (001) substrates for $0 < x <$ 50% is shown in Fig. 4.11. It was obtained using Eq. (4.19) and the fact that Ni and Cu form a solid solution in the bulk.

Although the Matthews-Blakeslee model gives a reasonable estimate of the functional dependence of the strain on the film thickness, it sometimes underestimates the strain remaining in the film [Nix, 1989]. This is because the Matthews-Blakeslee model is based purely on thermodynamic grounds and therefore omits the energy barrier that

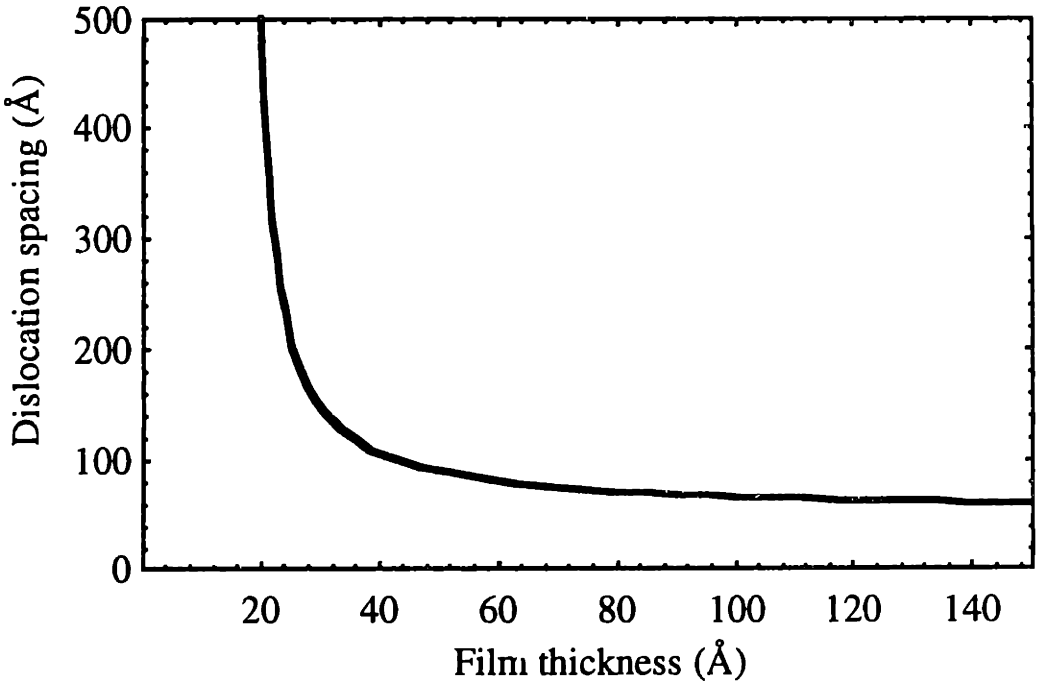

Figure 4.8: Misfit dislocations density as a function of film thickness in Ni/Cu (001) thin films as predicted by the Matthews-Blakeslee model.

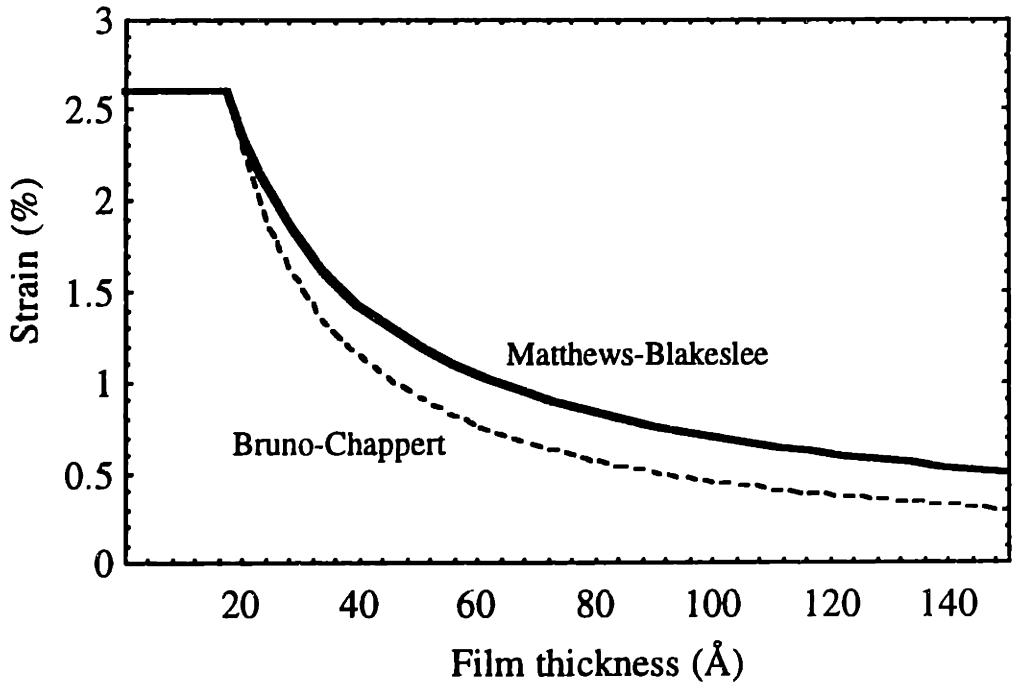

Figure 4.9: Average in-plane biaxial misfit strain as a function of film thickness for Ni/Cu (001) thin films according to the Matthews-Blakeslee (Eq. (4.21), solid line) and to the Bruno-Chappert (Eq. (4.22), dotted line) models.

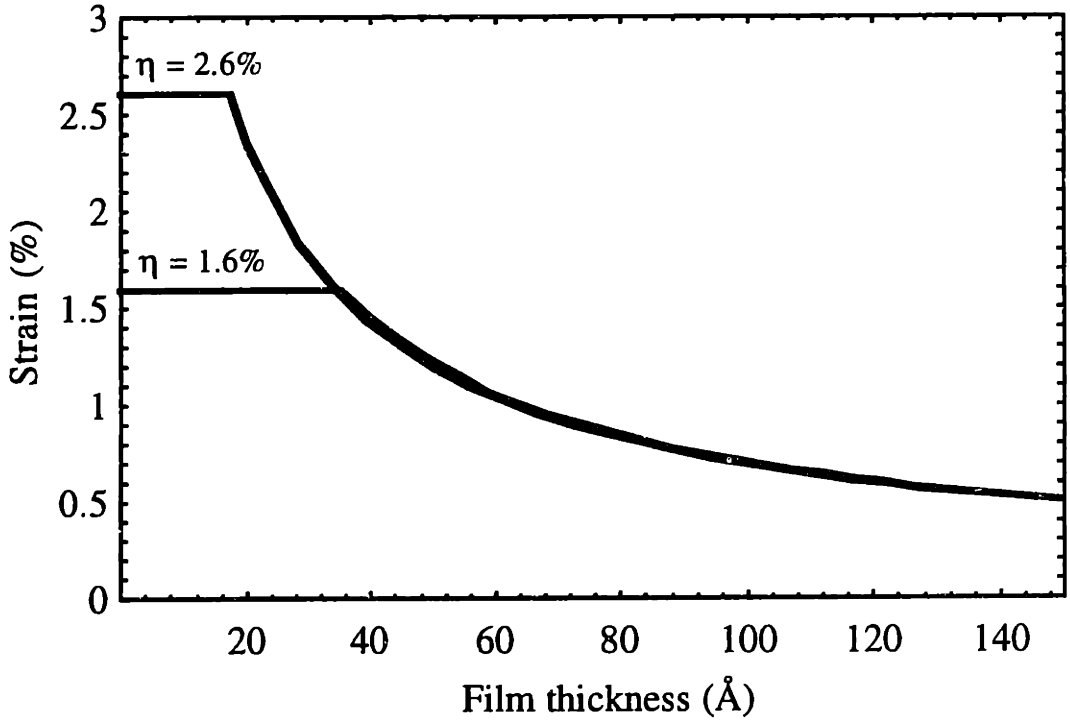

Figure 4.10: Average in-plane biaxial misfit strain as a function of Ni film thickness for Ni/Cu (001) (η = 2.6%, h_c = 18Å) and for $Ni/Cu_{60}Ni_{40}$ (001) (η = 1.6%, h_c = 35 Å), according to Eqs. (4.19) and (4.21).

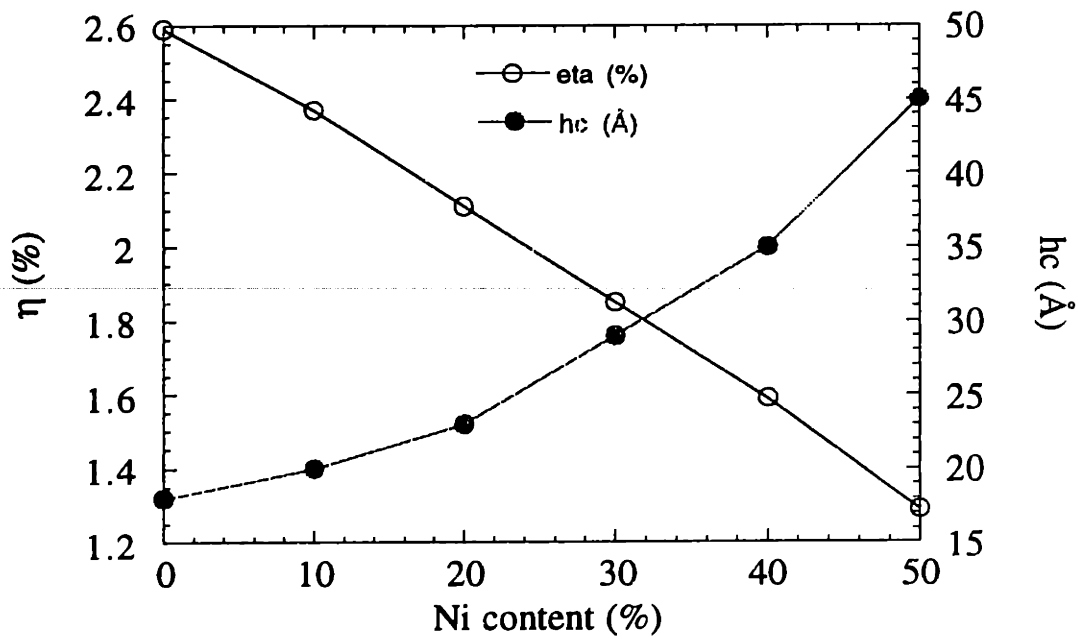

Figure 4.11: Lattice mismatch and critical thickness in $Ni/Cu_{1-x}Ni_x$ (001) as a function of Ni content (x) in the substrate.

needs to be overcome for the nucleation of misfit dislocations at the film's surface. It is a limitation of kinetic nature.

4.3. Misfit Strain in Ni/Cu (001) Thin Films

Quantitative measurements of strain relaxation in the Ni/Cu epitaxial system were first carried out by Gradmann [1966] for films grown with a (111) orientation. Matthews and Crawford [1970] studied the accommodation of misfit strain in epitaxial Ni/Cu (001) thin films evaporated on NaCl substrates. Their transmission electron micrographs showed that the onset of misfit dislocations in Ni/Cu (001) occurs at $h_c = 15 \pm 3$ Å, which is in good agreement with the value predicted by the Matthews-Blakeslee theory ($h_c = 18$ Å). Matthews and Crawford found a close agreement between the experimentally measured and the theoretically predicted dislocations density for Ni films with 15 Å $\leq h \leq$ 50 Å. For films thicker than h_c, the misfit strain accommodated by dislocations was determined from the average separation of the moiré fringes. Comparison of these spacings and the spacings calculated from the bulk lattice parameters of Ni and Cu enabled the elastic strain in the Ni films to be found. For films thicker than 50 Å, the elastic strain was found to be significantly larger than the predicted values. However, Bruno and Renard [1989] showed that the elastic strain data of Matthews and Crawford [1970] can be reasonably fit by the 1/h functional form of Eq. (4.22) for Ni thicknesses up to 100 Å. The data of Mattews and Crawford and the 1/h fit are shown in Fig. 4.12.

More recent characterizations of misfit strain accommodation in Ni/Cu (001) thin films were done by Inglefield *et al.* [1993] and Inglefield *et al.* [1995]. The Ni/Cu (001) bicrystals were evaporated on NaCl (001) and Si (001) substrates. The Cu layers were 2000 to 3000 Å thick whereas the Ni film thickness was much smaller, ranging from 15 to 200 Å. It was shown that the measured distance separating neighboring dislocations is larger than the one predicted by the Matthews-Blakeslee model, especially at small Ni thicknesses. The misfit strain in the Ni thin films was also measured as a function of film thickness using the moiré fringes spacing. These measurements are shown in Fig. 4.13. The solid line in the figure is the best fit to the data points using a power law functional form. The equation of the solid line is:

$$e_0 \approx \frac{10}{h^{0.53}} \tag{4.23}$$

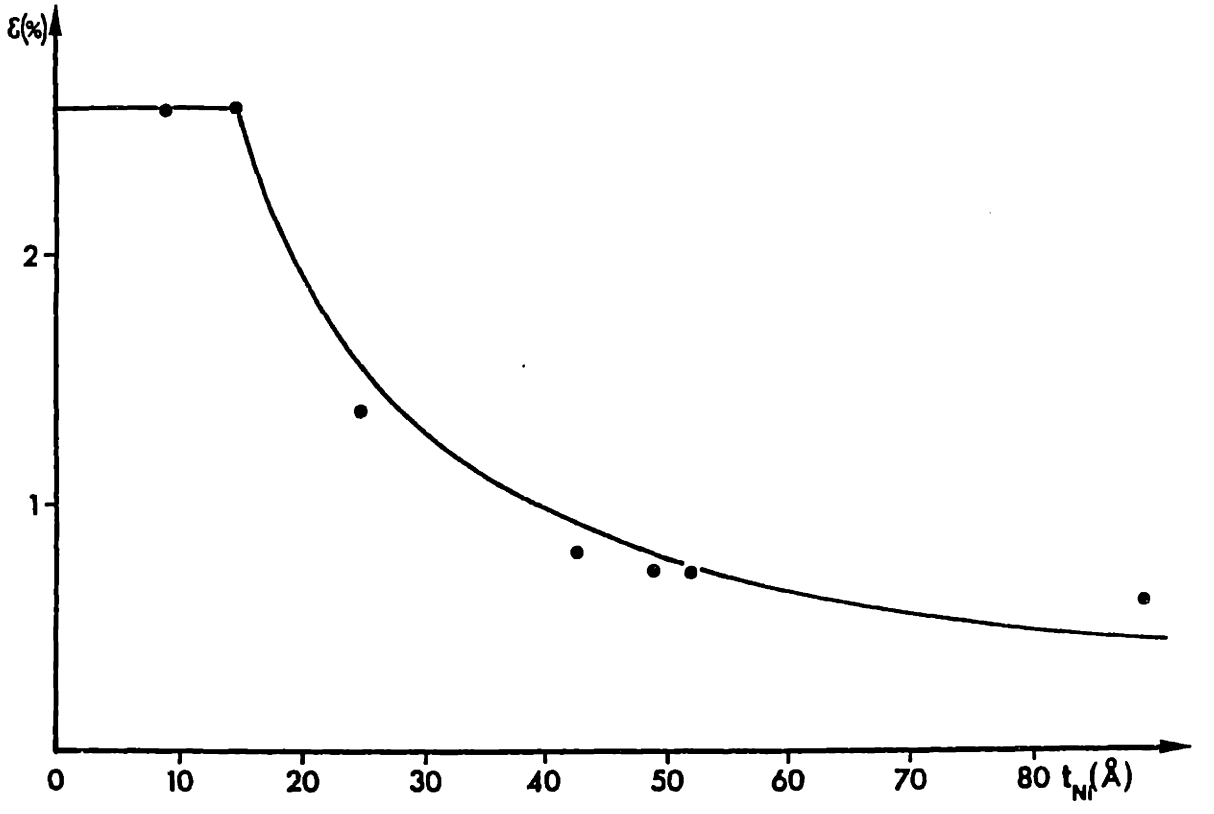

Figure 4.12: Thickness dependence of the strain in Ni thin films grown on Cu (001) substrates. The experimental points are the ones of Matthews and Crawford [1970]. The solid line is a plot of the Eq. (4.22) with $h_c = 15$ Å [Bruno and Renard, 1989].

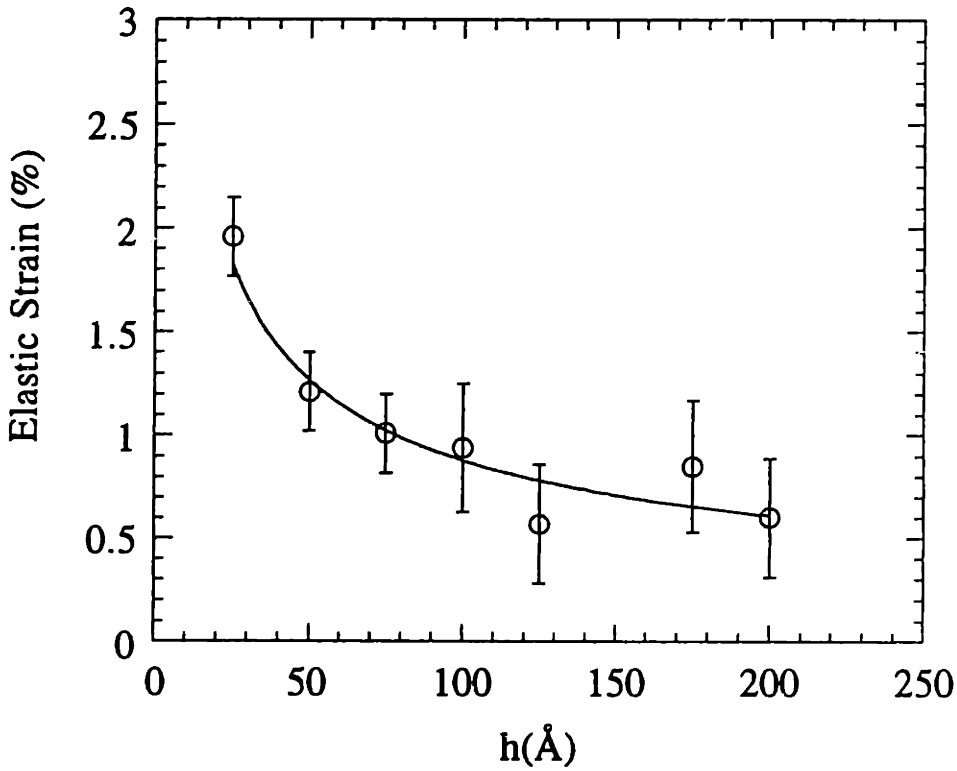

Figure 4.13: In-plane misfit strain in Ni/Cu (001) thin films evaporated on NaCl (001) substrates, measured using the moiré fringes method [Inglefield *et al.*, 1993]. The solid line represents the best fit to the data points using a power law functional form which is given by Eq. (4.23).

where h is in Å. Equation (4.23) differs significantly from the Chappert-Bruno functional dependence of Eq. (4.22). Inglefield *et al.* [1993] further showed that the residual strain expected from the measured dislocation density according to Eq. (4.12) is larger than that extracted from moiré fringes measurements. In other words the measured dislocation density cannot account for the misfit strain measured through moiré fringes: other strain relaxation mechanisms may also be at play. However, Inglefield *et al.* confirmed that misfit dislocations in Ni/Cu (001) thin films are mostly of the 60° type and run in the Ni-Cu interface along <110> directions. More recently, Inglefield *et al.* [1995] showed that 90° dislocations are also present at the Ni/Cu (001) interface. They also showed that the onset of misfit dislocations occurs at 15 Å < h_c < 25 Å, in agreement with other experimental observations [Matthews and Crawford, 1970; Jungblut *et al.*, 1994] and with the theoretical prediction of the Matthews-Blakeslee model.

Strain was also measured recently in Ni/2000 Å Cu/Si (001) thin films using a WYKO 6000 PC optical interferometer [Inglefield *et al.*, 1995]. This instrument uses optical reflection from a Si wafer compared with the reflection from a flat reference to determine the curvature of the Si wafer. By measuring the curvature of the wafer before and after deposition of the Cu layer, one can determine the curvature caused by the 2000 Å Cu layer. The curvature of the Ni/2000 Å Cu/Si (001) thin films was also obtained for different Ni film thicknesses. By subtracting the "background" curvature due to the Cu layer, one obtains the effective change in curvature $\Delta\kappa$ of the Si wafer due to the Ni film. A modified version of Stoney's equation [Ohring, 1992] can then be used to find the elastic strain in the Ni films for different Ni thicknesses:

$$e_0 = \frac{h_{Si}^2 M_{Si} \Delta\kappa}{6 M_{Ni} h} \tag{4.24}$$

where h and h_{Si} are the thicknesses of the Ni film and Si wafer, respectively. M_{Si} = 1.805×10^{11} Pa and M_{Ni} = 2.23×10^{11} Pa are the biaxial elastic moduli of Si and Ni, respectively. The resulting strain measurements, obtained by assuming that e_0(h = 15 Å) = 2.6%, are shown in Fig. 4.14. The strain measured by optical interferometry is larger than the strain measured using the moiré fringes and shown in Fig. 4.13. The solid line shown in Fig. 4.14 is the best fit of the data points using a power law functional form. The equation of the line is given by:

$$e_0 \approx \frac{18.15}{h^{0.70}} \tag{4.25}$$

with h in Å. The functional form of Eq. (4.25) also differs from the one given by the Chappert-Bruno model of Eq. (4.22).

In summary, the elastic strain in Ni/Cu (001) thin films has been measured using different techniques which give different results. The discrepancies may be due to the fact that all the techniques provide indirect measurements and require different kinds of sample preparation prior to the actual strain measurement, which may or may not affect the state of strain of the films. Moreover, all the above techniques are based on *ex-situ* measurements which result in the exposure of the films to air. Inglefield *et al.* [1995] have shown that the formation of a very thin oxide layer (h_{oxide} < 10 Å) at the Ni surface could affect the state of strain of the film. More accurate measurements of the strain in ultrathin films can be achieved *in-situ* using X-ray absorption fine structure techniques such as EXAFS [Heckmann, 1993] which are capable of resolving lattice spacings in

ultrathin films only a few monolayers thick. Unfortunately, these techniques are not readily available as they involve complex experimental set-ups and X-ray synchrotron sources.

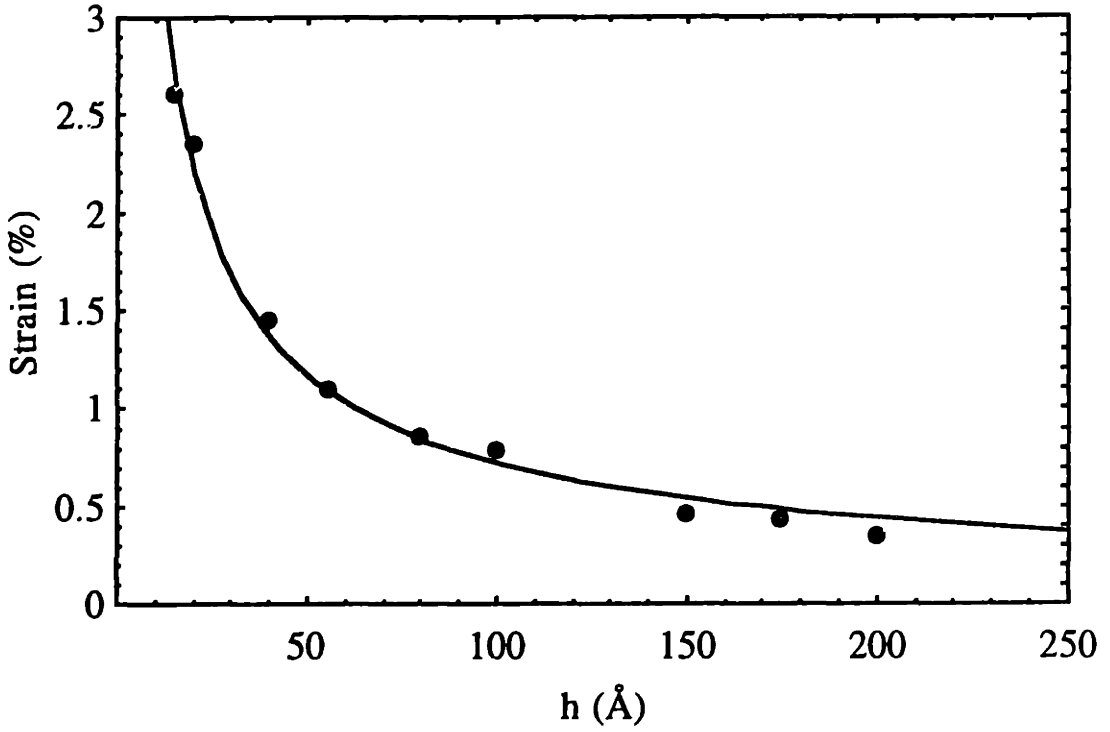

Figure 4.14: Thickness dependence of the strain in Ni/2000 Å Cu/Si (001) thin films measured by optical interferometry [Inglefield *et al.*, 1995]. The solid line represents the best fit to the data points using a power law functional form which is given by Eq. (4.25).

Chapter 5
Experimental Procedures

The Ni/Cu (001) thin films were evaporated on Si (001) wafers using a molecular beam epitaxy (MBE) deposition system. The structure and chemistry of the films were characterized *in-situ* using reflection high-energy electron diffraction (RHEED) and Auger electron spectroscopy (AES) and *ex-situ* using plan-view and cross-sectional transmission electron microscopy (TEM), X-ray diffraction, and optical interferometry. Plan-view TEM allowed the determination of the type, orientation, and spacing of the misfit dislocations located at the Ni/Cu interface whereas cross-sectional TEM was used to characterize the Cu/Si (001) and Cu/Ni (001) interfaces. Thin-film X-ray diffraction was employed to examine the crystallographic orientation of the Ni and Cu layers deposited on the Si (001) wafers, and to identify the products of a reaction occurring at the Cu/Si interface. The strain in the Ni and Cu films was measured *ex-situ* using a WYKO optical interferometer which was described in section 4.3. The structural characterization of Ni/Cu/Si (001) thin films forms the main subject of the doctoral thesis of Heather E. Inglefield [1995]. Most of the result relevant to the present work are summarized in section 5.3.

The magnetic anisotropy of the Ni/Cu films was characterized *in-situ* using the magneto-optic Kerr effect (MOKE) and *ex-situ* using a vibrating sample magnetometer (VSM). The experimental set-ups used in these characterizations are described in detail in section 5.2 whereas the results of the magnetic measurements form the subject of chapter 6. We will start by giving an overview of the MBE deposition system and of the sample preparation in section 5.1.

5.1. The Molecular Beam Epitaxy Deposition System

The metal films were all deposited on Si (001) wafers using a Perkin-Elmer molecular beam epitaxy (MBE) system originally designed for semiconductor growth. A schematic top view and a side view picture of the chamber are shown in Figs. 5.1 and 5.2, respectively. The chamber is equipped with a load-lock, two electron-beam evaporators (Cu and Ni), a RHEED set-up, an Auger spectrometer which looks down on the sample holder, a MOKE apparatus for *in-situ* magnetic measurements, and a mass spectrometer. A cryogenic pump and an ion pump continuously evacuate the chamber, maintaining the background pressure between $5x10^{-11}$ and $1x10^{-9}$ Torr. During the Cu and Ni evaporations, the chamber's walls, the evaporation guns, and the sample manipulator are water-cooled. As a result, the pressure does not rise above $1x10^{-7}$ Torr during the deposition of the Cu layer and does exceed $1x10^{-8}$ Torr during the deposition of the Ni films. The load-lock introductory chamber is extremely useful as it allows one to introduce and remove a sample from the main chamber without having to break the ultra-high vacuum there, thus allowing the user to deposit and characterize several samples per day under optimal conditions. A gate valve separating the introductory and main chambers is closed at all times except for the introduction and removal of a sample.

Prior to loading in the chamber, the Si wafers, which are typically 340 μm thick and have a 5mm x 5mm lateral extent, are first dipped in a 10% HF-deionized water solution for 30 to 45 seconds and then immersed in deionized water for about 15 seconds. This process removes the native silicon dioxide layer and terminates the Si surface with hydrogen, making the epitaxial growth of Cu on Si possible. The Si wafers are then attached onto a molybdenum sample holder using tantalum foils and loaded in the introductory chamber. While the gate valve is closed, the introductory chamber is pumped to ultra-high vacuum using liquid nitrogen sorption pumps and then a combination of cryogenic and ion pumps. When the pressure in the load-lock is lower than $1x10^{-8}$ Torr, which requires about one hour of pumping, the gate valve is opened and the sample holder is transferred into the sample manipulator at the center of the main chamber in such a way that the Si wafer is facing the Cu and Ni sources. The samples were not heat-cleaned in the chamber before the growth which was always carried out at room temperature. The deposition rates ranged between 1.5 Å/s and 3 Å/s for the Cu layers and between 0.5 Å/s and 1 Å/s for the Ni films. The deposition rates and the final thickness of the films were computer-controlled. The evaporation guns were calibrated

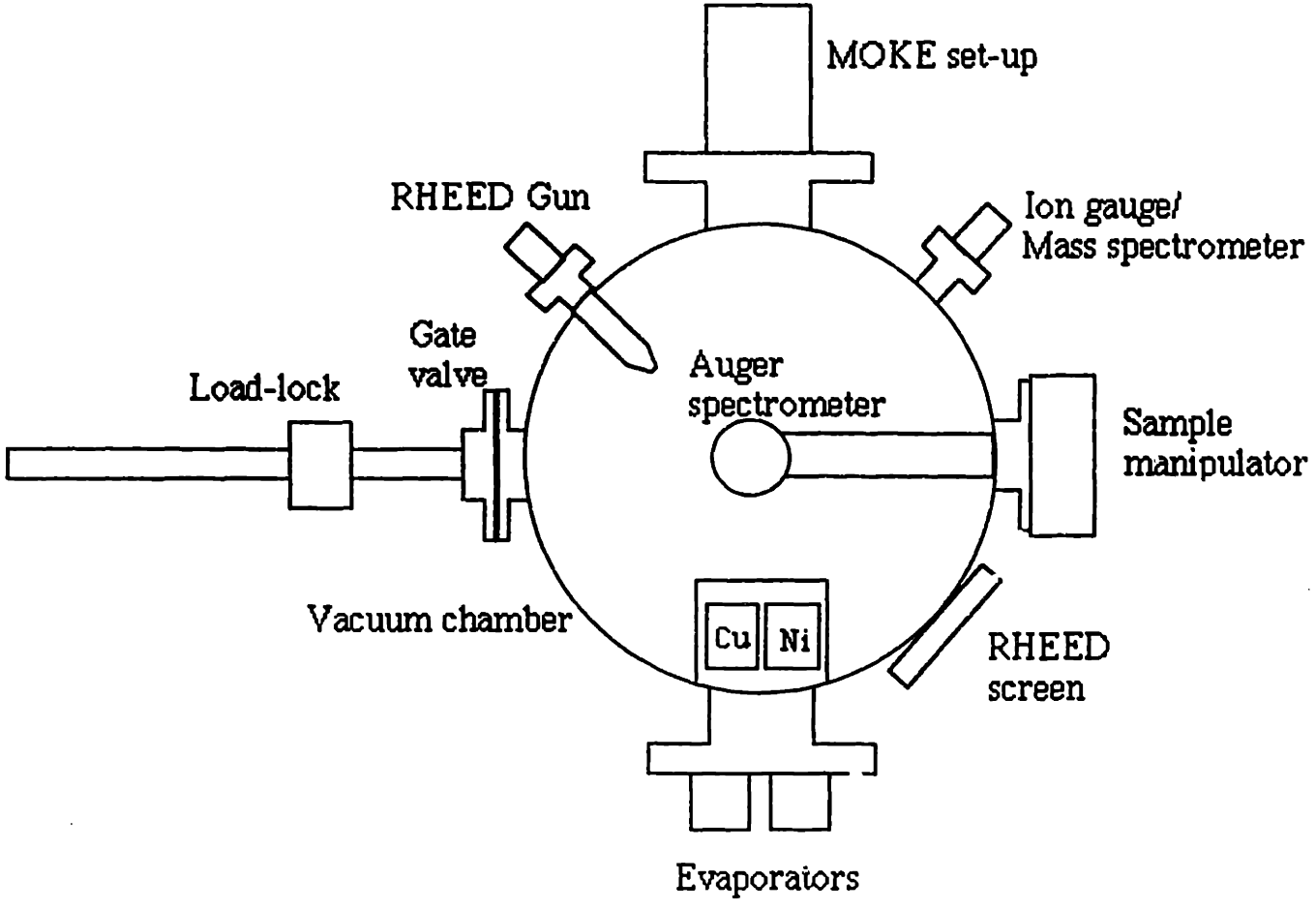

Figure 5.1: Schematic top view of the MBE chamber

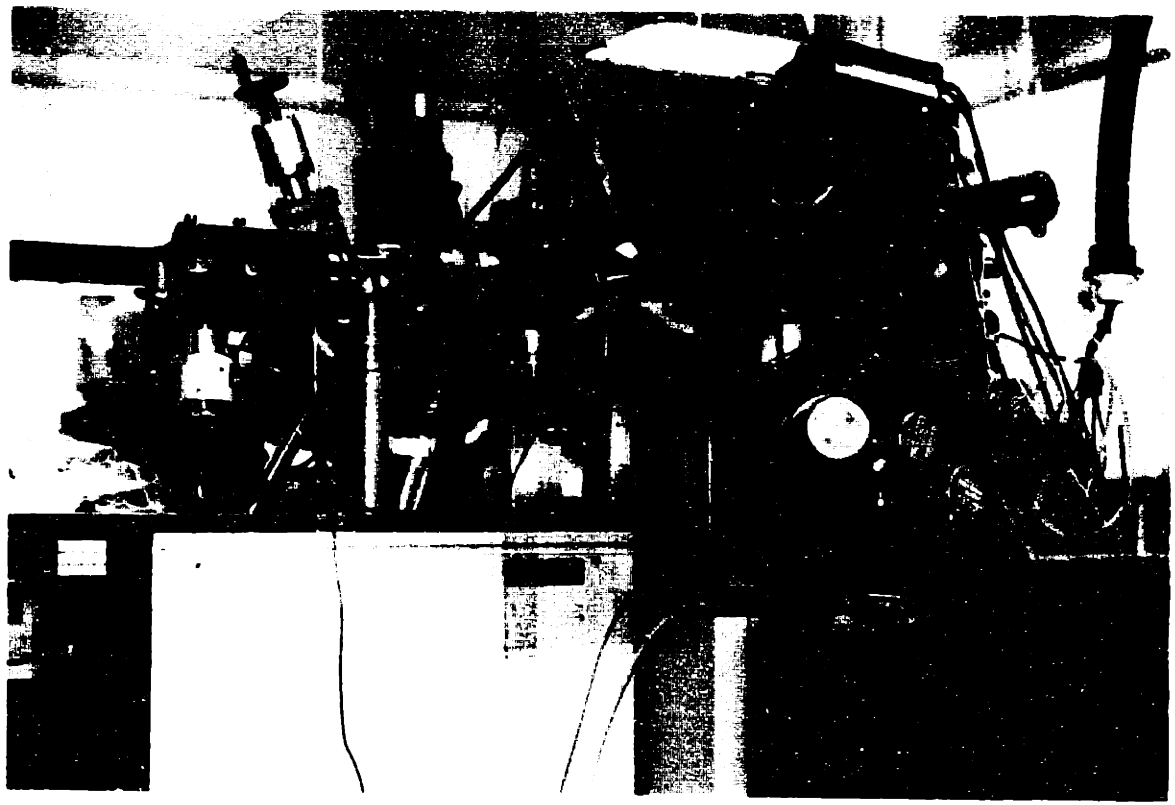

Figure 5.2: Side view picture of the MBE deposition chamber.

every time the main chamber was vented by separately depositing 1000 Å thick Cu and Ni layers on Si wafer substrates, measuring the real thickness of the metallic layers using a DEKTAK 8000 mechanical profilometer (which has a resolution of 5 Å), and adjusting the rate-controlling computer accordingly. The total error in the films thickness was approximately ± 5%. In order to obtain a good film thickness uniformity, the samples were spun in their own plane about their center at a rate of approximately 10 rotations per minute during the depositions of the Cu and the Ni films. Following each deposition, the Ni/Cu/Si (001) thin films were characterized *in-situ* by RHEED, AES, and MOKE.

RHEED is an *in-situ* film characterization technique capable of monitoring the structure of films during and after growth. The RHEED electron beam, which has an energy of 10 keV, is incident on the film's surface at a grazing angle. The outcoming beam has a specular and a diffracted component, and produces a diffraction pattern on a fluorescent screen diametrically opposed to the RHEED gun, as shown in Fig. 5.1. This pattern is characteristic of the surface crystallography of the film. If the thin film is epitaxial, both spotted and streaked patterns with a high degree of symmetry can be observed on the screen. Spots occur as a result of three-dimensional volume diffraction from islands or from a rough surface whereas parallel streaks are characteristic of a smooth layer-by-layer film growth. We will discuss the RHEED patterns that were obtained for Cu/Si (001) and for a Ni/Cu/Si (001) thin film in section 5.3. An important attribute to the RHEED technique is that the measurement apparatus does not interfere with the evaporation sources of the MBE system. This makes it possible to observe the intensity oscillations in the RHEED during MBE growth. During film growth, the intensity of the specular beam undergoes sinusoidal variations that monitor the layer-by-layer growth of the film. The period of the oscillations is equal to the monolayer formation time. Under optimal conditions the oscillations persist for many layers and serve to monitor film growth mode and thickness with a monolayer resolution [Huang *et al.*, 1994]. Unfortunately, we were not able to observe RHEED oscillations while growing our Ni/Cu/Si films because the deposition rates that we have used were too high. Ohring [1992] and Lagally and Savage [1993] give more details on the physics and measurement techniques of RHEED.

AES is a surface chemical characterization technique. It is broadly applicable to detecting, with few exceptions, all of the elements in the periodic table. The elements which are of particular interest to us are Ni, Cu and Si, as well as oxygen and carbon which are the usual contaminants. AES is a true surface analytical technique since the

detected Auger electrons are emitted from surface layers less than 15 Å deep. The surface coverage detection limit of the spectrometer is about 1%. From the peak intensities, it is possible to extract quantitative chemical analysis of the surface but the composition error is of the order of a few percent. As shown in Fig. 5.1, our Auger spectrometer is located right above the sample holder, also looking towards the evaporation sources. Following a deposition, the sample holder is rotated by 180° so that the Ni/Cu/Si sample can face the primary electron beam of the spectrometer. Ohring [1992] and Slaughter *et al.* [1992] give more details on the physics and the technique of Auger spectroscopy.

5.2. Magnetic Anisotropy Measurement Techniques

The magnetic properties of the Ni/Cu thin films were studied *in-situ* by MOKE. A schematic top view of the MOKE set-up, which was designed and partly machined by ourselves, is shown in Fig. 5.3. Following a film deposition, the molybdenum sample holder was rotated into a position which allowed us to apply an external magnetic field in the film plane and perpendicular to it, as shown in Fig. 5.3. The beam incident on the sample is a 10 mW He-Ne laser linearly polarized perpendicular to the plane of incidence but in the film plane. The reflected beam is passed through a quarter-wave plate (which compensates for the polarization distortion caused by the windows of the chambers) and then through another polarizer which is perfectly crossed with the first polarizer (i. e. the two polarizers are rotated by 90° with respect to each other). The intensity of the outcoming light is monitored by a photodiode which is connected to a data acquisition system through a lock-in amplifier. This intensity is proportional to the magnetization of the Ni film and a magnetization versus applied magnetic field can then be constructed by sweeping the magnetic field between two extreme values in opposite directions.

The magneto-optic Kerr effect can be observed by monitoring the change in polarization of a linearly-polarized light reflected from the magnetized ferromagnetic medium. It is illustrated in Fig. 5.4 for a thin film magnetized along its normal. The incident beam, shown on the left, is linearly polarized with the electric field **E** oriented in a direction which falls in the film's plane. This field induces an optical frequency current density **J** given by:

$$\mathbf{J} = \sigma \mathbf{E} \tag{5.1}$$

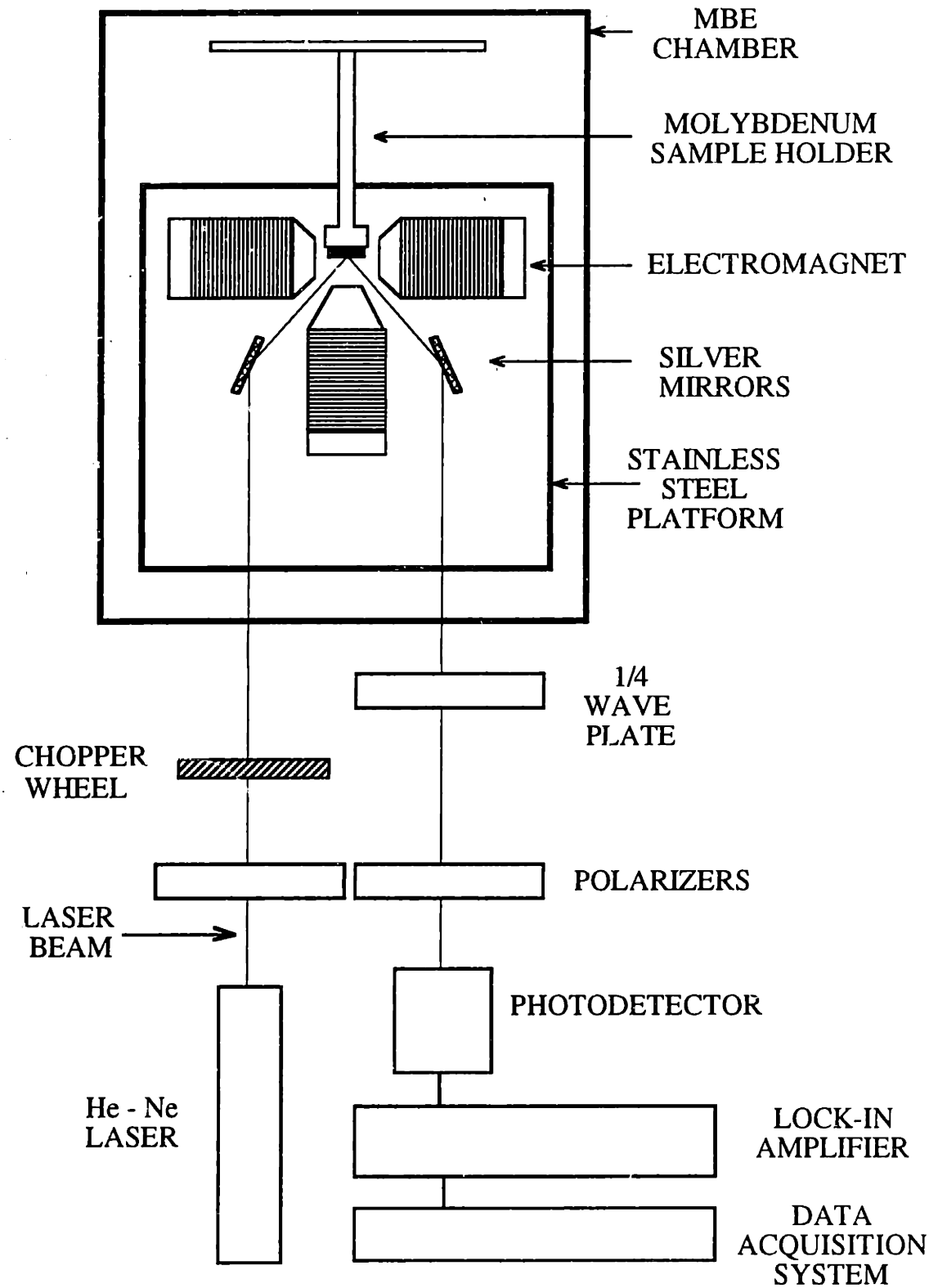

Figure 5.3: Schematic top view of the MOKE set-up used for the magnetic anisotropy characterization of the films in the MBE chamber.

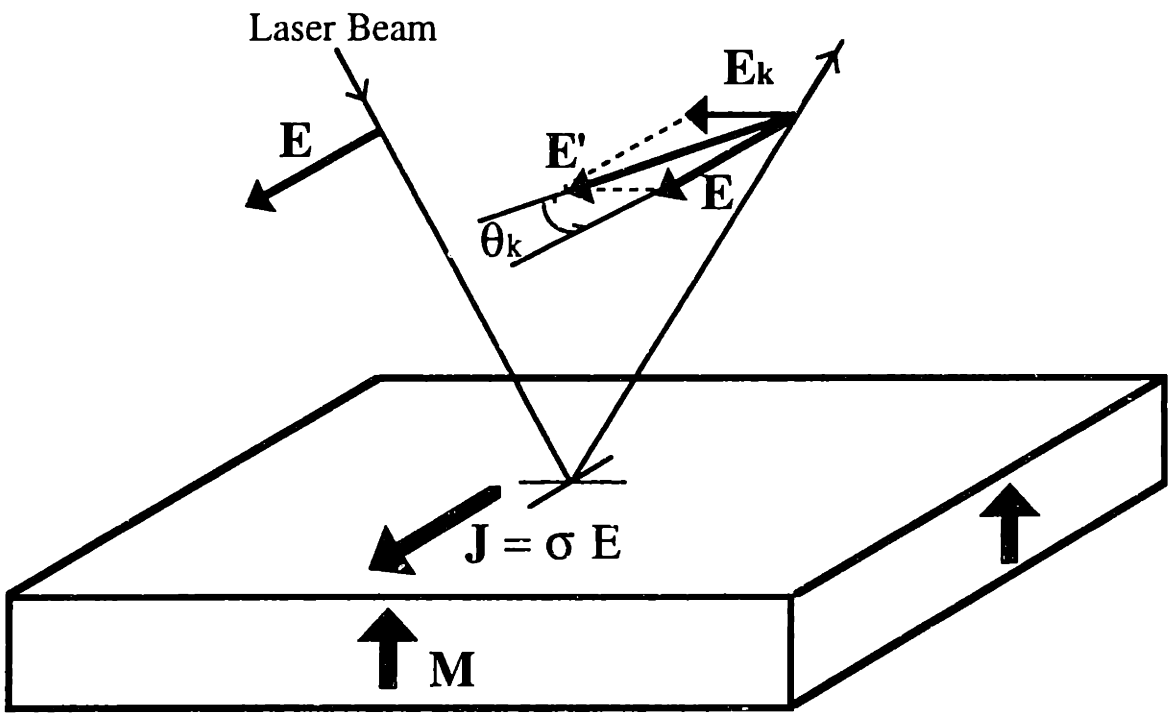

Figure 5.4: The magneto-optic Kerr effect for a thin film magnetized along its normal. The laser beam incident on the film's surface is linearly polarized with an electric vector **E** oriented in the film plane. Upon reflection of the beam, the electric field acquires a component $\mathbf{E_k}$. The field **E'** is rotated by the Kerr angle θ_k with respect to the original field **E**.

where σ is the optical conductivity of the metallic film. This current interacts with the magnetization of the medium giving rise to a Kerr component $\mathbf{E_k}$ to the electric field of the outgoing laser beam which is given by the following equation:

$$\mathbf{E_k} \propto \mathbf{J} \times \mathbf{M} \qquad (5.2)$$

which is perpendicular to both **J** and **M**. In the configuration shown in Fig. 5.4, the vector $\mathbf{E_k}$ is also oriented along a direction that falls in the film plane and makes an angle of 90° with **E**. The electric field of the laser beam therefore undergoes a rotation upon reflection and the electric field of the outgoing beam $\mathbf{E'} = \mathbf{E} + \mathbf{E_k}$ makes an angle θ_k, called the Kerr rotation, with the field **E**. A non-zero rotation θ_k is what gets filtered through the polarizer shown at the right of Fig. 5.3. The light intensity read by the photodiode, which is proportional to θ_k, is therefore proportional to the magnetization of the film. A plot of θ_k versus applied external magnetic field thus bears the same information contained in an M-H loop except that the θ_k - H loop measures the sample's

cross-section weighted by a factor $e^{-z/\delta}$ where z is the depth in the film measured from the free surface and where $\delta = \sqrt{\mu \sigma \omega}$ with μ and ω being the permeability of the film and the frequency of the laser, respectively. The experiment was done with the magnetic field applied in the plane of the film but perpendicular to **E** (longitudinal MOKE) and perpendicular to the film (polar MOKE). A very good review of MOKE and its application in the characterization of ultrathin magnetic films has been given by Bader [1991].

MOKE was shown to be an extremely sensitive and useful probe to study the magnetic anisotropy of ultrathin films while they are kept under ultra-high vacuum. In fact, magnetic hysteresis loops of films as thin as one monolayer have been detected with MOKE [Beier *et al.*, 1988]. With the MOKE set-up that we have built, the maximum magnetic fields that one can apply in the film plane and perpendicular to it are 1,000 Oe and 400 Oe, respectively. These fields are not enough to saturate the films in the hard direction in Ni/Cu (001) thin films. In fact, when the magnetization easy-axis is in the film's plane the anisotropy field that one needs to overcome in order to saturate the film along its normal could be as large as $4\pi M_s \approx 6100$ Oe (for Ni) which is much larger than the field that we can generate perpendicular to the film in the MBE chamber. Moreover, one cannot measure the absolute saturation magnetization M_s of the thin magnetic film with MOKE without knowledge of the optical constants. Rather one measures $\theta(H)$ relative to the maximum value of θ_k which is assumed to correspond to M_s. With reference to Fig. 2.4 , we were therefore unable to extract the effective anisotropy energy density of the Ni/Cu films as a function of Ni film thickness from *in-situ* MOKE measurements because we were unable to saturate the Kerr rotation. We have therefore decided to deposit a series of Cu/Ni/Cu (001) sandwiches by MBE (with an epitaxial Cu capping layer 20 Å thick) and characterize them *ex-situ* with a VSM. The advantages of the Cu capping layer are that it prevents the Ni films from getting oxidized and it makes the two interfaces of the Ni film identical. The advantages of our VSM are that magnetic fields as large as 10,000 Oe can be applied both in the film plane and perpendicular to it, and that the absolute value of the saturation magnetization can in principle be obtained. Moreover, with the VSM one can automatically demagnetize the films and obtain initial magnetization loops similar to the one shown in Fig. 2.4, making it easier to compute magnetic anisotropy energy densities.

5.3. Growth in the Ni/Cu/Si (001) Epitaxial System

Before depositing the Cu layer, the surface crystallography of the Si wafer was examined by RHEED. The diffraction pattern consisted of sharp parallel streaky lines characteristic of a Si (1x1) surface. We were also able to observe the Kikuchi lines which indicate a clean surface. Following these observations, a Cu layer was evaporated on the Si (001) substrate at room temperature. *In-situ* RHEED measurements and *ex-situ* standard X-ray diffraction and X-ray pole figures were used to determine the epitaxial relationship between the Cu layer and the Si (001) substrate. The θ - 2θ X-ray diffraction measurements indicated that the Cu layer grows as a single crystal with a (001) orientation, confirming the observations of Chang [J. Vac. Sci. Technol. A **8**, 3779 (1990); J. Appl. Phys. **67**, 566 (1990)] and of Naik *et al.* [1993]. However, the difference between the lattice parameters of Cu and Si is very significant which makes the epitaxial growth of Cu (001) on Si (001), with their <100> directions parallel in the plane of the interface, conceptually challenging. In fact, a_0 (Cu) = 3.615 Å and a_0 (Si) = 5.43 Å at room temperature which gives a lattice mismatch $\eta \approx 50\%$. However, a much improved in-plane epitaxial relation between the Cu and Si crystals can be achieved upon rotation of the Cu layer by 45° about its normal. The [100] axis of the Cu crystal is then parallel to the [110] axis of the Si crystal, thus decreasing the mismatch between the two lattices to $\eta' \approx 6\%$ and making the epitaxial growth of Cu (001) on Si (001) more favorable. We have confirmed this argument experimentally by *in-situ* RHEED measurements and by *ex-situ* X-ray pole figures [Inglefield *et al.*, 1993]. Our observations are supported by *ex-situ* grazing angle X-ray diffraction measurements [Chang *et al.*, 1990] and by *in-situ* RHEED patterns [Naik *et al.*, 1993]. A RHEED pattern obtained from a 2000 Å Cu layer deposited on Si (001) is shown in Fig. 5.5. The sharp streaks that appear for a bare Si (001) RHEED pattern are replaced by broad and rather diffuse spots, indicating that the Cu layer is epitaxial but rough which is probably a consequence of a three-dimensional film growth. The pattern shown in Fig. 5.5 also confirms the full fourfold azimuthal symmetry of the fcc Cu (001) lattice.

The roughness of the Cu layer has also been confirmed by cross-sectional TEM [Inglefield, unpublished] which has also revealed the presence of a 70 Å thick polycrystalline copper-silicide layer at the Cu-Si interface. The copper-silicide forms slowly at room temperature after the epitaxial relationship between the Cu and Si layers has been established since the portion of the Cu layer lying above the silicide remains a single-crystal with a (001) orientation and with the Cu [100] axis parallel to the [110] axis

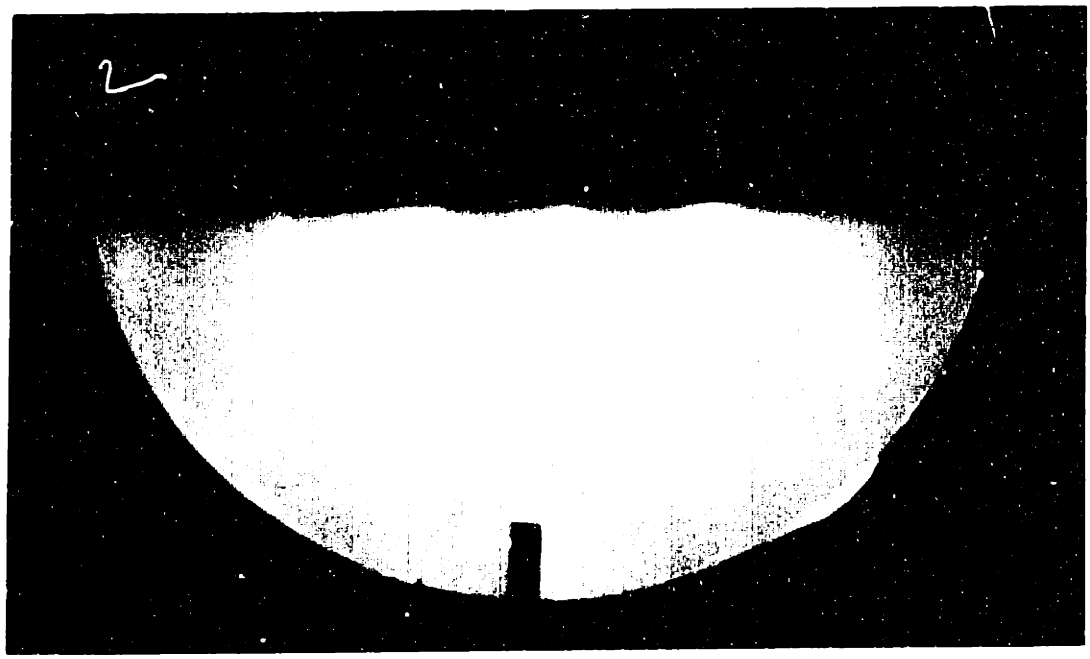

Figure 5.5: RHEED pattern of 1000 A Cu/Si (001) taken along a <100> direction.

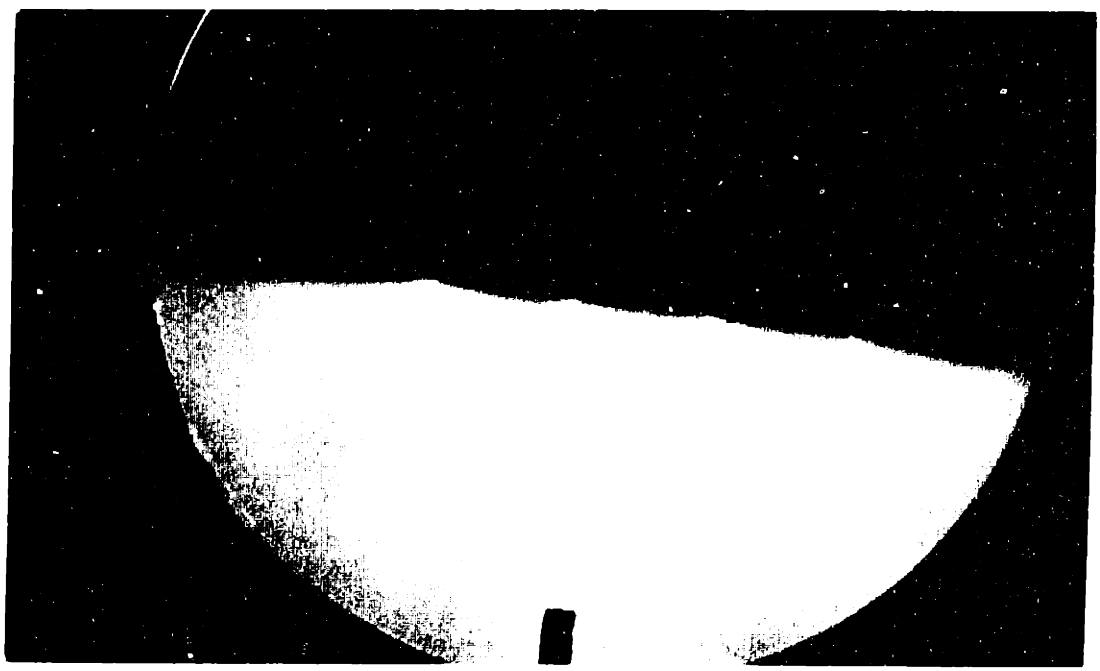

Figure 5.6: RHEED pattern of 200 A Ni/2000 A Cu/Si (001) taken along a <100> direction

of the Si. X-ray diffraction measurements [Inglefield, unpublished] also indicate that the silicide layer consists of the tetragonal phase η' - Cu_3Si. The silicide grains are fine with an average size of approximately 100 Å and have a predominant (211) orientation. These observations are consistent with the ones of Chang [J. Appl. Phys. **67**, 566 (1990)]. In order to make the as-grown silicide layer thin compared to the epitaxial Cu (001) layer and prevent it from reaching the Ni film, we have decided to grow the Cu with a total thickness ranging between 2000 and 3000 Å. *Ex-situ* wafer curvature measurements indicate that at these thicknesses the Cu layer is relaxed to less than 0.01% in-plane strain.

Ni thin films evaporated at room temperature on the Cu/Si (001) substrates are single-crystals and grow with a (001) orientation, as shown with X-ray diffraction by Chang [J. Appl. Phys. **67**, 566 (1990); J. Vac. Sci. Technol. A **8**, 3779 (1990)], Inglefield *et al.* [1993], and Naik *et al.* [1993]. Good epitaxial growth without interdiffusion of Ni thin films on Cu (001) single-crystals has also been shown by Mankey *et al.* [1991] and Huang *et al.* [1993]. A RHEED pattern obtained after the deposition of a Ni thin film on 2000 Å Cu/Si (001) is shown in Fig. 5.6. It was taken with the electron beam in the same crystallographic direction as the pattern for Cu/Si (001) shown in Fig. 5.5. The spots indicate that the Ni film is epitaxial and with a roughness comparable to that of the Cu sublayer. The roughness of the film's free surface has been investigated with more detail by cross-sectional TEM [Inglefield, unpublished]. The cross-sectional micrographs indicate a Ni surface roughness of the order of ± 20 Å extending over 400 Å in the film plane. The full fourfold symmetry of the RHEED spots in Fig. 5.6 is characteristic of the fcc (001) structure. Comparison of Figs. 5.5 and 5.6 indicates that the in-plane epitaxial relationship between the Ni film and the Cu substrate is as desired: the [100] axes of the two crystals are parallel.

Two important questions arise when one attempts to grow metallic thin films on metallic substrates. First, is there any interdiffusion occurring at the metal-metal interface? And second, is there any surface segregation of the substrate atoms? Mohamed *et al.* [1989] and Chen *et al.* [1991] showed that the Ni/Cu interface is thermally stable against interdiffusion to cycling temperatures up to 490 K. Moreover, Ni and Cu form a solid solution, so that the formation of an intermetallic phase is not expected at the Ni-Cu interface. This expectation has been confirmed by cross-sectional TEM [Inglefield, unpublished]. The answer to the second question is more involved and is particularly relevant for thin magnetic films a few Angstroms thick. The growth mode of a thin film

is very sensitive to the deposition rate of the film but most importantly to the substrate temperature. At room temperature and in the early stages of epitaxy, Ni tends to agglomerate (island growth) instead of wetting the Cu surface (layer-by-layer growth). This may explain why the Ni films have a three-dimensional structure, as indicated by the roughness measurements of RHEED and cross-sectional TEM. In addition, Cu atoms tend to segregate or float to the Ni surface where they reduce the surface energy [Egelhoff and Steigerwald, 1989]. These phenomena are also characteristic of the growth of Fe on Cu (001) [Steigerwald *et al.*, 1988] and have been shown to have tremendous consequences on the magnetic anisotropy of the Fe thin film [Swartzendruber *et al.*, 1993]. In fact, a six monolayer thick Fe film deposited on a Cu (001) substrate at 80 K was shown to be continuous and to have its magnetization easy-axis in its plane. But upon deposition of only one monolayer of Cu, the magnetization easy-axis was shown to prefer an orientation perpendicular to the film! The driving force behind the Ni or Fe agglomeration and the Cu surface segregation is the lowering of the total surface free energy of the epitaxial system. It has long been known that one monolayer of a high-surface-energy metal will not wet the surface of a low-surface-energy metal when the interfacial bonding is relatively weak (as it is between noble and transition metals). This phenomenon, which is illustrated schematically in Fig. 5.7, is expected to happen in Ni/Cu (001) since the surface free energy of Cu (001) (2300 erg/cm^2) is significantly lower than that of Ni (3050 erg/cm^2) [Smith and Banerjea, 1987]. However, when the thickness of the film exceeds a few layers, the islands coalesce, the segregated Cu monolayer gets buried and a simpler homoepitaxial growth regime (i. e. Ni on Ni, or Fe on Fe) is entered. In Fe/Cu (001), this happens when the Fe film is approximately 4 monolayers (7 Å) thick, as confirmed by Scanning Tunneling Microscopy [Chambliss *et al.*, 1992]. The results of our experiments on Ni/Cu (001) are in agreement with these observations. Our Auger electron spectroscopy (AES) studies show that for Ni film thickness greater than 15 Å there is no sign of Cu surface segregation. One way to avoid the segregation problem for ultrathin films is to grow the films at temperatures below 100 K [Swartzendruber *et al.*, 1993]. The same interfacial energy considerations make the growth of Cu thin films on Ni substrates in a nearly ideal layer-by-layer fashion possible at room temperature. This has been demonstrated by AES, RHEED and angle resolved ultraviolet photoelectron spectroscopy [Chambers and Jackson, 1975; Rogge and Neddermeyer, 1989]. The Cu layer is strained compressively to be coherent or semi-coherent with the Ni substrate.

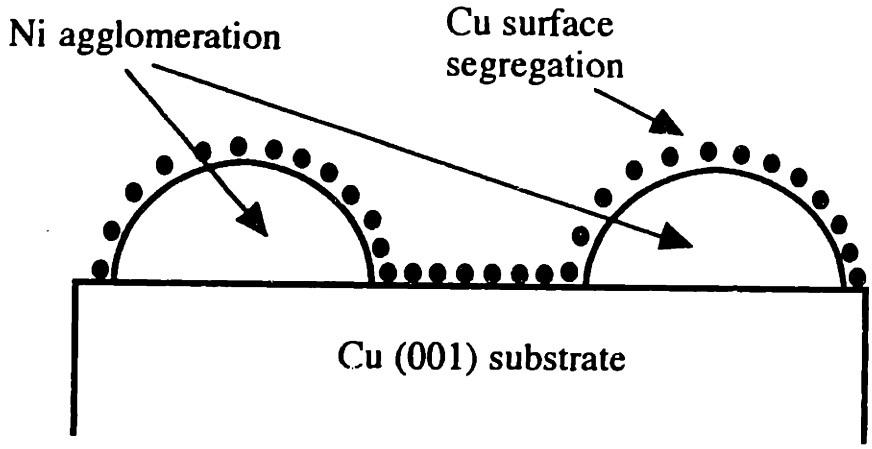

Figure 5.7: Schematic side view of a couple of monolayers thick Ni film grown on a Cu substrate at room temperature.

Chapter 6
Experimental Results

In order to answer the questions asked at the end of chapter 3, we have designed and performed four experiments on different Ni/Cu (001) heterostructures where the Ni film thickness, the film capping layer, and the substrate composition were independently varied. The films were deposited on Si (001) substrates using the MBE system and the experimental techniques described in chapter 5. The magnetic anisotropy was characterized with MOKE or VSM for the films kept under ultra-high vacuum and for those exposed to air, respectively. The experimental results form the subject of this chapter. We will discuss these results in the framework of the phenomenological model of chapter 2 and will demonstrate that such a model is inadequate to fully explain our quantitative data. We will review the Néel pair interaction model in chapter 7 and show that new terms in the phenomenological model, not considered in chapter 2, are predicted by this model if one includes strain in the computation of the magnetic surface anisotropy [Chuang *et al.*, 1994]. We will rediscuss our data in chapter 8 in the light of the findings of chapter 7.

6.1. Ni/Cu/Si (001) Thin Films

The first structure that we have examined is Ni/Cu/Si (001) thin films where the Cu layer was 3000 Å thick and where the Ni thin film thickness was varied between 10 Å and 200 Å [Bochi *et al.*, 1993]. This structure is shown schematically in Fig. 6.1. The films were characterized both *in-situ* with MOKE and *ex-situ* using VSM. The MOKE loops obtained with the magnetic field applied in the film plane and perpendicular to it are shown in Figs. 6.2 to 6.9. The M-H loops corresponding to the 150 Å, 100 Å, and 75

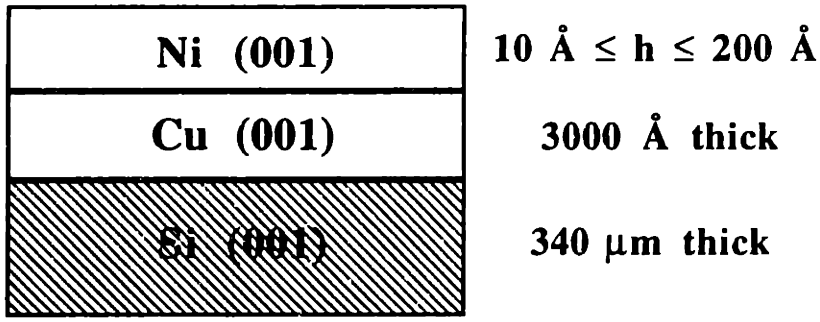

Figure 6.1.: Schematic cross-section of the Ni/Cu/Si (001) films.

Å thick films are very similar and indicate that the magnetization easy-axis lies in the film plane. In fact, the remanence of the loops taken with the magnetic field applied in-plane is relatively large whereas the loops taken with the field normal to the films exhibit a linear behavior and an insignificant remanence which are characteristic of hard-axis M-H loops. These results are not surprising since, as we explained in detail in chapter 2, the magnetostatic energy, which tries to keep the magnetization in the plane of a thin film, always dominates at sufficiently large film thicknesses. The magnetic anisotropy changes dramatically when the Ni film thickness is decreased below 60 Å, as indicated by Figs. 6.5 to 6.8. The polar M-H loops corresponding to the 50 Å, 35 Å, and 25 Å thick films are square and have a 100% remanence, indicating that the magnetization easy-axis is normal to the films. The corresponding longitudinal M-H loops are linear and have essentially zero remanence.

We have observed another significant change in the magnetic anisotropy at a Ni thickness between 10 Å and 15 Å. As indicated by Fig. 6.8, both the polar and the longitudinal M-H loops have a 100% remanence when the Ni film thickness is h = 15 Å. Such a situation can be explained if the 15 Å Ni film is either discontinuous or continuous but rough, with islands or regions magnetized in the film plane and others magnetized perpendicular to the film. The roughness of the Ni/Cu (001) films has been confirmed by RHEED and cross-sectional TEM, as explained in chapter 5. This mixed behavior of the magnetic anisotropy at h = 15 Å has been confirmed by Huang *et al.* [1994] who have deposited their films at room temperature on Cu (001) single-crystal substrates and characterized them at T = 160 K by MOKE. Huang *et al.* further demonstrated that the magnetization easy-axis falls in-plane at h = 13 Å. This transition of the magnetization easy-axis from perpendicular to in-plane, observed when the Ni thickness is decreased sufficiently, qualitatively supports the earlier results of Ballentine

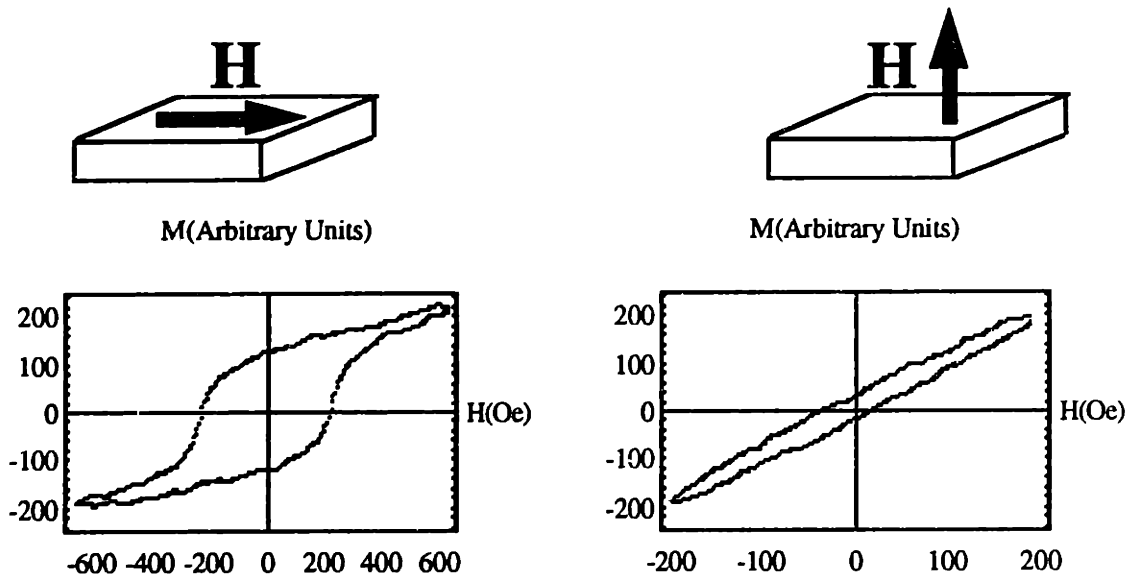

Figure 6.2: Longitudinal and polar MOKE loops of a 150 Å Ni/Cu/Si (001) film.

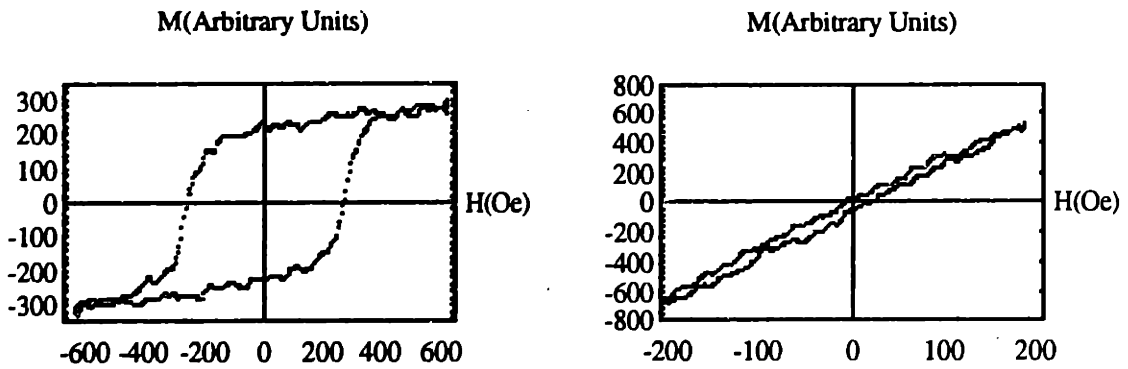

Figure 6.3: Longitudinal and polar MOKE loops of a 100 Å Ni/Cu/Si (001) film.

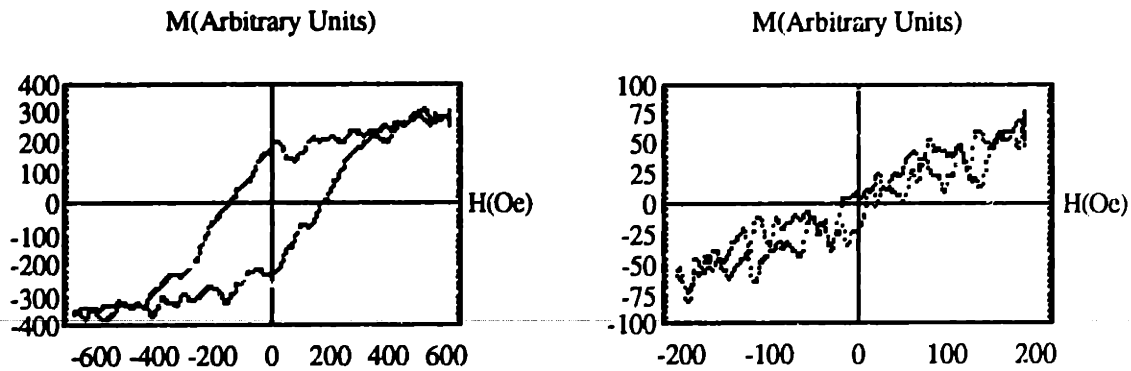

Figure 6.4: Longitudinal and polar MOKE loops of a 75 Å Ni/Cu/Si (001) film.

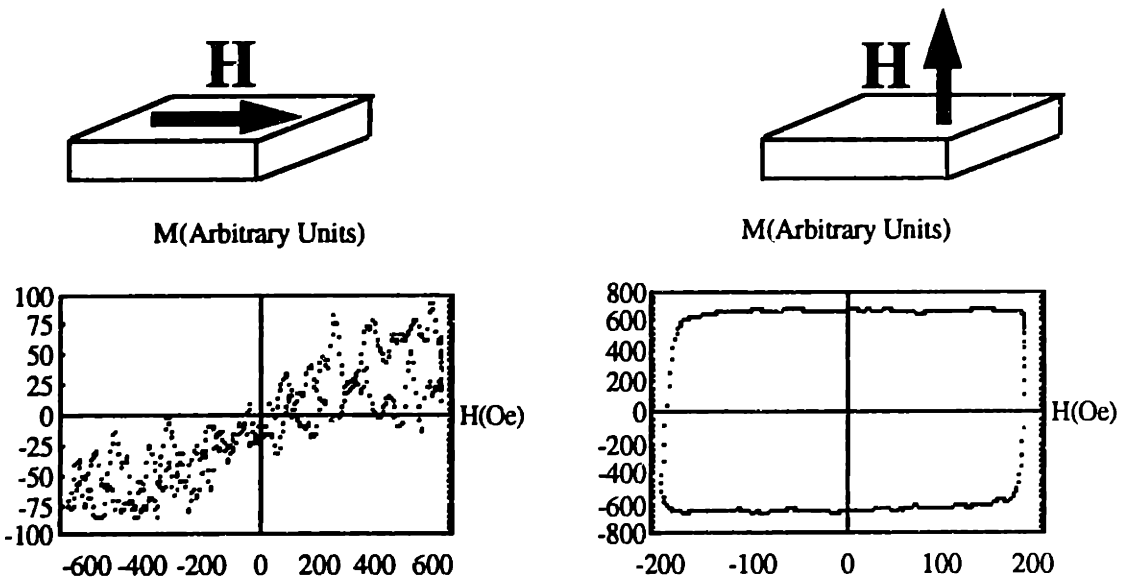

Figure 6.5: Longitudinal and polar MOKE loops of a 50 Å Ni/Cu/Si (001) film.

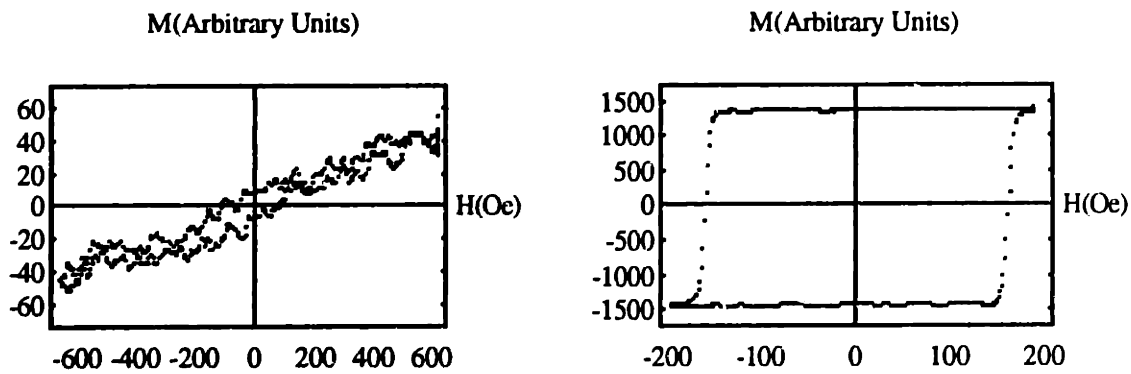

Figure 6.6: Longitudinal and polar MOKE loops of a 35 Å Ni/Cu/Si (001) film.

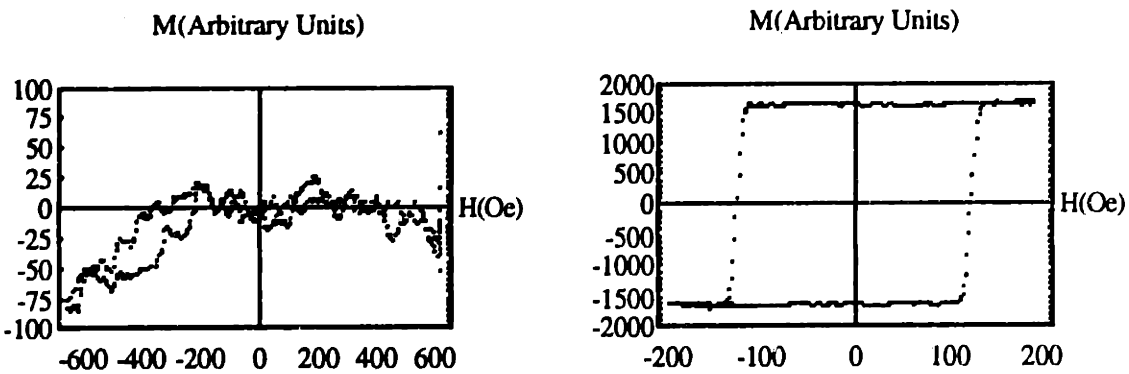

Figure 6.7: Longitudinal and polar MOKE loops of a 25 Å Ni/Cu/Si (001) film.

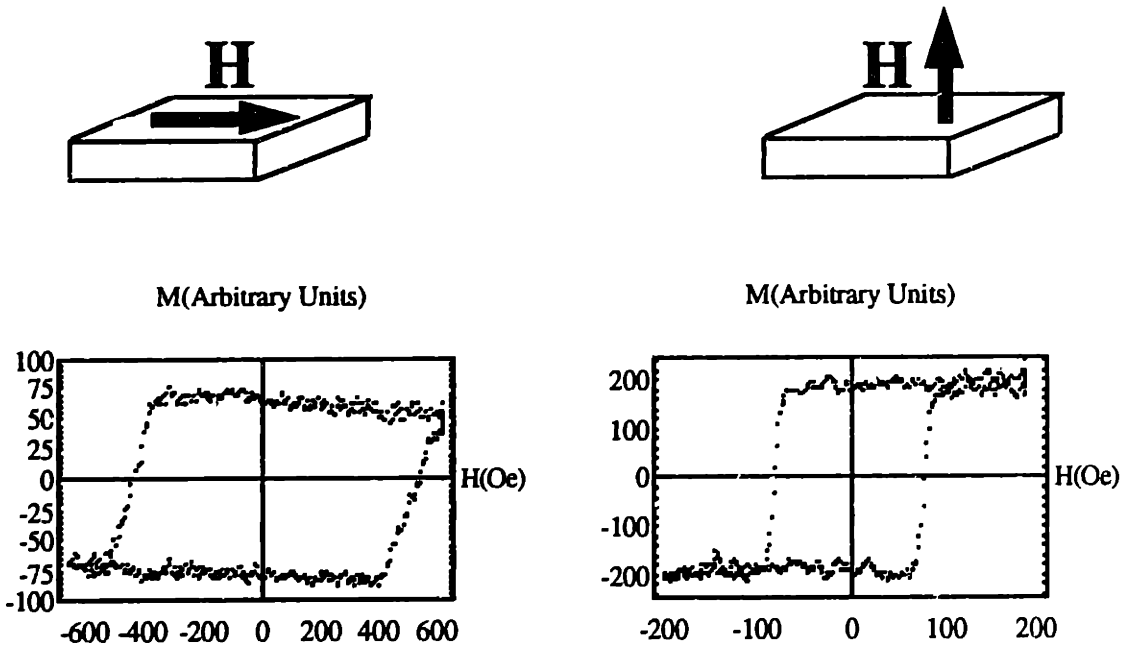

Figure 6.8: Longitudinal and polar MOKE loops of a 15 Å Ni/Cu/Si (001) film.

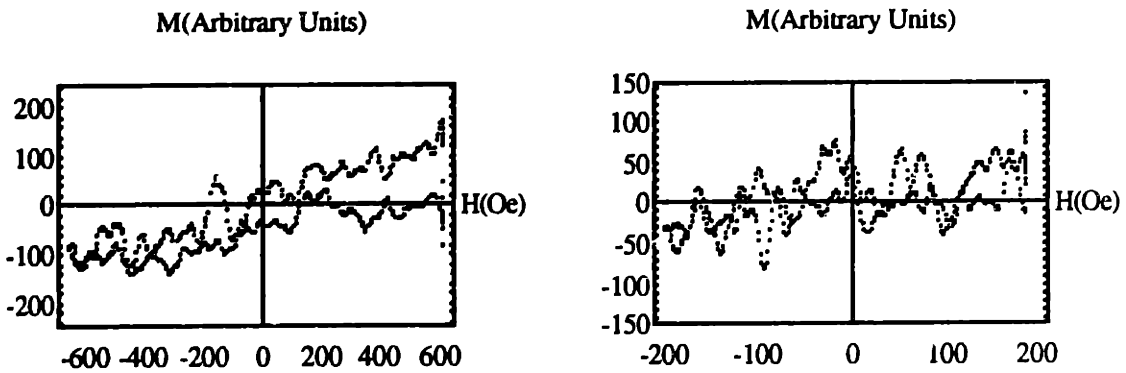

Figure 6.9: Longitudinal and polar MOKE loops of a 10 Å Ni/Cu/Si (001) film.

[1989]. By depositing his Ni/Cu (001) films at room temperature and characterizing them at T = 100 K with MOKE, Ballentine showed that the magnetization lies fully in-plane for h = 5.5 Å and exnibits a strong out-of-plane component for h = 8.3 Å. We tried to study this in-plane to out-of-plane magnetization easy-axis transition with our MOKE set-up by depositing Ni films thinner than 15 Å. However, magnetic measurements at these film thicknesses and at room temperature are very difficult since the saturation magnetization is very small, making the Kerr rotation very weak. This is illustrated by our MOKE M-H loops corresponding to h = 10 Å shown here in Fig. 6.9. Tjeng *et al.* [1991] and Huang *et al.* [1994] showed that the Curie temperature of 9 Å thick Ni films deposited on Cu (001) substrates is $T_c \approx 300$ K.

Following the MOKE measurements, the Ni/Cu/Si (001) films were brought up to air and characterized by VSM. The variation with Ni film thickness of the perpendicular remanence normalized to the saturation magnetization is shown in Fig. 6.10 both for films characterized *in-situ* and *ex-situ*. The solid data points indicate that the films kept under vacuum have a magnetization easy-axis perpendicular to the films up to a film thickness of 60 Å, as explained above. For films deposited by MBE and then exposed to air, the region of perpendicular magnetization extends up to approximately 125 Å, as indicated by the open data points. This significant difference between films characterized under vacuum and films characterized by VSM is due to the exposure of the films to air. In fact, when a 75 Å or a 100 Å thick Ni film is exposed to air and then returned to the MBE chamber, the MCKE loops indicate that the magnetization easy-axis remains perpendicular to the films. It can be speculated that the shift of the out-of-plane to in-plane magnetization easy-axis transition thickness of Fig. 6.10 is due to any combination of the following three possibilities: a loss of the Ni moment due to a significant oxidation of the Ni film, leading to a decrease of the magnetostatic energy of the film; a tensile stress imposed on the Ni film by the growing oxide leading to an increase of the positive bulk magnetoelastic anisotropy energy $2B_1e_0$ of the Ni film; and/or a significant increase in the magnetic surface anisotropy energy density K^s of the film due to the coverage of the Ni free surface by the oxide. Cross-sectional TEM studies have shown that the oxide layer growing on the Ni free surface is thinner than 10 Å [Kim, 1991; Inglefield, unpublished]. This would certainly not reduce the Ni moment enough to make a 100 Å oxidized film behave like an unoxidized 50 Å thick film kept under vacuum. We can evaluate the likelihood of the other two possibilities semi-quantitatively using the phenomenological model of Eq. (2.9) and the fact that the effective magnetic anisotropy energy density K^{eff} goes through zero when the magnetization easy-axis switches from

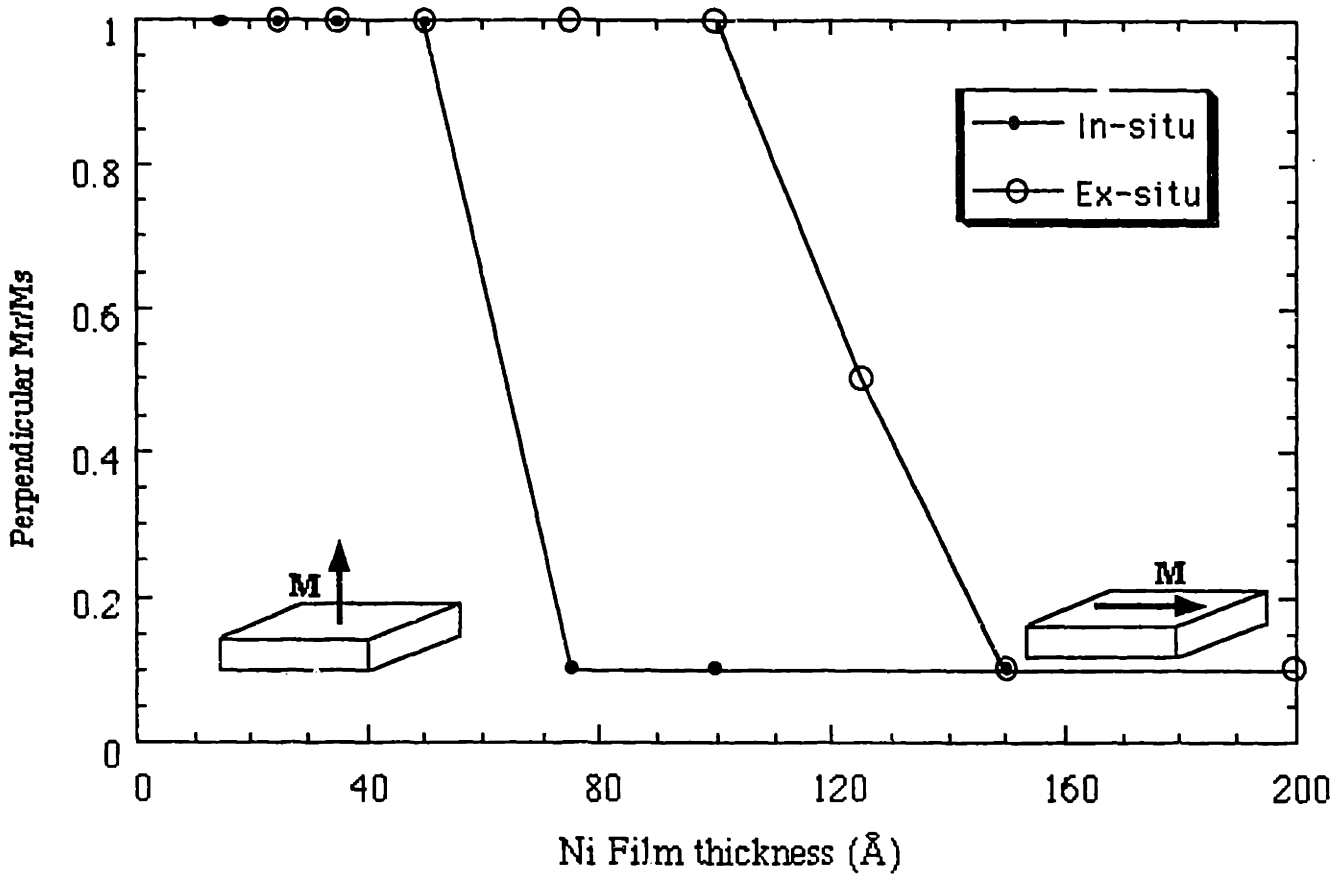

Figure 6.10: Perpendicular remanence normalized to the saturation magnetization as a function of Ni film thickness for Ni/Cu/Si (001) films characterized *in-situ* by MOKE and then *ex-situ* by VSM.

perpendicular to in-plane. Setting $K^{eff} = 0$ and substituting the 1/h strain of Eq. (4.22) in Eq. (2.9) yields:

$$K^s = h \cdot \left[2\pi M_s^2 - 2 B_1 \eta \frac{h_c}{h}\right], \qquad (6.1)$$

where K^s here represents the sum of the magnetic surface anisotropy energies corresponding to the two interfaces of the film. For films kept under vacuum, the switching thickness of the magnetization easy-axis is 60 Å. Substituting this thickness into Eq. (6.1) gives $K^s = 0.32$ erg/cm^2 for the combination of the vacuum/Ni (001) and the Ni/Cu (001) interfaces. Assuming that K^s remains unchanged when the films are brought up to air, we can estimate how much tensile strain the NiO layer would have to impose on the Ni film in order to extend the region of perpendicular magnetization from 60 Å to 125 Å through the positive bulk magnetoelastic anisotropy energy $2B_1 e_0$. From Eq. (2.9), we obtain the following relationship between the misfit strain in the Ni film and the other parameters of the model:

$$e_0(h) = \frac{1}{2 B_1}\left[2\pi M_s^2 - \frac{K^s}{h}\right]. \qquad (6.2)$$

Substituting h = 125 Å, $K^s = 0.32$ erg/cm^2 and the bulk values of B_1 and $2\pi M_s^2$ of Ni in Eq. (6.2), we obtain $e_0(125\text{ Å}) = 1\%$. According to Eq. (4.22), the residual misfit strain in an uncapped 125 Å thick Ni film deposited on a Cu (001) substrate is approximately 0.4%. Therefore the additional tensile strain that the NiO layer would have to impose on the Ni film to extend the region of perpendicular magnetization to 125 Å through bulk magnetoelastic coupling is approximately 1% - 0.4% = 0.6%. We cannot exclude such a possibility given the huge lattice mismatch between NiO and Ni. In fact, the lattice parameters of Ni and NiO at room temperature are 3.52 Å and 4.177 Å [CRC handbook], respectively, making the lattice mismatch between the two crystals approximately 19%. Moreover, using wafer curvature measurements, Inglefield [unpublished] showed that the NiO layer does impose a significant in-plane tensile strain on the Ni/Cu/Si films.

Using Eq. (6.1), we can also estimate how much the magnetic surface anisotropy energy density K^s of the Ni film would have to be increased in order to extend the region of perpendicular magnetization from 60 to 125 Å. By assuming that the strain in the Ni film remains unchanged through the formation of the oxide layer and setting h = 125 Å in Eq. (6.1), we find that K^s would have to increase from 0.32 erg/cm^2 to 1.30 erg/cm^2 due to the substitution of the vacuum/Ni (001) interface by the Ni/NiO (001) interface. We

cannot exclude such a result since magnetic surface anisotropy energies of a single interface are typically of the order of 0.5 erg/cm^2. We therefore conclude that the shift of the out-of-plane to in-plane magnetization easy-axis transition thickness of Fig. 6.10 is most likely due to both an increase in the magnetic surface anisotropy energy of the free surface of the Ni film and a tensile misfit strain imposed on the Ni film by the NiO layer.

In summary, we have demonstrated that perpendicular magnetization in Ni/Cu (001) thin films first observed by Ballentine [1989] is indeed reproducible. The Ni film thickness range over which perpendicular magnetic anisotropy dominates is very striking, as shown in Fig. 6.10. We were the first to report that the Ni/Cu (001) system exhibits the largest range of perpendicular magnetization of any epitaxial system studied so far [Bochi *et al.*, 1993]. This range is particularly large compared to the one observed in Fe/Cu (001), where the perpendicular to in-plane magnetization easy-axis transition thickness does not exceed 11 Å, as shown in chapter 3. This remarkable difference between Fe and Ni films deposited on the same substrate, at the same temperature and with the same crystallographic orientation is partly due to the fact that the magnetostatic energy density of Fe is approximately ten times larger than the one of Ni. But a complete understanding of this unique behavior of the magnetic anisotropy in Ni/Cu (001) can be achieved only if the dependence of the magnetoelastic and the magnetic surface anisotropy energies on film thickness is well understood.

6.2. Ni/$Cu_{60}Ni_{40}$/Cu/Si (001) Thin Films

As mentioned in chapter 3, Ballentine [1989] suggested that the in-plane to out-of-plane magnetization easy-axis transition occurring in Ni/Cu (001) as the Ni film thickness is increased through h ≈ 10 Å may be due to the onset of misfit dislocations. In order to test this idea, we have studied the magnetic anisotropy in Ni/$Cu_{60}Ni_{40}$/Cu/Si (001) thin films as a function of Ni thickness. The mismatch between the equilibrium lattice parameters of Ni and the $Cu_{60}Ni_{40}$ alloy is approximately 1.6% while the corresponding thermodynamic critical thickness for the onset of misfit dislocations is approximately 35 Å, as discussed in section 4.2. By measuring the magnetic anisotropy of Ni thin films deposited on $Cu_{60}Ni_{40}$ substrates for film thicknesses below and above 35 Å, one can then test the suggestion of Ballentine.

The choice of the alloy composition was made with two ideas in mind: the Ni content in the substrate must be large to make the critical thickness h_c large (Fig. 4.11); at

the same time, the Ni content in the substrate must be small enough so that the substrate can remain non-magnetic. The bulk Cu-Ni equilibrium phase diagram is shown in Fig. 6.11. The figure shows that, near room temperature, Ni and Cu form a solid solution which is non-magnetic provided that the Ni content in the alloy is less than 65 at. %. We chose the composition 60% Cu - 40% Ni.

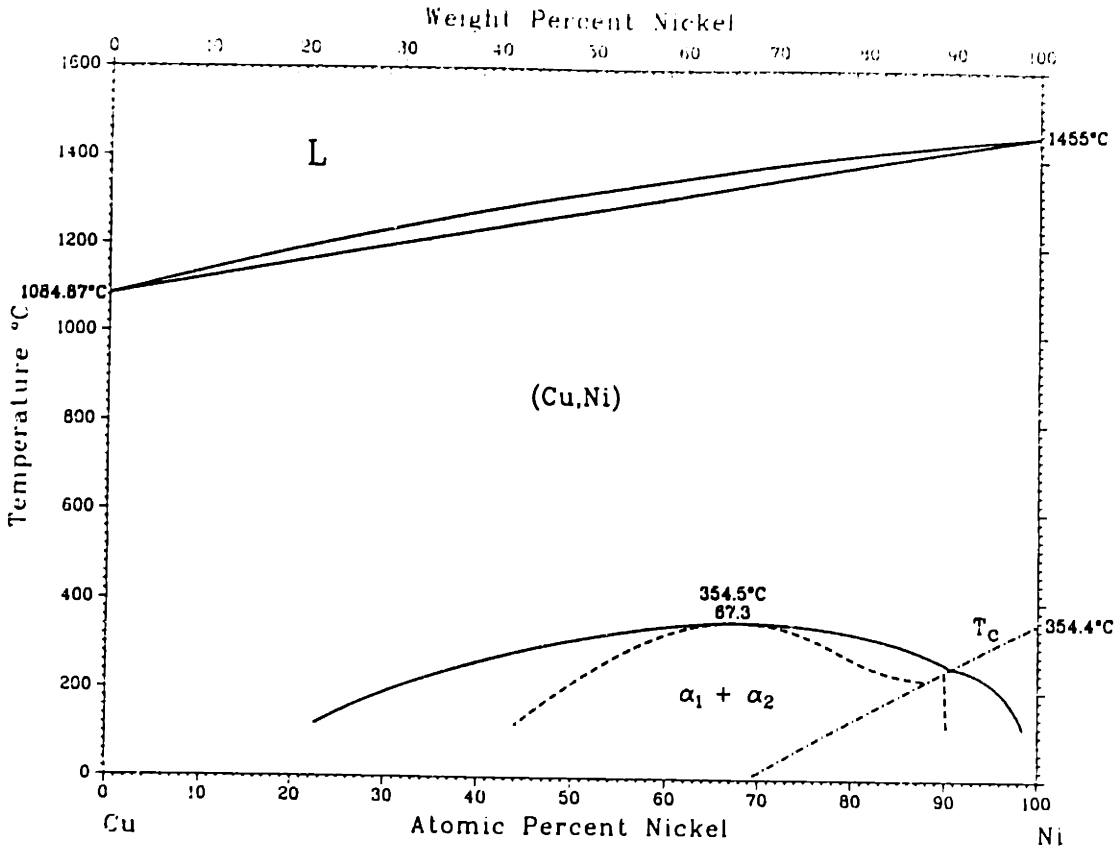

Fig. 6.11: Equilibrium phase diagram of the Cu-Ni binary system [Massalski, 1990].

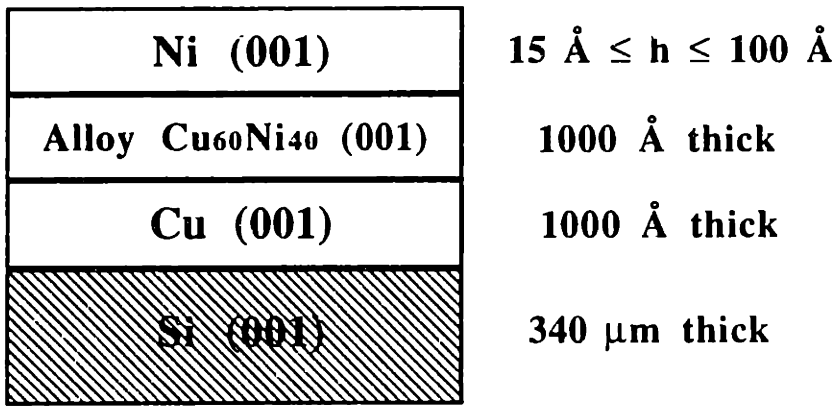

Figure 6.12.: Schematic cross-section of the Ni/$Cu_{60}Ni_{40}$/Cu/Si (001) films.

The structure of the films is shown in Fig. 6.12. A 1000 Å Cu buffer layer is first grown on the Si (001) wafer in order to make the epitaxial growth of the $Cu_{60}Ni_{40}$ layer with a (001) orientation possible. The Ni film thickness was varied between 15 Å and 100 Å. Before characterizing the Ni/$Cu_{60}Ni_{40}$/Cu/Si films, we characterized a $Cu_{60}Ni_{40}$/Cu/Si film using MOKE. No hysteresis loops were detected indicating that the alloy substrates were non-magnetic, as expected.

The M-H loops of the Ni/$Cu_{60}Ni_{40}$/Cu/Si (001) thin films, obtained using MOKE while the films were kept under vacuum, are shown in Figs. 6.13 to 6.18. The M-H loops indicate that the 100 Å, 75 Å, and 50 Å Ni films have an in-plane magnetization easy-axis. The magnetic anisotropy changes significantly around 40 Å. In fact, as can be seen in Figs. 6.16 and 6.17, the magnetization easy-axis is normal to the film plane for the 35 Å and 25 Å films since the remanence of the polar loops is 100%. Figure 6.18 shows the MOKE loops for the 15 Å film, the thinnest that we characterized. A weak hysteretic behavior is observed both for the magnetic field applied in-plane and perpendicular to the film, indicating that the 15 Å film is ferromagnetic at room temperature. The relatively small remanence in the polar loop indicates that the magnetization easy-axis may be falling back in-plane at this thickness. However, the weakness of the Kerr signal makes it difficult to draw a stronger conclusion. Nonetheless, Figs. 6.13 to 6.18 allow us to make two major conclusions. First, we have shown that the region of perpendicular magnetization extends from approximately 20 Å to 40 Å, which is narrower than the perpendicular region in Ni/Cu (001) films which extends from 15 Å to 60 Å. Second, the onset of misfit dislocations, which occurs above the thermodynamic critical thickness h_c = 35 Å, does not appear to be responsible for the in-plane to out-of-plane magnetization

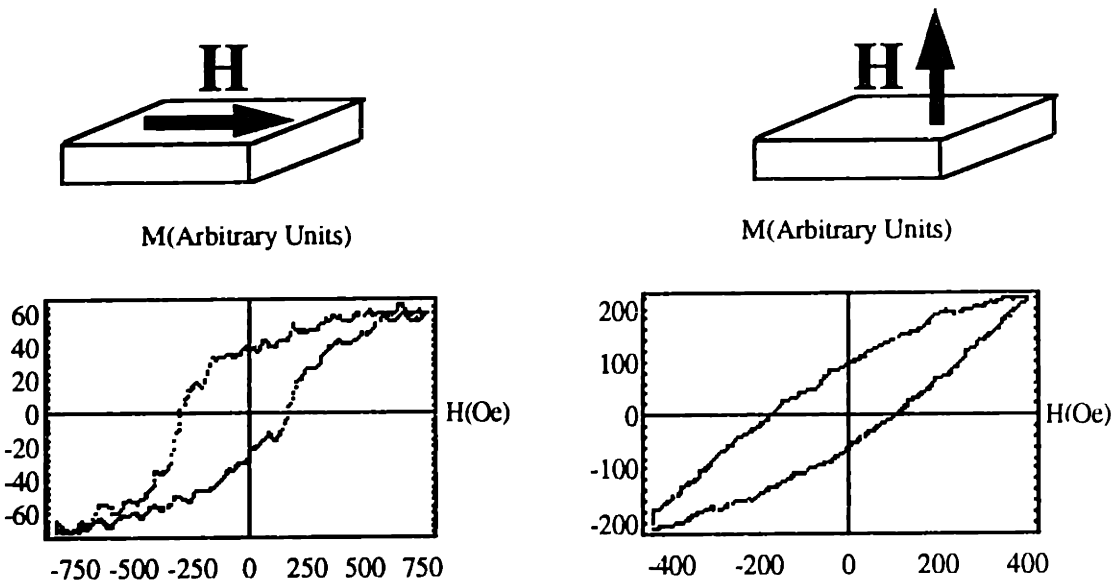

Figure 6.13: Longitudinal and polar MOKE loops of a 100 Å $Ni/Cu_{60}Ni_{40}$ (001) film.

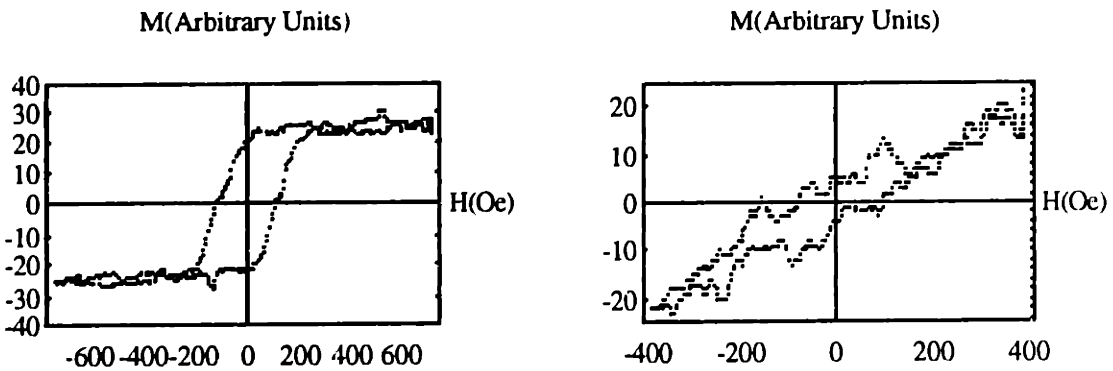

Figure 6.14: Longitudinal and polar MOKE loops of a 75 Å $Ni/Cu_{60}Ni_{40}$ (001) film.

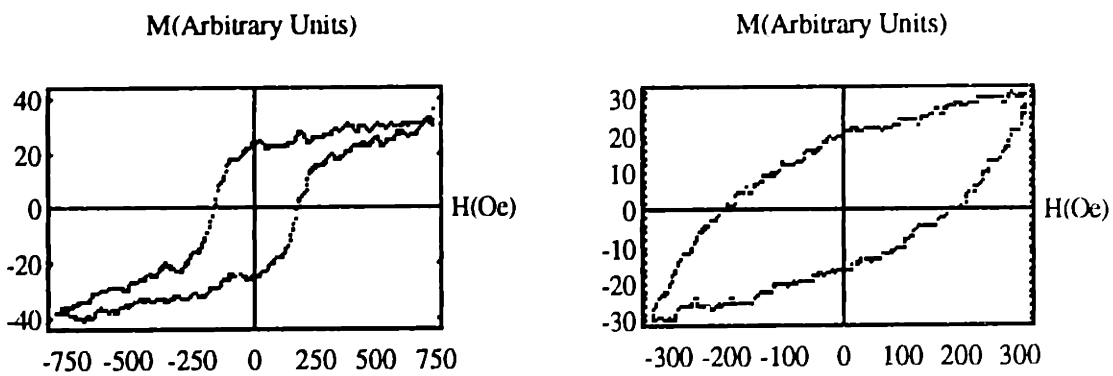

Figure 6.15: Longitudinal and polar MOKE loops of a 50 Å $Ni/Cu_{60}Ni_{40}$ (001) film.

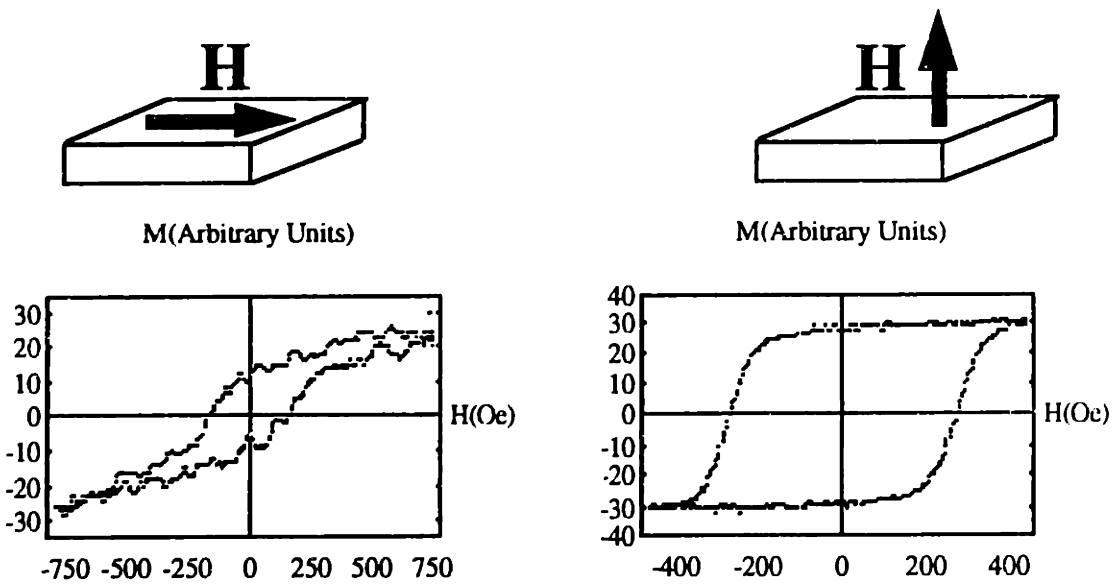

Figure 6.16: Longitudinal and polar MOKE loops of a 35 Å $Ni/Cu_{60}Ni_{40}$ (001) film.

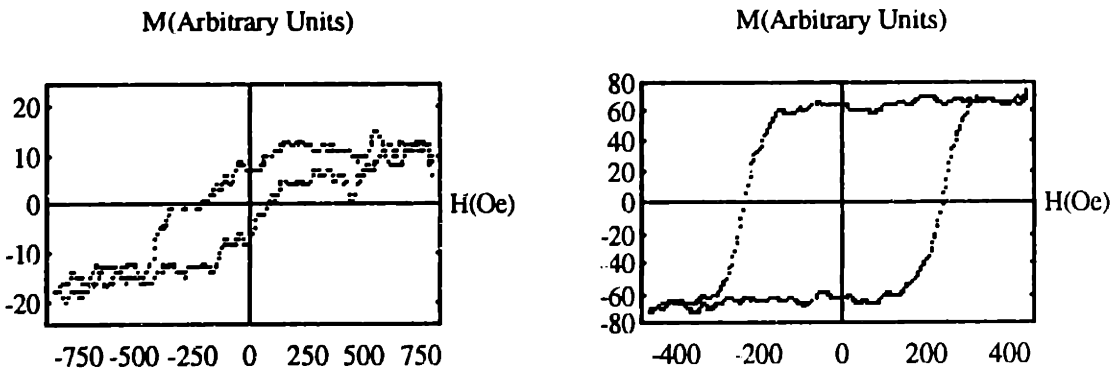

Figure 6.17: Longitudinal and polar MOKE loops of a 25 Å $Ni/Cu_{60}Ni_{40}$ (001) film.

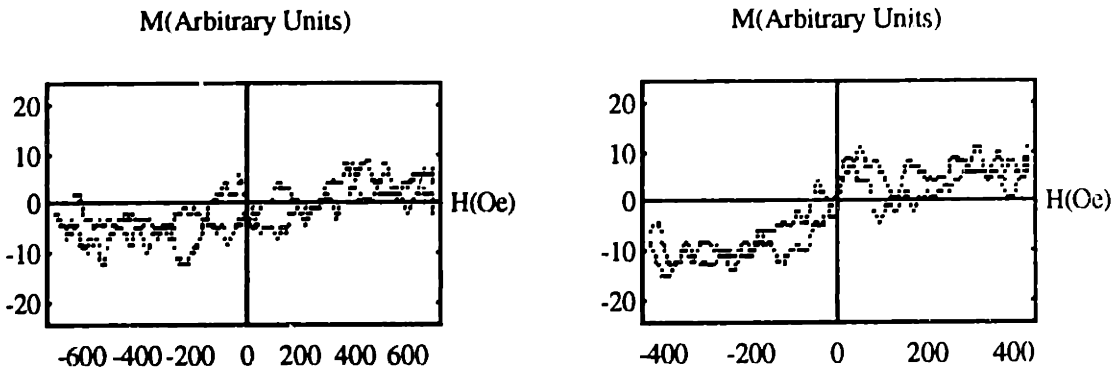

Figure 6.18: Longitudinal and polar MOKE loops of a 15 Å $Ni/Cu_{60}Ni_{40}$ (001) film.

easy-axis transition which occurs near 20 Å.

Two factors can explain why the region of perpendicular magnetization is narrower for the Ni/$Cu_{60}Ni_{40}$ (001) thin films than for the Ni/Cu (001) films. First, the in-plane biaxial tensile misfit strain in the Ni films is smaller in Ni/$Cu_{60}Ni_{40}$ (001) than in Ni/Cu (001). This is due to the fact that Ni has a much smaller misfit with the $Cu_{60}Ni_{40}$ alloy than with a Cu substrate, as illustrated in Figs. 4.10 and 4.11. As a result, the bulk magnetoelastic anisotropy energy, which gives rise to an important contribution to the perpendicular magnetic anisotropy in Ni, is smaller in Ni/$Cu_{60}Ni_{40}$ (001) than in Ni/Cu (001), at least up until approximately 40 Å Ni. Second, as we will show in chapter 8, the magnetic surface anisotropy energy of the Ni-Cu (001) interface is significant, positive and therefore contributes to perpendicular magnetic anisotropy. The Ni-$Cu_{60}Ni_{40}$ interface is chemically and structurally more similar to a Ni-Ni interface (created depositing a Ni thin film on a Ni single-crystal substrate) than the Ni-Cu interface is. To a first approximation, one therefore expects the Ni-$Cu_{60}Ni_{40}$ (001) interface to have a magnetic surface anisotropy energy density which is positive but weaker than the one of the Ni-Cu (001) interface. In other words, its contribution to the perpendicular magnetic anisotropy is weaker than the one of the Ni-Cu (001) interface, leading to a less extended perpendicular magnetization region.

6.3. Cu/Ni/Cu/Si (001) Sandwiches

In order to get a quantitative understanding of the remarkable behavior of the magnetic anisotropy in Ni/Cu (001), we decided to measure the dependence on Ni film thickness of the effective magnetic anisotropy energy density in Cu/Ni/Cu (001) sandwiches. The sandwiches were deposited by MBE and characterized *ex-situ* by VSM where magnetic fields as large as 10,000 Oe were available to saturate the sandwiches both in their plane and perpendicular to it. The structure of these sandwiches is shown schematically in Fig. 6.19. A 2000 Å thick Cu substrate was evaporated on the Si (001) wafer followed by a Ni thin film whose thickness ranged between 35 Å and 150 Å. A 20 Å Cu layer caps the Ni film in order to protect it from oxidation and to make both Ni interfaces chemically identical so that they both give the same contribution to the magnetic anisotropy. The advantage of the VSM is that it provides a quantitative measurement of the effective magnetic anisotropy energy density of Ni films as thin as 30 Å.

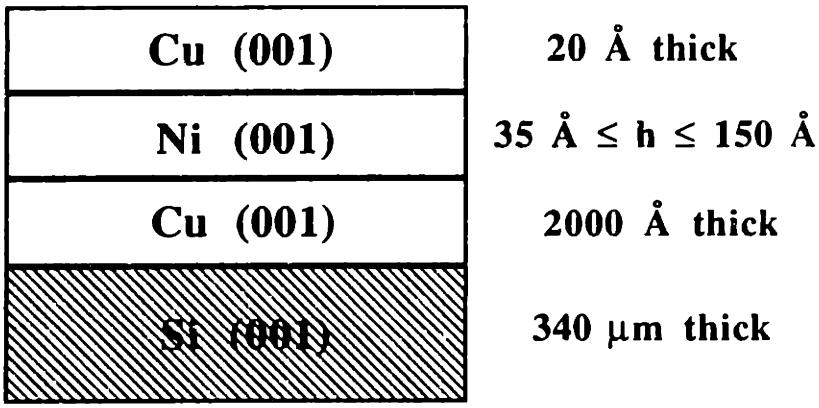

Figure 6.19: Schematic cross-section of the Cu/Ni/Cu/Si (001) sandwiches.

The longitudinal and perpendicular M-H loops corresponding to five different sandwiches are shown in Figs. 6.20 to 6.24. The maximum applied magnetic field in the VSM is 10,000 Oe. In these figures, we show the data for a field range of ± 1,000 Oe both in-plane and perpendicular to the sandwiches. The measured effective magnetic anisotropy energy density times the Ni film thickness is plotted as a function of film thickness in Fig. 6.25. The first important result is that the perpendicular magnetic anisotropy dominates up to Ni thicknesses of approximately 125 Å! This is in agreement with the VSM measurements of Chang [J. Appl. Phys. **68**, 4873 (1990)] on 1000 Å Cu/Ni/1000 Å Cu/Si (001) grown by electron-beam evaporation in a high vacuum system (base pressure ≈ 10^{-7} Torr), and the ferromagnetic resonance measurements of Naik *et al.* [1993] on 500 Å Cu/Ni/500 Å/Si (001) grown by MBE, both of which showed that the magnetization easy-axis is perpendicular to the sandwiches up to a Ni thickness of approximately 100 Å. In reference to the results of section 6.1 on Ni/Cu (001), the extent of the region of perpendicular magnetization essentially doubles upon depositing a Cu layer on the Ni films. This extended range of perpendicular magnetization could be due to a dramatic change in the magnetic surface anisotropy energy density of the Ni/Cu (001) system due to the replacement of the Ni (001) free surface with a Ni/Cu (001) interface. This would be true only if the Ni-Cu (001) interface has a positive magnetic surface anisotropy energy density. Several research groups have already shown that the deposition of a few monolayers of a capping layer on top of a thin ferromagnetic film can significantly alter its magnetic anisotropy. Swartzendruber *et al.* [1993] demonstrated that by evaporating one monolayer of Cu on a six monolayer thick fcc Fe/Cu (001) film, the magnetization easy-axis goes from in-plane to perpendicular to the film. Similarly, in Co/Pd (111) thin films, coverage of a 12 Å Co film by a 2 Å layer of Cu, Au, or Pd

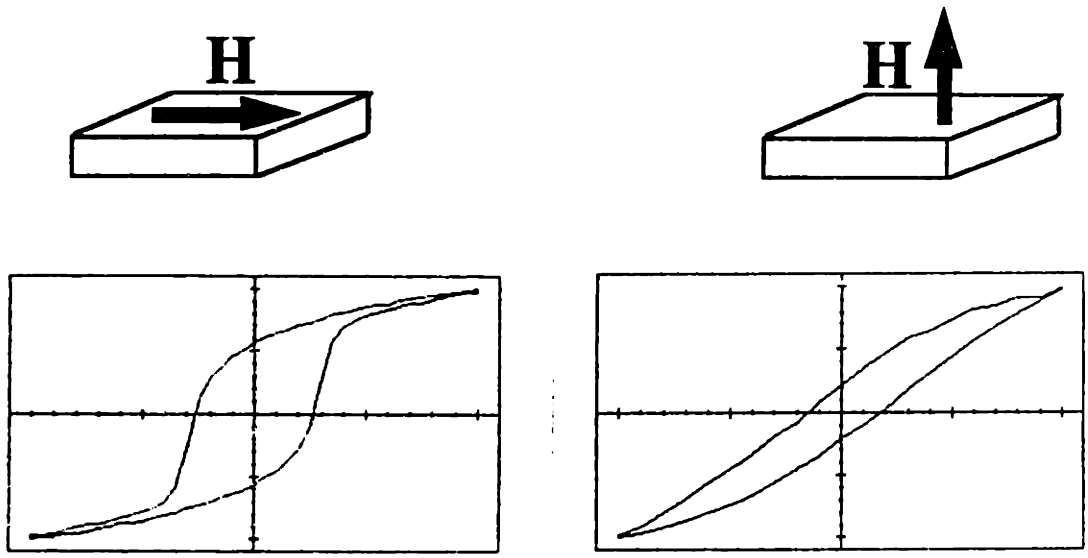

Figure 6.20: In-plane and perpendicular M-H loops for Cu/150 Å Ni/Cu/Si (001).

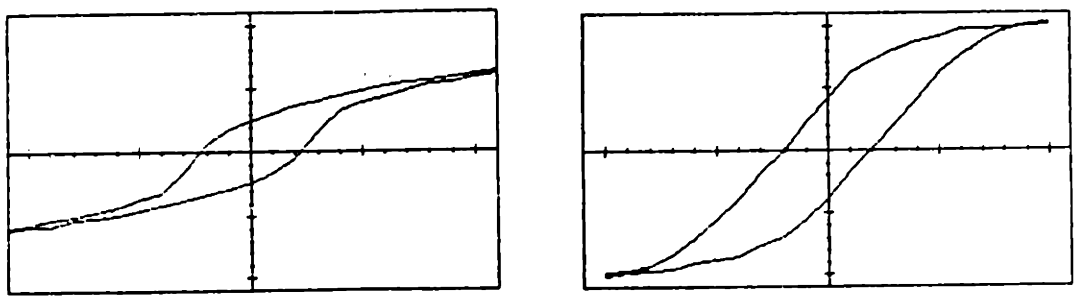

Figure 6.21: In-plane and perpendicular M-H loops for Cu/125 Å Ni/Cu/Si (001).

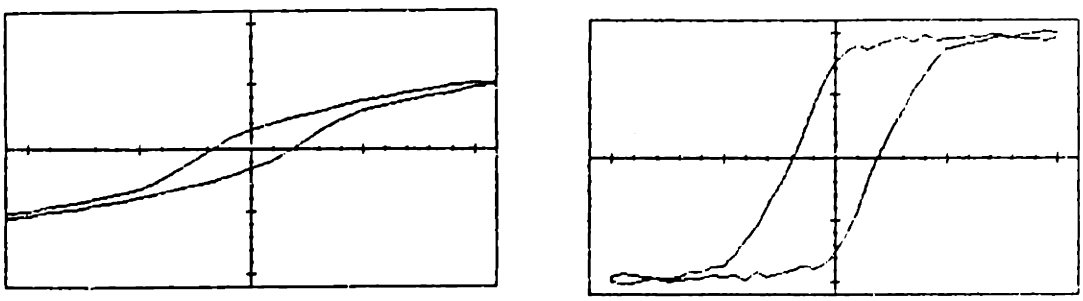

Figure 6.22: In-plane and perpendicular M-H loops for Cu/100 Å Ni/Cu/Si (001).

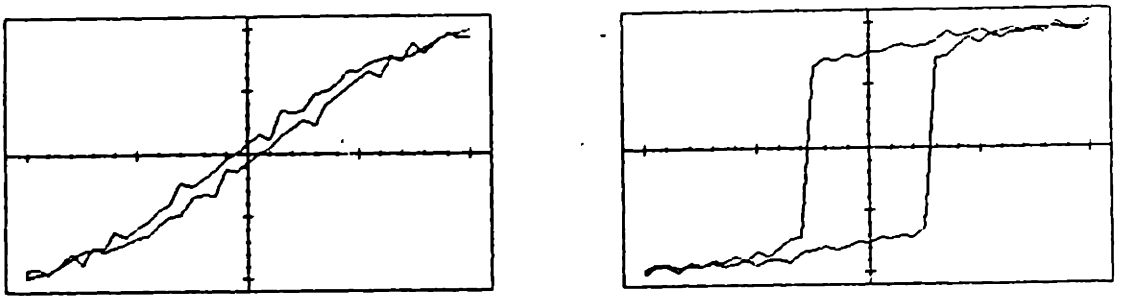

Figure 6.23: In-plane and perpendicular M-H loops for Cu/75 Å Ni/Cu/Si (001).

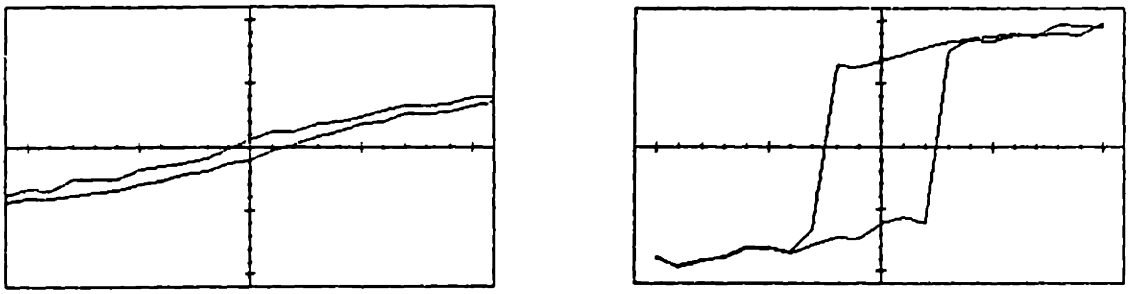

Figure 6.24: In-plane and perpendicular M-H loops for Cu/50 Å Ni/Cu/Si (001).

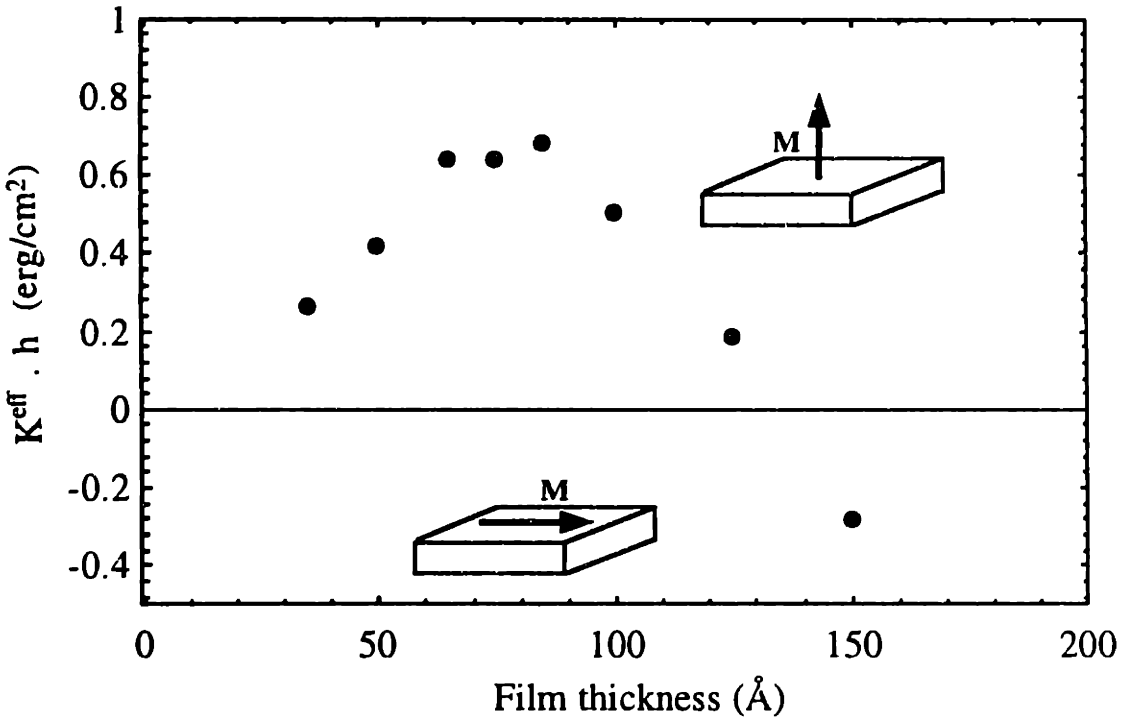

Figure 6.25: Effective magnetic anisotropy times Ni film thickness as a function of Ni film thickness for our Cu/Ni/Cu/Si (001) sandwiches. $K^{eff} > 0$ corresponds to perpendicular magnetization.

switches the magnetization easy-axis from in-plane to normal to the film [Wiedmann *et al.*, 1993]. However, in the case of Co/Au (111), Ould-Mahfoud *et al.* [1993] showed that capping a 12 monolayer Co film by 1.5 monolayer of Au makes the magnetization easy-axis go from perpendicular to in-plane. All these experiments prove that the magnetic anisotropy of a thin film depends strongly on the chemistry and the atomic arrangement of the interfaces of the film.

When the magnetization was found to lie in the plane of the film, we investigated the magnetic anisotropy within the film plane. As explained in chapter 2, when the film becomes thick enough, the magnetoelastic anisotropy and the magnetic surface anisotropy energies become negligible, and the bulk magnetocrystalline and shape anisotropies dictate the direction of the magnetization easy-axis. The magnetocrystalline anisotropy makes the <111> directions of the Ni crystal the preferred directions of the magnetization but at the same time the shape anisotropy of the film tries to keep the magnetization in-plane. The combination of these two effects makes the magnetization

prefer the in-plane <110> directions over the in-plane <100> directions in a thick film magnetized in-plane. This result can be proved rigorously by expanding Eq. (2.2) in terms of the spherical angular coordinates θ and ϕ of the magnetization vector, setting θ = 90° (or equivalently $\alpha_3 = 0$), and minimizing the remaining expression with respect to ϕ. Our measurements on the only sandwich fully magnetized in-plane (150 Å Ni) showed no sign of in-plane magnetic anisotropy. However, Chang [J. Magn. Magn. Mater. **92**, L1 (1990)] and Naik *et al.* [1993] demonstrated that when the thickness of the Ni film exceeds 500 Å the expected in-plane magnetic anisotropy can be detected.

Jungblut *et al.* [1993] have also measured the effective magnetic anisotropy energy as a function of Ni film thickness in Cu/Ni/Cu (001) sandwiches. The Ni layer, which was wedge-shaped, was deposited directly on a Cu (001) single-crystal, and was capped by 10 Å Cu followed by a 25 Å Au layer. Their plot of K^{eff} . h versus h, where h is the Ni thickness, is shown in Fig. 6.26. Our data of Fig. 6.25 and the results of Fig. 6.26 are in relatively good agreement. However, the data of Jungblut *et al.* [1993] seems

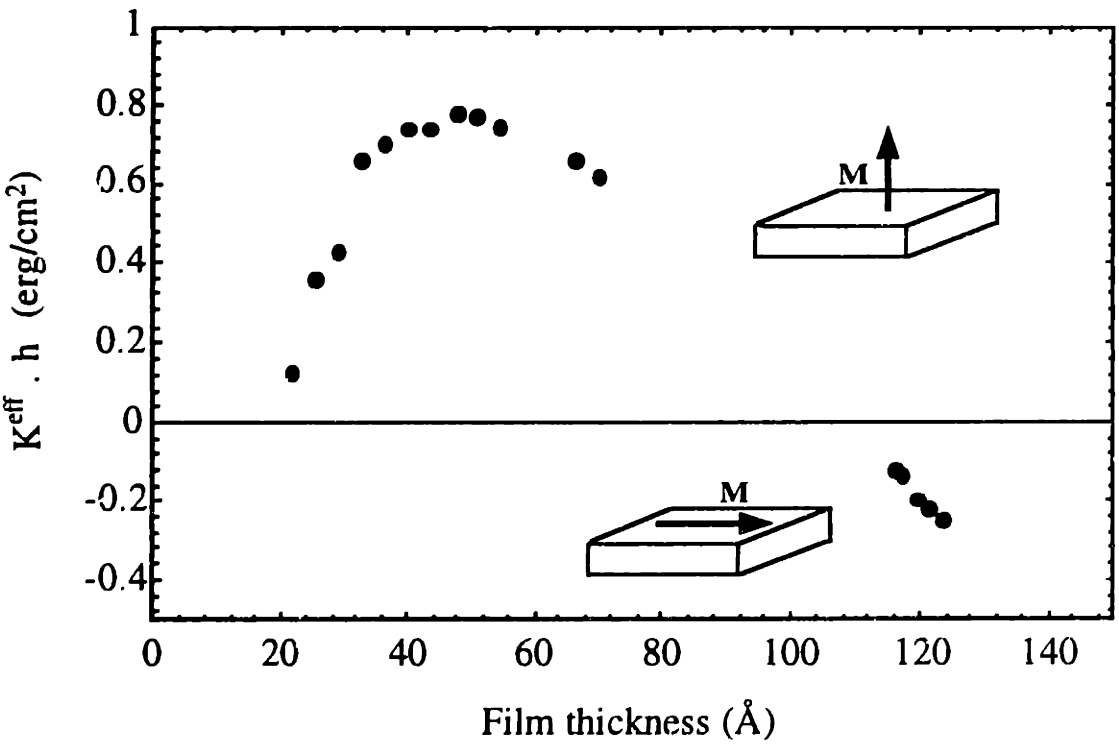

Figure 6.26: Effective magnetic anisotropy times Ni film thickness as a function of Ni film thickness for Au/Cu/Ni/Cu (001) sandwiches as measured by Jungblut *et al.* [1994]. $K^{eff} > 0$ corresponds to perpendicular magnetization.

to indicate that the perpendicular to in-plane transition occurs between 100 Å and 125 Å whereas our results show that the crossover is between 125 Å and 150 Å. Moreover, while our data indicate that $K^{eff} \cdot h$ peaks around 75 Å, Fig. 6.26 exhibits a peak near 50 Å. These differences between the data of Jungblut *et al.* and ours could be due to any of the following reasons: their films were grown directly on Cu (001) single-crystal substrates whose roughness is probably different from the one of our 2000 Å Cu/Si (001) substrates; their Ni films are wedge-shaped whereas ours consist of a series of planar films; their perpendicular anisotropies were found by forcing the magnetization away from the film's normal using an external magnetic field which only has an in-plane component whereas we measured the perpendicular anisotropy directly by applying an in-plane field of sufficient strength to saturate the sandwiches in the hard direction.

As explained in chapter 2, it is common practice to interpret the behavior of thin film magnetic anisotropy measurements in terms of a phenomenological model where the effective magnetic anisotropy energy density K^{eff} is the sum of the bulk magnetostatic anisotropy energy, the bulk magnetoelastic anisotropy energy, and a Néel magnetocrystalline surface anisotropy energy. Multiplying both sides of Eq. (2.9) by h and setting the two surface energies equal to K^s (corresponding to the Ni/Cu (001) interface), one gets:

$$K^{eff} \cdot h = \left(2 B_1 e_0(h) - 2\pi M_s^2\right) \cdot h + 2K^s \qquad (6.3)$$

for (001) oriented sandwiches where the ferromagnetic film is under an in-plane biaxial misfit strain $e_0(h)$. For $h < h_c$, the strain is thickness independent and is equal to the coherent misfit strain, $e_0(h) = \eta = 2.6\%$, for Ni/Cu (001). Equation (6.3) then predicts $K^{eff} \cdot h$ to be a linear function of h with a positive slope given by $2 B_1 \eta - 2\pi M_s^2$ and an intercept equal to $2K^s$. For $h > h_c$, $e_0(h)$ decreases with film thickness as explained in chapter 4. Substituting the 1/h strain suggested by Chappert and Bruno, Eq. (4.22), in Eq. (6.3) yields:

$$K^{eff} \cdot h = - 2\pi M_s^2 \cdot h + 2\left(B_1 \eta h_c + K^s\right) \qquad (h \geq h_c) \qquad (6.4)$$

which predicts that a plot of $K^{eff} \cdot h$ versus h should be a straight line with a slope $- 2\pi M_s^2$ and an intercept $2\left(B_1 \eta h_c + K^s\right)$. The two straight lines would intersect exactly at h_c thus forming a kink in the $K^{eff} \cdot h$ versus h plot. The data in Figs. 6.25 and 6.26 do suggest a kink at h = 75 Å and h = 50 Å, respectively. However, these thicknesses are significantly larger than the experimentally measured critical thickness $h_c \approx 18$ Å in Ni/Cu (001) (see chapter 5). Jungblut *et al.* [1994] argued that the shift of the peak in their data to a much

larger thickness is due to the 10 Å thick Cu capping layer which would push the critical thickness for dislocation formation to approximately 40 Å for Cu/Ni/Cu (001) sandwiches. This argument is hard to believe because they showed that misfit dislocations, which constitute a plastic deformation of the heterointerface, are present in their Ni/Cu (001) films when the Ni film is as thin as 15 Å. Moreover, Inglefield [unpublished] has recently demonstrated that Cu/Ni/Cu/Si (001) sandwiches where the Ni thickness is 30 Å contain interfacial misfit dislocations. We therefore believe that all the points in Figs. 6.25 and 6.26 lie above the critical thickness.

By moving the magnetostatic energy density to the left-hand side of Eq. (6.4), one obtains an equation which suggests that a plot of $\left(K^{eff} + 2\pi M_s^2\right) . h$ versus h should be a constant equal to $2\left(B_1 \eta h_c + K^s\right)$ if all the data points fall above the critical thickness. Using our own data points of Fig. 6.25, we plot $\left(K^{eff} + 2\pi M_s^2\right) . h$ versus h in Fig. 6.27 using the Ni bulk value for the saturation magnetization, $2\pi M_s^2 = 1.5 \times 10^6$ erg/cm^3. The dashed line in Fig. 6.27 corresponds to the fit of the data points with a constant equal to 1.66 erg/cm^2. The figure indicates that there is a strong disagreement between the phenomenological model and the measurements of K^{eff} if all the films are above the critical thickness. The inadequacy of the model may be due to the fact that bulk M_s of Ni does not apply to Ni thin films. However, a careful study by Huang *et al.* [1994] has shown that the Curie temperature of bulk Ni is valid for Ni films as thin as 35 Å. Another possible source of discrepancy between the model and the data could be the 1/h dependence that we have chosen for the misfit strain $e_0(h)$. We have therefore plotted $\left(K^{eff} + 2\pi M_s^2\right) . h$ versus h using a $1/h^{0.75}$ and a $1/h^{0.5}$ thickness dependence of the strain. Even in these cases there is still a strong divergence between the model and the measured effective magnetic anisotropy energy.

Another important result that falls out of Fig. 6.26 is that the magnetization easy-axis does not seem to have only one but two switching thicknesses: one near 125 Å which our measurements confirm, as shown in Fig. 6.25, and another one below 20 Å. As we saw in section 6.1, there are also two switching thicknesses for the magnetization easy-axis in Ni/Cu (001) thin films: one near 10 Å and the other near 60 Å. This result is very challenging because Eq. (6.4) predicts that the effective magnetic anisotropy energy density can change sign at most at one thickness. For example, if we choose $K^s = 0.5$ erg/cm^2 we find that the solution to $K^{eff} = 0$ is h = 105 Å. On the other hand, the solution is h = 18 Å for $K^s = -0.155$ erg/cm^2.

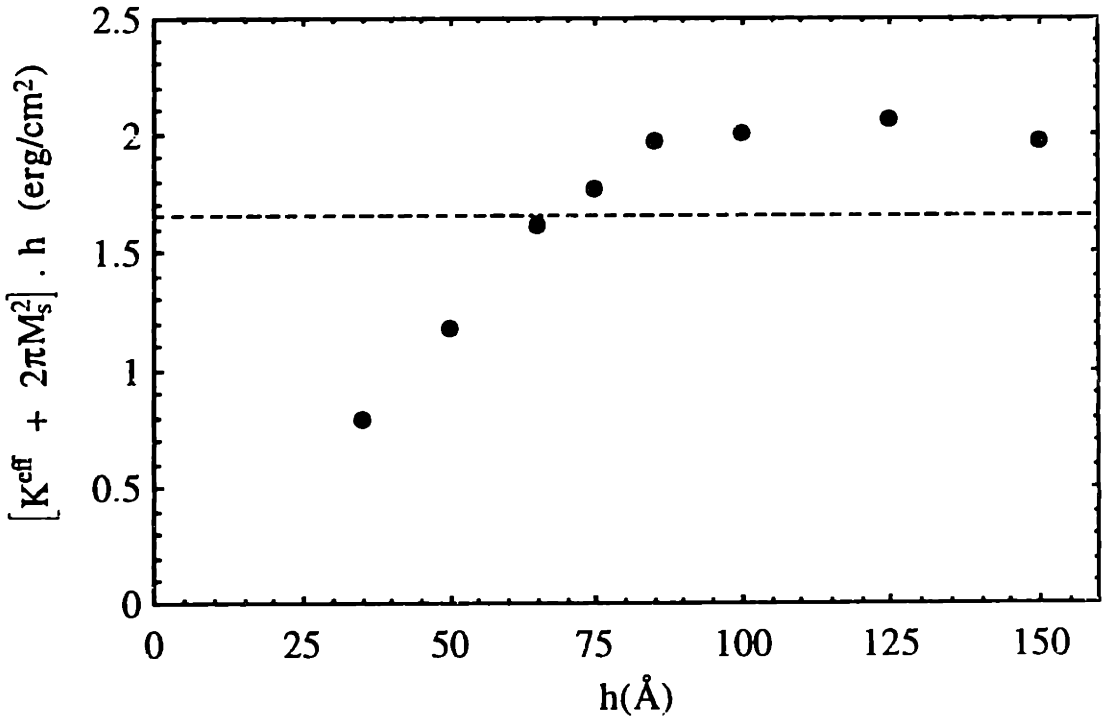

Figure 6.27: $(K^{eff} + 2\pi M_s^2) \cdot h$ versus h for our Cu/Ni/Cu/Si (001) sandwiches. The dashed line represents the fit to the data points according to the model of Eq. (6.4).

All the above intriguing observations make us believe that the commonly used phenomenological model presented in chapter 2 may be inadequate or least incomplete for describing the magnetic anisotropy in Ni/Cu thin films. We have explained that the reduced symmetry of the atomic environment about surface and interface sites gives rise to a uniaxial contribution to the magnetic anisotropy which can significantly affect the total effective magnetic anisotropy of a thin film:

$$K^{eff} = K^{bulk} + \frac{K^{surface}}{h}. \qquad (6.5)$$

However, it is not widely recognized that strain-dependent magnetic surface anisotropy, i.e. magnetoelastic surface anisotropy, comes as naturally from the Néel model [Néel, 1953; 1954] as does the strain-independent surface term K^s/h, even if the strain is uniform and independent of film thickness [Chuang, 1994; Chuang *et al.*, 1994]:

$$B^{eff} = B^{bulk} + \frac{B^{surface}}{h}. \qquad (6.6)$$

Sun and O'Handley [1991] showed experimental evidence for a difference between the magnetoelastic coupling at the surface and that in the interior of Fe-rich and Co-rich amorphous alloys. Lee *et al.* [1990] showed that it is necessary to use a modified bulk magnetostriction coefficient to interpret their magnetic anisotropy data in epitaxial Co/Cu (111) superlattices. More recently, Song *et al.* [1994] reported giant surface magnetostriction in polycrystalline Ni and NiFe thin films where the effective magnetoelastic coupling coefficients were found to diverge to positive values as the ferromagnetic thin film thickness was decreased below 50 Å. These observations indicate that knowledge of the surface magnetoelastic coupling coefficient B^s can be as important as the knowledge of the surface magnetocrystalline anisotropy energy K^s in order to fully understand the behavior of the magnetic anisotropy in thin films. Unfortunately, direct measurements of these magnetoelastic coefficients have not yet been reported for any single-crystal material and are often omitted in phenomenological models attempting to explain the behavior of the magnetic anisotropy in ultrathin films. We will review the strain dependent Néel pair-interaction model and its results on the phenomenological equations describing K^{eff} in thin films in chapter 7. We will then discuss the quantitative results of this section again in chapter 8 in the light of the results of chapter 7.

In summary, we have shown that Cu/Ni/Cu (001) sandwiches exhibit a dominant perpendicular magnetic anisotropy over an abnormally large Ni thickness range. The results of sections 6.1 and 6.3 seem to indicate that the Ni/Cu (001) interface plays an important role in supporting the perpendicular magnetization. The perpendicular remanence normalized to the saturation magnetization is plotted as a function of the Ni film thickness in Fig. 6.28 for Ni/Cu (001), Ni/$Cu_{60}Ni_{40}$ (001), and Cu/Ni/Cu (001) epitaxial structures showing the different ranges of the perpendicular magnetization. The existence of two switching thicknesses for the magnetization easy-axis and the disagreement between the phenomenological model and the data need to be addressed again in order to explain the perpendicular magnetic anisotropy in Ni/Cu (001).

6.4. 100 Å $Ni/Cu_{1-x}Ni_x/Cu/Si$ (001) Thin Films

In order to qualitatively test the effect of strain and of the magnetocrystalline surface anisotropy energy of the Ni-Cu (001) interface on the perpendicular magnetic anisotropy in Ni/Cu (001) thin films, we deposited a series of Ni/1000 Å $Cu_{1-x}Ni_x$/1000

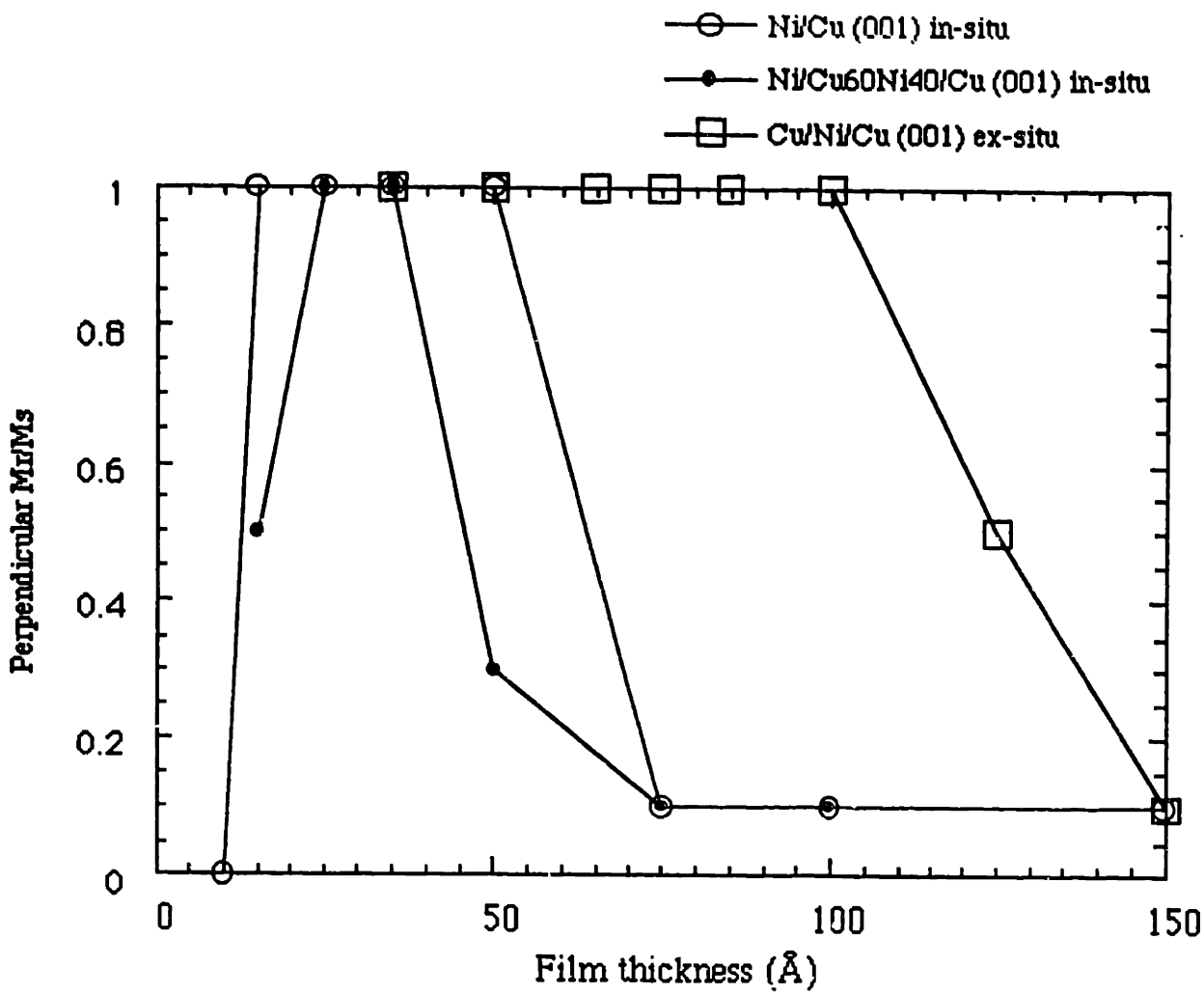

Figure 6.28: Perpendicular remanence normalized to the saturation magnetization as a function of Ni film thickness in Ni/Cu/Si (001), Ni/$Cu_{60}Ni_{40}$/Cu/Si (001), and Cu/Ni/Cu/Si (001) thin films.

Å Cu/Si (001) films and have characterized them *ex-situ* by VSM. The structure of these films is shown schematically in Fig. 6.29. As explained in section 6.2, the 1000 Å Cu buffer layer was first deposited on the Si (001) in order to make the epitaxial growth of the 1000 Å $Cu_{1-x}Ni_x$ layer with a (001) orientation possible. Contrary to the samples of section 6.2, the Ni film thickness was fixed here to 100 Å and the alloy composition was varied, never exceeding 50% Ni.

The experimental results are shown in Fig. 6.30 which is a plot of the perpendicular remanence normalized to the saturation magnetization as a function of the Ni content in the substrate expressed in atomic percent. As expected from Fig. 6.10, a Ni thin film deposited on a pure Cu substrate (x = 0) and characterized in air has a perpendicular magnetization easy-axis. As the Ni content in the substrate is increased, the perpendicular remanence gradually decreases and essentially vanishes for $x \geq 25\%$. One could think that as the Ni content in the substrate increases from 0 to 50%, the misfit between the film and the substrate decreases from 2.6% to 1.3% (as shown in Fig. 4.11) and would therefore decrease the misfit strain in the film accordingly. However, figure 4.10 shows that according to the Matthews-Blakeslee model the misfit strain in the Ni film is the same in Ni/Cu (001) and in $Ni/Cu_{50}Ni_{50}$ (001) as long as the Ni thickness exceeds the Ni critical thickness corresponding to $Ni/Cu_{50}Ni_{50}$ (001) which, according to Fig. 4.11, is 45 Å. Even if the Matthews-Blakeslee model is not very accurate, especially at large film thicknesses, the misfit strain remaining in a 100 Å thick Ni film deposited on Cu (001) is small enough that its contribution to perpendicular magnetic anisotropy is probably weak. We therefore do not expect the change observed in Fig. 6.30 to be due to misfit strain. We believe that this change in magnetic anisotropy is rather due to the change of the chemical composition of the Ni-substrate interface which affects the magnetocrystalline surface anisotropy energy of that interface. This speculation is only true if the Ni-Cu (001) interface favors perpendicular magnetic anisotropy which is very likely given the results of sections 6.1 to 6.3. In fact, as one increases the Ni content x in the substrate, the $Ni\text{-}Cu_{1-x}Ni_x$ interface goes from being a Ni-Cu interface to something closer to Ni-Ni, an interface which has zero magnetocrystalline surface anisotropy energy. In other words, if the Ni-Cu (001) interface has a positive K^s, adding Ni atoms into the substrate would weaken K^s which would eventually make the magnetization switch from perpendicular to in-plane when x is large enough.

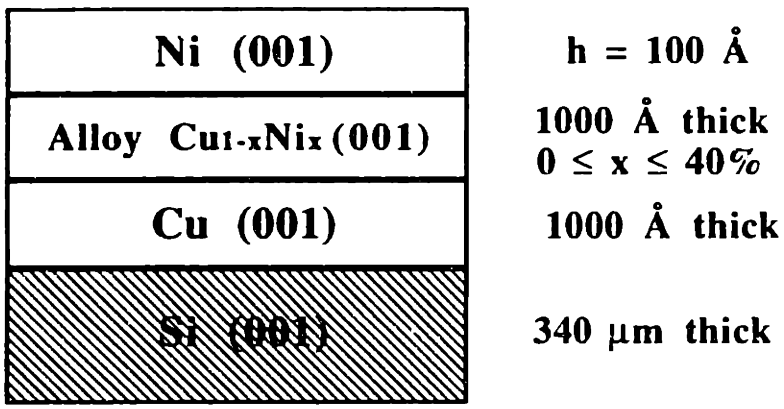

Figure 6.29: Schematic cross-section of the 100 Å $Ni/Cu_{1-x}Ni_x/Cu/Si$ (001) films.

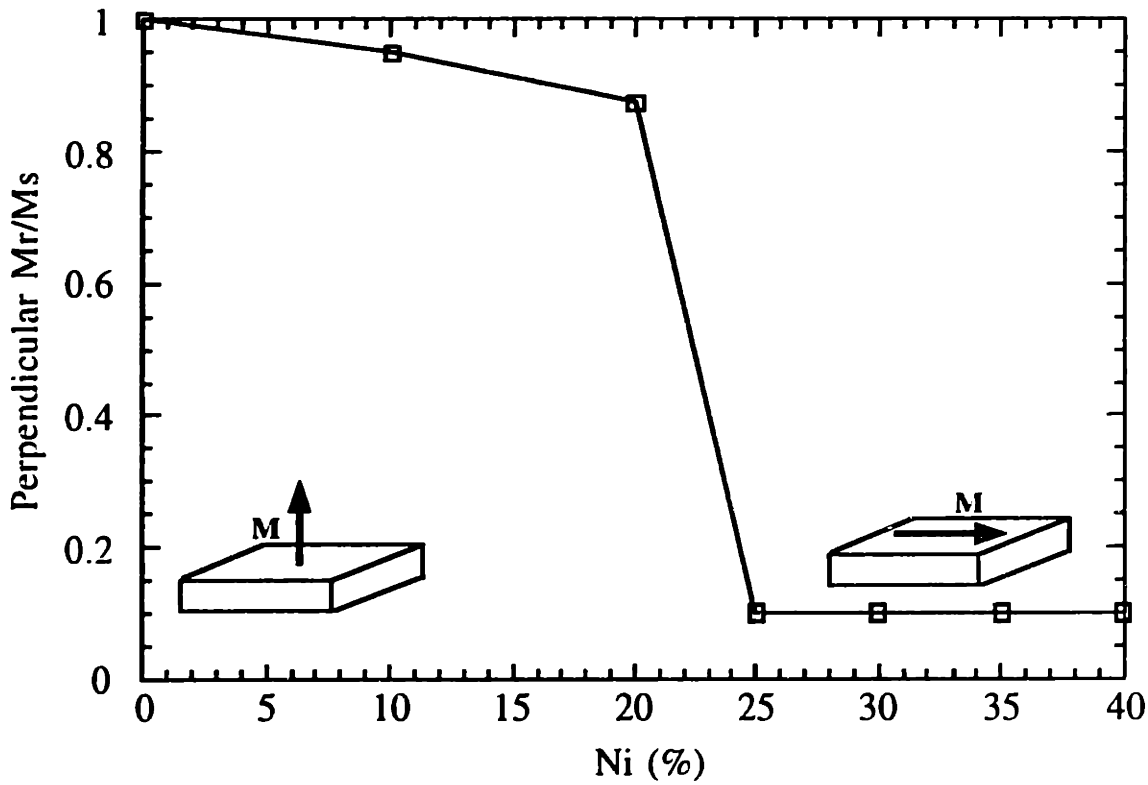

Figure 6.30: Perpendicular remanence normalized to the saturation magnetization as a function of Ni atomic percent content in the substrate for the 100 Å $Ni/Cu_{1-x}Ni_x/Cu/Si$ (001) thin film characterized in air by VSM.

Chapter 7
Phenomenological Model

In this chapter, we present the Néel pair-interaction model which represents the microscopic foundation to the macroscopic phenomenological model described in chapter 2. We will show how the broken symmetry in the atomic arrangement at a surface gives rise to the uniaxial magnetocrystalline surface anisotropy energy K^s which is of great importance in ultrathin films. Chuang *et al.* [1994] have recently modified the pair-interaction model to include the effects of an in-plane biaxial misfit strain in simple-cubic, fcc and bcc surfaces of different crystallographic orientations. Their calculations, which included only first nearest-neighbor sites, showed that a surface magnetoelastic anisotropy energy $B^s e_0(h)/h$ arises from the Néel model as naturally as the K^s/h term does. In the following sections, we will show how strongly this magnetoelastic surface contribution modifies the phenomenological models describing $K^{eff}(h)$ in the most commonly studied epitaxial systems: fcc (001), bcc (001), and fcc (111). We will also investigate the effect of including the contribution of the second nearest-neighbors on the total magnetic surface anisotropy energy.

7.1. The Néel Pair-Interaction Model

The pair-interaction model of the magnetic anisotropy, which was proposed by van Vleck [1937], is based on a pair-interaction energy w between any two neighboring atoms in a ferromagnet. By summing w over all of the first nearest-neighbors of a bulk atom, one obtains the bulk magnetocrystalline anisotropy energy and, if the bond lengths are strained and/or distorted, one also obtains the bulk magnetoelastic anisotropy energy:

$$E_A = \frac{1}{2}\sum_i w_i, \tag{7.1}$$

where the factor 1/2 accounts for double-counting. For example, in fcc and bcc crystals every bulk atom has 12 and 8 first nearest-neighbors, respectively. The magnetic pair-interaction energy can be expanded in terms of Legendre polynomials as follows [Chuang *et al.*, 1994]:

$$w(r,\psi) = G(r) + L(r)\left(\cos^2\psi - \frac{1}{3}\right) + Q(r)\left(\cos^4\psi - \frac{6}{7}\cos^2\psi - \frac{3}{35}\right) + \ldots \tag{7.2}$$

This energy depends on the distance r between the pair of atoms and the angle ψ between the direction of the magnetization and the atomic bond direction which are illustrated in Fig. 7.1.

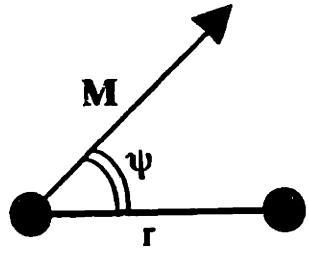

Figure 7.1: Coordinates used in the Néel pair-interaction model: r is the distance separating the pair of atoms and ψ is the angle between the magnetization vector and the bond axis.

The first term G(r) in Eq. (7.2) is independent of the angle ψ and does not contribute to the magnetic anisotropy. It includes isotropic magnetic interactions such as the Heisenberg exchange hamiltonian. The second term is dipolar in nature and gives rise to the uniaxial magnetoelastic anisotropy. The third term is the quadrupolar term which describes magnetic anisotropy of cubic symmetry. The coefficients in Eq. (7.2) are functions of the distance r between the pairs of atoms and can be expanded as follows for interactions between first nearest-neighbors:

$$L(r) = L(r_1) + \frac{dL}{dr}(r_1) \,.\, e \,.\, r_1 \tag{7.3}$$

$$Q(r) = Q(r_1) + \frac{dQ}{dr}(r_1) \,.\, e \,.\, r_1 \tag{7.4}$$

where r_1 is the bulk unstrained first nearest-neighbor bond length. When the summation in Eq. (7.1) is done over second nearest-neighbors, r_1 needs to be replaced by r_2, the bulk unstrained second nearest-neighbor distance. The term $e \cdot r_1$ in Eqs. (7.3) and (7.4) represents the difference $|\mathbf{r} - \mathbf{r}_1|$. The strain used by Chuang *et al.* [1994] in their calculations is given by Eq. (2.6) with $e_0(h)$ the average in-plane biaxial misfit strain discussed extensively in chapter 4. For a given pure material and a given crystal structure, the values of $L(r_1)$, $Q(r_1)$, and $dL/dr\ (r_1)$ are related to the bulk magnetocrystalline anisotropy constant K_1 and the bulk magnetoelastic coupling coefficients B_1 and B_2 as shown in Table 7.1. For example in an fcc crystal, where $r_1 = \frac{a}{\sqrt{2}}$: $L(r_1) = \frac{2B_1 - B_2}{4}$; $\frac{dL}{dr}(r_1)\, r_1 = \frac{3}{2}B_2 - B_1$; and $Q(r_1) = K_1$. We have computed these constants for Ni at 300 K and have included the results in Table 7.2.

Crystal structure	K_1	B_1	B_2
fcc	$Q(r_1)$	$3\,L(r_1) + \frac{1}{2}\frac{dL}{dr}(r_1)\, r_1$	$2\,L(r_1) + \frac{dL}{dr}(r_1)\, r_1$
bcc	$\frac{16}{9}Q(r_1)$	$\frac{8}{3}L(r_1)$	$\frac{8}{9}\left[L(r_1) + \frac{dL}{dr}(r_1)\, r_1\right]$

Table 7.1: Relationship between the bulk magnetocrystalline anisotropy energy density K_1, the bulk magnetoelastic coupling coefficients B_1 and B_2, and the pair-interaction model coefficients $Q(r_1)$, $L(r_1)$ and $\frac{dL}{dr}(r_1)$ [Chuang, 1994].

	K_1 (erg/cm^3)	B_1 (erg/cm^3)	B_2 (erg/cm^3)	$Q(r_1)$ (erg/cm^3)	$L(r_1)$ (erg/cm^3)	$(dL/dr)\, r_1$ (erg/cm^3)
fcc Ni	-4.5×10^4	6.2×10^7	8.5×10^7	-4.5×10^4	9.75×10^6	6.55×10^7

Table 7.2: Pair-interaction model coefficients $Q(r_1)$, $L(r_1)$ and $(dL/dr)\, r_1$ of fcc Ni at 300 K as derived from the bulk magnetocrystalline anisotropy energy density K_1 and the bulk magnetoelastic coupling coefficients B_1 and B_2 of Ni, according to the relationships of Table 7.1.

Using Eqs. (7.1), (7.2), and (7.3), and keeping only the dipolar term Chuang *et al.* [1994] first used the pair-interaction model to compute the bulk magnetic anisotropy energy of cubic ferromagnetic films biaxially strained in their plane. As expected from our discussion in chapter 2, they found that the bulk dipolar magnetic anisotropy energy is given by $2\,B_1\,e_0(h)\,\sin^2\theta$ for a (001) oriented film, where θ is the angle between the magnetization easy-axis and the film's surface normal, i.e. the [001] direction. For (111) oriented films, they found that the bulk dipolar magnetic anisotropy energy is equal to $2\,B_2\,e_0(h)\,\sin^2\theta$, where θ in this case is the angle between the magnetization easy-axis and the [111] direction.

Néel [1953, 1954] modified the pair-interaction model by allowing for missing and/or distorted bonds which lower the symmetry of surfaces and thin films. The magnetic surface anisotropy energy, which arises from these broken and/or distorted bonds at the interfaces of the ferromagnetic material, is obtained by summing $w(r, \psi)$ over the missing nearest-neighbors whose positions and distances with respect to the surface atoms need to be identified. Chuang *et al.* [1994] used the Néel model to compute the magnetic anisotropy energy due to the surfaces of cubic ferromagnetic films biaxially strained in their plane. It is important to point out that for interactions between atoms of different chemical composition, which occurs at the heterointerface of epitaxial thin films, the relationships in Table 7.2 become meaningless. Other interaction energies such as $L^{f\text{-}s}(r_1)$ and $\frac{dL^{f\text{-}s}}{dr}(r_1)$ need to be defined, where f and s correspond to the film and the substrate atoms, respectively. Numerical values for these parameters can be obtained by first-principles calculations [Victora and Mac Laren, 1993] or by comparison with experimental measurements since the magnetic surface anisotropy energies are related to $L^{f\text{-}s}(r_1)$ and $\frac{dL^{f\text{-}s}}{dr}(r_1)$ [Chuang *et al.*, 1994], as we will show in the next section.

7.2. Applications to selected (001) and (111) surfaces

The contribution of the surface to the magnetic anisotropy is determined by summing the pair-interaction energy of Eq. (7.2) over the broken bonds at the surface. Similarly, the contribution to the magnetic anisotropy of the film-substrate interface is obtained by summing the pair-interaction energy over the hybrid bonds formed at the interface. The total magnetic anisotropy of a thin film is then given by subtracting the

contribution of the broken surface bonds and adding the contribution of the interfacial hybrid bonds to the bulk magnetic anisotropy energy:

$$E^{film} = E^{bulk} - 2\frac{E^{surface}}{h} + \frac{E^{interface}}{h}, \qquad (7.5)$$

where h is the thickness of the film. By analogy, for a thin film sandwiched between two identical layers, the total magnetic anisotropy energy is given by:

$$E^{sandwich} = E^{bulk} - 2\frac{E^{surface}}{h} + 2\frac{E^{interface}}{h}. \qquad (7.6)$$

In order to find $E^{surface}$ and $E^{interface}$ in terms of the interaction energies of Eq. (7.2) we first need to identify the broken bonds at the film's surface. We will only discuss fcc (001), bcc (001) and fcc (111) surfaces since they are the most commonly studied in magnetic thin films.

The surface sites, the missing first nearest-neighbor sites and the missing second nearest-neighbor sites are shown schematically in Fig. 7.2 for fcc (001) and bcc (001) surfaces. In both surfaces, every surface atom has 4 first nearest-neighbors and 1 second nearest-neighbor missing. For fcc (111) surfaces, not shown in Fig. 7.2, every surface atom has 3 first nearest-neighbors and 3 second nearest-neighbors missing. It is important to note that when we try to account for the contributions of the second nearest-neighbors, we need to consider not only surface atoms but also sub-surface atoms. In fact, the second nearest-neighbors of the sub-surface atoms are the first nearest-neighbors of the surface atoms and are missing. The distance r_1 is equal to $\frac{a}{\sqrt{2}}$ and $\frac{\sqrt{3}}{2}a$ in fcc and bcc crystals, respectively. The distance r_2 is equal to a for both fcc and bcc crystals.

Chuang *et al.* [1994] computed the surface contribution of the first nearest-neighbors to the magnetic anisotropy for (001), (111), and (110) oriented sc, fcc, and bcc surfaces with and without steps. We used their results to compute the contributions of the second nearest-neighbors. The results for the first and second nearest-neighbors are given in Table 7.3 for fcc (001), bcc (001), and fcc (111) surfaces. The surface energies of Eqs. (7.5) and (7.6) are obtained by multiplying the energies in Table 7.3 by d, the thickness of a monolayer. The first important result of Table 7.3 is that the magnetic surface anisotropy energies generally have both a strain-independent and a strain-dependent component. The latter arises from including the strain in the pair-interaction energy $w(r,\psi)$. The second important result is that the strain-independent magnetic surface energy is nil for all bcc (001) surfaces if one only includes first nearest-neighbor

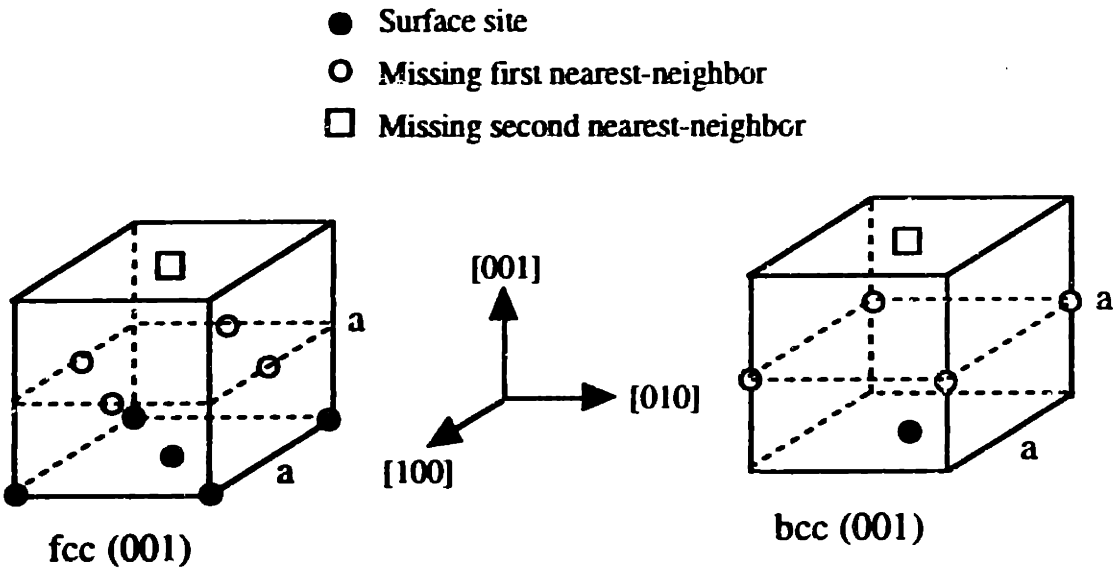

Figure 7.2: Illustration of the surface, missing first nearest-neighbor, and missing second nearest-neighbor sites in fcc (001) and bcc (001) surfaces. In the case of the fcc (001) surface, the missing sites are with respect to the atom located at the center of the surface.

	$\frac{E^{surface}}{d}$ First nearest-neighbors contribution	$\frac{E^{surface}}{d}$ Second nearest-neighbors contribution
fcc (001) surface	$-\left[\frac{1}{2} L(r_1) - 3 e_0 L(r_1)\right] \sin^2\theta$	$-\left[L(r_2) + e_0 \frac{dL}{dr}(r_2)\, r_2\right] \sin^2\theta$
bcc (001) surface	$\frac{8}{3} e_0 L(r_1) \sin^2\theta$	$-\left[L(r_2) + e_0 \frac{dL}{dr}(r_2)\, r_2\right] \sin^2\theta$
fcc (111) surface	$-\left[\frac{3}{4} L(r_1) - e_0\left(2L(r_1) + \frac{1}{4}\frac{dL}{dr}(r_1)\, r_1\right)\right] \sin^2\theta$	$24\, e_0 L(r_2) \sin^2\theta$

Table 7.3: Surface anisotropy energy densities (expressed per unit volume) resulting from first and second nearest-neighbor contributions for three different cubic structures. For the (001) orientation, we used the coordinate system: x = [100], y = [010], z = [001]. For the (111) orientation, we used the coordinate system: x = [11$\bar{2}$], y = [$\bar{1}$10], z = [111]. r_1 and r_2, which are the first and second nearest-neighbor distances, respectively, depend on the crystal structure. d is the monolayer height and depends on the crystal structure and the crystallographic orientation.

contributions. The third important result is that for fcc (001) surfaces, but not for fcc (111) surfaces, the first nearest-neighbor the strain-independent and the strain-dependent magnetic surface anisotropy energies are proportional to each other.

The results for fcc (001) films and sandwiches are of particular importance to us since we are interested in the magnetic anisotropy in Ni/Cu (001) thin films and Cu/Ni/Cu (001) sandwiches. In the case of an fcc (001) film sandwiched between two identical non-magnetic layers, the first nearest-neighbors contribution to the magnetic surface anisotropy energy is given by:

$$- 2\frac{E^{surface}}{h} + 2\frac{E^{interface}}{h}$$

$$= \left[- \frac{2}{h} \frac{d\left(L^{f\text{-}s} - L^{f\text{-}f}\right)}{2} + e_0 \frac{2}{h} 3d\left(L^{f\text{-}s} - L^{f\text{-}f}\right) \right] \sin^2\theta \qquad (7.7)$$

where we omitted the r_1 dependence of L in the equation and where $e_0 = e_0(h)$. Combining this result with the ones of chapter 2, the total magnetic anisotropy energy of the fcc (001) sandwich is then given by $E_A = E^{bulk} + \frac{E^{surface}}{h}$, where $E^{bulk} = (- 2\pi M_s^2 + K_1 + 2B_1 e_0) \sin^2\theta$, and where $E^{surface} = (2K^s + 2B^s e_0) \sin^2\theta$. Neglecting the bulk magnetocrystalline anisotropy energy K_1 with respect to the other bulk energies and using Eq. (7.7), the total magnetic anisotropy energy of the fcc (001) sandwich reduces to $E_A = K^{eff}_{fcc\,(001)} \sin^2\theta$, where:

$$K^{eff}_{fcc\,(001)} = - 2\pi M_s^2 + 2\left(B_1 + \frac{B^s}{h}\right) e_0(h) + \frac{2K^s}{h}, \qquad (7.8)$$

$$\text{where } K^s_{f/s\,(001)} = - \frac{d\left(L^{f\text{-}s} - L^{f\text{-}f}\right)}{2} \qquad (7.9)$$

$$\text{and } B^s_{f/s\,(001)} = 3d\left(L^{f\text{-}s} - L^{f\text{-}f}\right). \qquad (7.10)$$

K^s is the surface magnetocrystalline anisotropy energy defined macroscopically in chapter 2. The appearance of the surface magnetoelastic anisotropy energy $2\frac{B^s}{h} e_0(h)$, which we did not discuss in chapter 2, is the most important result of this section. The presence of such a term means that the effective magnetoelastic coupling coefficient $B^{eff} = B_1 + \frac{B^s}{h}$ is a function of the film thickness in an ultrathin film and can be significantly different from the bulk coefficient B_1. The coefficient B^{eff} could even change sign if B^s has the opposite sign of B_1. The coefficient B^s has never been

measured directly for any single-crystal material. However, using secondary electron spin polarization analysis, Sun and O'Handley [1991] found that the surface magnetoelastic coupling coefficient can differ sharply from the bulk value in Co-rich and Fe-rich amorphous alloys. Their measurements on CoCrB amorphous alloys showed that $B^{eff} \approx 3 \times B^{bulk}$, indicating that B^{eff} is shifted to more positive values due to surface effects. More recently, Song *et al.* [1994] measured the effective magnetoelastic coupling coefficient by a direct *in-situ* method in polycrystalline NiFe/Ag/Si, NiFe/Cu/Si, and Ni/SiO_2/Si thin films. These coefficients were shown to take giant positive values below 40 to 60 Å due to a significant surface contribution. In particular, for Ni/SiO_2/Si thin films, it was found that $B^s \approx 20$ erg/cm^2. The plot of B^{eff} versus h for Ni/SiO_2/Si is shown in Fig. 7.3. The figure indicates that B^{eff} starts diverging from the bulk value to more positive values for Ni thicknesses below 150 Å. The thickness dependence of B^{eff} versus h can be fitted by:

$$B^{eff} = B^{bulk} + \frac{B^s}{h - 55} \tag{7.11}$$

where h is in Angstroms. The 55 Å shift in the thickness scale, which is not predicted by the Néel model is not well understood. It may be due to the presence of a magnetically different layer arising from the chemical intermixing at the film-substrate interface confirmed by Auger depth profiling [Song *et al.*, 1994]. Zuberek *et al.* [1988] have measured the surface magnetostriction of Ni/Ag multilayers using strain-modulated ferromagnetic resonance. They found that the effective magnetoelastic coupling coefficient of these structures goes from positive to negative values as the Ni film thickness goes to zero. The magnetoelastic coupling coefficient has also been measured very recently in polycrystalline Fe/glass thin films using a cantilever beam technique while the films were kept under ultra-high vacuum [Weber *et al.*, 1994]. Significant deviations from the bulk value of the magnetoelastic coupling coefficient of polycrystalline Fe were observed for Fe thicknesses below approximately 100 Å. The effective magnetoelastic coupling coefficient was shown to change sign when the Fe film thickness was between 80 Å and 30 Å.

The second very important result of Eqs. (7.8) to (7.10) is that the value and sign of B^s, just like the ones of K^s, are characteristic of an interface and not of the bulk material, unlike other magnetic anisotropy constants such as K_1 and B_1. In fact, it follows from Eqs. (7.9) and (7.10) that the magnetic surface anisotropy energies of the film-vacuum interface are given by:

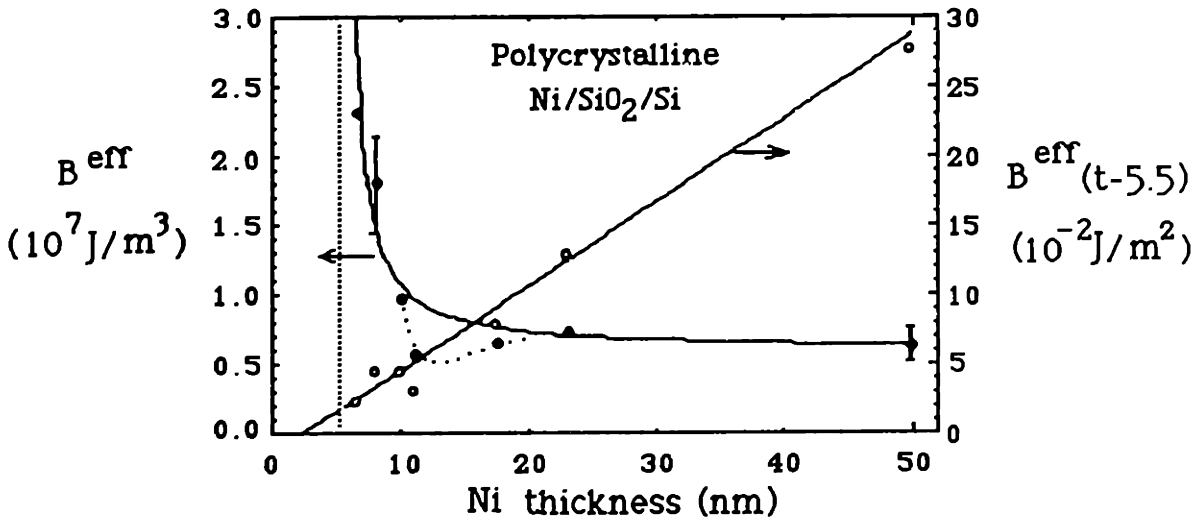

Figure 7.3: Solid data points: effective magnetoelastic coupling coefficient measured *in situ* for polycrystalline Ni/SiO_2/Si versus Ni film thickness expressed in nanometers. Open data points: B^{eff} x (h - 5.5) versus h showing the quality of fit to the Néel model. Note that the vertical scale for B^{eff} is in units of 10^7 J/m^3 = 10^8 erg/cm^3. The vertical dotted line indicates the thickness h = 5.5 nm [Song *et al.*, 1994].

$$K^s_{f/vac\,(001)} = \frac{d\,L^{f\text{-}f}}{2} \tag{7.12}$$

and $$B^s_{f/vac\,(001)} = -3d\,L^{f\text{-}f} \tag{7.13}$$

which are clearly different from the magnetic surface anisotropy energies of the film-substrate interface if $L^{f\text{-}s} \neq 0$. Using Table 7.2, we find that according to the Néel model $K^s_{Ni/vac\,(001)} = 0.09$ erg/cm^2 and $B^s_{Ni/vac\,(001)} = -0.51$ erg/cm^2 at room temperature.

The third very important result that follows from Eqs. (7.8) to (7.10) is that, for any fcc (001) sandwich and only first nearest-neighbor interactions, B^s and K^s are proportional and have opposite signs according to the Néel model:

$$B^s = -6\,K^s. \tag{7.14}$$

In fact, adding the contribution of the second-nearest neighbors listed in Table 7.3 to $E^{surface}$ and $E^{interface}$ yields:

$$K^s_{f/s\,(001)} = -d\left[\frac{L^{f\text{-}s}(r_1) - L^{f\text{-}f}(r_1)}{2} + L^{f\text{-}s}(r_2) - L^{f\text{-}f}(r_2)\right] \tag{7.15}$$

and $$B^s_{f/s\,(001)} = d\left[3\left(L^{f\text{-}s}(r_1) - L^{f\text{-}f}(r_1)\right) - r_2\left(\frac{dL^{f\text{-}s}}{dr}(r_2) - \frac{dL^{f\text{-}f}}{dr}(r_2)\right)\right] \qquad (7.16)$$

As explained earlier, $L^{f\text{-}s}(r)$ is not a known function of r *a priori*. For example, if $L^{f\text{-}s}(r) \propto \frac{1}{r}$, which would be a relatively strong interaction at small distances, then $L(r_2)/L(r_1) = L(a)/L(a/\sqrt{2}) \approx 0.7$, where we used the fact that $r_1 = a/\sqrt{2}$ and $r_2 = a$ in an fcc crystal. In this case the contribution of the second nearest-neighbors to the magnetocrystalline surface anisotropy energy of Eq. (7.15) would be large enough to break the simple relationship between $B^s_{f/s\,(001)}$ and $K^s_{f/s\,(001)}$, as can be seen from Eqs. (7.15) and (7.16). The simple relationship in Eq. (7.14) between B^s and K^s does not apply for bcc (001) and fcc (111) sandwiches even if one were to include only contributions from first nearest-neighbors to the magnetic surface anisotropy. In particular for bcc (001) sandwiches, the Néel model predicts that K^s is always equal to zero, if one includes only first nearest-neighbor contributions. By analogy to Eq. (7.8) and using Table 7.3, the effective magnetic anisotropy energy density for a bcc (001) sandwich where the film is biaxially strained in its plane is given by:

$$K^{eff}_{bcc\,(001)} = -2\pi M_s^2 + 2\left(B_1 + \frac{B^s}{h}\right)e_0(h) \qquad (7.17)$$

where $$B^s_{f/s\,(001)} = \frac{8}{3}d\left(L^{f\text{-}s} - L^{f\text{-}f}\right) \qquad (7.18)$$

and where we have omitted the r_1 dependence of the L's.

As explained in section 7.1, the bulk magnetoelastic anisotropy energy density of an fcc (111) thin film biaxially strained in its plane is given by $2\,B_2\,e_0(h)\sin^2\theta$. It follows from Eq. (7.8) and Table 7.3 that the total effective magnetic anisotropy energy density in an fcc (111) sandwich is:

$$K^{eff}_{fcc\,(111)} = -2\pi M_s^2 + 2\left(B_2 + \frac{B^s}{h}\right)e_0(h) + \frac{2K^s}{h} \qquad (7.19)$$

where $$K^s_{f/s\,(111)} = -\frac{3}{4}d\left(L^{f\text{-}s} - L^{f\text{-}f}\right) \qquad (7.20)$$

and $$B^s_{f/s\,(111)} = 2d\left(L^{f\text{-}s} - L^{f\text{-}f}\right) + \frac{r_1 d}{4}\left(\frac{dL^{f\text{-}s}}{dr} - \frac{dL^{f\text{-}f}}{dr}\right) \qquad (7.21)$$

if we only include the contributions from first nearest-neighbors. Equations (7.20) and (7.21) indicate that, unlike fcc (001) sandwiches, there is no simple relationship between $B^s_{f/s\,(111)}$ and $K^s_{f/s\,(111)}$ for fcc (111) sandwiches.

At this point, it would be interesting to discuss the predictions of the phenomenological equations for the above three different surfaces when the average in-plane biaxial misfit strain is proportional to 1/h. Substituting Eq. (4.22) into Eq. (7.8) yields:

$$\left[K^{eff}_{fcc\,(001)} + 2\pi M_s^2\right] . h = 2\left(B_1 \eta h_c + K^s\right) + \frac{2 B^s \eta h_c}{h}. \qquad (7.22)$$

Comparing Eqs. (7.22) and (6.4), we immediately see that the strain-induced magnetic surface anisotropy dramatically changes the phenomenological model presented in chapter 2. A plot of $\left[K^{eff}_{fcc\,(001)} + 2\pi M_s^2\right] . h$ versus h no longer needs to be a constant given the 1/h dependence on the right-hand side of Eq. (7.22). Fitting such a plot with the functional form $X + \frac{Y}{h}$ would then yield B^s and K^s of the sandwich in question. A similar result applies to fcc (111) sandwiches as can be seen by substituting Eq. (4.22) into Eq. (7.19):

$$\left[K^{eff}_{fcc\,(111)} + 2\pi M_s^2\right] . h = 2\left(B_2 \eta h_c + K^s\right) + \frac{2 B^s \eta h_c}{h} \qquad (7.23)$$

which has the same form as Eq. (7.22) except that the bulk magnetoelastic coupling coefficient B_1 is replaced by B_2. The variables h_c, B^s and K^s in Eqs. (7.22) and (7.23) need not be the same. In the case of bcc (001) sandwiches, replacing the strain of Eq. (4.22) into Eq. (7.17) yields:

$$\left[K^{eff}_{bcc\,(001)} + 2\pi M_s^2\right] . h = 2 B_1 \eta h_c + \frac{2 B^s \eta h_c}{h} \qquad (7.24)$$

Fitting a plot of $\left[K^{eff}_{bcc\,(001)} + 2\pi M_s^2\right] . h$ versus h with a functional form $X' + \frac{Y'}{h}$ would yield B^s of the bcc (001) sandwich. Contrary to X in Eqs. (7.22) and (7.23), X' is not an unknown but is equal to the constant $2 B_1 \eta h_c$ which is known *a priori*. In the case of bcc (001) sandwiches, the fit of $\left[K^{eff}_{bcc\,(001)} + 2\pi M_s^2\right] . h$ versus h would therefore have only one degree of freedom, given by B^s, if only first nearest-neighbor contributions are included.

We conclude this chapter by listing the possible limitations of the pair-interaction model [Chuang *et al.*, 1994]:

i) the model assumes structurally perfect films with sharp free surfaces and interfaces with no interdiffusion nor roughness at the film-substrate interface;

ii) the model assumes that the strain e(h) in the film is given by Eq. (2.6) where $e_0(h)$ is the average in-plane biaxial residual misfit strain in the film. No other sources of strain such as thermal strain or interfacial roughness strain are included. Further, the model does not take into account the huge localized strains due to defects such as interfacial misfit dislocations which we discussed in chapter 4;

iii) the model does not take into account the fact that the interactions potentials L(r) and Q(r) may themselves be different between the film's interfaces and in the interior;

iv) the model predicts delta function surface magnetocrystalline and magnetoelastic effects. Magnetic surface anisotropies can typically cause a significant departure from bulk behavior only for ultrathin films ($h \leq 10$ Å). However, surface effects have been shown to dominate the total magnetic anisotropy of thicker films through the exchange interaction which can drag the strong but localized magnetic surface anisotropy into the interior of the film over a distance of the order of a few hundred Angstroms [O'Handley and Woods, 1990]. This mechanism is not included in the Néel model.

Chapter 8
Discussion

In this chapter, we will re-analyze our experimental results and the ones of Jungblut *et al.* [1994] on the magnetic anisotropy of Cu/Ni/Cu (001) sandwiches using the more complete phenomenological model developed in chapter 7. We will show how a significantly improved fit to the data can be obtained by including a surface magnetoelastic coupling coefficient B^s for the Ni/Cu (001) interface. The magnitude and sign of this coefficient sheds some light on the existence of two magnetization easy-axis switching thicknesses in Ni/Cu (001), which we discussed in chapters 3 and 6. This analysis also yields an estimate of the surface magnetocrystalline anisotropy energy corresponding to the Ni/Cu (001) interface. In the second section of this chapter, we will discuss more in detail the energies that dominate the balance in the perpendicular magnetic anisotropy in Ni/Cu (001), namely the magnetic surface anisotropy energies and the bulk magnetoelastic anisotropy energy. We will conclude by applying the phenomenological model of chapter 7 to published data [Lee *et al.*, 1990; Lamelas *et al.*, 1989] on the magnetic anisotropy and the strain in fcc Co/Cu (111) superlattices. This study yields the surface magnetocrystalline anisotropy energy and the surface magnetoelastic coupling coefficient of the Co/Cu (111) interface [Bochi *et al.*, 1994].

8.1. Magnetic Anisotropy in Cu/Ni/Cu (001) Sandwiches

In chapter 6, we attempted to interpret our experimental results on the effective magnetic anisotropy energy K^{eff} in Cu/Ni/Cu (001) sandwiches and showed that the data of $\left[K^{eff} + 2\pi M_S^2\right] . h$ versus h cannot be explained using the phenomenological model of chapter 2 in which K^{eff} is a sum of the magnetostatic anisotropy energy, the bulk

magnetoelastic anisotropy energy, and a surface magnetocrystalline anisotropy energy. In chapter 7, we showed that it is a natural consequence of the strain-dependent pair-interaction model that the magnetic surface anisotropy energy includes a strain-dependent term, the surface magnetoelastic anisotropy energy $2B^s e_0(h)/h$. By including this term, we showed that the phenomenological equation describing $K^{eff}(h)$ for an epitaxial (001) sandwich becomes:

$$\left[K^{eff} + 2\pi M_s^2\right] . h = 2\left(B_1 + \frac{B^s}{h}\right) e_0(h) . h + 2 K^s . \qquad (8.1)$$

Substituting the 1/h dependent strain given by Eq. (4.22) for $h \geq h_c$ into Eq. (8.1) yields:

$$\left[K^{eff} + 2\pi M_s^2\right] . h = 2\left(B_1 \eta h_c + K^s\right) + 2\frac{B^s \eta h_c}{h}, \qquad (8.2)$$

which differs from Eq. (6.4) only through the presence of the B^s term. Contrary to the predictions of Eq. (6.4), a plot of $\left[K^{eff} + 2\pi M_s^2\right] . h$ versus h does not have to be a constant but can be the sum of a constant and a 1/h dependent term which is multiplied by B^s. We plot $\left[K^{eff} + 2\pi M_s^2\right] . h$ versus h for our Cu/Ni/Cu (001) sandwiches in Fig. 8.1. The data points are the same as the ones in Fig. 6.27. The dashed line represents the fit to the data using a constant term equal to 1.66 erg/cm^2. The solid line is the fit to the data points using a functional form $X + \frac{Y}{h}$, as suggested by Eq. (8.2). The figure clearly shows that including the B^s/h term significantly improves the fit to the experimental data. The equation describing the solid line is:

$$\left[K^{eff} + 2\pi M_s^2\right] . h = 2.55 - \frac{62.4}{h} \text{ , in erg/cm}^2. \qquad (8.3)$$

By comparing Eqs. (8.2) and (8.3), we can obtain estimates of B^s and K^s for the Ni/Cu (001) interface. We use the values $B_1 = 6.2 \times 10^7$ erg/cm^3 and $2\pi M_s^2 = 1.5 \times 10^6$ erg/cm^3 for bulk Ni. The lattice mismatch and the critical thickness for Ni/Cu (001) are given by $\eta = 2.6\%$ and $h_c = 18$ Å, respectively, as explained in chapters 4 and 5. Using these values, we conclude that B^s(Ni/Cu)(001) $\approx$ - 67 erg/cm^2 and K^s(Ni/Cu)(001) $\approx$ + 0.98 erg/cm^2 from the above fit.

We have also tried to fit our experimental data using the Ni thickness dependence of the strain in Ni/Cu (001) thin films measured by optical interferometry [Inglefield *et al.*, 1995] and described by the fit $e_0(h) = \frac{0.1815}{h^{0.70}}$ of Eq. (4.25). Substituting this strain in Eq. (8.1) yields:

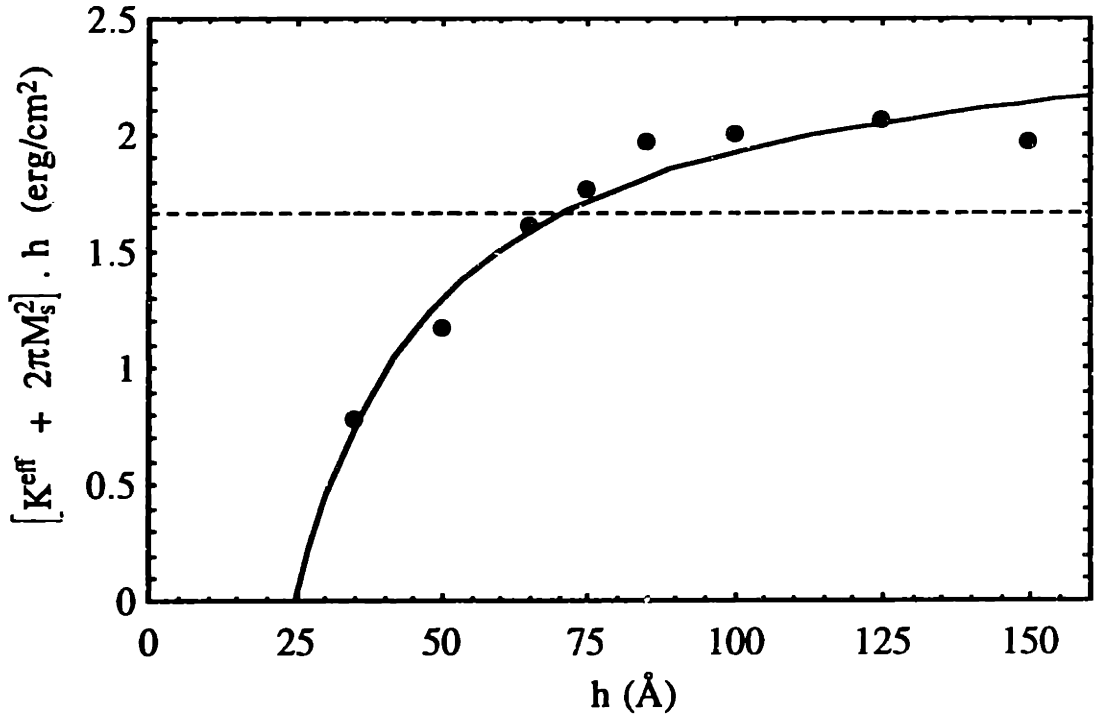

Figure 8.1: $[K^{eff} + 2\pi M_s^2] . h$ versus h for our Cu/Ni/Cu (001) sandwiches. The dashed and solid lines represent the best fit to the data points using the phenomenological model of Eq. (8.2) with $B^s = 0$ and $B^s \neq 0$, respectively.

$$[K^{eff} + 2\pi M_s^2 - 2B_1 e_0(h)] . h = 2K^s + 2\frac{(0.1815)\, B^s}{h^{0.7}}. \qquad (8.4)$$

According to this model, a plot of $[K^{eff} + 2\pi M_s^2 - 2B_1 e_0(h)] . h$ versus h can be modeled by the sum of a constant equal $2K^s$ and a $1/h^{0.7}$ term multiplied by B^s. Such a plot also demonstrates that the B^s/h term improves the fit to our experimental data points. The equation of the curve that best fits the data is given by:

$$[K^{eff} + 2\pi M_s^2 - 2B_1 e_0(h)] . h = 1.77 + \frac{19.02}{h^{0.7}} \text{ , in erg/cm}^2. \qquad (8.5)$$

Comparing Eqs. (8.4) and (8.5) yields B^s(Ni/Cu)(001) ≈ - 52 erg/cm² and K^s(Ni/Cu)(001) ≈ + 0.88 erg/cm². The difference between these results and the ones of the previous paragraph is due to the choice of the average in-plane biaxial misfit strain $e_0(h)$. In the first case, we used $e_0(h) \propto 1/h$ whereas in the second case we substituted the strain $e_0(h) \propto 1/h^{0.7}$ into the phenomenological equation 8.1. This shows how sensitive the results of the fit are to the choice of the thickness dependence of the strain in the film.

We have also applied the phenomenological model of Eq. (8.2) to the experimental measurements of Jungblut *et al.* [1994] on Cu/Ni/Cu (001) sandwiches; their data are shown in Fig. 6.26. The plot of $\left[K^{eff} + 2\pi M_s^2\right] . h$ versus h for these data points is shown in Fig. 8.2. The dashed and solid lines again represent the best fit to the data for $B^s = 0$ and $B^s \neq 0$, respectively. As with our data on Cu/Ni/Cu (001), figure 8.2 clearly indicates that the inclusion of the surface magnetoelastic anisotropy energy significantly improves our understanding of the behavior of $K^{eff}(h)$ in Cu/Ni/Cu (001) sandwiches. The equation of the solid line in Fig. 8.2 is:

$$\left[K^{eff} + 2\pi M_s^2\right] . h = 1.94 - \frac{28.76}{h} \text{, in erg/cm}^2. \qquad (8.6)$$

Jungblut *et al.* [1994] showed that in their Ni/Cu (001) thin films, the onset of misfit dislocations occurs at $h_c = 15$ Å. Using this value and $\eta = 2.6\%$ gives the following magnetic surface energies when we compare Eqs. (8.2) and (8.6): B^s(Ni/Cu)(001) ≈ - 37 erg/cm^2 and K^s(Ni/Cu)(001) ≈ + 0.73 erg/cm^2. In their analysis, Jungblut *et al.* found that K^s(Ni/Cu)(001) ≈ - 0.40 erg/cm^2 by using the phenomenological model of chapter 6

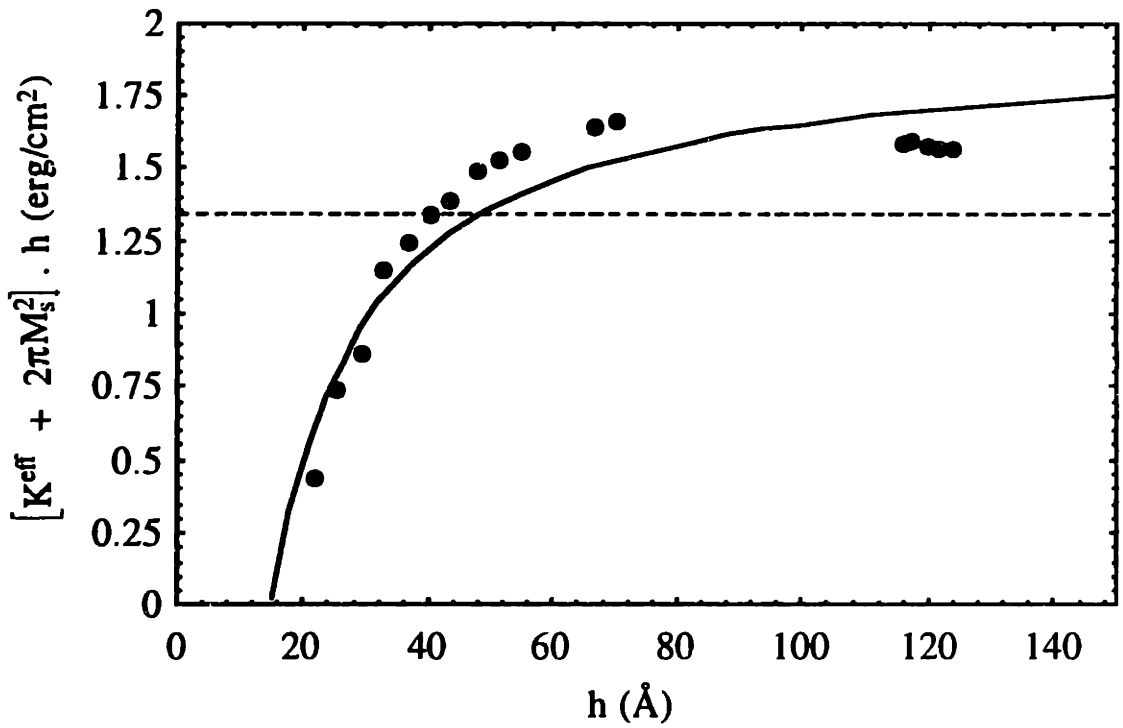

Figure 8.2: $\left[K^{eff} + 2\pi M_s^2\right] . h$ versus h for the data of Jungblut *et al.* [1994] on Cu/Ni/Cu (001) sandwiches. The dashed and solid lines represent the best fit to the data points using the phenomenological model of Eq. (8.2) with $B^s = 0$ and $B^s \neq 0$, respectively.

and setting B^s(Ni/Cu)(001) = 0 *a priori*.

We summarize all the above results on the surface magnetocrystalline energy and the surface magnetoelastic coupling coefficient of the Ni/Cu (001) interface in Table 8.1.

Cu/Ni/Cu (001) Sandwiches	B_1 (Ni) (erg/cm^3)	B^s (Ni/Cu)(001) (erg/cm^2)	K^s (Ni/Cu)(001) (erg/cm^2)
Our data $e_0(h) = \frac{\eta\, h_c}{h}$	6.2×10^7	- 67	+ 0.98
Our data $e_0(h) = \frac{0.1815}{h^{0.7}}$	6.2×10^7	- 52	+ 0.88
Data of Jungblut *et al.* [1994] $e_0(h) = \frac{\eta\, h_c}{h}$	6.2×10^7	- 37	+ 0.73
Results of Jungblut *et al.* [1994]	6.2×10^7	---	- 0.40

Table 8.1: Surface magnetoelastic coupling coefficient and surface magnetocrystalline anisotropy energy for the Ni/Cu (001) interface. In the first three rows we display the results obtained by applying the phenomenological model of Eq. (8.1) to our data and to the ones of Jungblut *et al.* [1994] on Cu/Ni/Cu (001) sandwiches. For our data, we have used both a 1/h and a $1/h^{0.7}$ Ni film thickness dependence of the strain. The results in the last row are the ones reported by Jungblut *et al.* using the model of Eqs. (6.3) and (6.4).

The first two rows show the results of the fits of our data using two different Ni thickness dependence of the misfit strain $e_0(h)$. The third row shows the results we obtain by fitting the data of Jungblut *et al.* [1994] using the phenomenological model of Eq. (8.2). The result in the last row of the table is the one reported by Jungblut *et al.* who set $B^s = 0$ *a priori* and used the phenomenological model of Eqs. (6.3) and (6.4) for $h \leq h_c$ and $h \geq h_c$, respectively. As explained more in detail in chapter 6, they also argued that $h_c \approx 40$ Å for the Cu/Ni/Cu (001) sandwiches. They obtained K^s(Ni/Cu)(001) ≈ - 0.40 erg/cm^2 which has the same order of magnitude but the opposite sign of the surface energies we report in Table 8.1. The surface magnetocrystalline anisotropy energies we found using the model of Eq. (8.1) are all positive indicating that K^s(Ni/Cu)(001) favors perpendicular magnetic anisotropy. The average value of the surface energies of the first three rows of Table 8.1

is $K^s(Ni/Cu)(001) \approx + 0.85$ erg/cm^2. On the other hand, all the surface magnetoelastic coupling coefficients of Table 8.1 are negative indicating that, contrary to the bulk magnetoelastic anisotropy energy $2B_1 e_0(h)$, the surface magnetoelastic anisotropy energy $2B^s e_0(h)/h$ favors an in-plane magnetization in Ni/Cu (001) where the misfit strain is tensile. The results summarized in Table 8.1 also indicate that the value of B^s obtained from the fit is sensitive to the measured K^{eff} data and to the thickness dependence of the strain in the Ni film. The average value is $B^s(Ni/Cu)(001) \approx - 50$ erg/cm^2 which is approximately 60 times larger than the absolute value of the average surface magnetocrystalline anisotropy energy $K^s(Ni/Cu)(001) \approx + 0.85$ erg/cm^2.

In chapter 7, we showed that from the pair-interaction model one expects that $B^s = - 6 K^s$ for any fcc (001) surface if we include only first nearest-neighbor interactions at the interfaces of the film:

$$K^s_{f/s\,(001)} = - \frac{d\left(L^{f\text{-}s} - L^{f\text{-}f}\right)}{2} \tag{8.7}$$

$$B^s_{f/s\,(001)} = 3d\left(L^{f\text{-}s} - L^{f\text{-}f}\right). \tag{8.8}$$

Our results disagree with this prediction which could mean that second nearest-neighbor interactions are necessary in order to explain our measurements. In fact, as shown in chapter 7, adding the contribution of the second-nearest neighbors in the computation of $E^{surface}$ and $E^{interface}$ yields:

$$K^s_{f/s\,(001)} = - d\left[\frac{L^{f\text{-}s}(r_1) - L^{f\text{-}f}(r_1)}{2} + L^{f\text{-}s}(r_2) - L^{f\text{-}f}(r_2)\right] \tag{8.9}$$

and $$B^s_{f/s\,(001)} = d\left[3\left(L^{f\text{-}s}(r_1) - L^{f\text{-}f}(r_1)\right) - r_2\left(\frac{dL^{f\text{-}s}}{dr}(r_2) - \frac{dL^{f\text{-}f}}{dr}(r_2)\right)\right], \tag{8.10}$$

r_1 and r_2 being the bulk unstrained first nearest-neighbor and second nearest-neighbor distances, respectively. Unfortunately, since we do not know the interaction energy $L^{Ni\text{-}Cu}(r)$ *a priori*, we are not able to quantitatively find the effects of second nearest-neighbor interactions on the surface energies. Equations (8.9) and (8.10) indicate that if the contribution of the second nearest-neighbors to the surface anisotropy energies is large enough, it can break the simple relationship $B^s_{f/s\,(001)} = - 6 K^s_{f/s\,(001)}$. The results of our fit however do indicate that $B^s(Ni/Cu)(001)$ and $K^s(Ni/Cu)(001)$ have opposite signs, in agreement with the predictions of the pair-interaction model. It is interesting to note that, according to our experimental results, $K^s(Ni/Cu)(001) \approx - e_0 B^s(Ni/Cu)(001)$ for a strain $e_0 = 2\%$ meaning that the surface magnetocrystalline and magnetoelastic anisotropy

energies have comparable strengths but opposite contributions to the perpendicular magnetic anisotropy. It is also interesting to note that large values of $B^s \approx 20$ erg/cm^2 have been reported by Song *et al.* [1994] for *polycrystalline* $Ni/SiO_2/Si$ thin films. Moreover, in section 8.3, we estimate $B^s \approx -24$ erg/cm^2 for the fcc Co/Cu (111) interface.

Using the average surface magnetoelastic coupling coefficient $B^s(Ni/Cu)(001) \approx -50$ erg/cm^2, we plot the effective magnetoelastic coupling coefficient $B^{eff} = B_1 + \frac{B^s}{h}$ in Cu/Ni/Cu (001) sandwiches in Fig. 8.3. The figure indicates that deviations from the bulk value B_1 occur for films as thick as 200 Å and that B^{eff} changes sign around 80 Å because $B^s < 0$ for the Ni/Cu (001) interface. This striking result implies that surface effects on magnetoelastic interactions are not limited to the atomic layer located near the film's interfaces but are dragged into the bulk of the film. Song *et al.* [1994] explained that such a phenomenon could occur through exchange coupling which is not considered by the pair-interaction model of chapter 7. As shown in Fig. 7.3, their measurements of B^{eff} in polycrystalline $Ni/SiO_2/Si$ indicate a departure from the bulk value for films as thick as 150 Å. Moreover, Weber *et al.* [1994] showed that the effective magnetoelastic coupling coefficient in Fe/glass thin films changes sign at a large film thickness between 30 Å and 80 Å.

Using the magnetic surface anisotropy energies corresponding to the Ni/Cu (001) interface, we can plot $K^{eff}(h)$ versus Ni film thickness using Eq. (8.2) where the $e_0(h) = \eta\, h_c/h$ is implicitly built into the equation. The result is shown in Fig. 8.4 together with our experimental data points. We used the surface energies B^s and K^s reported in the first row of Table 8.1. As in Fig. 8.1, the solid line gives a reasonable fit to the data points. But most importantly the solid curve intersects the $K^{eff} = 0$ axis at *two* thicknesses: $h_{low} \approx 30$ Å and $h_{high} \approx 140$ Å. At these thicknesses the magnetization easy-axis goes from in-plane to out-of-plane and vice-versa, respectively, as we increase the Ni film thickness. As explained in chapter 6 and as indicated by our data points, we did observe the transition near 140 Å. The lower thickness is predicted by the model and is a direct consequence of the fact that we have included a negative surface magnetoelastic coefficient. In fact, if we were to set $B^s = 0$, equation 8.2 would predict that a plot of $K^{eff} \cdot h$ versus h should be a straight line with a negative slope equal to $-2\pi M_s^2$ which can intersect the $K^{eff} = 0$ line at one thickness at the most. As explained in chapter 6, a double cross-over in the magnetization easy-axis also exists in Ni/Cu (001) thin films characterized under ultra-high vacuum by MOKE. In the latter case, $h_{low} \approx 10$ Å and $h_{high} \approx 60$ Å.

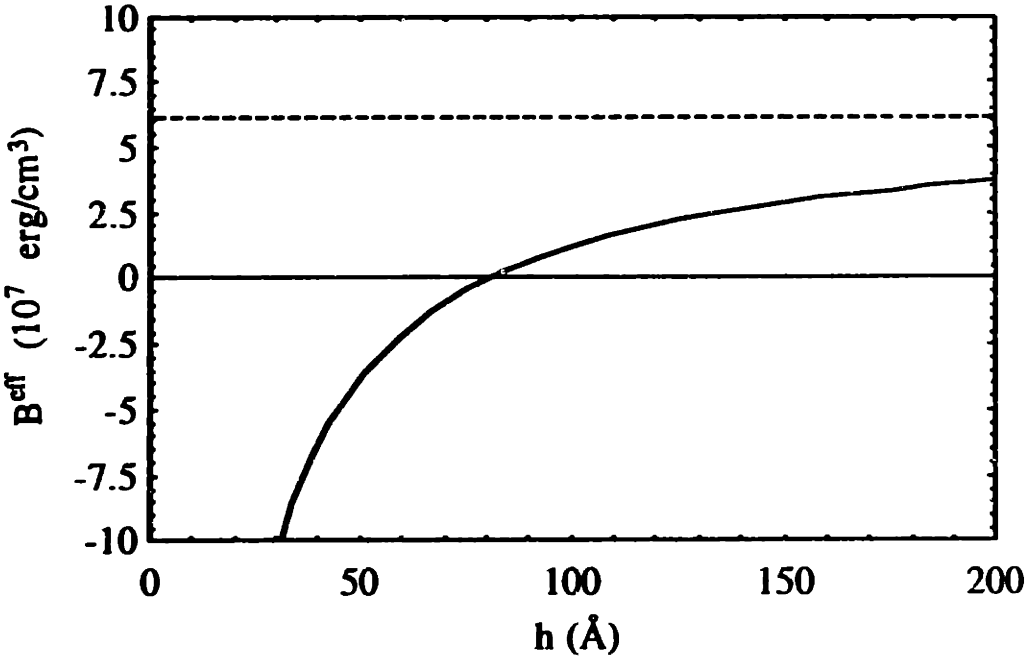

Figure 8.3: Dependence of the effective magnetoelastic coupling coefficient on Ni film thickness in Cu/Ni/Cu (001) sandwiches. We used the average value B^s(Ni/Cu)(001) = -50 erg/cm^2 obtained from the data in Table 8.1. The dashed line indicates the bulk value of the magnetoelastic coupling coefficient of Ni.

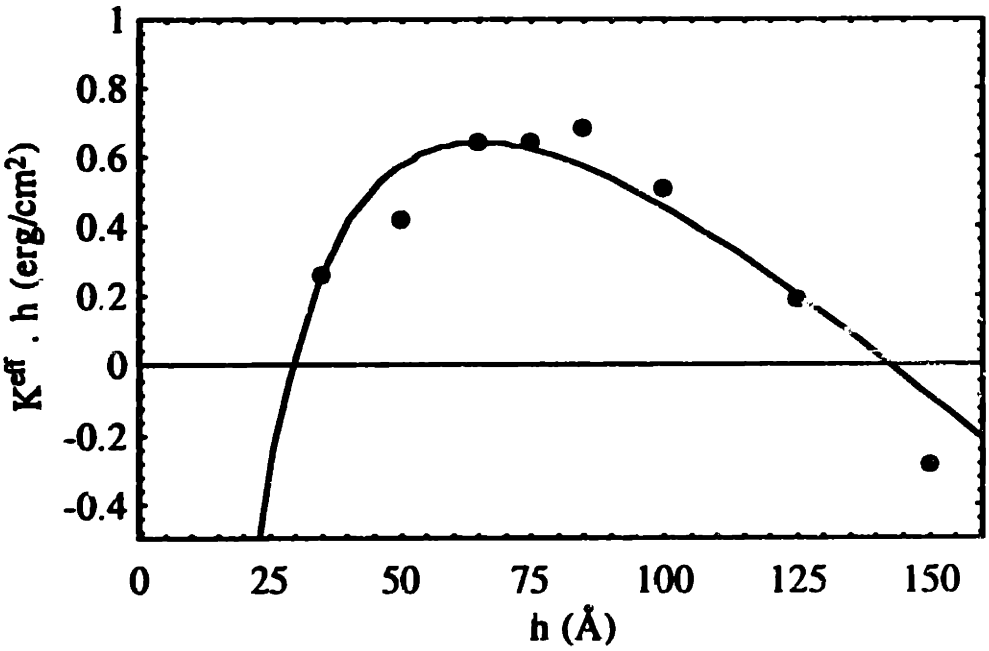

Figure 8.4: K^{eff} . h versus Ni film thickness for our Cu/Ni/Cu (001) sandwiches. The solid curve is a plot of $K^{eff}(h)$ of Eq. (8.2) using the magnetic surface anisotropy energies reported in the first row of Table 8.1.

In summary, the inclusion of the surface magnetoelastic anisotropy energy in the phenomenological model has significantly improved our quantitative understanding of the behavior of the effective magnetic anisotropy in Ni/Cu (001). We were able to estimate the magnetic surface anisotropy energies B^s(Ni/Cu)(001) ≈ - 50 erg/cm^2 and K^s(Ni/Cu)(001) ≈ + 0.85 erg/cm^2. This important result implies that the surface magnetocrystalline and magnetoelastic anisotropy energies have opposite contributions to the perpendicular magnetic anisotropy: K^s/h favors perpendicular magnetization whereas $B^s e_0(h)/h$ favors an in-plane magnetization easy-axis. The negative sign of B^s, which makes the effective magnetoelastic coupling coefficient change sign near 80 Å, provides a good explanation for the existence of two thicknesses where the magnetization easy-axis switches from perpendicular to the film to in-plane, a phenomenon which remained a puzzle in chapter 6. This shows the importance of B^s and of the strain in determining the total magnetic anisotropy in the Ni/Cu (001) epitaxial system. In the next section, we discuss more in detail the energy balance that determines the perpendicular magnetic anisotropy in Ni/Cu (001).

8.2. The Origin of Perpendicular Magnetic Anisotropy in Ni/Cu (001)

In chapter 2, we briefly explained that the origin of perpendicular magnetic anisotropy in Ni/Cu (001) can most probably be found in magnetoelastic interactions and in the magnetic surface anisotropy. Since then we have shown that the magnetic surface anisotropy can be further separated into the surface magnetocrystalline anisotropy energy $2K^s/h$ and the surface magnetoelastic anisotropy energy $2B^s e_0(h)/h$ and we have estimated the surface energies B^s and K^s corresponding to the Ni/Cu (001) interface. The surface magnetocrystalline anisotropy energy $2K^s/h$ is strong and favors perpendicular magnetization at all Ni thicknesses but its strength decreases as 1/h with increasing film thickness. However, magnetoelastic interactions in the Cu/Ni/Cu (001) sandwiches have two simultaneous but opposite contributions to the magnetic anisotropy at all film thicknesses. On one hand, the bulk magnetoelastic anisotropy energy $2B_1 e_0(h)$ is positive for all h and therefore favors perpendicular magnetization. Its strength roughly decreases as 1/h due to the strain $e_0(h)$. On the other hand, the surface magnetoelastic anisotropy energy $2B^s e_0(h)/h$ is negative and tends to keep the magnetization easy-axis in-plane. Its strength decreases roughly as $1/h^2$ since the strain $e_0(h)$ decreases approximately as 1/h. The energies $2K^s/h$, $2B_1 e_0(h)$, and $2\left(B_1 + \frac{B^s}{h}\right) e_0(h)$ are plotted as a function of h in Fig.

8.5 using $e_0(h) = \eta\, h_c/h$ (where η = 2.6% and h_c = 18 Å) and the average magnetic surface energies B^s(Ni/Cu)(001) ≈ - 50 erg/cm^2 and K^s(Ni/Cu)(001) ≈ + 0.85 erg/cm^2. The figure shows that the surface magnetocrystalline anisotropy dominates the perpendicular magnetic anisotropy. Although bulk magnetoelastic interactions give an important contribution to perpendicular magnetization, it seems that the effective magnetoelastic anisotropy energy, $2\left(B_1 + \frac{B^s}{h}\right)e_0(h)$, is weak above about 60 Å and goes negative below that thickness, thus tending to keep the magnetization in-plane at small Ni thicknesses.

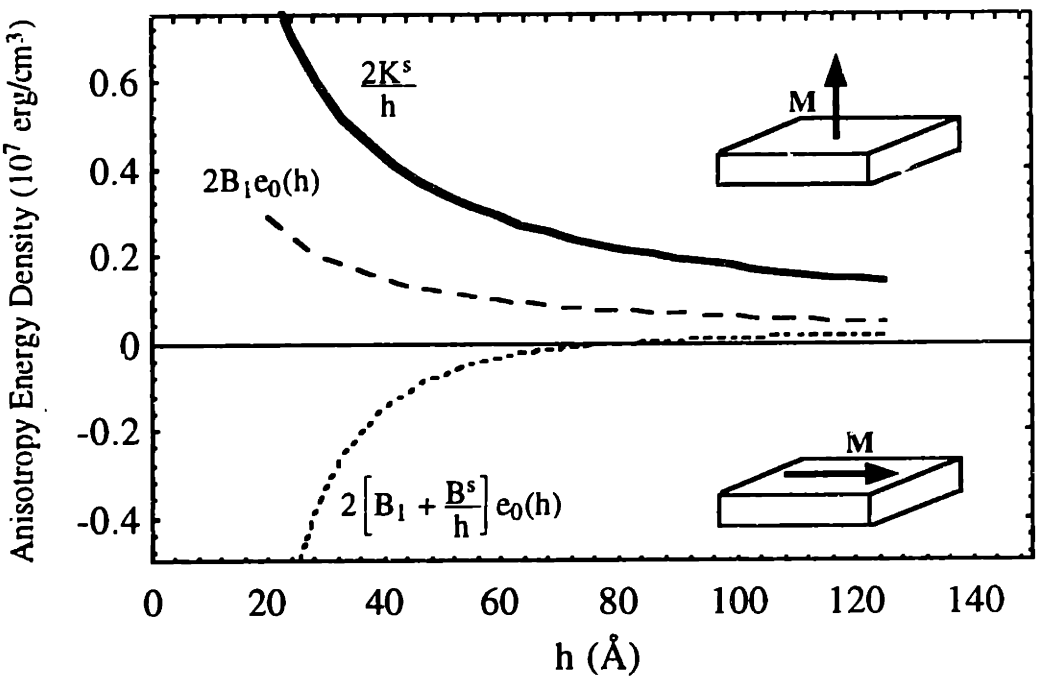

Figure 8.5: Dependence of three different magnetic anisotropy energies on film thickness in Cu/Ni/Cu (001).

It is important to emphasize that the strain $e_0(h)$ is an average in-plane biaxial tensile misfit strain and that the local strain e(x,y,z) due to the misfit dislocations alone, although very localized, is very large and compressive near the dislocations cores. The strain e(x,y,z) could pin the magnetization easy-axis at the dislocation cores through the local magnetoelastic anisotropy energy $B^s e(z = 0)$. This energy plus the exchange interaction could make the magnetization easy-axis uniform throughout the film if the film thickness and the dislocation spacing are small enough. This phenomenon is completely ignored by the pair-interaction model.

8.3. Magnetic Anisotropy in fcc Co/Cu (111) Superlattices

Lee *et al.* have grown a series of Co/Cu superlattices on GaAs (110) substrates by molecular beam epitaxy [Lee *et al.*, 1990; Lamelas *et al.*, 1989]. Their work is among the most complete and thorough in the literature on ultrathin films because it includes measurements of magnetic anisotropy energy density, strain and saturation magnetization as a function of Co film thickness. The Co thickness h was varied from 5 to 40 Å while the Cu thickness was fixed at 25 Å. The total superlattice thickness was 1500 Å in all the samples. Their measurements of the effective magnetic anisotropy energy, which were carried out using a superconducting quantum interference device (SQUID) magnetometer, indicated the magnetization easy-axis to be in the film plane at all thicknesses. They also measured the saturation magnetic moments in the various superlattices and showed that the average, 1241 emu/cm^3, is a good value for all thicknesses thus making $2\pi Ms^2 = 9.7 \times 10^6$ erg/cm^3. Their structural characterizations indicated that the Co layers grow in a (111) orientation with fcc stacking. Finally, they measured the strain in the Co layers as a function of Co thickness using X-ray diffraction and demonstrated that it can be well fit by the following equation:

$$e_0(h) = \eta \frac{h_{Cu}}{h + h_{Cu}} \tag{8.11}$$

where $h_{Cu} = 25$ Å and $\eta = 1.9\%$ is the fcc Co-Cu lattice mismatch.

Lee *et al.* [1990] found that an expression $K^{eff}(h)$ containing the bulk hcp Co magnetocrystalline energy, the bulk hcp Co magnetoelastic coupling coefficients and the measured value for $2\pi M_s^2$ does not fit their data of K^{eff} . h versus h for fcc Co/Cu (111) superlattices. They limited themselves to showing that they can fit their anisotropy data by arbitrarily reducing the magnetoelastic anisotropy energy to 82%, and the magnetocrystalline anisotropy energy to 20% of the values of bulk hcp Co in the expression of $K^{eff}(h)$. However, they attributed no physical significance to their fitting parameters and assumed *a priori* that the surface magnetocrystalline anisotropy energy of the Co/Cu (111) interface is nil. In contrast, we analyzed their data using a more general phenomenological model that includes a surface magnetocrystalline as well as a surface magnetoelastic anisotropy term, as shown below. When we fitted their data with this model, we obtained physically plausible and meaningful results which was possible only because they reported a careful measurement of the saturation magnetization and of the thickness dependence of the strain in their superlattices.

As shown by Table 2.1, the magnetocrystalline anisotropy energy of fcc Co is negligible compared to the other magnetic anisotropy energies at play; in particular K^{MC} (fcc Co) $\approx$ 0.1 K^{MS} (fcc Co). The dependence of the total effective magnetic anisotropy energy density on Co film thickness h can therefore be described by the phenomenological model of Eq. (7.19), where K^s and $B^s e_0(h)$ are the surface magnetocrystalline and surface magnetoelastic anisotropy energies of the fcc Co/Cu (111) interface, respectively. Substituting the strain of Eq. (8.11) into Eq. (7.19) yields:

$$K^{eff} = -2\pi M_s^2 + 2\eta\left(B_2 + \frac{B^s}{h}\right)\frac{h_{Cu}}{h + h_{Cu}} + 2\frac{K^s}{h} \qquad (8.12)$$

where B_2 is the bulk magnetoelastic coupling coefficient of fcc Co. Equation 8.12 can be written more conveniently as follows:

$$\left[K^{eff} + 2\pi M_s^2\right] . h . (h + h_{Cu}) = 2\left(K^s + \eta\, h_{Cu}\, B_2\right) . h + 2\, h_{Cu}\left(K^s + \eta\, B^s\right) \qquad (8.13)$$

By plotting $\left[K^{eff} + 2\pi M_s^2\right] . h . (h + h_{Cu})$ versus h and fitting the points with a straight line we could therefore determine K^s(Co/Cu) (111) and B^s(Co/Cu) (111) knowing B_2 of fcc Co. We emphasize the fact that although it may be possible to fit the magnetic anisotropy data by omitting the B^s/h term, as one can see from Eq. (8.13), the physical significance of the magnetic surface anisotropy energy that one would extract from such a fit may remain questionable. Figure 8.6 shows the plot of $\left[K^{eff} + 2\pi M_s^2\right] . h . (h + h_{Cu})$ versus h for the data of Lee *et al.* [1990]. The straight line represents the fit to data points using the model of Eq. (8.13). We used the measured value $2\pi Ms^2 = 9.7 \times 10^6$ erg/cm^3 in obtaining Fig. 8.6. The equation of the straight line is given by:

$$\left[K^{eff} + 2\pi M_s^2\right] . h . (h + h_{Cu}) = 0.3406\, h + 0.1152 \text{ , in } 10^{-7} \text{ erg/cm} \qquad (8.14)$$

where h is in Å on the right-hand side of the equation. Fujiwara *et al.* [1983] extrapolated, from their data on fcc Co-Pd alloys, that for fcc Co $\lambda_{111} = -6.7 \times 10^{-5} = -\frac{1}{3}\frac{B_2}{c_{44}}$ at T = 0 K. Taking c_{44} (fcc Co) = 1.28×10^{12} erg/cm^3 [Landolt-Börnstein, 1984], one can extrapolate $B_2 = 2.6 \times 10^8$ erg/cm^3 for fcc Co. This value is the best experimental value available for the bulk magnetoelastic coupling coefficient of fcc Co [Chuang *et al.*, 1994]. Comparing Eqs. (8.13) and (8.14), we obtain: K^s(Co/Cu) (111) $\approx$ + 0.47 erg/cm^2 and B^s(Co/Cu) (111) $\approx$ - 24 erg/cm^2 which indicates that $B^s e_0 \approx -K^s$ for the fcc Co/Cu (111) interface using a strain e_0 = + 2%. This result is very interesting because it means that the surface magnetoelastic anisotropy energy is comparable in strength to surface magnetocrystalline anisotropy energy for the fcc Co/Cu (111) interface. It also implies

that $B^s e_0$ and K^s have opposite contributions to the total magnetic anisotropy energy in fcc Co/Cu (111): $B^s e_0$ favors an in-plane magnetization whereas K^s favors perpendicular magnetic anisotropy. The magnetic anisotropy energies characteristic of the fcc Co/Cu (111) epitaxial system are summarized in Table 8.2.

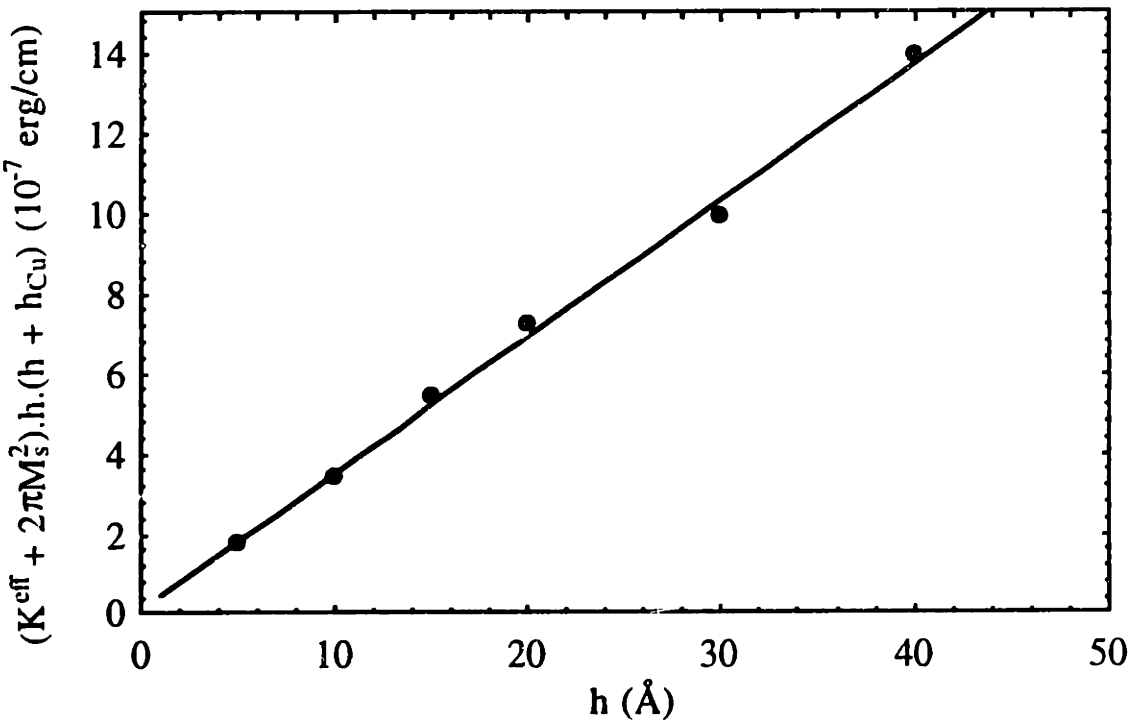

Figure 8.6: $\left[K^{eff} + 2\pi M_s^2\right] . h . (h + h_{Cu})$ as a function of Co film thickness in fcc Co/Cu (111) superlattices [Bochi *et al.*, 1994]. The data points were obtained from Lee *et al.* [1990]. The straight line represents the fit to the data points using Eq. (8.13).

	B_2 (erg/cm^3)	B^s (erg/cm^2)	K^s (erg/cm^2)
fcc Co/Cu (111)	2.6×10^8	- 24	+ 0.47

Table 8.2: Magnetic anisotropy energies characteristic of the fcc Co/Cu (111) epitaxial system. K^s and B^s are the results of the fit of Fig. 8.6.

Using the above estimate of B^s(Co/Cu) (111), we plot the dependence on Co film thickness of the effective magnetoelastic coupling coefficient of Co in fcc Co/Cu (111) superlattices in Fig. 8.7. The plot indicates that B^{eff} decreases below 100 Å due to surface effects and becomes negative for $h \leq 9$ Å. This result therefore questions the assumption, often encountered in the literature, that bulk Co magnetoelastic coupling coefficients also apply for ultrathin Co films. The estimate B^s(Co/Cu) (111) = - 24 erg/cm^2 for fcc Co might seem large at first sight. However, the surface magnetoelastic coupling coefficient was recently measured in polycrystalline Ni/SiO_2/Si thin films by a direct method [Song *et al.*, 1994] and was found to be approximately + 20 erg/cm^2. Therefore, unlike magnetic surface anisotropy energy densities which are of the order of 1 erg/cm^2, surface magnetoelastic coupling coefficients B^s can be an order of magnitude greater and may strongly affect the value or even the sign of the effective magnetoelastic coupling coefficient, as shown in Fig. 8.7.

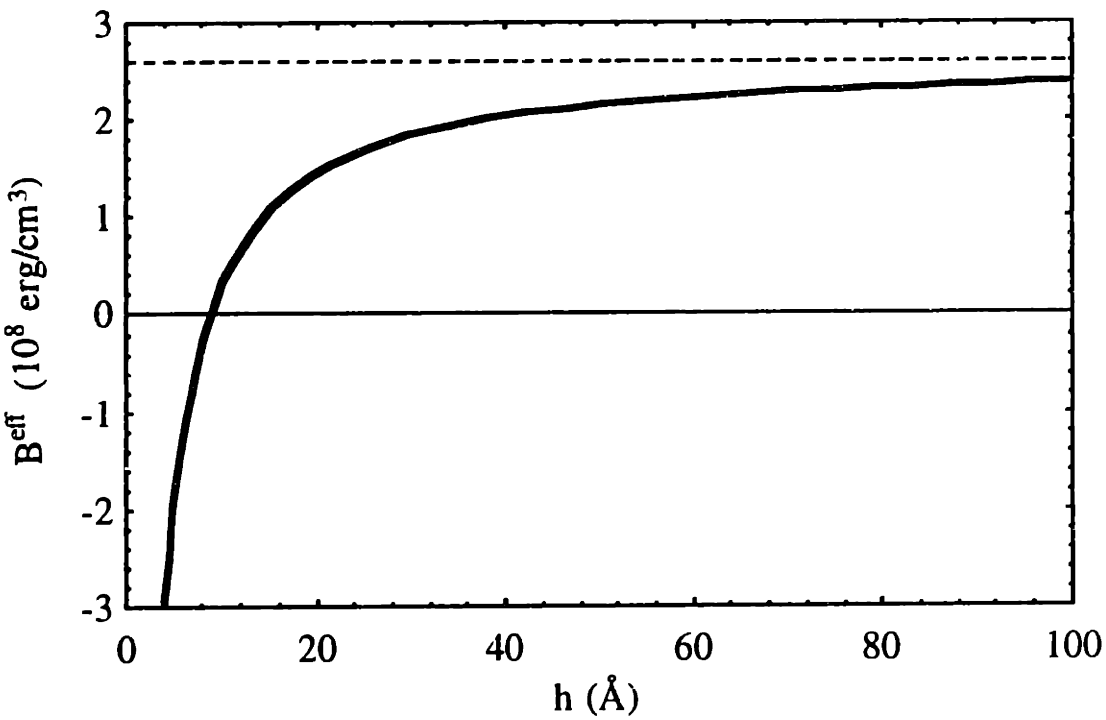

Figure 8.7: Effective magnetoelastic coupling coefficient $B^{eff} = B_2 + \frac{B^s}{h}$ as a function of Co film thickness in fcc Co/Cu (111) superlattices [Bochi *et al.*, 1994]. The dashed line indicates the bulk magnetoelastic coupling coefficient of fcc Co.

Chapter 9
Conclusions

This thesis has described our studies of the magnetic anisotropy in Ni/Cu/Si (001) films, $Ni/Cu_{1-x}Ni_x/Cu/Si$ (001) films ($0 < x < 50\%$), and Cu/Ni/Cu/Si (001) sandwiches under ultra-high vacuum conditions using the magneto-optic Kerr effect (MOKE) and in air using a vibrating sample magnetometer (VSM). The Ni thickness ranged between 10 Å and 150 Å whereas the Cu substrates were 2000 Å to 3000 Å thick. The films were deposited at room temperature using a molecular beam epitaxy (MBE) system and were characterized *in-situ* using Auger electron spectroscopy and RHEED and *ex-situ* using plan-view as well as cross-sectional TEM and X-ray diffraction. The average in-plane biaxial tensile strain in the Ni films was measured *ex-situ* using an optical interferometry technique. The following is a summary of our main results:

• The Ni and Cu thin films grow epitaxially with a (001) orientation on hydrogen terminated Si (001) wafers.

• The most stable growth of Cu/Si (001) occurs with the [100] axis of Cu parallel to the [110] axis of Si.

• The Ni films are continuous but rough. Cross-sectional TEM showed that the Ni surface roughness is of the order of ± 20 Å extending over a wavelength of 400 Å in the film plane.

• TEM micrographs also revealed the presence of a 70 Å thick polycrystalline copper-silicide layer at the Cu-Si interface. The Cu layer lying above the silicide remains single-

crystal. This suggests that the silicide layer forms slowly at room temperature after the epitaxial relationship between the Cu and the Si has been established.

• Ultrathin Ni films grow pseudomorphically on the thick Cu substrates with an in-plane biaxial tensile misfit strain equal to the Ni-Cu lattice mismatch $\eta = 2.6\%$. Above the critical thickness h_c, misfit dislocations form at the Ni-Cu interface to partially relieve the strain in the Ni films. Plan-view TEM micrographs showed that 15 Å $< h_c <$ 25 Å in Ni/Cu (001), in close agreement with the prediction $h_c = 18$ Å of the Matthews-Blakeslee thermodynamic model.

• The experimentally observed misfit dislocations are of the 60° and the 90° type and run along the <110> directions at the Ni-Cu interface thus forming a square grid.

• For $h > h_c$, the dislocation density increases with h. This decreases the average in-plane biaxial tensile misfit strain $e_0(h)$ in the Ni roughly as the $\eta h_c/h$ functional dependence predicted by the Matthews-Blakeslee model. Inglefield *et al.* [1995] showed experimentally that the strain in the Ni decreases with film thickness approximately as $1/h^{0.7}$.

• We emphasize that $e_0(h)$ is an *average* in-plane biaxial tensile misfit strain and that the local strain e(x,y,z) due to the misfit dislocations alone, although very localized, is very large and compressive near the dislocation cores.

• We have discovered that the Ni/Cu (001) epitaxial system exhibits the largest thickness range of perpendicular magnetization of any epitaxial thin film system reported so far.

• When the films are kept under ultra-high vacuum, the perpendicular magnetic anisotropy energy dominates the total magnetic anisotropy energy from $h \approx 10$ Å to $h \approx 60$ Å in Ni/Cu/Si (001) (in similar epitaxial systems, such as Fe/Cu (001), the perpendicular magnetic anisotropy dominates the total magnetic anisotropy only up to a film thickness of approximately 11 Å. This is because the magnetostatic anisotropy energy $2\pi M_s^2$, which is much larger in Fe than in Ni, tends to keep the magnetization in-plane in thin films).

• The perpendicular magnetic anisotropy energy dominates the total magnetic anisotropy energy from $h \approx 15$ Å to $h \approx 40$ Å in Ni/$Cu_{60}Ni_{40}$/Cu/Si (001) thin films characterized in ultra-high vacuum. We attribute the difference in the extent of the perpendicular region between Ni/Cu (001) and Ni/$Cu_{60}Ni_{40}$ (001) to the smaller tensile misfit strain and to the

smaller positive film-substrate surface magnetocrystalline anisotropy energy in $Ni/Cu_{60}Ni_{40}$ (001).

• The region of perpendicular magnetization extends up to approximately 125 Å when the Ni/Cu (001) films are exposed to air or capped with a 20 Å thick Cu layer.

• The in-plane to out-of-plane transition in the magnetization easy-axis occurring in Ni/Cu (001) at h ≈ 10 Å is most likely not due to the onset of misfit dislocations at the Ni-Cu interface. In fact, in $Ni/Cu_{60}Ni_{40}$ (001), the onset of misfit dislocations occurs at h ≥ 35 Å yet 25 Å thick films have a perpendicular magnetization easy-axis.

• We have measured the effective magnetic anisotropy energy density K^{eff} as a function of Ni film thickness in Cu/Ni/Cu/Si (001) sandwiches. We have carried out the most thorough analysis yet reported for the measured $K^{eff}(h)$ versus h by using our own measurements of the strain and a more complete phenomenological model which includes strain-dependent pair interactions in the computation of the magnetic surface anisotropy energy. We have also extended this calculation to include the effects of second nearest-neighbor interactions at the film's interfaces.

• In our phenomenological model for fcc (001) ferromagnetic films sandwiched between two identical non-magnetic layers, $K^{eff}(n)$ can be written as follows:

$$K^{eff}_{fcc\,(001)} = -2\pi M_s^2 + 2\left(B_1 + \frac{B^s}{h}\right)e_0(h) + \frac{2K^s}{h}. \qquad (9.1)$$

The magnetic surface anisotropy energy has two components: the surface magnetocrystalline anisotropy energy $2K^s/h$ and the surface magnetoelastic anisotropy energy $2B^s e_0(h)/h$. Equation 9.1 also includes the bulk magnetoelastic anisotropy energy $2B^{bulk}e_0(h)$ which favors perpendicular magnetic anisotropy in Ni/Cu (001), and the bulk magnetostatic anisotropy energy $2\pi M_s^2$ which tends to keep the magnetization in-plane. The bulk magnetocrystalline anisotropy energy K_1 is relatively negligible in Ni films thinner than 100 Å and has therefore been omitted.

• Our quantitative analysis yielded $K^s(Ni/Cu)\ (001) \approx +0.85\ erg/cm^2$. The large and positive surface magnetocrystalline anisotropy energy $2K^s/h$ and the positive bulk magnetoelastic anisotropy energy $2B_1e_0(h)$ are the origin of the strong perpendicular magnetic anisotropy in Ni/Cu (001).

• The analysis also showed that the inclusion of a surface magnetoelastic coupling coefficient B^s, often omitted in phenomenological models, is necessary in order to explain our data. We have estimated that B^s(Ni/Cu) (001) ≈ - 50 erg/cm^2.

• The negative surface magnetoelastic anisotropy energy $2B^s e_0(h)/h$ favors an in-plane magnetization easy-axis in Ni/Cu (001). For h ≤ 25 Å, this energy dominates the positive strain-independent magnetic surface anisotropy energy $2K^s/h$ and the positive bulk magnetoelastic anisotropy energy $2B^{bulk}e_0(h)$, thus forcing the magnetization in-plane. This provides an explanation for the existence of the lower (h ≈ 10 Å) in-plane to out-of-plane magnetization easy-axis switching thickness in Ni/Cu (001).

• The negative sign and the magnitude of B^s imply that the effective magnetoelastic coupling coefficient $B^{eff} = B_1 + \frac{B^s}{h}$ depends strongly on the Ni film thickness in Ni/Cu (001) films thinner than 200 Å and that it changes sign near h = 80 Å.

• K^s(Ni/Cu) (001) and B^s(Ni/Cu) (001) have opposite signs, in agreement with the predictions of the strain-dependent Néel first nearest-neighbor pair-interaction model.

• Our measured B^s is larger compared to K^s than predicted by the first nearest-neighbor pair-interaction model. For fcc (001) surfaces, the first nearest-neighbor model predicts $B^s = - 6 K^s$. Inclusion of the second nearest-neighbors in the computation of the magnetic surface anisotropy energy breaks this simple relation and may explain the large value we observe for B^s.

• By fitting $K^{eff}(h)$ data with the Néel model one generally obtains larger than expected magnetic surface anisotropy energies. We believe that this discrepancy reflects the fact that surface magnetoelastic and surface magnetocrystalline effects are not limited to the first few atomic layers located next to the film's interfaces but are dragged well into the bulk of the film through the exchange interaction, a mechanism which is not considered by the Néel model and which has received inadequate attention in the literature.

• The local strain e(x,y,z) due to the misfit dislocations alone, although very localized, is very large and compressive near the dislocations cores. The strain e(x,y,z) could pin the magnetization easy-axis at the dislocation cores through the local magnetoelastic anisotropy energy $B^s e(z = 0)$ which in general will differ from the bulk and average surface magnetoelastic energies. This energy plus exchange could therefore make the magnetization easy-axis nearly uniform throughout the film if the film thickness and the dislocation spacing are small enough. This effect is also ignored by the Néel model.

• Our preliminary calculations on ultrathin Ni-Cu bicrystals show that semi-empirical computations of the strain relaxation at the Ni-Cu interface are feasible using the embedded-atom potential method. However, long and complex computations may be necessary to achieve accurate and practical results.

In summary, we have studied the epitaxial Ni/Cu/Si (001), Ni/$Cu_{60}Ni_{40}$/Cu/Si (001), and Cu/Ni/Cu/Si (001) systems over thickness ranges and using techniques not heretofore used in combination. New and important results have emerged from these studies. In order to interpret our new data, we have had to carry the analysis of these results to a higher level of completeness and have arrived to new frontiers. As we show in the next section, more experiments can be performed in order to improve our understanding of the complex behavior of the magnetic anisotropy in Ni/Cu (001).

The above unique results on Ni/Cu (001) not only have deepened our understanding of the fundamentals of magnetic anisotropy in thin films but they also have potential applications in the magnetic recording industry and some general implications on the design of advanced magnetic devices. The strong perpendicular magnetic anisotropy over an exceptionally broad Ni thickness range in Cu/Ni/Cu (001) sandwiches make this epitaxial system a candidate for magneto-optical (MO) recording. Although it still requires further development, the high density MO recording technology has attained practical use [Hashimoto *et al.*, 1990; Zeper *et al.*, 1991]. A good MO recording medium has the following properties: strong perpendicular magnetic anisotropy; square perpendicular M-H loops with a relatively large (≈ 1000 Oe) coercive field; large polar Kerr rotation in the visible electromagnetic spectrum; thermal stability; and corrosion resistance. Two systems are currently being investigated for use as MO storage media: amorphous rare-earth transition-metal films such as Gd-Tb-Fe and Tb-Fe-Co; and ultrathin Co/Pt and Co/Pd multilayered films.

The rare-earth transition-metal systems are easily oxidized due to the rare-earth elements, and so some protective layer as well as the addition of another element such as Cr, Ti, or Pt is needed for corrosion resistance. The addition of the other elements degrades the MO properties and the protective layer requires additional processing steps during manufacturing. Nevertheless, Tb-Fe-Co MO disks are being made by companies such as 3M. Although Co/Pt and Co/Pd media were shown to have high corrosion resistance, large Kerr rotations, and square polar loops with appropriate coercive fields, they are difficult, slow, and expensive to manufacture. In fact, since Co/Pt and Co/Pd thin films exhibit perpendicular magnetization over a small Co thickness range (see

chapter 3), they are usually multilayered in order to obtain MO media with a large signal-to-noise ratio and a high density. In these multilayers, which are deposited by MBE, the thicknesses of the Co film (typically a few Angstroms thick) and the non-magnetic spacer layer (typically 10 Å thick) as well as the roughness of the layers need to be controlled with a high degree of accuracy thus making the manufacture of Co/Pt and Co/Pd based MO media still challenging.

The Cu/Ni/Cu/Si sandwiches, on the other hand, are much easier to fabricate. Although MBE is preferred for the deposition of these structures, only three relatively thick epitaxial layers are involved in the fabrication process. It is not known whether sputtered or electrodeposited Cu/Ni/Cu sandwiches would also exhibit perpendicular magnetization up to 100 Å. Our studies showed that a 2000 Å thick Cu substrate layer is appropriate. The Ni thickness must be between 85 Å and 100 Å: in this thickness range the sandwiches have a strong perpendicular magnetic anisotropy and square perpendicular M-H loops. The capping layer must be chosen in such a way as to strengthen the perpendicular magnetic anisotropy, enhance the Kerr rotation, protect the Ni films from oxidation, and increase the coercive field (which was only about 250 Oe in our Cu/Ni/Cu (001) sandwiches). Our results clearly showed that a 20 Å thick Cu capping layer strongly enhances the perpendicular magnetic anisotropy in Ni/Cu (001). However, we propose to try other capping layers such as Ag, Au, Pd and Pt since they oxidize less easily than Cu. Pt and Pd are particularly attractive since they tend to get polarized by adjacent ferromagnetic layers (in our case Ni) thus enhancing the Kerr rotation of the epitaxial structure (as was shown in Co/Pt and Co/Pd multilayers [Zeper *et al.*, 1991]). In order to increase the Kerr rotation, we also propose to alloy the Ni film with other elements such as Co or Fe.

Our results on the magnetic anisotropy and magnetoelastic interactions in Ni/Cu (001) thin films also have more general implications on the design of magnetic recording heads and media which are currently dominated by thin films. The thickness of these films is typically 4 microns for inductive heads, a few tenths of a micron for thin film media, and about 400 Å for magnetoresistive heads [O'Handley and Song, 1993]. In the near future, magnetic films thinner than 100 Å are expected to be used in recording heads (in particular, spin-valves and giant magnetoresistance heads). In the present thesis, we showed that magnetoelastic interactions in the above thickness regime are sharply different from those of the bulk due to surface effects. These interface effects can significantly alter and even dominate the behavior of the magnetic anisotropy in a way which is not known *a priori* but they are larger the larger the stresses imposed on the

films. Thin films in magnetic devices are subject to large stresses from a variety of sources including epitaxial misfit, surface oxidation, entrapped sputtering gas, and, perhaps most importantly, thermal expansion difference between the film and the coating layers [O'Handley and Song, 1993]. Further, these stresses are often concentrated at surfaces and interfaces where B^{eff} is greatest. Hence, pinning of the surface magnetization may result if stress or strain or B^{eff} is not controlled carefully. For example, magnetoresistive heads are sandwiched by SiO_2 layers whose thermal expansion coefficient is much smaller than that of permalloy or other magnetic metals. The small thickness of the magnetic layers and their mechanical softness generally makes them the victims of large thermal-expansion-induced strains. The next generation of thin film magnetoelastic sensors will be particularly affected by the above giant magnetoelastic effects since the size of these devices is becoming smaller and smaller. Efficient design will be achieved only if the appropriate surface magnetoelastic coupling coefficients and strains are known *a priori*, and are taken into account in the phenomenological equations with the appropriate reduced symmetry [O'Handley *et al.*, 1993; Chuang *et al.*, 1994; Bochi *et al.*, 1994].

Chapter 10
Suggested Future Work

In the previous chapters, we demonstrated that we have achieved a good understanding of the behavior of the magnetic anisotropy in the Ni/Cu/Si (001), $Ni/Cu_{60}Ni_{40}/Cu/Si$ (001), and Cu/Ni/Cu/Si (001) epitaxial structures. This was possible only because we have performed a thorough analysis of the quantitative measurements of the thickness dependence of the effective magnetic anisotropy energy and of the strain using a complete phenomenological model. In this chapter, we propose three specific experiments that can further expand our understanding of the complex behavior of the magnetic anisotropy and its relation to misfit strain in epitaxial Ni/Cu (001) thin films. In addition, we list several other areas where further work would be fruitful.

• Ni/Cu/Ni/Cu/Si (001) Multilayers

The first experiment consists in measuring the thickness dependence of the effective magnetic anisotropy energy, the saturation magnetization, the magnetostriction, and the strain in Ni/Cu/Ni/Cu/Si (001) multilayers using VSM and high resolution X-ray diffraction. Multilayers have two valuable advantages over thin film and sandwich structures. First, the multilayers would contain not one but several Ni thin films of the same thickness separated by Cu spacing layers of equal thickness. This should allow us to obtain *ex-situ* VSM measurements of the thickness dependence of the effective magnetic anisotropy energy K^{eff} and of the saturation magnetization M_s which are significantly more accurate than the ones obtained with Cu/Ni/Cu sandwiches, thanks to an improved signal-to-noise ratio. We should also be able to measure $K^{eff}(h)$ and $M_s(h)$ in Ni films thinner than 35 Å and possibly thinner than the critical thickness for the onset

of misfit dislocations ($h_c \approx 18$ Å in Ni/Cu (001)) using multilayers. The latter measurements, which were impossible to perform in our Cu/Ni/Cu (001) sandwiches, are very important because, as we will show below, they can allow us to investigate whether or not the magnetic surface anisotropy energies K^s and B^s corresponding to the Ni/Cu (001) interface are the same below and above the onset of misfit dislocations. As explained in chapter 6, the Curie temperature of 9 Å thick Ni/Cu (001) films is approximately 300 K so that Ni films thinner than 9 Å are non-magnetic at room temperature. This difficulty can also be overcome in the VSM since measurements of the magnetization's behavior can be performed at temperatures as low as 77 K in our DMS Magnetometer.

The second major advantage of multilayers is that we can obtain direct and accurate measurements of the thickness dependence of the strain in the Ni thin films using high-resolution X-ray diffraction, if the thickness of the Ni films is comparable to the thickness of the Cu spacing layers. X-ray diffraction patterns would yield the average interplanar atomic spacing in the Ni and Cu layers which can be easily translated into average in-plane strain by comparing the average in-plane lattice parameter of the layers with the bulk equilibrium lattice parameters of Ni and Cu. Unfortunately, we were not able to take advantage of X-rays for strain measurements in our Ni/Cu/Si (001) thin films because the Cu substrates were at least ten times thicker than the adjacent Ni films and because the (002) diffraction peaks of Ni and Cu are extremely close to each other. As mentioned in chapter 4, the strain in Ni/Cu (001) thin films has already been measured using several techniques but they all were based on indirect probes. On the other hand, we also realize that studying strain relaxation in Ni/Cu (001) multilayers using X-rays is not a trivial experiment since it requires an involved analysis of complex diffraction patterns as well as the use of unique and not-easily accessible experimental set-ups such as synchrotron sources or X-ray absorption fine structure diffractometers (EXAFS). However, when combined with measurements of $K^{eff}(h)$, X-ray measurements of strain have proved to be extremely useful in understanding the quantitative behavior of magnetic anisotropy in superlattices [Lee *et al.*, 1990; Engel *et al.*, 1991].

The only disadvantage of multilayers is that they require very careful preparation and therefore very accurate control of the growth parameters such as the deposition rates of Ni and Cu and the substrate temperature. Many depositions may be necessary before one can achieve nearly-ideal Ni/Cu (001) superlattices with smooth interfaces, negligible interdiffusion, and negligible Cu surface segregation during growth. *In-situ* characterization using RHEED and *ex-situ* characterization using cross-sectional TEM

following every deposition are highly recommended. In order to avoid any potential surface segregation of the Cu during evaporation and to control the smoothness of the interfaces, one could grow the multilayers at very low temperatures (such as T = 100 K), as explained in chapter 5. The superlattices may then need to be annealed following the evaporation in order to smooth out the rough interfaces that may form as a result of the low temperature growth.

The Cu substrate/buffer layer deposited directly on the Si (001) wafers has to be thin enough so that it does not interfere with the X-ray measurements but it also has to be thick enough in order to prevent the copper-silicide layer forming at the Cu-Si interface from reaching the Ni/Cu multilayer, and in order to ensure that the multilayer grows epitaxially with a (001) orientation. Chang [J. Vac. Sci. Technol., 1990] showed that 1000 Å thick Ni films can be grown epitaxially by evaporation on Cu/Si (001) substrates where the Cu is as thin as 50 Å. Naik *et al.* [1993] have used 500 Å thick Cu substrates in their epitaxial Cu/Ni/Cu/Si (001) sandwiches. We therefore propose to use a Cu substrate layer with a thickness ranging between 250 Å and 500 Å for the Ni/Cu (001) multilayers. The Ni film thickness would have to range between 10 Å and 200 Å whereas the Cu spacer layer thickness would have to be the same in all the superlattices. A thickness of 50 Å for the Cu seems reasonable but thinner and thicker layers also may be worth trying in order to improve the growth of the multilayers. In order to achieve a good signal-to-noise ratio in the measurements of the M-H loops and of the strain, we propose to grow at least ten successive Ni-Cu bilayers on top of the Cu substrate/buffer layer.

Following the MBE growth, the multilayers would be brought up to air and K^{eff} and M_s would be measured as a function of Ni thickness with a VSM. For $h > h_c$, we would plot $\left[K^{eff} + 2\pi M_s^2\right] . h$ versus h and fit the data with the phenomenological model of Eq. (8.1) using the strain $e_0(h)$ measured with X-ray diffraction. Such a fit should allow us to obtain more accurate values for K^s and B^s corresponding to the Ni/Cu (001) interface than the ones we measured in chapter 8. For $h < h_c$, the Ni films are pseudomorphic with the Cu substrates which means that the average in-plane biaxial tensile strain in the Ni is thickness independent and equal to the Ni-Cu lattice mismatch: $e_0(h) = \eta$. Substituting this strain in Eq. (8.1) yields:

$$\left[K^{eff} + 2\pi M_s^2\right] . h = 2B_1\eta . h + 2\left(K^s + \eta B^s\right) \qquad (10.1)$$

We therefore expect that a plot of $\left[K^{eff} + 2\pi M_s^2\right] . h$ versus h in this thickness regime to be a straight line with the known slope $2B_1\eta$ and the intercept $2\left(K^s + \eta B^s\right)$. By comparing $\left[2(K^s + \eta B^s)\right]_{h < h_c}$ and $\left[2(K^s + \eta B^s)\right]_{h > h_c}$, we can conclude whether or not the same magnetic surface anisotropy energies apply to the Ni/Cu (001) films below and above the critical thickness for the onset of misfit dislocations.

Finally, we propose to measure the effective magnetoelastic coupling coefficient B^{eff} in the Ni/Cu (001) multilayers using a direct method [O'Handley *et al.*, 1993; Song *et al.*, 1994; Weber *et al.*, 1994] and to compare it to the value obtained from fitting the $K^{eff}(h)$ data with the phenomenological model of chapter 8. Very recently, two methods have been proposed and applied successfully to measure B^{eff} in polycrystalline Ni, NiFe, and Fe thin films. Song *et al.* [1994] showed that they can measure B^{eff} directly in thin films kept under ultra-high vacuum by applying an external stress to the films and monitoring the change in their magnetic anisotropy. Weber *et al.* [1994] showed that they can measure the saturation magnetostriction (which is inversely proportional to the negative of the magnetoelastic coupling coefficient [Chikazumi, 1964]) in ultrathin films under ultra-high vacuum conditions. Their method is based on a cantilever beam technique in which the displacements of the free end of a cantilever beam substrate can be accurately detected upon applying an external magnetic field on the thin film. Both of these methods show that $B^{eff} = B^{bulk} + \frac{B^{surface}}{h}$ in magnetic thin films.

• *In-situ* Quantitative Measurements of Magnetic Anisotropy in Ni/Cu/Si

The second experiment that we propose consists in measuring quantitatively the effective magnetic anisotropy energy as a function of the Ni film thickness in Ni/2000 Å Cu/Si (001) thin films using MOKE while the films are kept under ultra-high vacuum. The experimental set-up required for this experiment has been described in detail in chapter 5. However, that set-up needs to be modified so that magnetic fields as large as 10 kOe can be applied both in-plane and perpendicular to films in order to saturate the samples in both directions. We also propose that these experiments be carried out at temperatures as low as T = 100 K in order to improve the signal-to-noise ratio in the magnetic measurements. By plotting $\left[K^{eff} + 2\pi M_s^2\right] . h$ versus h and fitting the data with phenomenological model of chapter 8, we can determine K^s and B^s corresponding to the combination of the Ni/vacuum (001) and Ni/Cu (001) interfaces. In this analysis, we can make use of the measurements of $M_s(h)$ obtained in the previous experiment. Using the

known surface magnetocrystalline and magnetoelastic anisotropy energies of the Ni/Cu (001) interface, we can then extract K^s and B^s corresponding to the Ni/vacuum (001) interface alone and compare them to the theoretical predictions $K^s_{Ni/vac\ (001)} = + 0.09$ erg/cm^2 and $B^s_{Ni/vac\ (001)} = - 0.51$ erg/cm^2 (at room temperature) of the first nearest-neighbor pair-interaction model. The experimental values of K^s and B^s for both the Ni/vacuum (001) and Ni/Cu (001) interfaces will help us understand on a quantitative basis why the region of perpendicular magnetization extends to higher thicknesses in Cu/Ni/Cu (001) sandwiches than in Ni/Cu (001) films. As explained in chapter 8, we suspect that the difference in these two epitaxial systems is due to the fact that K^s(Ni/vacuum)(001) is positive but significantly smaller than K^s(Ni/Cu)(001).

• Magnetic Domain Observations in Ultrathin Films

In the third experiment, we propose to study the domain wall structure and the behavior of the magnetization easy-axis on a microscopic scale in Ni/Cu (001) thin films using magnetic probes such as a scanning electron microscope with polarization analysis (SEMPA) or a magnetic force microscope (MFM). SEMPA consists of a scanning electron microscope which is modified to detect the local behavior of the magnetization by counting the spin asymmetry of the secondary electrons emitted from a ferromagnetic sample. It has an in-plane resolution of approximately 100 Å to 300 Å. The measurements are conducted while the sample is kept under ultra-high vacuum conditions. The strength of SEMPA has been shown by Oepen and Kirschner [1989] who demonstrated that one can resolve the rotation of the magnetization inside domain walls in Fe crystals using this instrument. Using SEMPA, Allenspach [1994] showed recently that, contrary to expectations, ultrathin films with perpendicular magnetization are not necessarily in a single domain configuration but can have anomalous domain wall structures. A SEMPA microscope is currently under construction in Dr. O'Handley's laboratory.

From our perspective, SEMPA is an extremely powerful and unique tool because it could allow us to investigate the effects of misfit dislocations lying at the Ni-Cu interface on the localized behavior of the magnetization vector. As explained in chapter 4, the misfit dislocations are separated by several hundred Angstroms in Ni/Cu (001) when the Ni thickness is smaller than about 50 Å. One should therefore be able to resolve the effects of misfit dislocations, if any, on the local magnetization in Ni/Cu (001)

thin films using SEMPA. We also showed in chapter 4 that the local strain e(x,y,z) due to misfit dislocations, although very localized around dislocation cores, is compressive and significantly larger than the average in-plane biaxial tensile misfit strain e_0. The strain e(x,y,z) could therefore pin the magnetization easy-axis at the dislocation core through the local magnetoelastic anisotropy energy $B^s e$. One can imagine several scenarios for the behavior of the local magnetization easy-axis depending on the distance separating the dislocation lines, the film thickness, the magnitude and sign of B^s at the Ni/Cu (001) interface and at the misfit dislocation cores, and the strength of the exchange interaction in the Ni film.

An interesting scenario is likely to occur in Ni/Cu (001) thin films at Ni thicknesses between 20 Å and 50 Å where the dislocations spacing is several hundred Angstroms. As shown in chapter 6, the magnetization easy-axis is perpendicular to the films in this thickness range. However, if the surface magnetoelastic coefficient at the misfit dislocation core at the Ni/Cu (001) interface is large and positive, $B^s e$ would be large and negative at the dislocation cores and could pin the magnetization in the film plane there. Since the "average" magnetization easy-axis is perpendicular to the films in that thickness range, the preferred direction of the magnetization must be normal to the films in the rectangular regions surrounded by the dislocation lines. By scanning the primary electron beam of SEMPA across a dislocation line along a <110> direction, one could therefore observe the local magnetization going from perpendicular to in-plane and back out-of-plane in an oscillatory, quasi-periodic fashion. We can determine whether or not these very interesting interfacial magnetic phenomena really exist in Ni/Cu (001) thin films only if we have access to a high resolution magnetic probe such as SEMPA.

Other experiments that can further extend our understanding of the magnetic anisotropy in thin films and in particular of perpendicular magnetization include:

• *in-situ* quantitative measurements of the thickness dependence of the strain and of the magnetic anisotropy in epitaxial Ni/Cu/Si (111) thin films to study the effects of the crystallographic orientation of the films;

• *in-situ* quantitative measurements of the temperature dependence of the behavior of the effective magnetic anisotropy energy in Ni/Cu/Si (001) and in Ni/Cu/Si (111);

• *in-situ* quantitative measurements of the thickness dependence of strain and magnetic anisotropy in other thin film systems, especially fcc Fe/Cu and bcc Fe/Ag.

Appendix

Semi-empirical computations of stress relaxation at the Ni-Cu interface: a feasibility study

We emphasized several times throughout this work the importance of strain for understanding the magnetic anisotropy in thin films and multilayers. Strain affects the preferred direction of the magnetization through magnetoelastic interactions. We showed how the average in-plane biaxial misfit strain e_0 always appears in phenomenological equations but we also pointed out that the localized strain e(x,y,z) around misfit dislocations plays an extremely important role since it is very large and can therefore pin the magnetization easy-axis at film-substrate interfaces. Several models have been proposed to describe the thickness dependence of the average in-plane biaxial misfit strain e_0, the most commonly referred to being the Matthews-Blakeslee model. Although this model gives a reasonable approximation to $e_0(h)$, it has several limitations: it is a thermodynamic model; it considers misfit dislocations as the only mechanism for strain relief; it ignores dislocation interactions; and as a continuum model, it induces a singularity at dislocation cores. As far as the computations of the strain e(x,y,z) are concerned, we showed in chapter 4 that the Peierls-Nabarro model yields very interesting results by taking into account the periodicity of the lattice and removing the artificial divergence at dislocation cores. However, this model has several shortcomings: the two crystals that form the interface are both semi-infinite; the model makes use of linear elasticity theory; it ignores dislocations interactions; and it considers 90° dislocations as the only mechanism for strain relief.

Atomistic simulations of the interface structure and energy provide significant improvements over the simple thermodynamic and elastic models described above since

atomic positions, dislocation strain fields, average strain fields, and absolute surface and interface energies can be explicitly determined. Moreover, calculations at finite temperatures are possible. In these computations, interatomic forces are described by the embedded atom method (EAM) which is a many-body scheme that includes both structure-dependent and density-dependent contributions to the total energy of the interface. Although semi-empirical, the method is based on density functional theory which has successfully predicted many of the bulk and the defect properties of fcc or nearly-filled d-band transition metals. In particular, it has proved very effective in reproducing the structural, chemical, and kinetic properties of certain crystalline interfaces such as grain boundaries [Majid *et al.*, 1989; Needles *et al.*, 1992; Countermen *et al.*, 1992].

We have performed preliminary computations on the Ni/Cu (001) interface at T = 0 K using the embedded atom method. The structure consisted of two atomic layers of Ni and two atomic layers of Cu. The Ni square slab was formed by 38x38 unit cells (5776 atoms) whereas the Cu slab was made out of 37x37 unit cells (5476 atoms), thus creating a near-coincidence site lattice with a mismatch of only 0.004%. Periodic boundary conditions were used in the plane (x and y directions) of the structures and the computation took into account the free surfaces of Ni and Cu. The duration of the full relaxation was approximately two and a half hours on a Cray X-MP supercomputer. The results of the calculations are shown graphically in Figs. A1 to A9 which illustrate the positions of the atoms in the four layers before and after the relaxation.

The flat Cu and Ni interface layers are shown in Figs. A1 and A2, respectively, before the relaxation is started. The Cu and Ni surface layers prior to relaxation are identical to the ones shown in Figs. A1 and A2, respectively. Figure A3 is a top view of the Ni-Cu interface prior to relaxation. At the end of the relaxation, the Ni-Cu interface becomes perfectly coherent, as illustrated by Fig. A4. The structures of the four atomic layers following the relaxation are shown in Fig. A5 to A8. The figures indicate that the layers become three-dimensional and have a four-fold symmetry. The structure of the Cu surface layer is very interesting because it indicates that a square grid formed by atoms running along the <110> directions is missing from that layer due to relaxation. This phenomenon is illustrated even better in Fig. A9 which is a top view of the Cu surface layer following the relaxation. It therefore seems that the four layer thick Ni-Cu ultrathin bicrystal cannot support misfit dislocations which apparently propagate to the Cu surface layer leaving behind a perfectly coherent interface. Figure A9 indicates that the dislocations spacing is approximately 100 Å in these structures. Although this

preliminary study shows that computations of strain relaxation at the Ni-Cu interface are feasible with EAM, further computations involving much thicker Cu layers are clearly necessary if these calculations are to accurately complement experimental measurements of strain. If further work were contemplated along these lines, it is suggested to use at least ten layers in the Cu substrate and various thicknesses for the Ni thin film. Further, a larger grid size would reduce the chances that misfit dislocations spacing is influenced by grid size. A full pursuit of these ideas was not possible because of limited computer, manpower, and funding resources.

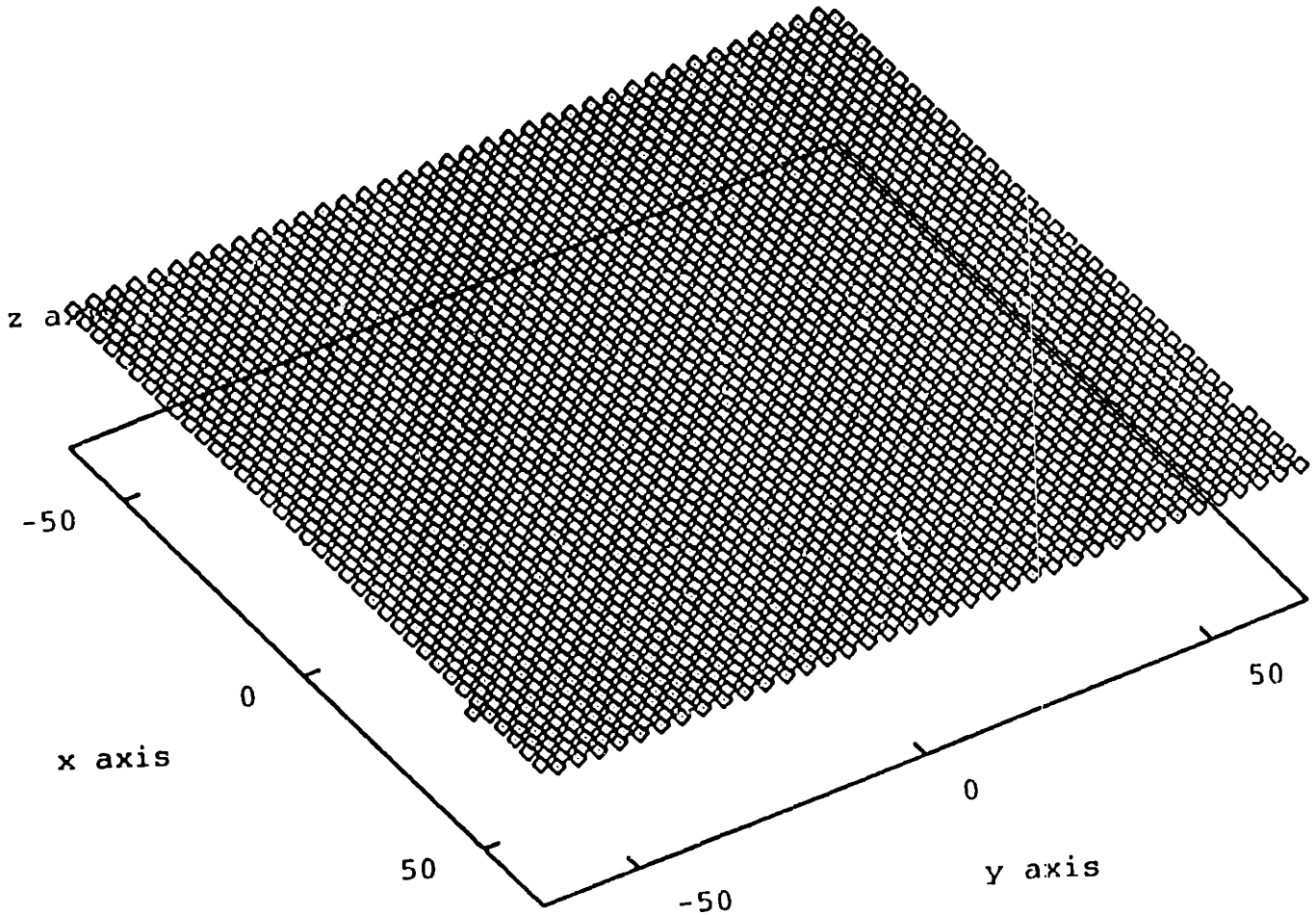

Figure A1: Cu interface layer before relaxation. The dimensions in the x and y axes are in Angstroms.

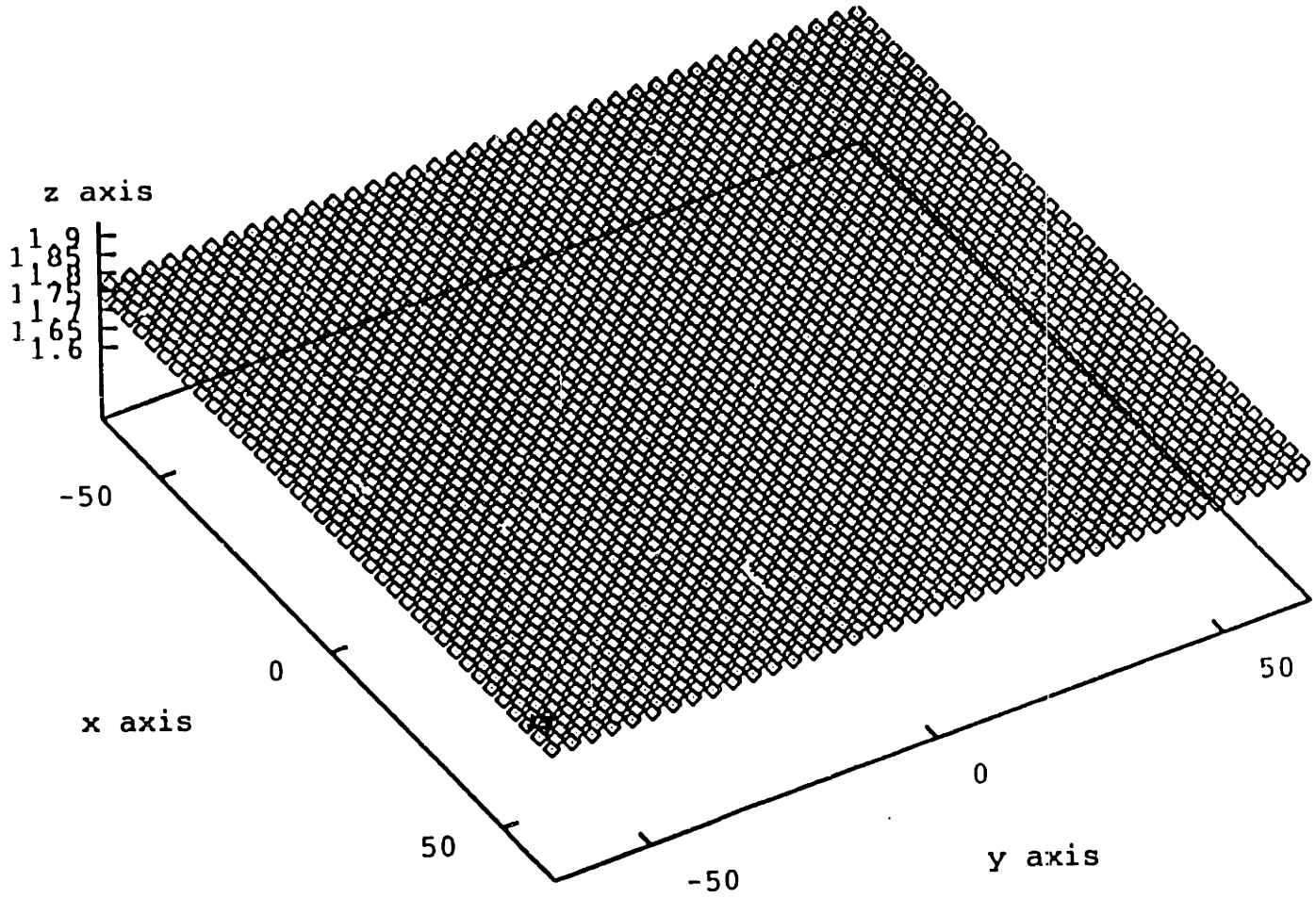

Figure A2: Ni interface layer before relaxation. The dimensions in the x and y axes are in Angstroms.

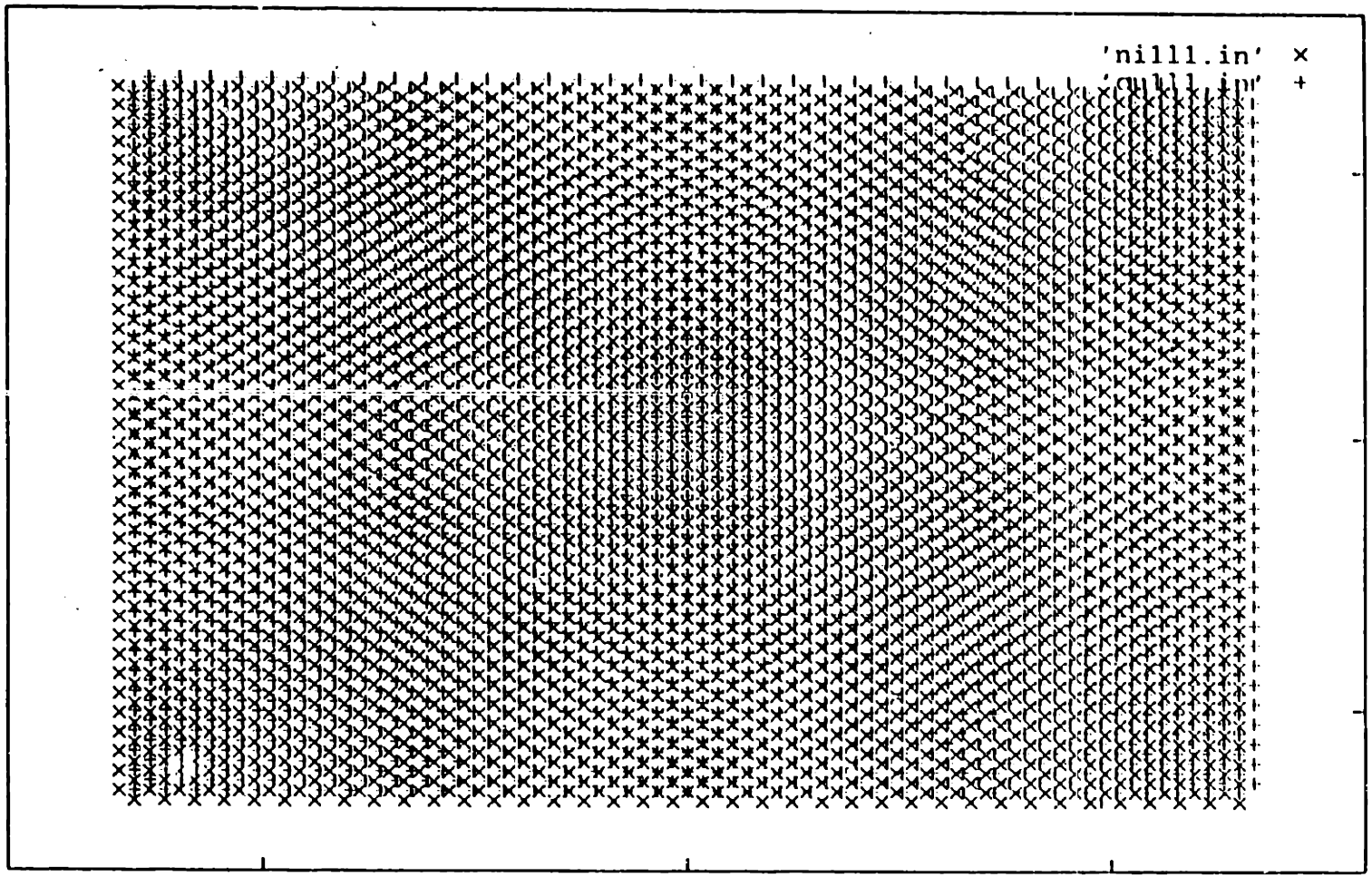

Figure A3: Top view of the Ni-Cu interface before relaxation. The Ni and Cu atoms are indicated by the x and + symbols respectively.

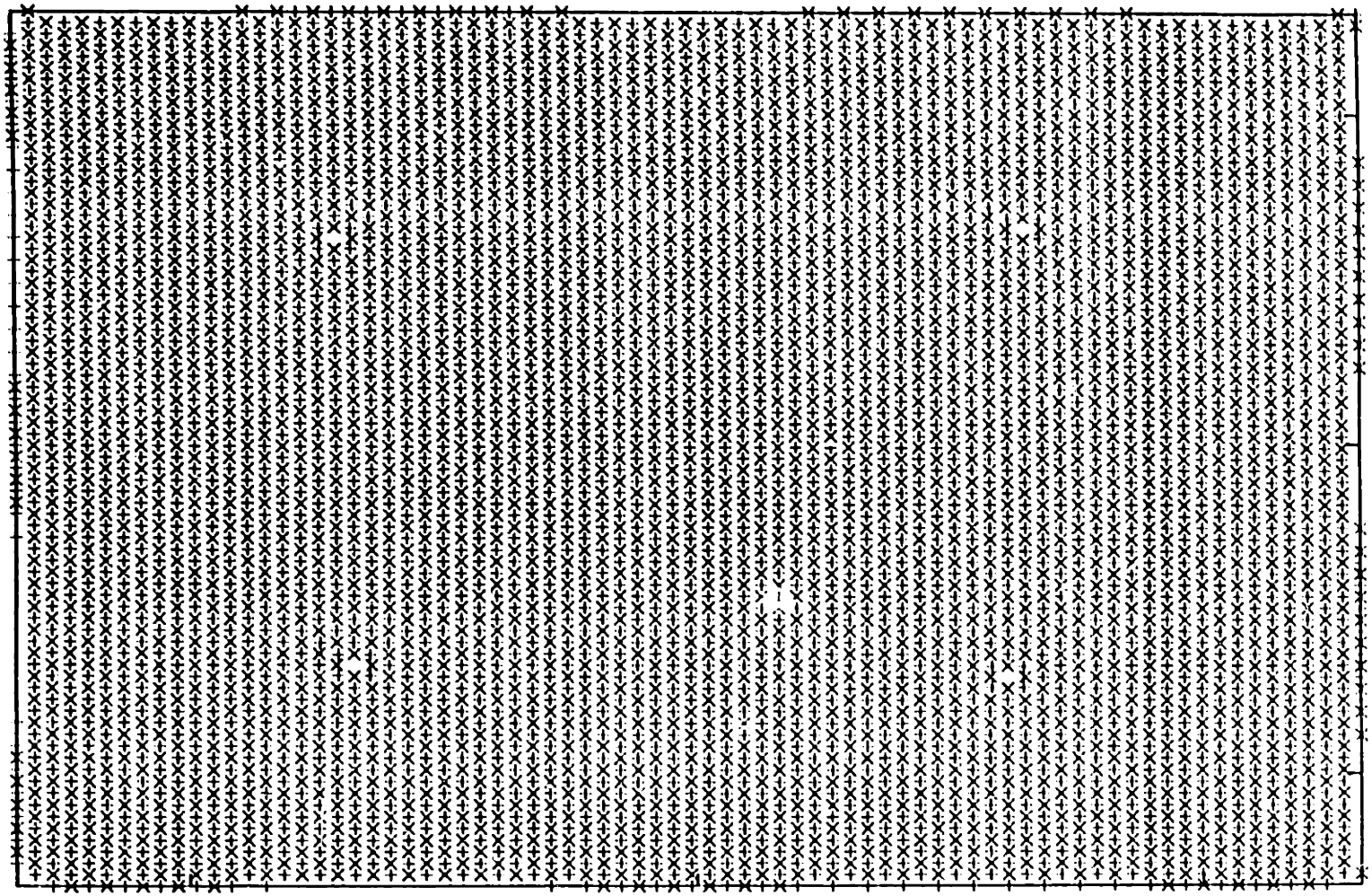

Figure A4: Top view of the Ni-Cu interface after relaxation. The Ni and Cu atoms are indicated by the x and + symbols respectively. The atoms indicate that the interface becomes perfectly coherent after relaxation.

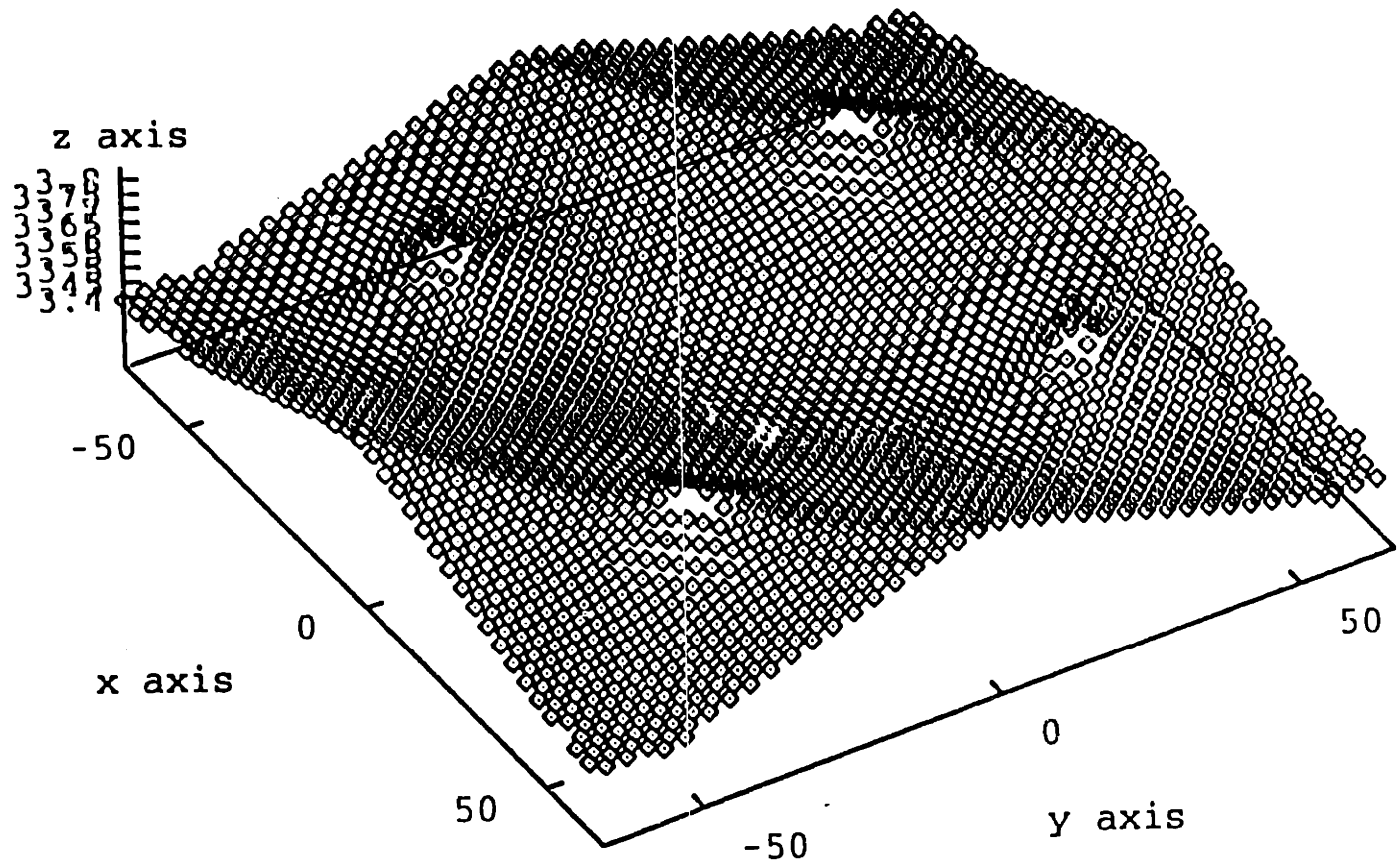

Figure A5: Ni surface layer after relaxation. The dimensions in the x and y axes are in Angstroms.

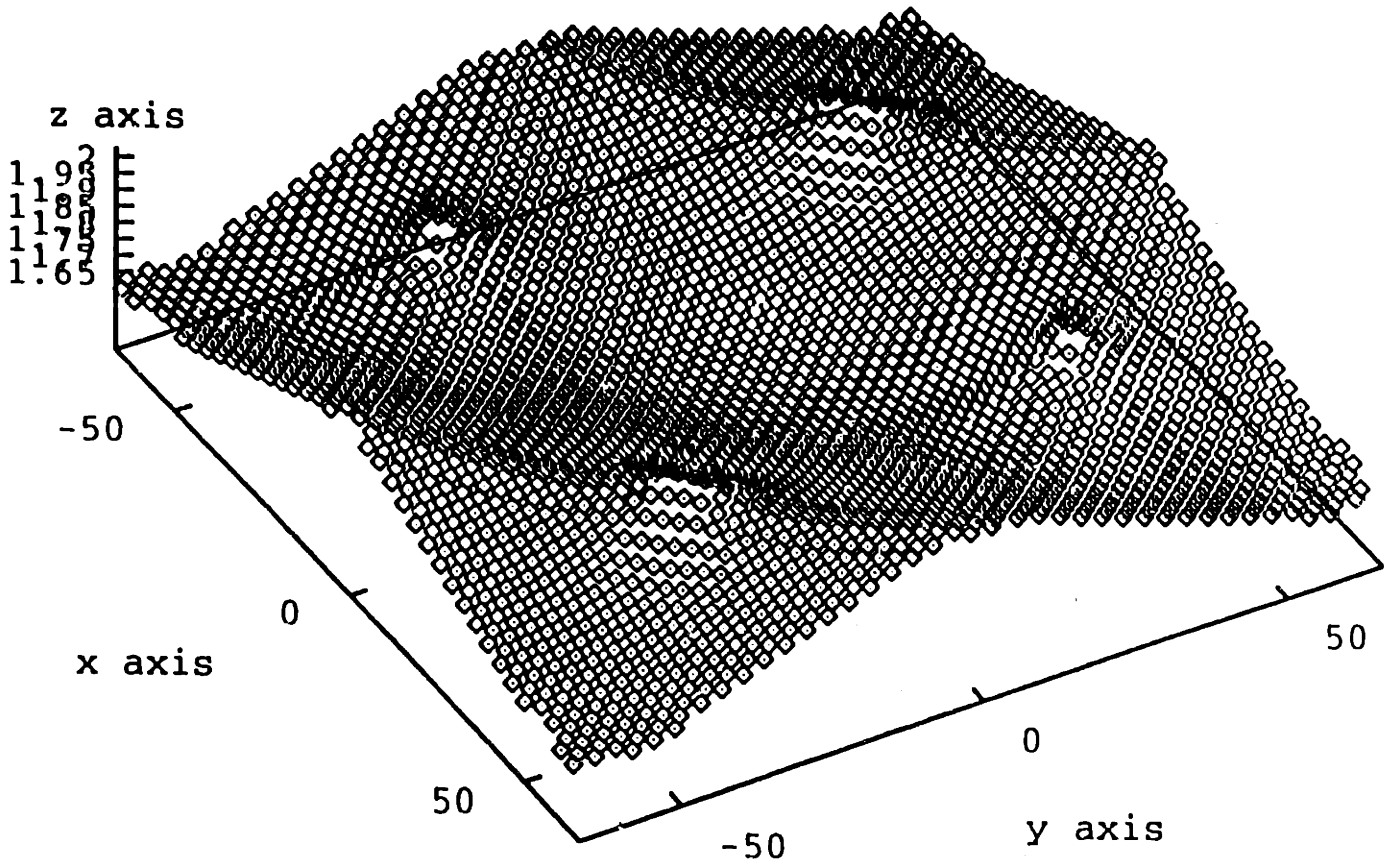

Figure A6: Ni interface layer after relaxation. The dimensions in the x and y axes are in Angstroms.

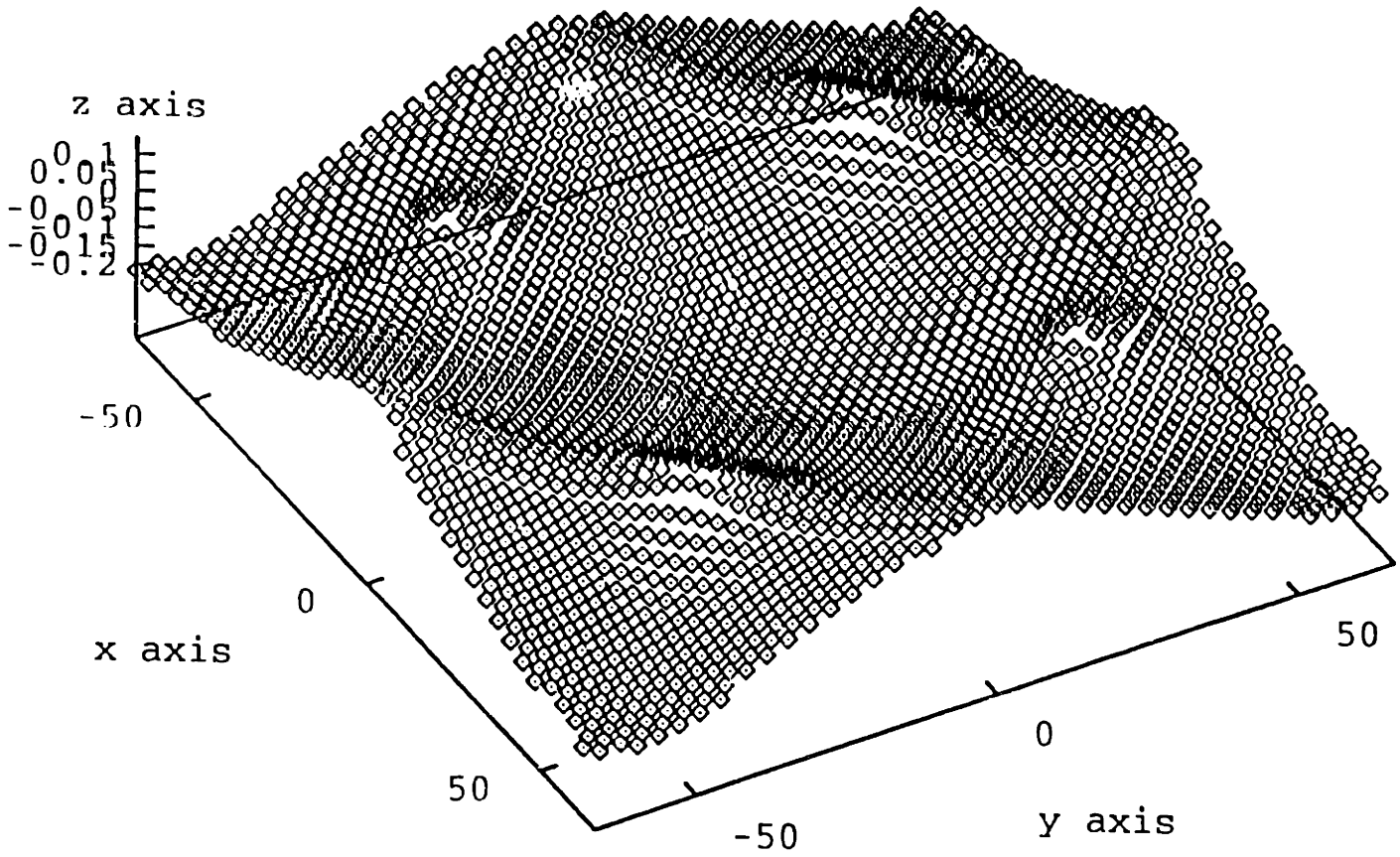

Figure A7: Cu interface layer after relaxation. The dimensions in the x and y axes are in Angstroms.

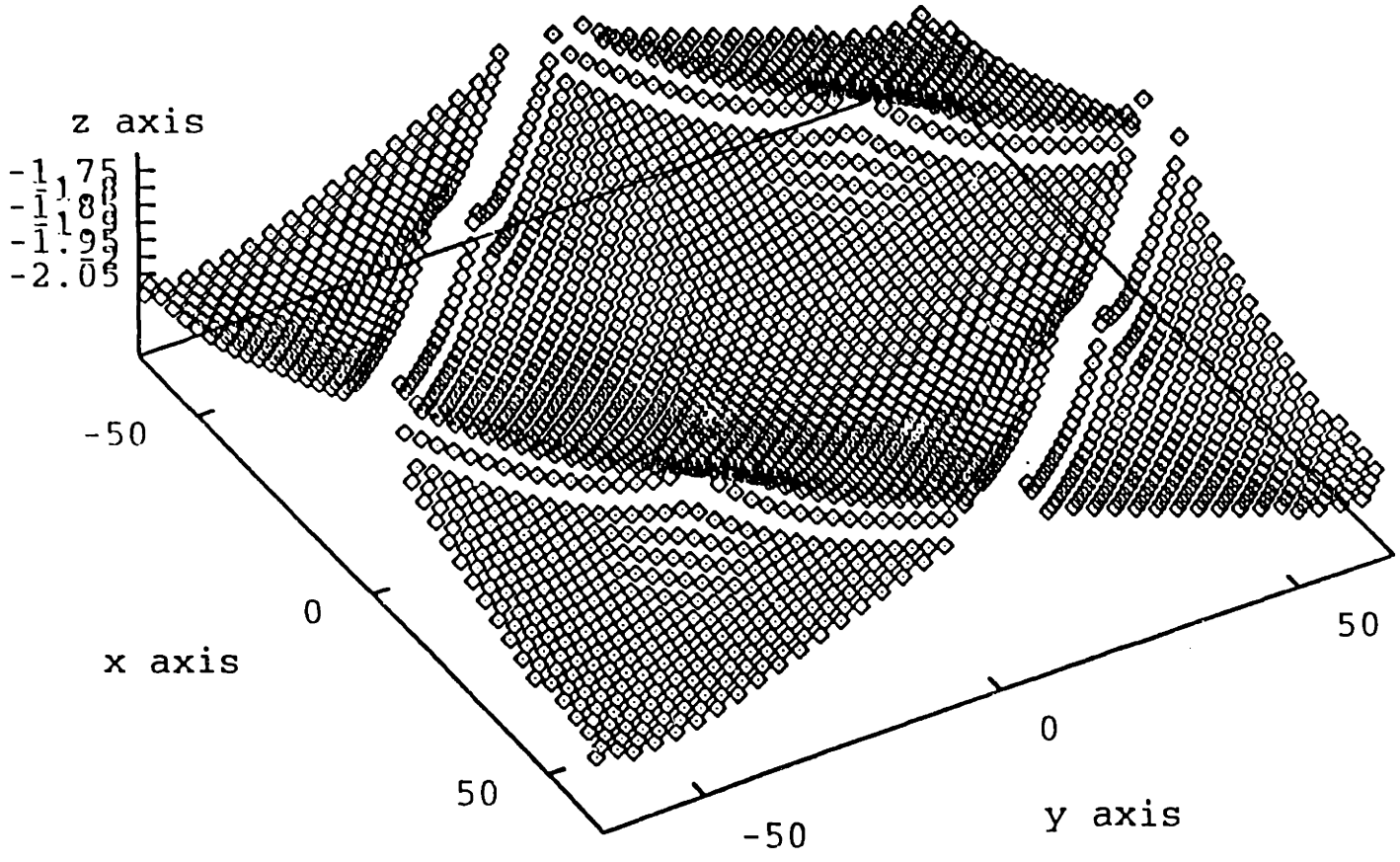

Figure A8: Cu surface layer after relaxation. The dimensions in the x and y axes are in Angstroms.

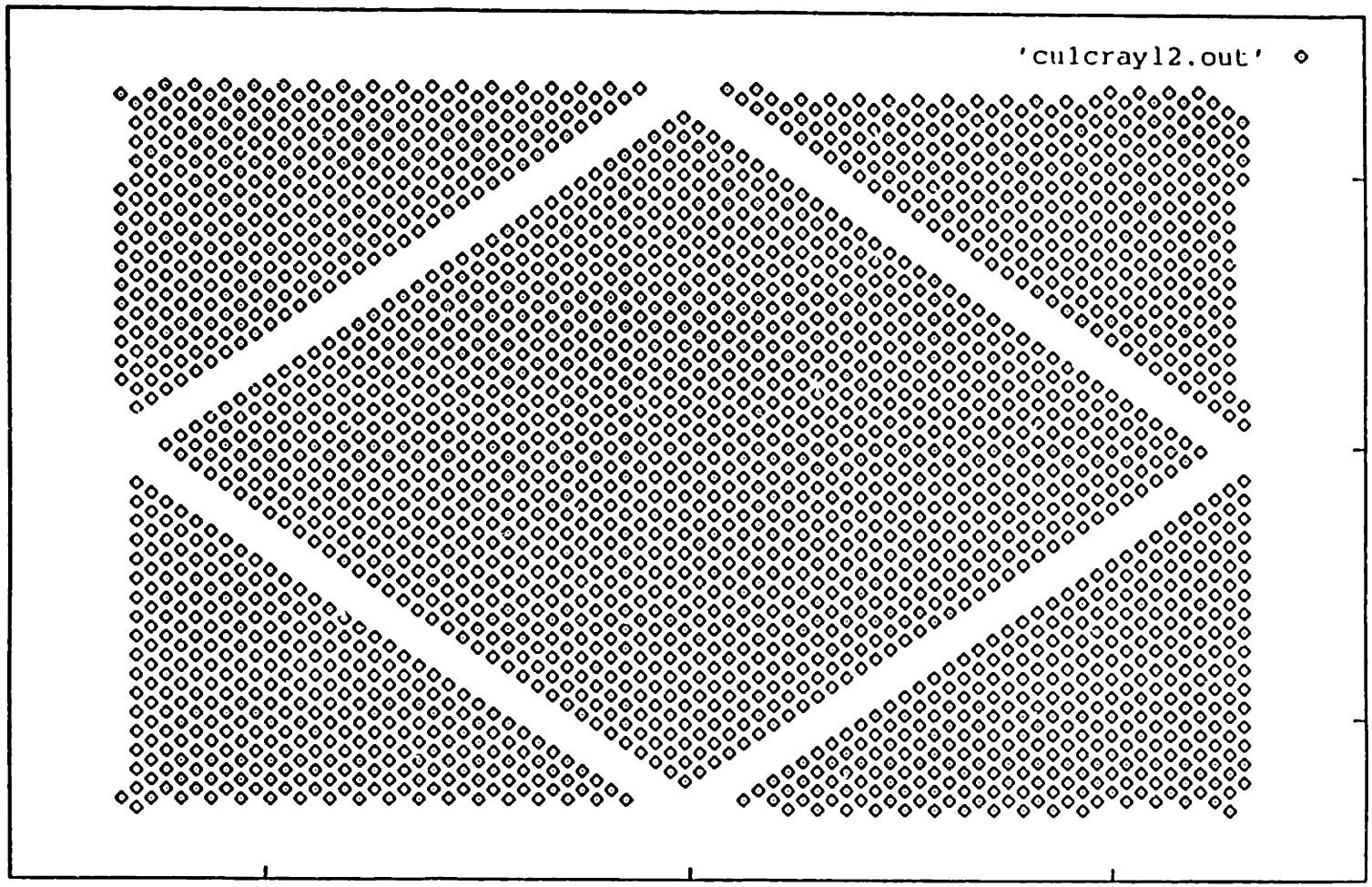

Figure A9: Top view of the Cu surface layer after relaxation. The figure clearly shows the appearance of dislocation-like lines at the Cu surface due to the formation of a coherent Ni-Cu interface.

Bibliography

R. Allenspach, M. Stampanoni, and A. Bischof, Phys. Rev. Lett. **65**, 3344 (1990).

R. Allenspach and A. Bischof, Phys. Rev. Lett. **69**, 3385 (1992).

R. Allenspach, J. Magn. Magn. Mat. **129**, 160 (1994).

J. Araya-Pochet, C. A. Ballentine, and J. L. Erskine, Phys. Rev. B **38**, 7846 (1988).

C. A. Ballentine, Ph. D. Thesis, University of Texas at Austin, 1989.

C. A. Ballentine, R. L. Fink, J. Arayat-Pochet, and J. L. Erskine, Appl. Phys. A **49**, 459 (1989).

S. D. Bader, J. Magn. Magn. Mater. **100**, 440 (1991).

T. Beier, H. Jahrreiss, D. Pescia, Th. Woike, and W. Gudat, Phys. Rev. Lett. **61**, 1875 (1988).

G. Bochi, C. A. Ballentine, H. E. Inglefield, S. S. Bogomolov, C. V. Thompson, and R. C. O'Handley, Mater. Res. Soc. Symp. Proc. **313**, 309 (1993).

G. Bochi, O. Song, and R. C. O'Handley, Phys. Rev. B **50**, 2043 (1994).

P. Bruno and J.-P. Renard, Appl. Phys. A **49**, 499 (1989).

R. C. Cammarata and K. Sieradzki, Phys. Rev. Lett. **62**, 2005 (1989).

A. Chambers and D. C. Jackson, Philos. Mag. **31**, 1357 (1975).

D. D. Chambliss, R. J. Wilson, and S. Chang, J. Vac. Sci. Technol. A **10**, 1993 (1992).

C.-A. Chang, J. Vac. Sci. Technol. A **8**, 3779 (1990).

C.-A. Chang, J. Appl. Phys. **67**, 566 (1990).

C.-A. Chang, J. Appl. Phys. **68**, 4873 (1990).

C.-A. Chang, J. Magn. Magn. Mater. **92**, L1 (1990).

C.-A. Chang, J. C. Liu, and J. Angilello, Appl. Phys. Lett. **57**, 2239 (1990).

C. Chappert and P. Bruno, J. Appl. Phys. **64**, 5736 (1988).

Y. Chen, S. T. Tong, J. S. Kim, M. H. Mohamed, and L.L. Kesmodel, Phys. Rev. B **43**, 6788 (1991).

S. Chikazumi, Physics of Magnetism, Krieger Publishing Company, 1964.

D. S. Chuang, C. A. Ballentine, and R. C. O'Handley, Phys. Rev. B **49,** 15084 (1994).

D. S. Chuang, Ph. D. Thesis, Massachusetts Institute of Technology, September 1994.

B. M. Clemens, R. L. White, W. D. Nix, and J. A. Bain, Mater. Res. Soc. Symp. Proc. **231**, 459 (1991).

C. A. Countermen, I. Majid, P. D. Bristowe, and R. W. Balluffi, Mater. Res. Soc. Symp. Proc. **238**, 449 (1992).

CRC handbook of chemistry and physics, D. R. Lide editor, 71st edition, CRC press Inc.

G. H. O. Daalderop, P. J. Kelly, and F. J. A. den Broeder, Phys. Rev. Lett. **68**, 682 (1992).

H. L. Davis, J. B. Hannon, K. B. Ray, and E. W. Plummer, Phys. Rev. Lett. **68**, 2632 (1992).

F. J. A. den Broeder, W. Hoving, and P. J. H. Bloemen, J. Magn. Magn. Mater. **93**, 562 (1991).

D. J. Dunstan, S. Young, and R. H. Dixon, J. Appl. Phys. **70**, 3038 (1991).

W. F. Egelhoff, in Ultrathin Magnetic Structures I: an Introduction to Electronic, Magnetic and Structural Properties, J. A. C. Bland and B. Heinrich, Eds., Springer-Verlag, Berlin, 1994.

W. F. Egelhoff and D. A. Steigerwald, J. Vac. Sci. Technol. A **7**, 2167 (1989).

B. N. Engel, C. D. England, R. A. Van Leeuwen, M. H. Wiedmann, and C. M. Falco, Phys. Rev. Lett. **67**, 1910 (1991).

B. N. Engel, C. D. England, R. A. Van Leeuwen, M. H. Wiedmann, and C. M. Falco, J. Appl. Phys. **70**, 5873 (1991).

L. M. Falicov, Physics Today, October 1992 issue, p. 46.

L. M. Falicov, D. T. Pierce, S. D. Bader, R. Gronsky, K. B. Hathaway, H. J. Hopster, D. N. Lambeth, S. S. P. Parkin, G. A. Prinz, M. Salamon, I. K. Schuller, and R. H. Victora, J. Mater. Soc. **5**, 1299 (1990).

F. C. Franck and J. H. van der Merwe, Proc. Roy. Soc. Lond. **189** Ser. A, 205 (1949).

A. J. Freeman and C. L. Fu, J. Appl. Phys. **61**, 3356 (1987).

A. J. Freeman and K. A. Gschneider, Editors, Magnetism in the Nineties, North-Holland, 1991.

C. L. Fu and A. J. Freeman, Phys. Rev B **35**, 925 (1987).

H. Fujiwara, H. Kadomatsu, and T. Tokaunaga, J. Magn. Magn. Mat. **31**, 809 (1983).

J. G. Gay and R. Richter, Phys. Rev. Lett. **56**, 2728 (1986).

D. W. Gidley, Phys. Rev. Lett. **62**, 811 (1989).

U. Gradmann, Ann. Physik **7**, 91 (1966).

U. Gradmann, Appl. Phys. **3**, 161 (1974).

U. Gradmann, J. Magn. Magn. Mat. **54**, 733 (1986).

U. Gradmann, Magnetism in ultrathin transition metal films; in the Handbook of Magnetic Materials, Vol. 7, Elsevier Science Publishers B. V., 1993.

G. C. Hadjipanayis and G. A. Prinz, Editors, Science and Technology of Nanostructured Magnetic Materials, Plenum Press, 1991.

S. Hashimoto, Y. Ochiai, and K. Aso, J. Appl. Phys. **67**, 2136 (1990).

O. Heckmann, H. Magnan, P. Lefevre, and D. Chandesris, Mater. Res. Soc. Symp. Proc. **313**, 245 (1993).

B. Heinrich, K. B. Urquhart, A. S. Arrott, J. F. Cochran, K. Myrtle, and S. T. Purcell, Phys. Rev. Lett. **59**, 1756 (1987).

B. Heinrich, J. F. Cochran, A. S. Arrott, S. T. Purcell, K. B. Urquhart, J. R. Dutcher, and W. F. Egelhoff, Appl. Phys. A **49**, 473 (1989).

J. P. Hirth and J. Lothe, Theory of Dislocations, second edition, Krieger Publishing Company, 1992.

F. Huang, G. J. Mankey, M. T. Kief, and R. F. Willis, J. Appl. Phys. **73**, 6760 (1993).

F. Huang, M. T. Kief, G. J. Mankey, and R. F. Willis, Phys. Rev. B **49**, 3962 (1994).

H. E. Inglefield, C. A. Ballentine, G. Bochi, S. S. Bogomolov, R. C. O'Handley, and C. V. Thompson, Mater. Res. Soc. Symp. Proc. **308**. 765 (1993).

H. E. Inglefield, G. Bochi, C. A. Ballentine, R. C. O'Handley, and C. V. Thompson, Materials Research Society Conference Proceedings, Fall 1994, Boston (in press).

H. E. Inglefield, unpublished.

H. E. Inglefield, Ph. D. Thesis, Massachusetts Institute of Technology, 1995.

R. Jungblut, M. T. Johnson, J. aan de Stegge, A. Reinders, and F. J. A. den Broeder, J. Appl. Phys. **75**, 6424 (1994).

C. K. Kim, Ph. D. Thesis, Massachusetts Institute of Technology, 1991.

T. Kingetsu and K. Sakai, J. Appl. Phys. **73**, 7622 (1993).

T. Kingetsu and K. Sakai, Phys. Rev. B **48**, 4140 (1993).

N. C. Koon, B. T. Jonker, F. A. Volkening, J. J. Krebs, and G. A. Prinz, Phys. Rev. Lett. **59**, 2463 (1987).

P. Krams, F. Lauks, R. L. Stamps, B. Hillebrands, and G. Güntherodt, Phys. Rev. Lett. **69**, 3674 (1992).

M. G. Lagally and D. E. Savage, MRS Bulletin, January 1993.

F. J. Lamelas, C. H. Lee, Hui He, W. Vavra, and Roy Clarke, Phys. Rev. B **40**, 5837 (1989).

Landolt-Börnstein Numerical Data and Functional Relationships in Science and Technology, vol. 18, K.- H. Hellwege and O. Madelung, eds., Springer-Verlag, 1984.

C. H. Lee, Hui He, F. J. Lamelas, W. Vavra, C. Uher, and Roy Clarke, Phys. Rev. B **42**, 1066 (1990).
C. Liu, E. R. Moog, and S. D. Bader, Phys. Rev. Lett. **60**, 2422 (1988).
I. Majid, P. D. Bristowe, and R. W. Balluffi, Phys. Rev. B **40**, 2779 (1989).
G. J. Mankey, M. T. Kief, and R. F. Willis, J. Vac. Sci. Technol. **A7**, 1595 (1991).
T. B. Massalski, editor-in-chief; H. Okamoto, P. R. Subramanian, and L. Kacprzak, editors. Binary Alloy Phase Diagrams, second edition, volume 2, 1990.
J. W. Matthews and J. L. Crawford, Thin Solid Films **5**, 187 (1970).
J. W. Matthews and A. E. Blakeslee, J. Cryst. Growth **27**, 118 (1974).
J. W. Matthews and A. E. Blakeslee, J. Cryst. Growth **29**, 273 (1975).
J. W. Matthews, J. Vac. Sci. Technol. **12**, 126 (1975).
M. H. Mohamed, J. S. Kim, and L. L. Kesmodel, Phys. Rev. B **40**, 1305 (1989).
R. Naik, C. Kota, J. S. Payson, and G. L. Dunifer, Phys. Rev. B **48**, 1008 (1993).
M. Needels, A. M. Rappe, P. D. Bristowe, and J. D. Joanopoulos, Phys. Rev. B **46**, 9768 (1992).
L. Néel, Compt. Rend. **237**, 1468 (1953).
L. Néel, J. Phys. Radium **15**, 225 (1954).
W. D. Nix, Metall. Trans. A **20**, 2217 (1989).
H. P. Oepen and J. Kirschner, Phys. Rev. Lett. **62**, 819 (1989).
R. C. O'Handley, Magnetic Materials: Principles and Applications, unpublished.
R. C. O'Handley and J. Woods, Phys. Rev. B **42**, 6568 (1990).
R. C. O'Handley and S. W. Sun, Mater. Res. Soc. Proc. **231**, 485 (1992).
R. C. O'Handley, O. Song, and C. A. Ballentine, J. Appl. Phys. **74**, 6302 (1993).
R. C. O'Handley and O. Song, Proceedings of the 3rd IUMRS - International Conference on Advanced Materials, Tokyo, 08/31 - 09/04, 1993 (V Ea 10.4).
M. Ohring, The Materials Science of Thin Films, Academic Press, 1992.
S. Ould-Mahfoud, R. Megy, N. Bardou, B. Bartenlian, P. Beauvillain, C. Chappert, J. Corno, B. Lecuyer, G. Sczigel, P. Veillet, and D. Weller, Mater. Res. Soc. Symp. Proc. **313**, 251 (1993).
D. P. Pappas, K.-P. Kämper, and H. Hopster, Phys. Rev. Lett. **64**, 3179 (1990).
D. P. Pappas, K.-P. Kämper, B. P. Miller, H. Hopster, D. E. Fowler, A. C. Luntz, C. R. Brundle, and Z.-X. Shen, J. Appl. Phys. **69**, 5209 (1991).
A. P. Payne, W. D. Nix, B. M. Lairson, and B. M. Clemens, Phys. Rev. B **47**, 13730 (1993).
D. Pescia, M. Stampanoni, G. L. Bona, A. Vaterlaus, R. F. Willis, and F. Meier, Phys. Rev. Lett. **58**, 2126 (1987).

D. Pescia, G. Zampieri, M. Stampanoni, G. L. Bona, R. F. Willis, and F. Meier, Phys. Rev. Lett. **58**, 933 (1987).

D. Pescia, M. Stampanoni, G. L. Bona, A. Vaterlaus, F. Meier, G. Jennings, and R. F. Willis, Phys. Rev. Lett. **60**, 2559 (1988).

Z. Q. Qiu, J. Pearson, and S. D. Bader, Phys. Rev. Lett. **70**, 1006 (1993).

C. Rau and M. Robert, Phys. Rev. Lett. **58**, 2714 (1987).

V. Rogge and H. Neddermeyer, Phys. Rev. B **40**, 6030 (1989).

J. M. Slaughter, W. Weber, G. Güntherodt, and C. M. Falco, MRS Bulletin, December 1992.

J. R. Smith and A. Banerjea, Phys. Rev. Lett. **59**, 2451 (1987).

O. Song, Ph.D. Thesis, Massachusetts Institute of Technology, May 1994.

O. Song, C. A. Ballentine, and R. C. O'Handley, Appl. Phys. Lett. **64**, 1 (1994).

B. J. Spencer, P. W. Voorhees, and S. H. Davis, J. Appl. Phys. **73**, 4955 (1993).

B. J. Spencer, S. H. Davis, and P. W. Voorhees, Phys. Rev. B **47**, 9760 (1993).

M. Stampanoni, A. Vaterlaus, M. Aeschlimann, and F. Meier, Phys. Rev. Lett. **59**, 2483 (1987).

D. A. Steigerwald, I. Jacob, and W. F. Egelhoff, Surf. Sci. **202**, 472 (1988).

D. A. Steigerwald and W. F. Egelhoff, Phys. Rev. Lett. **60**, 2558 (1988).

S. W. Sun and R. C. O'Handley, Phys. Rev. Lett. **66**, 2798 (1991).

L. J. Swartzendruber, L. H. Bennett, M. T. Kief, and W. F. Egelhoff, Jr., Mater. Res. Soc. Symp. Proc. **313**, 237 (1993).

J. Tersoff and L. M. Falicov, Phys. Rev. B **26**, 6186 (1982).

J. Thomassen, F. May, B. Feldmann, M. Wuttig, and H. Ibach, Phys. Rev. Lett. **69**, 3831 (1992).

L. H. Tjeng, Y. U. Idzerda, P. Rudolf, F. Sette, and C. T. Chen, J. Appl. Phys. **70**, 5939 (1991).

J. Y. Tsao, Materials Fundamentals of Molecular Beam Epitaxy, chapter 5, Academic Press, 1993.

J. H. van der Merwe, J. Appl. Phys. **34**, 123 (1963).

J. H. van Vleck, Phys. Rev. **52**, 1178 (1937).

R. H. Victora and J. M. MacLaren, Phys. Rev. B **47**, 11583 (1993).

D. Wang, R. Wu, and A. J. Freeman, Phys. Rev. Lett. **70**, 869 (1993).

M. Weber, R. Koch, and K. H. Rieder, Phys. Rev. Lett. **73**, 1166 (1994).

R. L. White, IEEE Transactions on Magnetics **28**, 2482 (1992).

M. H. Wiedmann, B. N. Engel, R. A. Van Leeuwen, K. Mibu, T. Shinjo, and C. M. Falco, Mater. Res. Soc. Symp. Proc. **313**, 531 (1993).

C. L. Wooten, J. Chen, G. A. Mulhollan, J. L. Erskine, and J. T. Markert, Phys. Rev. B **49**, 10023 (1994).

A. Yamaguchi, S. Ogu, W.-H. Soe, and R. Yamamoto, Appl. Phys. Lett. **62**, 1020 (1993).

W. B. Zeper, H. W. van Kesteren, B. A. J. Jacobs, and J. H. M. Spruit, J. Appl. Phys. **70**, 2264 (1991).

X. Zhu, H. Huang, and J. Hermanson, Phys. Rev. B **29**, 3009 (1984).

R. Zuberek, H. Szymczak, R. Krishnan, and M. Tessier, J. de Phys. C **49**, 1761 (1988).

Biographical Note

Gabriel Bochi was born in Beirut, Lebanon on March 25, 1969. While in Beirut, he attended the Collège du Sacré-Cœur for one year. He lived in Cairo, Egypt between 1976 and 1979 where he attended the Collège de la Salle. Between 1979 and 1987, he lived in Milan, Italy, where he attended the Sainte Jeanne d'Arc French School first (1979-1980) and then the Lycée Stendhal (1980-1987) French School. He obtained his French Baccalauréat in Mathematics and Physics from the Academy of Grenoble, France, in June 1987. In 1987, he moved to Montreal, Canada, to attend McGill University. He obtained a Bachelor of Science in Physics with First Class Honors in June 1990. While at McGill, he was named twice Faculty Scholar, he received a William MacDonald Scholarship, won an undergraduate Natural Sciences and Engineering Research Council (NSERC) summer scholarship to work with Prof. J. Barrette at the Foster Radiation Laboratory of McGill (summer 1989), and obtained a two-year NSERC Postgraduate Scholarship. The author started his graduate education in the fall of 1990 at M.I.T. in the Department of Aeronautics and Astronautics. In the spring of 1991, he was a Teaching Assistant in the Department of Physics for the introductory course in Electricity and Magnetism (8.02). He joined the group of Dr. R. C. O'Handley in June 1991 to start his doctoral research in Materials Science and Engineering with a concentration in Electronic Materials. In the spring of 1994, he was a Teaching Assistant to Prof. Tuller in the graduate course on Electronic Materials Design (3.42).